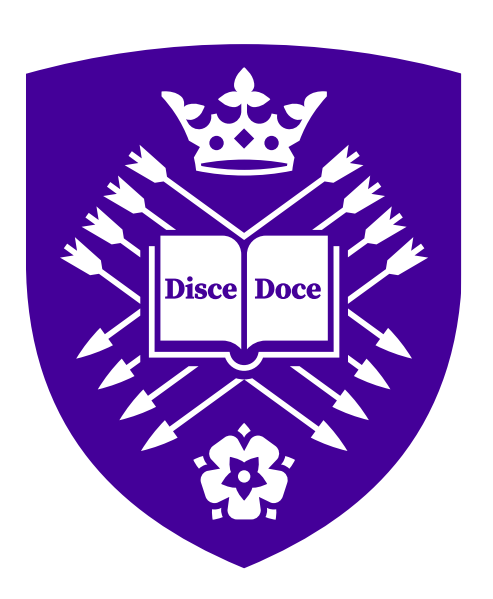
The Investigation, Development, and Analysis of Models of Electrodialysis

Jack Ledingham



AUGUST 2024

THE UNIVERSITY OF SHEFFIELD

Department of Chemical and Biological Engineering

Doctor of Philosophy

Acknowledgements

All that I am and all that I have I owe to those around me. My family, my friends, mentors, and teachers I thank you all for what you have given me. Now my formal education is finally complete, I want to give my sincere gratitude for those who got me here.

My parents, thank you for your unending belief in me and your eternal support. Thank you for investing so much in my upbringing and my education, I hope you feel that it paid off - you can call this thesis a dividend payment. You never stipulated what I had to do with my life but were always there driving me to be the best version of myself. It was the placid guiding hand I needed and for that I will forever be grateful. All my successes I attribute to you

All through my life my family has been the one constant. Thank you to my brother, aunts, cousins, and grandparents for the parts you played throughout my life. To my grandmas, I will endeavour to keep making you proud.

New friends, old friends, my path in life would not be the same if it were not for you. Alex, it was genuinely one of the greatest pleasures of my life being your friend these last few years. You are a man of immaculate taste and lightning wit, and although my liver may be significantly worse off, take it as a compliment that I struggle to say no to the next beer when you're asking. Yash, I'm always in awe of your ability to tell a great story and apropos of nothing make me burst. Lottie, thank you for providing the chaotic fun and being a suitable distraction from oft monotonous work. Ed, for replying to that message and being the first friend I made in Sheffield. Minos, for keeping me sane during lockdown through the state-mandated long walks and many dinners together. Abrar, for being there for me when I needed you and always replying so promptly to my texts. Ian, thanks for being my oldest friend and the decade-and-a-half of memories. Brandon and Kathryn, thanks for the weekly escape from reality.

Kyra and Alasdair, thank you for your guidance and mentorship over these last few years. I appreciate the faith you had in my abilities and the wisdom you had to step in when needed. I am undoubtedly a better thinker as a result. Ben and Lucas, thank you for always being available to provide an industrial perspective to my research. Having you as a regular audience to present was invaluable for framing my work and building my confidence. Samy, thank you for believing in me and making this PhD project possible.

To Grant Sanderson, thank you for showing me the emergent beauty that comes from solving problems and how a change in perspective can be worth 80 IQ points. Dan Olson, thank you for showing me the intense satisfaction that arises from unbridled obsession and how the right narrative can make even the most complex topics understandable. James and Mason, thank you for the hundreds of hours of red-hot content

And finally, thank you to the £2 coin that I correctly called tails on the 22nd of May 2019.



 $Honnor\ thy\ error\ as\ hidden\ intention$

- Brian Eno



${\bf Contents}$

| List of I | Publications | vii |
|-----------|--|------|
| Abstrac | zt | viii |
| Chapter | r 1: Introduction | 1 |
| 1.1 | Background | 2 |
| 1.2 | Research aims and objectives | 5 |
| 1.3 | Methods of water treatment: why electrodialysis? | 6 |
| 1.4 | Electrodialysis engineering and phenomenological description | 8 |
| 1.4. | 1 Engineering design and transport phenomena | 8 |
| 1.4. | 2 Ion exchange membranes | 11 |
| 1.4. | 3 Cost optimisation: ED and RO | 13 |
| 1.5 | Electrodialysis variations | 15 |
| Chapter | r 2: Contextualisation to literature | 19 |
| 2.1 | Introduction | 20 |
| 2.2 | Methods of ED modelling | 21 |
| 2.2. | 1 Nernst-Planck models | 22 |
| 2.2. | 2 Circuit-based models | 23 |
| 2.2. | 3 Semi-empirical models | 24 |
| 2.2. | 4 Non-equilibrium thermodynamic models | 25 |
| 2.3 | Investigation of stipulated-equation models | 26 |
| 2.3. | 1 Differing model aspects | 28 |
| 2.3. | 2 Further established model commonalities | 33 |
| 2.4 | Computational fluid dynamics simulations | 36 |
| 2.4. | 1 Overview | 36 |
| 2.4. | 2 Applications of CFD in ED modelling | 41 |
| 2.4. | 3 Model validation | 45 |
| 2.5 | Conclusion | 46 |
| Part I: | Maldistribution in Electrodialysis | 49 |
| Chapter | r 3: Maldistribution though simulation | 51 |
| 3.1 | Introduction | 52 |
| 3.2 | Model development | 54 |
| 3.2. | 1 Ansys Fluent CFD model | 54 |
| 3.2. | 2 Dimensionless maldistribution model | 56 |



| 3.2.3 | Limiting current density model | 58 |
|------------|---|-------|
| 3.2.4 | Resistance model | 61 |
| 3.3 | Results – quantifying maldistribution | 62 |
| 3.3.1 | Maldistribution model validation | 63 |
| 3.3.2 | Inlet flow rate | 65 |
| 3.3.3 | Channel width | 66 |
| 3.3.4 | Distributor angle | 67 |
| 3.3.5 | Number of manifolds | 69 |
| 3.3.6 | Number of cell pairs | 70 |
| 3.3.7 | Length-to-width ratio | 71 |
| 3.4 | Consequences of maldistribution | 72 |
| 3.4.1 | Limiting current density | 72 |
| 3.4.2 | Stack resistance | 75 |
| 3.5 | Maldistribution of Z-configuration stacks | 76 |
| 3.6 | Conclusion | 79 |
| Chapter 4 | 4: Experimental validation of maldistribution | 81 |
| 4.1 | Introduction | |
| 4.2 | Validating the presence of maldistribution using red-blue PIV | |
| 4.2.1 | Method | |
| 4.2.1 | Results and discussion | |
| 4.2.2 | Statistical analysis | |
| 4.2.3 | PIV experimental setup | |
| | Validation of the effect of maldistribution on the limiting current density | |
| 4.3.1 | Method | |
| 4.3.2 | Results and discussion | |
| 4.4 | Conclusion | 101 |
| D / II 1 | | |
| Part II: N | Modelling Electrodialysis | . 103 |
| Chapter | 5: A model of conventional ED | . 105 |
| 5.1 | Introduction | 106 |
| 5.1.1 | Background and motivation | 106 |
| 5.1.2 | Modelling strategies for electrodialysis | 108 |
| 5.2 | Model development | 112 |
| 5.2.1 | Model overview | 112 |
| 5.2.2 | Inner layer: computing current density | 113 |
| 5.2.3 | Middle layer: electrical resistance and spatial material balance | 114 |



| 5.2.4 | Outer layer: temporal material balance | 119 |
|----------|--|-----|
| 5.3 | Model validation | 121 |
| 5.3.1 | Validation methods | 121 |
| 5.3.2 | Temporal experimental validation | 121 |
| 5.3.3 | Steady-state validation | 126 |
| 5.4 | Exploration of novel model aspects | 129 |
| 5.5 | Conclusion | 131 |
| 5.6 | Tabulated model | 133 |
| 5.7 | Nomenclature | |
| Chapter | 6: A model of bipolar membrane ED | 137 |
| 6.1 | Introduction | |
| 6.2 | Model formulation | |
| 6.2.1 | Inner layer: solving for current density | |
| 6.2.2 | | |
| 6.2.3 | · | |
| 6.3 | Experimental validation | |
| 6.3.1 | Temporal validation | |
| 6.3.2 | - | |
| 6.4 | Model exploration | |
| 6.4.1 | The impact of a delayed temporal balance | |
| 6.4.1 | Investigating the rate of reactions | |
| 6.5 | Conclusion | |
| 6.6 | Tabulated model | |
| 6.7 | Nomenclature | |
| | | |
| Chapter | 7: Conclusion and future work | |
| 7.1 | Thesis conclusion | |
| 7.2 | Future work | |
| 7.2.1 | Predictive maldistribution | |
| 7.2.2 | Maldistribution on scaleup and remediation | |
| 7.2.3 | | |
| 7.2.4 | | |
| 7.3 | Final thoughts | |
| Cited wo | rke | 18/ |



<thesis>



List of Publications

Publications are listed in the order they were published. The chapters of this thesis that use material from the papers are given too. Abridgements and additions are described in footnotes in the appropriate sections

Author contributions: All papers are the direct work of JL, with co-authors providing supervisory support. KSC and ANC provided ongoing supervision at the University of Sheffield. BIV and LK provided supervision from an industrial sponsor. JH gave support for specific instrumentation used in one set of experiments (Section 4.2). NYY assisted with one aspect of modelling used in both Chapters 5 and 6.

Ledingham, J., Campbell, K.L.S., in 't Veen, B., Keyzer, L. and Campbell, A.N., 2022. Barriers to electrodialysis implementation: Maldistribution and its impact on resistance and limiting current density. Desalination, 531, p.115691. https://doi.org/10.1016/j.desal.2022.115691 (Chapter 3)

Ledingham, J., Campbell, K.L.S., in 't Veen, B., Keyzer, L., Yip, N.Y. and Campbell, A.N., 2024. The development and validation of a novel, parameter-free, modelling strategy for electromembrane processes: Electrodialysis. Desalination, 576, p.117386. https://doi.org/10.1016/j.desal.2024.117386 (Chapter 5)

Ledingham, J., Campbell, K.L.S., Keyzer, L., Yip, N.Y. and Campbell, A.N., 2024. The development and evaluation of a parameter-free circuit-based model of bipolar membrane electrodialysis for process design and optimisation. Chemical Engineering Journal, 497, p.154895. https://doi.org/10.1016/j.cej.2024.154895 (Chapter 6)

A paper was submitted to the Journal of Membrane science on the 24th of July 2024 under the title 'Experimental validation of the presence of maldistribution in electrodialysis and its effect on the limiting current density' by Ledingham, J., Howse, J., Campbell, A.N., in 't Veen, B., Keyzer, L., and Campbell, K.L.S. This paper entered review on the 29th of July and is still in review at the time of submission. A live update of the current state of the paper may be found *via* this link (Chapter 4)



Abstract

Electrodialysis is an emerging electromembrane salt separation technology, industrial implementation of which is currently inhibited by the risk-averse nature of industry and poor optimisation of units. The work presented in this thesis involves understanding how electrodialysis is modelled, rigorously testing one of the most basic assumptions, and developing more advanced modelling strategies. A review of existing published literature revealed there is a wide variety of models both in their fundamental construction and the assumptions taken to neglect phenomena. Despite this, good agreement with empirical data is near ubiquitous but attributed to an over-reliance on fitting parameters. One assumption taken by all researchers is channel uniformity whereby the repeating geometry is leveraged to significantly reduce model complexity. In Part I, this assumption was investigated through computational fluid dynamics simulations through which significant flow maldistribution between channels was revealed. Further, an analytical model was found to capture the degree of maldistribution well in a dimensionless number and revealed how it can be influenced. A study on the impact of maldistribution revealed that while the electric resistance is marginally affected, the limiting current density is significantly reduced. Particle image velocimetry experiments empirically demonstrated the presence of maldistribution and transport experiments validated its impact. In Part II, an advanced process model of electrodialysis was developed using the analogy of an electric circuit. This model was designed to be adaptable and avoid the use of empirical fitting parameters. A membrane transport number and resistance model proved vital in ensuring predictive accuracy over a range of concentrations and voltages. To demonstrate the generality of the model, it was extended to describe bipolar membrane electrodialysis which similarly showed good agreement with experimental data. Overall, this work has contributed significant advancements to how electrodialysis is analysed, designed, and modelled.





Chapter 1

Introduction



1.1 Background

In Hemingway's 1926 novel 'The Sun Also Rises', the character of Bill asks Mike "how did you go bankrupt?". Mike replies: "Two ways. Gradually, then suddenly" [1].

*

The 2020 United Nations (UN) World Water Development Report (WWDR) [2] entitled 'Valuing Water' sets out how one of the underlying root causes of the global water crisis is the lack of respect that we all hold for this most important resource. Water scarcity has been a key issue for decades and will continue to be one of the major ecological challenges for many more to come. As such, ensuring the continued availability of clean water to all parts of society is one of the 17 UN sustainable development goals (number six). One of the results of a lack of respect for water as an abundant but finite resource is that it is undervalued by society. Demand for clean water is greater than any other commodity due to it being essential for sustaining life and the functioning of modern society though agricultural and manufacturing industries. Annually, humanity consumes over 4000 km³ of freshwater. This is increasing year-on-year and is approaching the maximum sustainable withdrawal rate [3]. However, individuals living in developed countries still enjoy effectively limitless access to clean water because overall supply still exceeds the demand. Crucially, this has a huge psychological impact whereby water continues to be regarded as a ubiquitous and disposable resource. However, a consistent rise in the demand and fall in the supply of water shows a worrying trend, especially for the more than four billion people living in regions already under water stresses [4].

The global water shortage is among anthropogenic climate change as one of the great environmental challenges of the 21st century. However, their societal effects and abatement strategies are fundamentally different. This primarily stems from the fact that while CO₂ is an atmospheric pollutant, water is a commodity.

The potential cataclysmic effects of CO₂ and other greenhouse gasses are an indirect effect of modern societal activity. Its high stability makes CO₂ a preferred product of energetically favourable carbonaceous chemical reactions performed in an oxygenated atmosphere. Consequently, much of human activity results in CO₂ being incidentally released to the atmosphere. Increased atmospheric CO₂ leads to global warming which in turn leads to increased extreme weather events and the subsequent destruction of infrastructure [5]. The complexity of global weather and climate led to the presence and origins of climate change being misunderstood, intentionally obfuscated, and ignored for decades. However, this crucially also means the impact of climate change takes hold over several generations, giving very public realisations of its consequences but also leaving enough time to mitigate the most disastrous effects. Recent upticks in the rate of heatwaves, wildfires, floods, droughts, and blizzards get a lot of media attention, and their association with climate change is now considered a fact by both the scientific community and wider society. The recent surge in public demand for action on climate change has revolutionised global climate policy, with most countries (191 parties as of August 2021, accounting for 97% of global emissions [6]) pledging net zero CO₂ emissions by 2050 or 2060.

In contrast, the effects from water scarcity will be rapidly felt and one likely more malign in nature as we run out 'gradually, then suddenly'. Further, while the effects of global warming and climate change will be felt at the



global scale, water scarcity will be a more localised concern and hit hardest in the most deprived regions [7]. Water is consumed in industry, agriculture, and domestically, but does not often undergo chemical conversion. Instead, semantically, freshwater is converted into wastewater in an entropically favourable process which is then discharged into the environment. Its ubiquity in biological and chemical processes stems from it being an excellent solvent in the conditions of our environment. Freshwater is naturally replenished in the water cycle using energy from the Sun, but this is a slow and unpredictable process. When the overall demand for water is lower than the regeneration rate, the amount of water available appears infinite when compared to the needs of a single person. This inevitably leads to apathy in many as their individual consumption appears to have no impact on water scarcity. However, once demand locally exceeds supply, the impacts are immediately felt, and it is already too late to avoid economic and humanitarian disasters. Primal and emotionally charged actions taken in the name of self-preservation by those at risk would undoubtedly result in untold pain and misery. Therefore, global action and policy for tackling water scarcity must be implemented swiftly and with a guise to safeguard water as a human right. Ecological and humanitarian disasters are likely to transpire unless significant revisions to anthropological intrusions on the water cycle are made [8]

Demand for water has grown by nearly an order of magnitude in the last century (from 500 km³/y in 1900 to 4,600 km³/y presently [4]) due to a combination of population growth and societal development. Growth in demand is expected to continue at a rate of around 1% per year. The greatest increase in demand will most likely occur in Africa, where water stresses are already high. By sector, agriculture is currently the greatest consumer of water, at 69%, followed by industry at 19% and municipal consumption comprising the other 12% [4]. A larger population with a higher standard of living demands a greater rate of water consumption in all three categories. In Africa, the population is expected to increase by 108% by 2050, and many African economies are expected to transition from developing countries to emerging markets. The concurrent increase in population and the standard of living is expected to drive an increase in industrial and municipal water demand of 800% and 300%, respectively.

Meanwhile, global freshwater sources are rapidly declining [9]. One major cause of this is the discharge of polluted wastewater to surface waters, of which 80% undergoes no treatment at all [2]. The main sources of water pollution are from municipal sewage (730 Mt/y) and industry (300-400 Mt/y). At present, 30% of the world's population has no form of sanitation and 12% drink from unsafe water sources. Agricultural runoff leads to nutrient loading (phosphate and nitrate) in water bodies, leading to eutrophication and increased pathogen loading, further degrading potential sources of surface freshwater. This type of pollution is expected to increase by 180% due to greater use of fertilisers to accommodate for a higher food demand and a surge in biofuel production [9]. The effects of this pollution will be particularly strong in Africa, arising from a population and living standard surge, as well as lack of wastewater treatment infrastructure. Globally, the effects of water scarcity will affect low- and middle-income households worst, leading to greater economic disparity.

The increased stresses on surface freshwater have led to the construction of deeper wells in many aquifer systems and has prevailed as a successful short-term solution to further increase groundwater abstraction [10]. Also, in many regions, industrial wastewater is injected deep into groundwater pore spaces with the hopes that



natural filtration will provide a relatively low-cost method of treatment as the water is purified as it proceeds to the surface. The combination of excessive withdrawal from deeper wells and injection of waste is leading to greater stresses on the natural ecology which drives the water cycle. This is worsened by climate change driven extreme weather events such as droughts and flooding, as well as longer-term ecological changes such as salt intrusion into coastal aquifers.

The increase in demand and fall in supply of water puts access to clean and safe water in serious jeopardy for billions of people. In a worst-case scenario, a water deficit will lead to a collapse in a region's agricultural productivity, resulting in the death of billions through both dehydration and famine. The prelude to this is beginning to be seen in already-stressed nations. In Madagascar in August of 2021, the worst drought in decades led to more than a million people experiencing famine [11]. International aid provided some relief, but it is likely that events like this will become more common in the future. Beyond food insecurity, water shortages result in increases in the rates of disease as people are forced to turn to unsterile water sources for drinking, and municipal sanitation systems are suspended to conserve water. These effects will be most apparent with the poorest members of society and could lead to a 'water apartheid' [12]. It is also foreseeable that global conflicts may arise over control of freshwater resources [13]. Wildlife habitats will be destroyed as well, reducing biodiversity. The treatment of the impacts of water shortage is far more costly than its prevention.

To avoid a catastrophic water shortage, sustainable water management is key [2,13]. This must involve both reducing the demand for freshwater abstraction and increasing its supply. A study by GlobeScan and SustainAbility, an international stakeholder opinion researcher and think tank, respectively, identified 19 consensus solutions to the water crisis from experts [14]. Many involve societal and behavioural changes such as holistic ecosystem management, better education, and developing new agricultural practices. However, several of the proposed solutions concern water management technologies and their role in balancing the water deficit. These include reducing freshwater demand though more effective wastewater recycling and increasing its supply using efficient desalination and better pollution control. For these to be realised, a great deal of research into both current and emerging water treatment technologies must be conducted to overcome the significant barriers to widespread adoption.

Enhanced process modelling carries with it myriad benefits for both researchers and commercial operators [15]. Theoretical frameworks may be evaluated against empirical data and a great depth of understanding into individual chemical and physical processes may be gained. For engineering researchers, this can help to refine existing assumptions about the relative importance of different phenomena as well as directing future research to areas in which it can have the greatest impact. For industrial designers, accurate models valid over a wide range of conditions can reduce the development time as well as derisking elements of the process. There are a number of emerging water treatment technologies which at present are too expensive and untested relative to the established mature technologies. Consequently, the risk-averse nature of industry is greatly inhibiting their adoption. However, they present potential benefits over the existing solutions if realised. As such, enhanced process modelling can make great strides to derisk and drive adoption of these novel technologies.



One such emerging technology is electrodialysis (ED). In ED, an electric field is used to drive the transport of ions from one stream to another through ion exchange membranes (IEMs) in a geometry analogous to a plate-and-frame heat exchanger. Streams are distributed to alternate channels, separated by IEMs which act as semi-permeable barriers, selective to just one charge of ion. Invented over one hundred years ago, ED has only recently become commercially viable due to the membranes historically being too expensive and having poor performance [16]. Many new applications of ED are being established in research due to its many strengths over existing technologies, detailed in Section 1.3. Further, novel membranes with enhanced and bespoke properties are currently in development. However, commercial instillations of ED are still rare due to its immaturity relative to the established processes and the risk-averse nature of industry. Nevertheless, there is continued substantial investment into new ED units, currently exceeding 300 M\$/y. Consequently, advanced process models of ED have the potential to facilitate its adoption in industry and revolutionise salt separation processes. Further, ED adjacent electromembrane processes are similarly limited by the hesitancy of industry which can be overcome with advanced process models. It is not unforeseen that in the future, a suite of electromembrane separation processes could be used with great effect to enhance water recycling in industrial plants with the ultimate goal of zero liquid discharge.

1.2 Research aims and objectives

The central theme of this doctoral thesis is the evaluation and improvement of the modelling of electrodialysis processes. A literature review (Chapter 2) revealed that existing models vary greatly in their formulation, but in general all are able to achieve good agreement with experimental data. An overreliance on model fitting parameters and training data was deemed to be the cause of this. Consequently, the research undertaken is subdivided into two parts:

Part I: Maldistribution in electrodialysis. During the literature review, it was established that a great number of assumptions are commonly undertaken in developing published models. These assumptions varied from model to model, but one ubiquitous assumption was that of channel uniformity. That is, all channels behave identically, and so only one need be modelled, and the results scaled out to an arbitrary number. The aim of the research undertaken in Part I is to fully scrutinise this assumption both numerically and empirically. The particular objectives can be reduced to the following questions:

- Does flow maldistribution exist within ED according to computational fluid dynamics (CFD) simulations?
- How does the geometry and process conditions affect maldistribution?
- Can maldistribution be described with a simple analytical model?
- What is the impact of maldistribution on the performance of ED?
- Can the results seen in the numerical models be replicated empirically?

The investigation conducted can be found in Chapters 3 and 4.



Part II: Developing advanced models of electromembrane processes. In Part II, the development of a new, advanced ED process model was undertaken. In the literature review, a huge variety of differing model aspects was seen. It was concluded that this was because for different applications of ED, different phenomena may dominate, and so different model aspects become important. However, each additional aspect introduces more empirical fitting parameters. This makes fitting the model to the validation data easier but reduces the insight gained through the results. In light of these observations, a new modelling framework of ED was developed. Several guiding principles were established to ensure the model quality, namely that it should be:

- Flexible, such that additional phenomena could be included if deemed necessary for a given application.
- Applicable to ED-adjacent electromembrane processes.
- Valid over a broad range of process conditions to facilitate process design and optimisation.
- Not reliant on training data and empirical fitting parameters to accurately model processes.

This model was developed and experimentally validated for both conventional ED and ED with bipolar membranes in Chapters 5 and 6, respectively.

1.3 Methods of water treatment: why electrodialysis?

Many forms of water treatment technologies exist for industrial wastewater treatment and desalination [17]. They can be broadly classified into biological, thermal, and physical processes. Each individual technology is typically suited to a specific class of pollutant, and so a suite of different technologies is often required in series to create a holistic treatment process. This segmentation also allows each to be independently optimised for greater overall efficacy. Biological treatment processes use the biochemical reaction cycles of microbes to digest a wide range of organic pollutants. However, as this work is principally focused on the removal of inorganic pollutants, biological treatment processes will not be discussed further.

Thermal processes involve heating the feed stream to enact separation through a phase transition of water, utilising the non-volatile nature of salts. The highly concentrated solution is then of much lower volume and easier to dispose of. This technique is highly effective, but the high latent heat of vaporisation of water makes this an energetically costly process. Overall energy requirements have been reduced by reclaiming heat in more advanced technologies such as solar desalination, multi-stage flash distillation, and multi-effect evaporation but come at an increased capital cost.

Physical processes include membrane and adsorption techniques and tend to utilise an (electro)chemical potential gradient (differentials in pressure, concentration, or an electric field) as a driving force to remove pollutants from a feed stream. Also included here are sedimentation techniques such as chemical flocculation whereby colloidal particles are introduced to achieve aggregation and facilitate phase separation. While adsorption technologies typically involve a resin or other adsorbent that must be intermittently recharged in a semi-batch process, membrane processes implement a theoretically unchanging selective barrier between flowing streams and thus are continuous. Reverse osmosis (RO), nanofiltration (NF), and ultrafiltration (UF) use a pressure gradient



to drive water transport through the membrane retaining the pollutants on the feed side. Electrodialysis uses an electric field to drive the transport of charged ions through ion exchange membranes from a diluate stream to a concentrate stream. All these require the input of energy as the system entropy is decreased and transport is driven against a concentration gradient.

Membrane separations have several key strengths over thermal methods including high recovery ratios (the fractional volume of feedwater recovered as a treated stream), compactness, modularity, adaptability, lower specific energy costs (about a factor of five [18]) and controllability [19]. One of the most mature membrane technologies, RO, currently has a greater installed capacity than all thermal processes combined [20]. As a result of its reliability and ease of membrane manufacturing, it is currently the most common form of water treatment [21]. Despite this, membrane processes are still considered emerging technologies since research is ongoing into optimising membrane materials for bespoke purposes and reducing the cost of manufacturing [22]. Nevertheless, it is very likely that membrane processes will continue to dominate water treatment in the future, and so broad research covering all aspects should continue.

The prevalence and maturity of RO over ED primarily stems from the relative simplicity of the membranes. Whilst IEMs use the electrostatic repulsion of fixed charge groups embedded in the matrix of the membrane to achieve selectivity, RO membranes need only to have pore sizes small enough to retain pollutants while allowing water molecules to permeate. The higher complexity of ED membranes has historically meant that they were of too low performance and too costly to be commercially viable [23]. However, ED has many inherent strengths which has maintained interest since its conceptualisation in 1890 [16]. These arise from the fact that in ED, it is the minority species (the salt) which permeates, whereas in RO it is the majority (water). Consequently, ED has a huge thermodynamic advantage when removing salts from lower concentration streams and as such benefits from a higher rate of separation (thereby a lower membrane area and more compact process) and lower energy consumption [24]. Further strengths include a lower susceptibility to fouling since the flow is tangential to the membranes, a greater membrane lifespan, low pressure operation, easy controllability and operability, and a higher recovery ratio. There is also a great deal of variability in ED, where it is possible to use monovalent selective membranes to preferentially retain multivalent ions in the feed stream, or bipolar membranes to induce water splitting and alter the pH of streams directly using electricity. As such, the agnostic nature of ED means it has incredibly broad applications from large-scale desalination and purification to the selective transport of charged ion complexes [25,26].

Steady advances in IEM quality and a reduction in manufacturing cost have led to significant growth in the number of publications concerning ED (Figure 1.1). Consequently, ED has recently become broadly commercially viable for the first time, further increasing academic and industrial interest. Despite this, there still exists significant knowledge gaps in the published literature which are explored in depth in Chapter 2. Fundamental research into ED is therefore timely and important and is the focus of the research undertaken in this Ph.D. project.



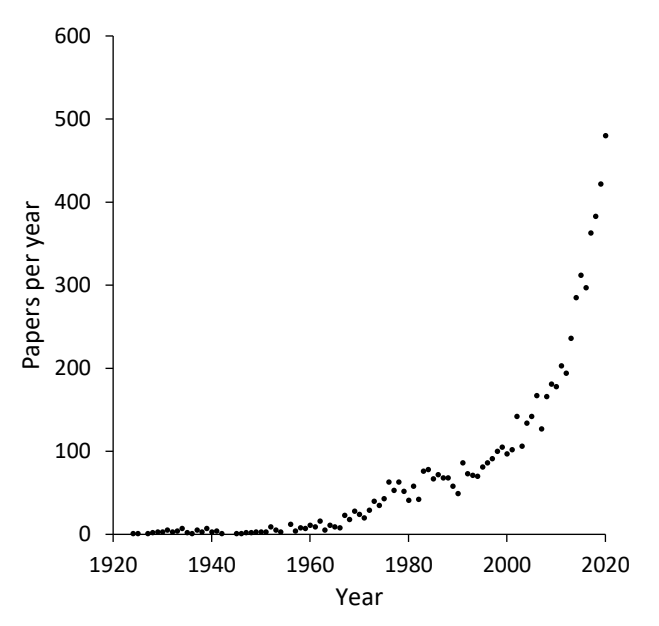


Figure 1.1: Historic trends of the number of ED publications per year. Data taken from the database Scopus. Publications were identified with the keyword 'Electrodialysis' in the title, abstract or keywords.

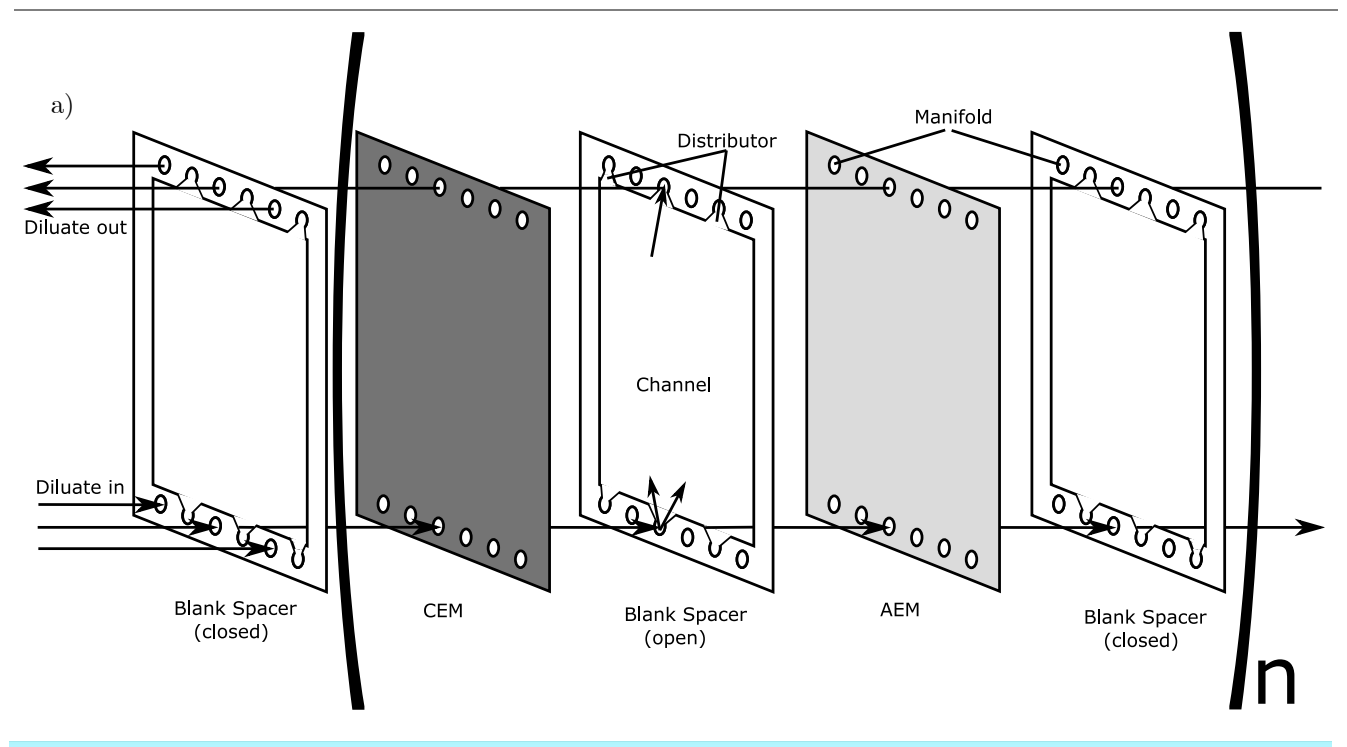
1.4 Electrodialysis engineering and phenomenological description

1.4.1 Engineering design and transport phenomena

Electrodialysis is an emerging electromembrane process with broad applications in salt separation processes such as desalination, resource recovery, and wastewater treatment [27]. In ED, a potential difference is employed to drive the transport of ions through ion exchange membranes. These act as semi-permeable barriers, theoretically permitting the selective transport of either cations or anions only, depending on the identity of the fixed charges in the membrane pores. In conventional ED, anion and cation exchange membranes (AEMs and CEMs) are layered in an alternating pattern separated by membrane spacers which create channels through which salt solutions flow, driven by a pump (Figure 1a). The electric field drives ion transport from one channel (the diluate), through the appropriate IEM and into the other (the concentrate) (Figure 1b). Here, they are blocked from migrating further by the oppositely charged IEM. Ions with a charge identity to which a membrane is selective to (e.g. cations in CEMs) are referred to as counterions, and those rejected are known as co-ions. The identity of the diluate and concentrate channels is dictated by the direction of the electric field and the layout of the membranes. Several sets of membranes and channels (cell pairs: the repeating unit) are held between two electrodes, comprising the separation system referred to as an ED stack. Manifolds in the rim of the membranes and spacers transport fluid to and from the channels, while alternating open and closed distributors ensure that streams are fed to every other channel. Net-like geometries are used in the membrane spacers to promote turbulent mixing within the channel bulks.

The electric field is generated by wire mesh electrodes housed in end-compartments either side of the stack of membranes. An electrode washing solution, separate from the diluate and concentrate, flows over the electrodes





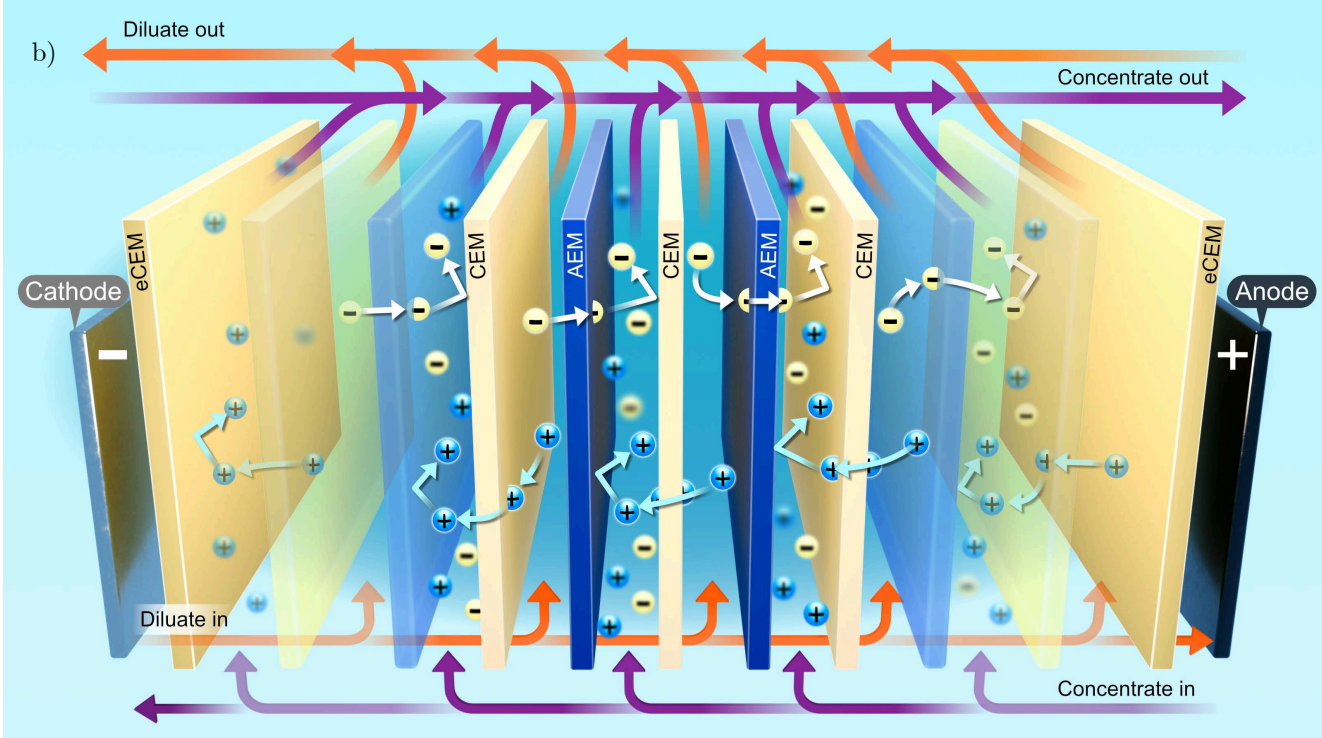


Figure 1.2: a) A schematic diagram of an ED stack. Flow enters and exits from the left-hand side and is distributed to every other channel through open spacer distributors. For simplicity, the concentrate stream is not shown, this would enter through the right-hand side. b) A schematic representation of the transport of ion in conventional ED. Dark colour represent positive charges (cations, anode and AEM) and light colours represent negative charges (anion, cathode and CEM). Two and a half repeating cells are shown.

and is completely separated from the rest of the stack by end IEMs. Careful consideration must be given to the electrode material, washing solution and end membranes to ensure the stack is robust and safe. Anodes are typically platinised titanium to prevent oxidative dissolution, whereas cathodes can be made of cheaper materials, typically stainless steel. Washing solutions are chosen with desired electrode reactions in mind. Sodium chloride



(NaCl) is unsuitable as chlorine gas would be evolved at the anode. Sodium sulfate is a common choice, as oxygen and hydrogen are evolved at the anode and cathode, respectively. End membranes are typically thicker than operating IEMs due to the harsher environments and stricter requirements on selectivity and tend to be cation selective to prevent any chloride ions present reaching the anode. The choice of two cation exchange membranes also ensures that the electrode rinsing solution maintains a constant concentration: cations lost from the anolyte chamber are recouped in the catholyte.

Ions are transported through three separate domains. These are: turbulent mixing in the bulk, migration through the boundary layers, and transport through the membrane. Continuity of mass and current ensures that the overall flux in these domains must be equal. In steady-state operation, Ions are also transported by three different mechanisms: convection, diffusion, and electromigration. These mechanisms are driven by fluid flow, concentration gradients, and electric potential gradients, respectively. Transport by convection and electromigration are rapid within the turbulent bulk and the membrane, respectively, due to the chaotic flow patterns and high ion concentrations. However, these are not present within the boundary layers. Here, flow is only tangential to the membrane surface, and lower concentrations here than within the membranes results in lower electromigration. Consequently, concentration gradients form within boundary layers to provide additional transport by diffusion to maintain continuity of flux in a process known as concentration polarisation (Figure 1.3a). The membrane-diluate interface concentration is lower than the diluate bulk concentration since the additional diffusive flux must be provided to get ions from the diluate bulk as the additional flux is used to drive ions from the membrane to the bulk.

The magnitude of the concentration polarisation is related to the current density. As the current density increases, the membrane-diluate interfacial concentration decreases, eventually resulting in the interfacial

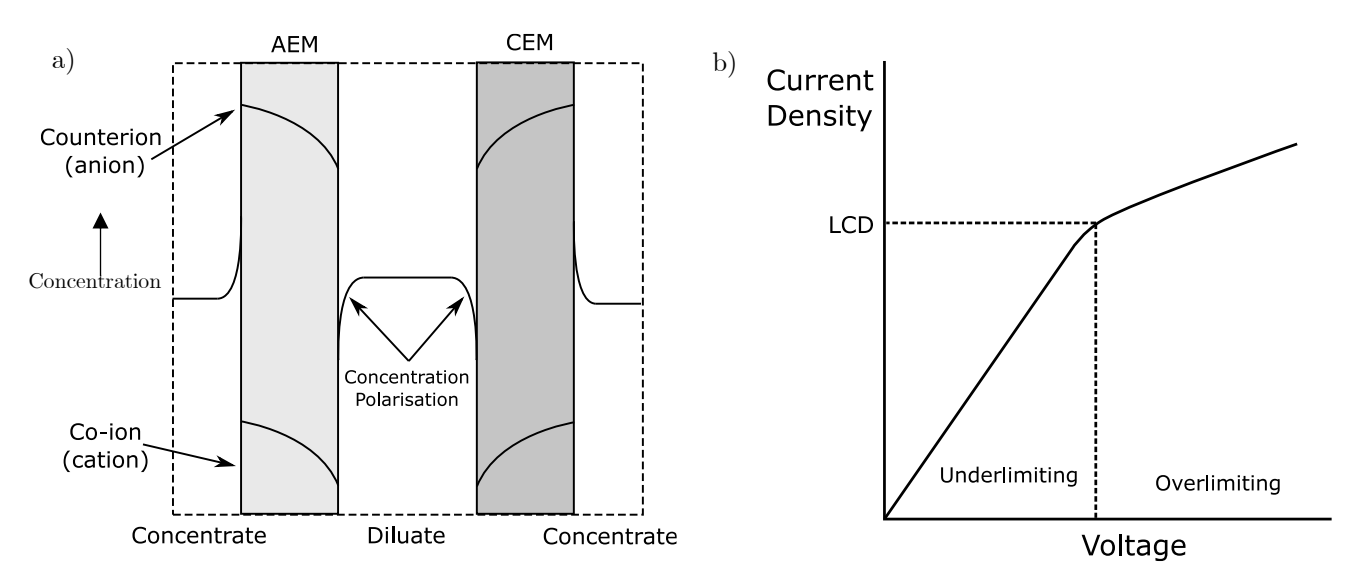


Figure 1.3: a) A schematic diagram of concentration polarisation in ED. In the flow, the concentrations of anion and cation are equal, whereas in the membranes the counterion concentration is significantly greater. A bulk mixed region is seen in the centre of the flow and curved boundary layers are present near the membranes. b) An ideal current-voltage curve demonstrating an underlimiting and overlimiting region as well as the limiting current density.



concentration vanishing at a point known as the limiting current density (LCD). A classical theory based on the Nernst-Planck equation and the assumption of electroneutrality (Section 2.2.1) suggests that at this point, no more ions can flow and a hard limit on the current is reached. However, in practice, an 'overlimiting' condition is reached, where additional current will flow, but with a greatly increased apparent resistance (Figure 1.3b). The causes of this have been linked to water splitting and electroconvection. Water splitting at the membrane-diluate interface produces the additional ions to increase the current and the associated energy penalty contributes to the increased apparent resistance. The water splitting also results in the pH of the streams unwantedly changing. Electroconvection is the phenomenon whereby fluid flows tangentially to the membrane surface resulting from a large electric potential gradient interacting with the permanent dipole of water molecules. It is captured numerically through an additional body force in the Navier-Stokes equations [28]. When ion depletion occurs at the membrane surface, a so-called 'space-charge' region is formed where the condition of electroneutrality is broken, and the fluid has an overall charge. This is captured through the Poisson equation and is associated with a very large potential gradient. Consequently, electroconvection is initiated which mixes fluid within the boundary layer and allowing higher fluxes to occur.

1.4.2 Ion exchange membranes

The characteristic charge of an IEM is determined by the identity of fixed charge groups. These are strong or weak acid or base groups bonded to a polymeric hydrocarbon backbone [29]. The electrostatic attractions and repulsions between these fixed charges and the free ions migrating through the membrane are the foundations of the IEM functionality and determine its charge selectivity. The negatively charged fixed groups in CEMs are most commonly sulfonic acid (strong) or carboxylic acid (weak) groups. For AEMs, quaternary or tertiary amine groups are used for strong or weak bases, respectively. A higher membrane charge density, either from a higher concentration of fixed charges or the use of a stronger acid or base fixed charge group increases membrane conductivity and lowers electrical resistance. However, it also leads to greater swelling of the membrane, increasing the pore size and reducing the permselectivity and mechanical strength. The trade-off between the selectivity and electrical resistance of an IEM is fundamental and is analogous to the selectivity-permittivity trade-off for more traditional membrane separation processes (Robeson upper bound [30]).

There are two primary classifications of IEM: homogenous and heterogenous. The form of a given membrane type is determined by its method of manufacture and strongly influences its internal structure (Figure 1.4). Homogenous membranes have a continuous polymeric matrix throughout and are activated by introducing a charged moiety. The charge distribution throughout the matrix is resultantly uniform and isotropic. They are typically manufactured by casting a solution containing the dissolved polymer into a thin sheet before removing the solvent and precipitating the membrane. Heterogenous membranes are manufactured by suspending a finely powdered ion-exchange resin inside a binder polymer, which is then pressed and sintered into a flat sheet. This method of membrane production is far cheaper and can be used to turn virtually any semi-batch ion exchange adsorption unit into a continuous ED process. However, heterogenous membranes tend to have a higher electrical



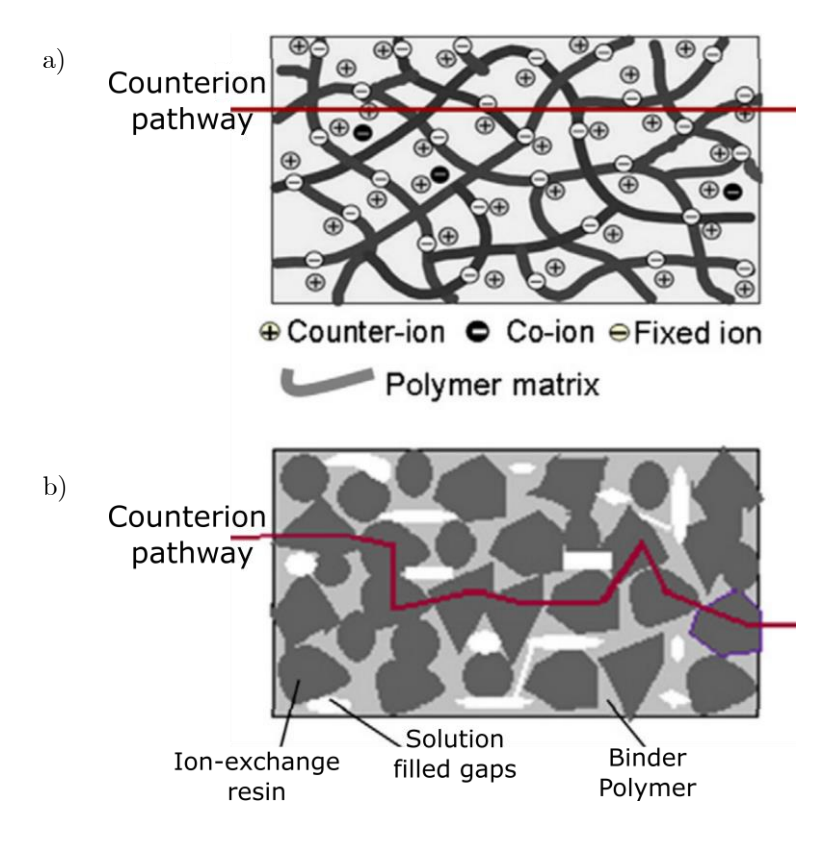


Figure 1.4: A schematic showing homogeneous(a) and heterogenous (b) membrane structures. Adapted from [27]

resistance due to the more tortuous path encountered by the ions, and a lower permselectivity due to small, solution-filled gaps in the membrane. Because of this, modern membranes typically tend to be homogeneous. Nafion is a homogeneous CEM which uses a perfluorinated carbon backbone, and sulfonic acid fixed charge groups. It is well characterised and has excellent thermal and chemical stability, and so has historically been regarded as a 'gold standard' CEM, often used for proton exchange in fuel cells.

Membranes are often not perfectly selective towards one charge identity. Instead, some co-ions migrate from the concentrate back to the diluate through the process of back-migration. Membrane ion permeation selectivity (permselectivity) is characterised by a transport number which denotes the fraction of charge carried through a membrane by counterions. Low permselectivity results in counterproductive co-ion transport from the concentrate back to the diluate, reducing the current (Faradic) efficiency (defined as the fraction of current resulting in a net transport from the diluate to the concentrate) and wasting energy. Transport numbers decrease as the concentration difference between the concentrate and diluate becomes more positive due to increased back-migration from the increased driving force on the ions in the concentrate relative to the diluate.

Other desirable properties of IEMs include a high mechanical strength, low electrical resistance, high chemical and thermal stability, low water uptake (swelling) and low production cost. However, many of these properties are mutually exclusive. For example, reducing swelling typically involves using a more hydrophobic polymer backbone, which leads to greater electrical resistance.



1.4.3 Cost optimisation: ED and RO

Due to its brevity and similarity to a recent publication by Patel *et al.* [31] the following work is presented here as a demonstration, rather than as part of a research chapter in this thesis. It should be noted that the models here are highly simplified and only account for the membrane and driving force costs.

One of the key trade-offs in ED is between membrane area and specific power consumption. This is best expressed through investigating Ohm's Law:

$$V = I \frac{\hat{R}}{A_m} \tag{1.1}$$

where \hat{R} is the electrical area resistance of a single cell (in Ω m²), A_m is the active area of a membrane, V is the potential difference across a cell and I is the current. The electrical area resistance is primarily driven by the membranes and electrolyte concentrations and thus for a given steady-state system can be considered more-orless constant. The current is the rate of transfer of charge and thus is determined by the difference between the inlet and outlet equivalent concentrations and the volumetric flow rate. As such, for a given system, the current can also be considered constant. Hence, the power consumption (P) of a unit can be calculated from the equation:

$$P = I^2 \frac{\hat{R}}{A_m} \tag{1.2}$$

Here, the membrane area and power consumption are inversely proportional to each other, revealing the trade-off. The capital cost of an ED unit is strongly driven by the membrane cost, whereas the operating expenditure is almost entirely comprised of the electricity consumption. Increasing the operating voltage per cell pair increases the power consumption but decreases the required membrane area. In the limit, a voltage of zero results in no power consumption but an infinite membrane area, and a stack with an infinitesimal membrane area would require an infinite voltage. As such, there is an optimum operating voltage to be found which minimises the overall cost.

To numerically demonstrate the CAPEX-OPEX trade-off, a model was built in MATLAB R2023b. The results of this can be seen in Figure 1.5a where the OPEX and annualised CAPEX (based on membrane replacement every 5 years) are presented as a function of the overall membrane area for a given system. The CAPEX is directly proportional to the membrane area and the OPEX is inversely proportional. A minimum overall cost can be seen where the CAPEX and OPEX are equal.

A very similar optimisation problem arises for RO, a competitor to ED in many applications. In RO, water is driven across the membrane and salts are retained within the feed. The flux of water (J_w) which is used to determine the total membrane area required can be computed from the RO design equation:

$$J_w = \frac{Q_w}{A_m} = A_w (\Delta P - \Delta \pi)$$
 [1.3]

Here, A_w is the membrane permeability, Q_w is the permeate volumetric flowrate, ΔP is the trans-membrane pressure drop and $\Delta \pi$ is the trans-membrane osmotic pressure difference. The osmotic pressure difference is a



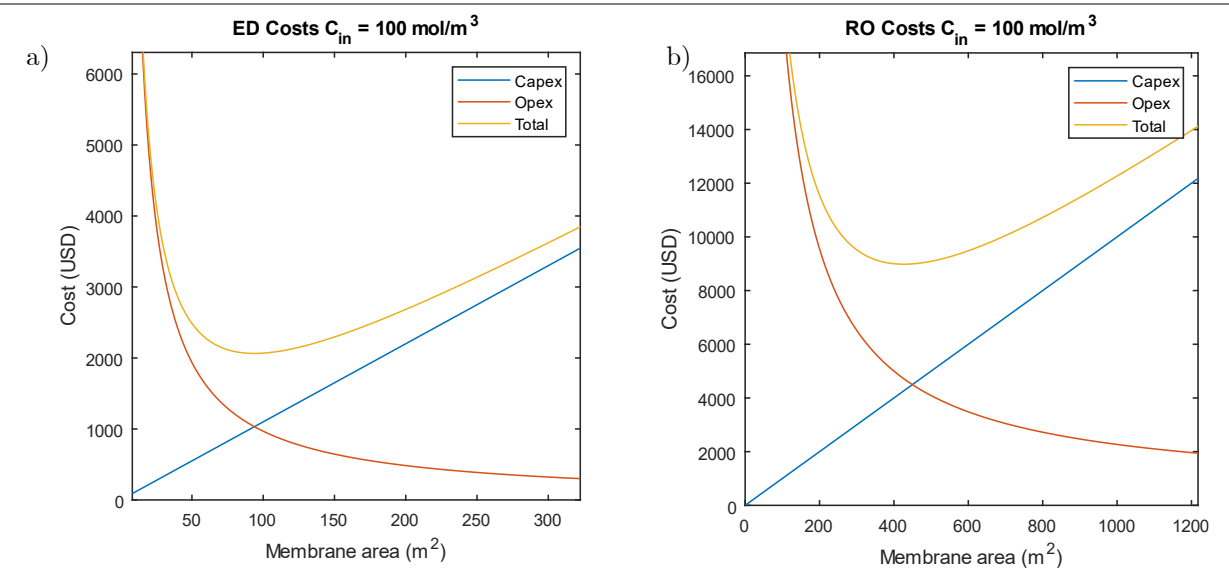


Figure 1.5: Annualised cost curves for ED (left, part a) and RO (right, part b) as a function of membrane area for a given inlet concentration. OPEX is driven by the electricity cost which comes from pumping power for RO and ion transport for ED. CAPEX is driven by membrane cost for both technologies. The total cost (OPEX + CAPEX) is shown as well, demonstrating a minimum overall cost.

function of the solution concentration (here assumed to be proportional), and the permeability is dependent on the membrane. As such, for a given application, increasing the feed pressure (which increases ΔP) increases the water flux and thus reduces the required membrane area. However, this requires a greater power consumption within the pump ($\sim \Delta P \times Q_w$) to achieve the higher feed pressures. Again, a similar trade-off between membrane area and power requirements arises (Figure 1.5b).

The optimum cost for both ED and RO changes as the feed concentration changes. With a fixed outlet concentration, a higher feed salinity increases the required current in ED and increases the osmotic pressure drop in RO. These changes increase the cost through either an increased power consumption or an increased membrane area requirement. To demonstrate how these optima are affected by feed concentration, a programme was written in MATLAB R2023b to compute the unit size which minimises the total annual cost for a range of inlet concentrations. A fixed outlet concentration of 1 mol/m³ was chosen and it is assumed that all membranes have perfect selectivity. Because of these assumptions, it is necessary to incorporate a bypass for the RO unit for a fair comparison. A membrane lifetime of five years was selected for both membranes to annualise the CAPEX.

The model results are presented in Figure 1.6 and show an intersection of the optimum cost curves such that ED is preferred at lower concentrations and RO is preferred at higher concentrations. For RO, even at low concentrations, an energy penalty must be expended to drive the water over the membrane. However, for ED, energy is only expended driving salts across the membranes. A lower amount of salt to remove results in a lower energy penalty. As the inlet concentration is increased, the energy penalty for both ED an RO increases through a greater required current and osmotic pressure, respectively. However, the gradient of the increase in the optimum cost of RO is lower and so the cost curves intersect. One key driver of this differing gradient is the relative cost of the membranes. Membranes for RO are considerably cheaper than ED membranes and so ED becomes less favourable as larger units are needed. Analysis like this can reveal for a given application whether ED or RO is more suitable.



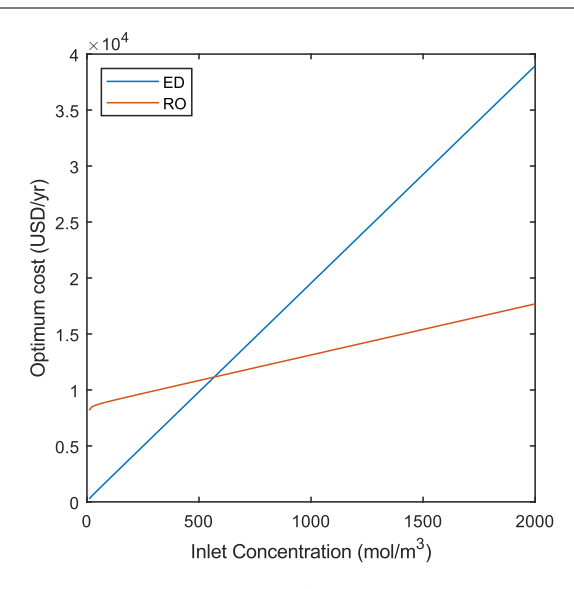


Figure 1.6: The optimum cost (i.e. minimum of total cost in Figure 1.5) for ED and RO as a function of the inlet concentration.

1.5 Electrodialysis variations*

One of the greatest strengths of electromembrane technologies is the ability to change elements of the unit cell to adapt the functionality to suit different processes [32]. These modifications can be used to increase the effectiveness of ED under different circumstances or to change the chemical environment of the streams. The primary different forms of electromembrane processes are outlined below, and schematics of some of them can be found in Figure 1.7. These variations have similar principles to conventional ED, and consequently have similar challenges. Any novel research that provides insight into conventional ED will also have benefits for the variations.

- Bipolar membrane electrodialysis (BPMED): A bipolar membrane (BPM) consists of an anion exchange layer and cation exchange layer. As such, neither anions nor cations can permeate, only water molecules are able to diffuse in. Once a threshold voltage has been crossed, water splitting occurs at the bipolar junction between the two layers, and the hydroxide and hydronium ions are transported in opposite directions into the adjacent compartments. An additional CEM and AEM are placed adjacent to the BPM, and so three streams are formed: the diluate, acid, and base streams. Consequently, BPMED is useful for adjusting the pH of streams using only electricity or forming concentrated acid and base streams from salt solutions. Modelling this electromembrane process is the subject of Chapter 6.
- Electrodialysis Metathesis (EDM): The repeating unit of EDM is effectively two conventional ED cells and thus has two diluate and two concentrate streams with two different salts present initially in each of the diluate streams. In EDM, salt pairs are effectively swapped. This can have significant impacts on the properties of the components of each stream, most notably the salt solubility [33]. As such, EDM can function as a very effective pre-treatment step for precipitation or crystallisation reactors without increasing the overall salt concentration.

Ledingham, J., Campbell, K.L.S., in 't Veen, B., Keyzer, L., Yip, N.Y. and Campbell, A.N., 2024. The development and validation of a novel, parameter-free, modelling strategy for electromembrane processes: Electrodialysis. Desalination, 576, p.117386

The only modifications are the addition of a reference to Chapter 6 within the discussion of BPMED and a brief discussion of monovalent selective membranes and electrodialysis reversal.



^{*} This section has been adapted from the following publication:

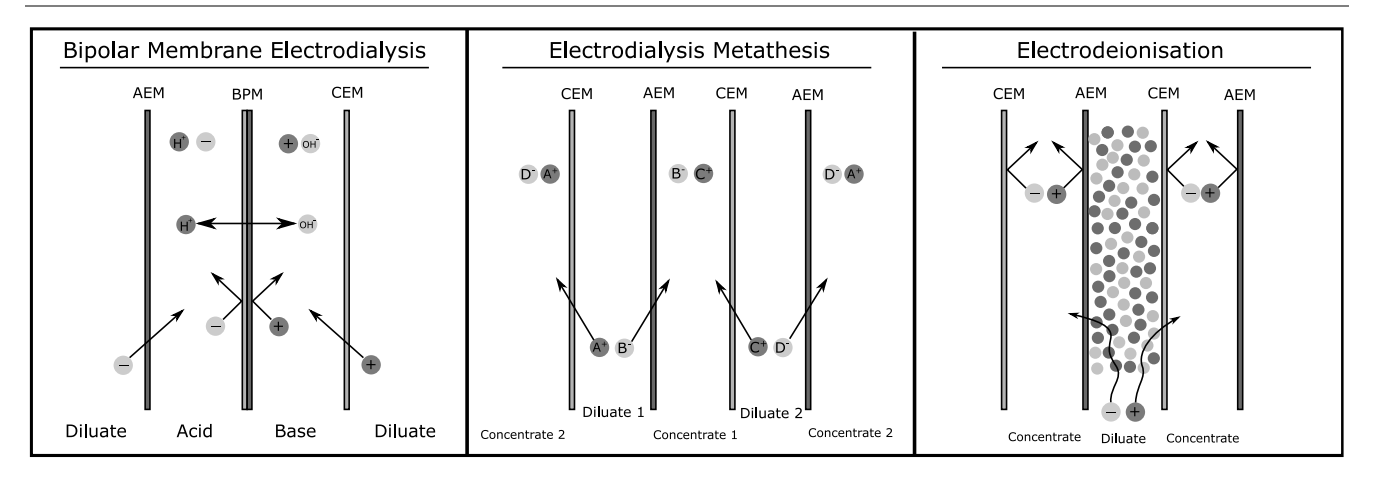


Figure 1.7 Schematic representations of other electromembrane processes.

- Electrodeionisation (EDI): In EDI, ion exchange resins are placed within (typically) the diluate channel to aid transport at low salt concentrations for 'polishing' separations. The resin increases the overall conductivity of the diluate channel and provides a low resistance path for current when salt concentrations are low. Consequently, EDI translates the benefits of ion adsorption separations into a continuous process.
- Complexation electrodialysis (CPED): Complexing agents are added into solutions of a conventional ED
 process which can be used to change the charge of individual ions by forming complexes. This can drastically
 alter the selectivity of ED between different like-charged ions by neutralising or increasing the specific charge
 on certain species.
- Reverse electrodialysis (RED): In RED the electrochemical potential difference between two streams of differing concentration drives the diffusion of salts from the diluate to the concentrate, driving electrons around an external electric circuit. Generator plants could be placed at river estuaries, utilising the difference in salinity and electrochemical potential between the river water and seawater to generate electricity.
- Electromembrane reactors (EMR): An EMR stack is different to all previous processes mentioned in that the electrodes form part of the repeating unit. Membranes are also used to segregate different flows, which can be either gaseous or liquid solutions. Typical examples of EMR are the chlor-alkali process, where sodium chloride solutions are reacted into sodium hydroxide and chlorine gas, and CO₂ electrolysis where gaseous CO₂ is reduced to useful feedstock chemicals such as ethylene.
- Monovalent selective electrodialysis (MVED): monovalent selective membranes consist of a standard IEM with a thin layer of the opposite charge identity fixed group grafted to the depleting side. This thin layer will repel counterions but will have a much greater effect on multivalent counterions than monovalent counterions. Selectivities, defined as the ratio of the permeability of monovalent ion to multivalent ion, of over 10 have been achieved [47].
- Electrodialysis reversal (EDR): EDR is an advanced version of ED which is effective when there is a high proclivity for fouling. Here, the polarity of the electric field is reversed and the feed manifolds of the diluate and concentrate are reversed. Consequently, the direction of transport through membranes is reversed from concentrate to diluate. Any charged colloidal substances are subsequently removed from the membrane surface, extending the lifespan of the membrane.

Examples of potential and industrially implemented uses of each of these technologies are presented in Table 1.1.



 ${\it Table 1.1: Application \ examples \ of \ electromembrane \ processes \ in \ recent \ publications.}$

| Technology | Application | Ref |
|------------|---|------|
| BPMED | Carbon capture solvent regeneration | [34] |
| | Production of Biohydrogen | [35] |
| | Copper recovery from electroplating sludge | [36] |
| | Biomass pretreatment solvent regeneration | [37] |
| | Treatment and recovery of Salicylic acid wastewater | [38] |
| EDM | Ammonia wastewater chemical recovery | [39] |
| | Potassium nitrate synthesis and purification | [40] |
| | Production of a wide range of ionic liquids | [41] |
| | Softening nanofiltration brine to prevent scaling | [42] |
| EDI | Continuous arsenic removal from wastewater | [43] |
| | Total desalination to produce deionised water | [44] |
| | Boron removal using selective resins | [45] |
| | Pineapple juice deacidification | [46] |
| CPED | selective zinc removal from electroplating wastewater | [47] |
| | heavy metal removal | [48] |
| | organic contaminant removal | [48] |
| RED | LiBr heat engine to convert low grade waste heat to electricity | [49] |
| | Desalination of oilfield produced waters with concurrent power generation | [50] |
| | Power generation from natural waters | [51] |
| EMR | Partial oxidation of organic pollutants | [52] |
| | Adiponitrile synthesis from acrylonitrile | [53] |





Chapter 2

Contextualisation to literature



2.1 Introduction

Interest in electrodialysis (ED) has grown rapidly in recent years due to increasing commercial attention arising from improvements in the quality of ion exchange membranes (IEMs) and a reduction in their manufacturing costs [23]. Resultantly, ED is currently considered to be an 'emerging technology'. These go through many transitions in research attention as the technique matures and the number of commercial developments increase. To evaluate the focus of ED research at the project outset, a meta-survey was performed on 100 recent publications in the field. The keyword "electrodialysis" was used in a search for articles on the database Scopus. Corrigendum, review papers, and conference entries were omitted, and the ultimate collection of publications spanned publication dates from the 15th of February 2021 to 15th of November 2021. The research topics of the ED papers were then categorised into four groups:

- **Novel Membranes:** Studies dedicated to the fabrication and characterisation of new IEMs and manufacturing methods. They typically involve using a novel polymer backbone or fabrication method in the hopes of improving IEM properties such as selectivity or electrical resistance.
- Modelling: These research papers present a novel or adapted method of ED modelling or apply a model to a new system. They tend to have similar themes and reach the conclusion that the model fits experimental data well. This trend is discussed in much greater detail later in this chapter.
- New applications: The emergence of ED as an effective separation technology has led to many studies on different ways in which it can be applied. This category of publication experimentally tests the performance of ED on a new system or in conjunction with another technology. Because of this, they tend to be focused on proof-of-concept rather than fundamental understanding and usually reach the conclusion that ED is an effective technology for that application.
- Foundational research: Researchers attempt to understand fundamental ED behaviours through experiments or modelling. They investigate cause and effect links between input variables and output data to understand the phenomena underpinning ED, which can then direct research in the other categories.

The outcome of the survey (Figure 2.1) revealed that the majority (68 %) of research papers are focussed on ED applications. This is characteristic of a promising emerging technology as research funded by commercial entities is usually interested in the efficacy of ED for a specific purpose. Research into novel membranes was the second most prevalent (15%), demonstrating that there are still hopes of valuable improvements in membrane properties yet to be realised. Foundational research (10%) and modelling (7%) are the least common. These last two are fundamentally linked, as models are a mathematical representation of the phenomenological behaviour of systems. Model flaws are characteristic of fundamental knowledge gaps, which can be explored experimentally and in turn used to develop more advanced models. It could be concluded from the lack of fundamental research that ED is fully understood and thus there is less of a need for it. However, this is not the case, as will be explored later in this chapter. The lack of research into fundamentals limits the depth of understanding the application studies can achieve and the extent to which systems can be optimised.

Despite the relatively little research attention given to ED modelling and foundational research, there is still significant value in studying the underpinning phenomena. This is because the current understanding of ED is



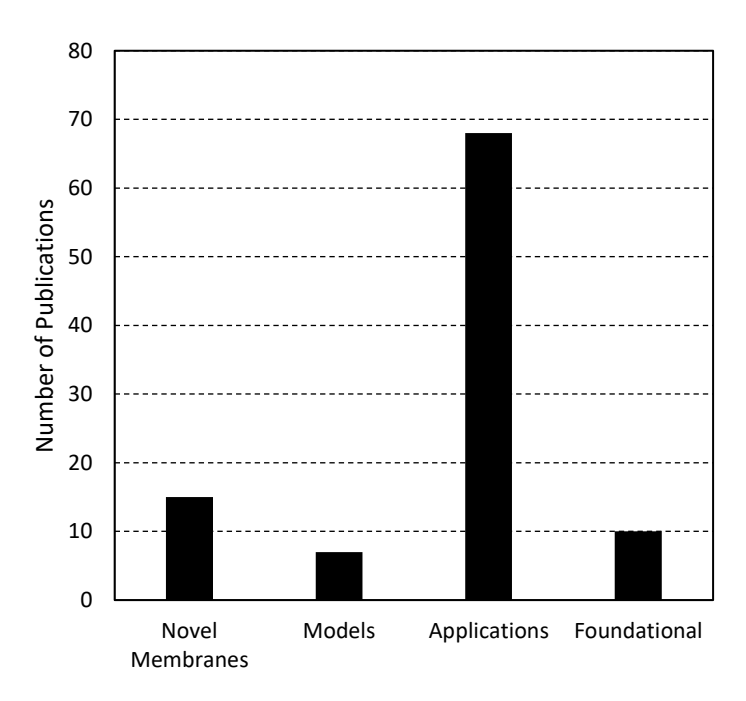


Figure 2.1: The results of a meta-analysis into the research area of 100 recent publications, classified into their topic of research.

incomplete. Many phenomena at the macro, micro, and nano scales interact to dictate overall ED behaviour. These range from the turbulent mixing provided by the netted spacer to the electric double layer and space charge regions adjacent to the membranes. At present, accurate models rely on empirical parameters which lump together several phenomena and are tuned to ensure a good fit of the data. Modelling studies do give examples of phenomena which may contribute to these empirical parameters, but experimental validation of these claims is extremely difficult. The multifaceted nature of ED means that isolation of confounding variables is challenging and leads to models being bespoke to one system.

This literature review aims to evaluate the current state of ED modelling to identify commonalities between studies and where research gaps lie. An overview of the different methods of modelling ED is presented along with an evaluation of their strengths and weaknesses. Following this, the research landscape of the two main classes of implementing ED models are investigated in detail to identify common techniques, trends, and research gaps. These classes are stipulated-equation models where a comprehensive list of equations comprising a closed system is provided by the authors and computational fluid dynamics (CFD) which use multiphysics software with in-built models. Stipulated-equation models tend to have greater variability since they are built from the ground up whereas CFD models typically modify pre-existing application modules. However, the sophisticated solvers used in CFD models allows for more complex, higher-dimensional simulations to be solvable.

2.2 Methods of ED modelling

Models of ED have been classified into four types: Nernst-Planck Models, circuit-based models, semi-empirical models, and irreversible thermodynamics models. The foundational equations will be discussed here along with assumptions and common simplifications. These models are then evaluated in Section 2.3



2.2.1 Nernst-Planck models

Nernst-Planck (NP) models solve phenomenological partial differential equation (PDE) representations of ion flux to generate concentration fields [54]. The NP equation is an extension of the convection-diffusion transport equation to include an electrophoretic contribution to the overall flux:

$$\boldsymbol{J}_{i} = c_{i} \boldsymbol{v} - D_{i} \boldsymbol{\nabla} c_{i} - D_{i} \frac{z_{i} F}{R_{g} T} c_{i} \boldsymbol{\nabla} \phi$$
[2.1]

Here, the three right-hand terms represent convective, diffusive, and electrophoretic flux, respectively, from left to right. The flux of ion i is J_i , c_i is the ion concentration, \mathbf{v} is the flow velocity, D_i is the diffusivity, z_i is the ion charge, F is the Faraday constant, R_g is the universal gas constant, T is the temperature, and ϕ is the electric potential. Accompanying this is the equation of continuity of flux:

$$\nabla \cdot \mathbf{J} = 0 \tag{2.2}$$

The combination of the NP and continuity equations contributes one partial differential equation for each species present. Generally, NP models have one dependent variable for each species (its concentration), plus an additional one for the electric potential. Thus, for model closure, an additional equation is required, known as the charge condition. There are two common forms of this condition which is also used to define the charge of the membrane domains. The simplest of these is the assumption of electroneutrality, where the overall charge at all locations is assumed to be zero.

$$\sum_{i} z_{i} c_{i} + z_{m} c_{m} = 0 {[2.3]}$$

The membrane charge (z_m) is +1 for an AEM and -1 for a CEM. The membrane fixed charge concentration (c_m) is very influential in determining overall membrane characteristics such as the electrical resistance and transport number. The relaxed version of electroneutrality is the Poisson equation, where regions with an overall charge are allowed but are related to an electric potential drop:

$$\nabla \cdot (-\epsilon \nabla \phi) = \rho \tag{2.4}$$

Here, ϵ is the permittivity of the membrane or solution, and ρ is the space charge density. The latter is the net charge per unit volume at any point in space and is calculated by summing up the charge contributions from both free and fixed ions.

$$\rho = \sum_{i} z_i c_i + z_m c_m \tag{2.5}$$

The extremely low value for the permittivity (order of 10^{-12} F/m) ensures even small values of ρ lead to sharp gradients in the potential. These only exist at the membrane-solution interfaces and can be vital for qualitative model accuracy at or above the limiting current density (LCD) when ion depletion occurs [28,55,56]. However, the use of the Poisson equation introduces an additional variable in ρ which tends to be quite



numerically stiff and thus greatly increases numerical complexity. Resultantly, for models operating below the LCD, it is common to assume electroneutrality to lessen the computational burden.

The Donnan potential is a sharp change in the electric potential at the membrane-solution interface and is a common inclusion for NP models. There is an abrupt change in concentration in the electric double layer adjacent to the membrane, with the concentration of counterions and co-ions rapidly increasing and decreasing from the solution domain into the membrane, respectively. There must be a complementary change in the voltage across this region to maintain the equilibrium of electrochemical potential

$$\Delta \phi = -\frac{R_g T}{z_i F} ln \left(\frac{c_{i,m}}{c_{i,e}} \right)$$
 [2.6]

The membrane and electrolyte concentration terms $(c_{i,m})$ and $c_{i,e}$ are valid for all co-ions and counterions, and so a concentration equilibrium at the membrane surface can be established. For every pair of ions present, the following relation is defined:

$$\left(\frac{c_{1,e}}{c_{1,m}}\right)^{z_1} = \left(\frac{c_{2,e}}{c_{2,m}}\right)^{z_2}$$
 [2.7]

Further, the electroneutrality condition ensures that the anion and cation charge densities are equivalent and that the charge densities in the membrane sum to the fixed charge density. Therefore, the co-ion and counterion concentrations in the membrane and electrolyte domain are not independent, and utilising the above equations decreases the computational complexity. For a single monovalent salt, the relation is quadratic and thus can be solved analytically (Chapter 5, Eq. 5.18).

Due to their complexity and the multitude of partial differential equations employed, NP models are commonly solved in Multiphysics programs such as COMSOL or Ansys Fluent. These lend themselves to investigating ED more comprehensively by accounting for the convection field through solving the Navier-Stokes equations. Section 2.4 investigates such models in depth. However, many stipulated-equation NP models do exist. The remaining three modelling methods detailed below are all stipulated-equation type.

2.2.2 Circuit-based models

Circuit-based models take a more macroscopic approach to ED modelling, where the stack is represented as an arbitrary number of resistors in series, each contributing to an overall stack resistance [54]. These resistances can then be modelled separately and used to represent individual transporting domains. Membrane resistances are typically assumed to be constant, and electrolyte resistances (R_e) are calculated through the solution conductivity:

$$R_e = \frac{d}{\kappa} \tag{2.8}$$

where d is the intermembrane distance (channel thickness) and κ is the solution conductivity. The latter is often correlated to the solution concentration through a proportionality constant known as the molar conductivity [57] or computed using the Nernst-Einstein equation:



$$\kappa = \frac{F^2}{R_g T} \sum_i z_i^2 c_i D_i \tag{2.9}$$

Ohm's law can then be used to calculate a current density (i) from the resistance (R_{cell}) and voltage (V_{cell}) across a cell pair

$$i = \frac{V_{cell}}{R_{cell}}$$
 [2.10]

The condition of continuity of current ensures that this current density is the same across all cell pairs. It should be noted that the resistance used throughout is the area resistance, with units of ohm square metre (Ωm^2) . Doubling the area through which current flows halves the overall resistance and doubles the current but does not change the current density. Thus, using an area resistance is important when computing the current flowing through an infinitesimal area. Once a resistance is known, Faraday's first law can be used to determine a transmembrane flux (\dot{N}) :

$$\dot{N} = \frac{i\varphi}{F} \tag{2.11}$$

where φ is the current efficiency, defined here as the proportion of current which leads to a net salt transport from the diluate to the concentrate channel. Once the transmembrane flux is known, the change in stream concentrations can be calculated by approximating the channel material balance as a PFR or a CSTR.

PFR:
$$\frac{dc}{dx} = -\frac{1}{ud} \dot{N}$$
 [2.12]

CSTR:
$$\frac{\Delta c}{L} = -\frac{1}{ud}\dot{N}$$
 [2.13]

Circuit-based models are unparalleled in their flexibility as they allow for virtually any phenomenon to be represented through contributions to the resistance and material balance. The key variables of the solution concentrations and current density make them ideal for process models of any scale. As such, the work presented in Chapters 5 and 6 utilise this technique for the development of models of conventional ED and BPMED, respectively.

2.2.3 Semi-empirical models

Semi-empirical models can account for a very wide range of phenomena through the use of empirical tuning parameters and training data. They typically use a Nernst-Planck style equation to determine an overall flux from convective, diffusive, and electrophoretic contributions. One used by Kalab & Palaty [58] is:

$$J = \Xi_1 c_d + \Xi_2 (c_d - c_c) + \Xi_3 i$$
 [2.14]

Where Ξ_1, Ξ_2 and Ξ_3 are empirical parameters which represent convective, diffusive, and electrophoretic flux parameters, respectively. The simplification of the terms to single parameters allows for easy extension of the model to additional phenomena without requiring a total understanding, the most common being that of water transport. Water flux is calculated in a similar way to ion transport, with contributions from water osmosis and



electroosmosis (water transport with solvated ions). Other model aspects that can be added include concentration polarisation, reactions such as water splitting when the LCD is exceeded, and sub-models for the molar conductivity and transport number. A high degree of agreement with experimental data can be obtained using these models especially when the number of tuning parameters is large. However, this is not surprising. As John Von Neumann said: 'with four parameters I can fit an elephant, with five I can make him wiggle his trunk' [59]. When too many parameters are used to fit a limited data set, the model can become overfit, where many distinct permutations of the values of fitting parameters can be used to achieve the same accuracy. As such, the use of semi-empirical models results in a lack of fundamental insight. The extreme form of this type of modelling uses artificial neural networks with a vast number of tuning parameters [60]. These models are appropriate for industrial applications where predictability is more important than understanding or for very complex phenomena, such as membrane fouling [60], where full mechanistic modelling is not practical.

2.2.4 Non-equilibrium thermodynamic models

Non-equilibrium thermodynamic (NET) models, sometimes referred to as irreversible thermodynamic (IT) models, have a similar macroscopic approach to circuit-based models [54]. The key difference is that in NET models have a direct focus on the flows of different energies between the channels and the evolution of other thermodynamic variables. The work on continuum mechanics by Lars Onsager in the 1930s [61,62] typically features substantially. Models of NET type tend to vary quite widely in their formulation, but all use some kind of driving force for ion migration, typically either the electrochemical potential gradient between the channels or an entropy generation term.

The use of pure thermodynamic variables rather than electric resistances allows for the consideration of phenomena which are not readily modellable with circuit-based models. For example, Solberg *et al.* used an NET model to assess the viability of a waste-heat to hydrogen process using a reverse electrodialysis (RED) stack [63]. Here, the driving force transporting ions and generating a current is primarily the trans-membrane temperature difference and is readily captured through the electrochemical potential. Such an effect is challenging to capture using other modelling techniques.

Often, NET models are formulated in a linear equation matrix of the form:

$$\begin{bmatrix} J_e \\ J_w \\ i \end{bmatrix} = \begin{bmatrix} L_{ee} & L_{we} & L_{\phi e} \\ L_{we} & L_{ww} & L_{\phi w} \\ L_{\phi e} & L_{w\phi} & L_{\phi\phi} \end{bmatrix} \cdot \begin{bmatrix} \Delta \mu_e \\ \Delta \mu_w \\ \Delta \mu_\phi \end{bmatrix} \left(-\frac{1}{T} \right)$$
[2.15]

Here, the general form of the equation is flux (J) = transport coefficient (L) × driving force $(\Delta\mu)$. The three rows of the equation represent the flux of the electrolyte (e), the water flux (w), and the current density/electric potential (i/ϕ) . The matrix, often referred to as the Onsager matrix, represents the interactions between all fluxes and all driving forces. Each term in the Onsager matrix is representative of one or more phenomena. For example, L_{ee} describes the flux of salt driven by the difference in salt chemical potential (concentration), and thus represents diffusion. The two forms of water transport, osmosis and electroosmosis, are handled by L_{ww} and L_{we} ,



respectively. As such, this formulation makes it very easy to account for the large number of interacting phenomena in ED. The Onsager relation is a shortcut which concludes that the matrix is symmetric, i.e. $L_{ij} = L_{ji}$ and is often cited by NET models. A great deal of useful information may be extracted from the Onsager matrix such as the current efficiency:

$$\varphi = F \frac{L_{\phi e}}{L_{\phi \phi}} \tag{2.16}$$

Drawbacks of NET models stem from their complexity and focus on fundamentals. Whilst circuit-based models always have the macroscopic process itself in mind and relate important measurable variables such as the current density, NET models principally consider fundamental thermodynamic variables. Whilst these relationships are very rigorous and stem from the laws of thermodynamics, they require significant assumptions and simplifications to make them tractable and applicable to real processes. Further, under most conditions in ED, only one driving force dominates. Implementing this assumption simplifies the Onsager matrix and results in a formulation very similar to a circuit-based model. Therefore, the additional fundamental insight that NET models provide is usually not worth the added complexity and associated assumptions. Due to their rarity, NET models are not discussed any further in this literature review.

2.3 Investigation of stipulated-equation models

Stipulated-equation models of ED [18,58,64–90] are defined here as those developed for the first time within a study (rather than using a pre-existing program) and constitute a closed system of algebraic and differential equations. They are the sort of model that would be readily implemented either explicitly in software such as MATLAB or Python, or implicitly in programs such as gPROMS. In general, they aim to provide key insights into individual phenomena or overall process behaviour. Their value lies in the hope that investigating the model will lead to a greater understanding of the importance of different phenomena and how they interact. Further, many of them are well suited for the development of process models which can reliably predict ED performance for industrial design purposes. However, ED is an incredibly complex and multifaceted technology, and thus certain simplifications must be made to develop tractable models. As such, the many published works each have varying degrees of complexity and phenomena which are included or neglected.

There exists an inherent trade-off between model complexity and experimental burden, as greater model intricacy leads to a greater number of empirical parameters, all of which should be determined independently. It is thus unsurprising that many researchers tend to focus on the desalination of brine or brackish water as a case study. It has clear application with a strong societal impact and is also a well characterised and behaved system with no fouling or acid-base equilibria and is often approximated as pure sodium chloride.

Campione et al. [23] categorised ED models into simplified and advanced. Simplified models [67,71,73,81,83] use lumped experimental parameters to account for neglected phenomena and can be used quickly and accurately for initial process design purposes. They are typically one dimensional, with variation only in the direction of flow. Further, they tend to incorporate simplifying assumptions such as perfect permselectivity and the neglection



of concentration polarisation, diffusion and water transport [71]. The purpose of these models is to estimate key costing parameters such as power consumption and membrane area for given operating conditions (flow rates, concentrations, and voltages). However, due to their simplified nature and reliance on training data, they are highly specialised models and can only be applied to the conditions on which they were trained. Further, the neglection of more complex mass transfer phenomena means they don't directly account for the LCD. Instead, this is either considered through ancillary empirical relations or it is assumed that the current density is always below the limiting value.

For a greater accounting of phenomena for detailed process design and mass transfer investigation, more 'advanced' models are required. These are more common in the literature than simplified models, since conclusions based on individual phenomena can be drawn, rather than the whole system. Campione *et al.* subdivided the category of 'advanced models' further into Nernst-Planck models and semi-empirical models. The equations that these models are based on are described in Section 2.2.

Nernst-Planck models [64,65,68,74,76,85–87,91] use rigorous equations to solve a concentration field and account for convective, diffusive and electrophoretic mass transfer. This is the most common form overall of ED modelling and can predict the degree of concentration polarisation as well as the Donnan potential. However, it is also the most computationally demanding form of modelling since equations are based on vector calculus. Without the inclusion of a CFD Multiphysics solver (Section 2.4), Nernst-Planck models are limited to simple geometries or require assumptions such as perfect permselectivity and neglection of water transport to decrease complexity.

Semi-empirical models [58,75,78] take a basis in ED mass transfer theory, accounting for many of the same phenomena as Nernst-Planck models. However, they simplify these equations into several key variables and lumped empirical parameters which are tuned to fit the model to experimental data. A great many experiments are then undertaken to characterise all the empirical parameters. Each parameter can directly be associated with a certain phenomenon, and so a fair amount of qualitative and semi-quantitative information can be found. However, the experimental burden for semi-empirical models can be quite extensive. For example, Kaláb & Palatý [58] built a semi-empirical ED model, and characterised it with 45 distinct experiments, changing inlet concentrations and current densities, and measuring the stream concentration over time. Another weakness with this kind of model is the lack of globality. Extrapolating results outside of the conditions used to characterise the model may give unreliable results and full characterisation must be repeated when applied to another system.

A further model type which was not specified by Campione et al., but occasionally overlaps more with simplified models, is that of analogous circuit models [64,66,69,77,80,82,83,90]. These are the most common form of models which are solved without multiphysics simulators and are also the most varied in terms of the model formulation. The ability to simply sum up the different contributions to resistance makes this form of modelling adaptable. Additional resistance and efficiency terms may be added to account for losses and improve accuracy. However, the inclusion of complex phenomena in simplified terms can lead to the real behaviour becoming obscured especially if empirical fitting parameters are used. The large number of confounding variables in ED,



each of which can have their own fitting parameter, means fitting the model to data is computationally straightforward but does not necessarily lead to an accurate behavioural representation.

The modelling of ED typically concerns a batch-type system, rather than continuous or feed-and-bleed. This is because batch systems are used in laboratory experiments, and so directly modelling this facilitates validation. When ED is operated in batch mode, the streams are held in reservoirs and are continuously circulated to the stack and back to the reservoir (Figure 2.2). As such, the diluate and concentrate stream concentrations change over time. A separate reservoir is used for the electrode washing solution, typically with Na₂SO₄, within which oxygen and hydrogen are generated from the electrode reactions.

2.3.1 Differing model aspects

Due to the high complexity of ED and the multitude of coinciding phenomena, a wide variety of assumptions and simplifications are used to improve model tractability. Hence, there is a high degree of variability between different published models. This section examines the different phenomena that stipulated-equation models include or neglect for their importance to the overall ED process and their effect on physical accuracy.

Electric representation of the unit cell

Models based on the Nernst-Planck equation directly equate electrophoretic flux to the electric potential gradient. Circuit-based and semi-empirical models vary in whether the current or voltage is established as an input variable, demonstrated by a fixed current model from Luiz et al. [82] and a fixed voltage model from Ortiz et al. [90]. Further variation is seen for fixed voltage models as to whether it is the voltage over a single cell pair or the voltage over the entire stack which changes. Fixed current models are intrinsically easier to solve since the flux and current are proportional to one another through Faraday's law. As such, the material balance is solved first, and the voltage requirements are calculated retroactively. However, maintaining a constant current along a flow path is not realistic as the changing resistance means the voltage must vary. In reality, it is the stack voltage which is constant along the flow path, dictated by the external power supply. The current density changes as the

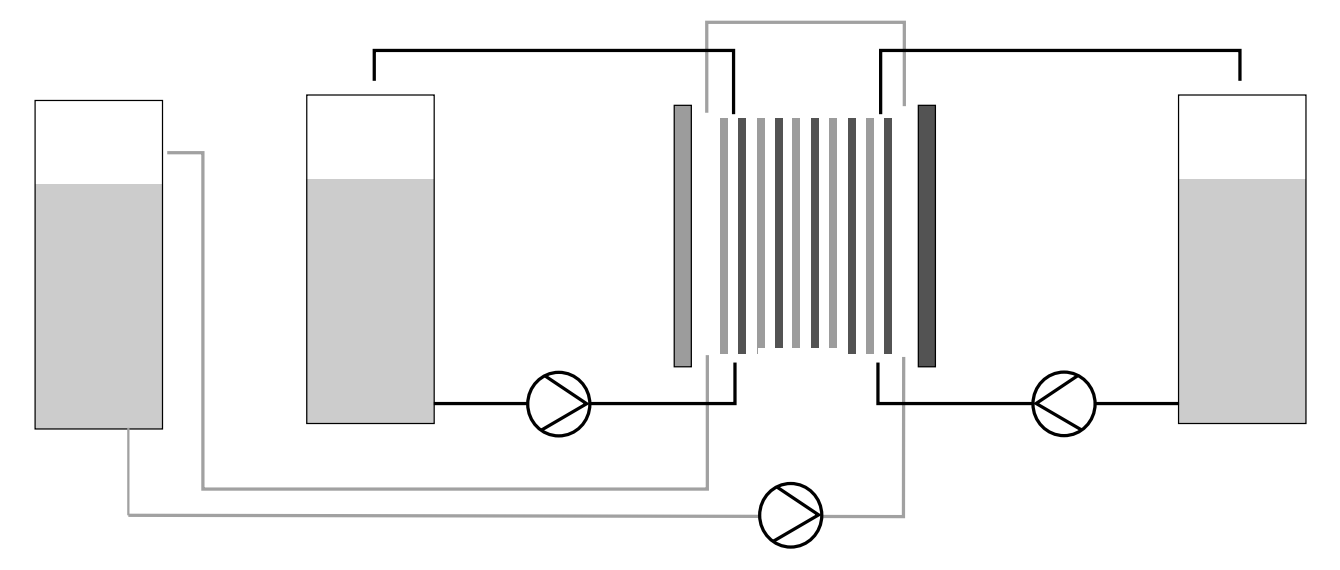


Figure 2.2: A schematic representation of a recirculating batch ED system. Three reservoirs are shown which feed solutions to a stack.



electric resistance varies due to changing electrolyte concentrations. Further, the cell voltage varies due to the changing overpotential at the electrodes which can be determined with the Tafel equation. Despite this, it is most common to fix the cell voltage. The current density and flux are then calculated from the cell resistance, which may be composed of ohmic and non-ohmic contributions [77], or just ohmic [90]. Non-ohmic contributions tend to be a 'catch-all' category which includes the resistance from concentration polarisation and voltage drops from electrode overpotentials. These have very non-linear dependences on current density and are often accounted for in empirical terms. A resistance term can be used to account for phenomena which are not a resistance but have similar effects on the flux, such as the electrode overpotential. Validation typically only comes from concentration-time data for a batch system, and so these confounding variables are easily hidden.

Permselectivity

Membrane selectivity is a key performance parameter and is directly related to the current efficiency and specific energy consumption. The membrane permselectivity is captured in a transport number which represents the fraction of charge transported through a membrane by counterions, with the rest coming from co-ions. As such, they range from zero to unity, but feasibly must be greater than 0.5 to preferentially transport counterions over co-ions. A common assumption is perfect permselectivity [80,82,83,85,87], where the counterion transport numbers for both membranes are set at unity. They can also be fixed at non-ideal values [64,67,77,81] or calculated using an empirical or theoretical (derived from the Donnan equilibrium equations) transport number model which considers the electrolyte concentration [66,69,89]. The use of imperfect permselectivity is more important when dealing with acids [66] as protons pass through AEMs with relative ease due to their size, and so selectivity is likely to be far from ideal.

Transport numbers are used to explain the discrepancy between a measured current density and the charge transferred from an ion flux determined from a concentration-time profile. This is because the transport numbers directly link the current density and ion flux through Faraday's law. Like with the nebulous resistance terms often added, there are many confounding phenomena which can be accounted for through the transport number due to their similar effects. For example, water transport leads to a dilution of the concentrate stream and so the concentration does not increase as fast as expected, leading to a lower apparent flux. This is the same effect that back-migration has on the concentration, and so can be accounted for in the model by reducing the transport number. Observations of the liquid volume in reservoirs over time would be able to discern between these two phenomena; however, detailed analysis of this has not been seen.

Ion diffusion and concentration polarisation.

Trans-membrane ion diffusion between the diluate and concentrate arises due to the difference in the interfacial electrolyte concentration between the two channels. This can either increase or decrease the rate of ion removal from the diluate depending on their relative concentrations. Concentration polarisation arises due to the presence of boundary layers where transport is slowest, leading to the accumulation or depletion of ions at membrane surfaces. These two phenomena are linked, but their inclusion varies significantly between models. The



omittance of concentration polarisation assumes a completely flat concentration profile characteristic of plug flow. This may result in predicting diffusion in the wrong direction (Figure 2.3). Further, both these phenomena can be accounted for through confounding variable models. The effect of concentration polarisation is to increase the overall resistance to account for the low concentrations reached at the diluting side of the membrane and can be accounted for through a nebulous non-ohmic resistance term. Diffusion affects the rate of ion transport, and so changing the transport number will ensure both the current density and concentration profiles fit experimental data.

Inclusion of the limiting current density.

The limiting current density is achieved when extreme concentration polarisation leads to a depletion of ions at the diluting surface of a membrane. This serves as an effective upper bound to ED operation above which the electrical resistance dramatically increases and water splitting occurs. The LCD is reliant on the complex channel hydrodynamics as well as the inlet concentration. Typically, when the LCD is accounted for, an empirical power law is used, usually of the form:

$$i_{lim} = a_1 \ u^{a_2} \ c_0^{a_3}$$

where a_1 , a_2 , and a_3 are empirical fitting parameters, u is the velocity and c_o is the inlet concentration [92]. If the LCD is not included, but concentration polarisation is, then an infinite resistance is reached as the interfacial concentration falls to zero. However, if concentration polarisation is not included, then there is no way to know if the limiting current density has been exceeded. Many phenomena that are difficult to quantify or measure experimentally have been identified as leading to a reduced LCD. These are things like solution leakage between channels [93] and ionic shortcuts or shunt-currents where charge is transferred through manifolds [94]. The degree

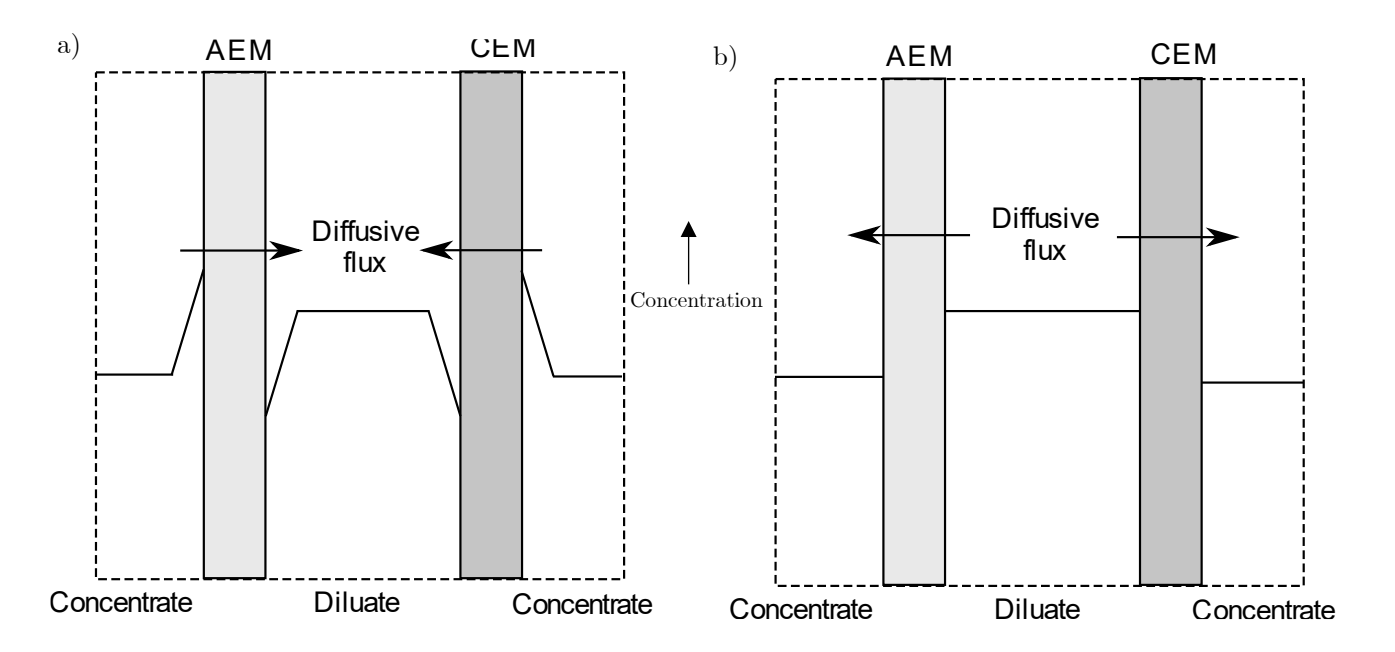


Figure 2.3: A representation of how the inclusion of concentration polarisation can affect the magnitude and direction of the diffusive flux. Both left and right figures have the same channel concentration. However, the inclusion of concentration polarisation (left) leads to concentrate to diluate diffusion, whereas the omittance of it (right) gives diluate to concentrate diffusion.



of turbulence generated by the spacer also affects the thickness of boundary layers, changing the LCD in a nonlinear way. It is therefore very difficult to accurately model the LCD without using empirical models.

Water transport.

Water is transported across the membrane by two mechanisms: Osmosis due to a salt concentration gradient leading to an osmotic pressure difference, and electroosmosis due to the association of water molecules to transported ions. Transport can be explicitly accounted for in models through a water balance with terms that include osmotic permeability parameters and hydration numbers (molecules of water transported per ion) to account for osmosis and electroosmosis, respectively. Water transport can significantly alter the volumes of both diluate and concentrate reservoirs when a more hydrophilic membrane is used, and overall counteracts the concentrating effects of ED. Further, the drawing out of water from membranes at high salt concentrations can lead to a reduction in the pore size and consequently an increase in the electrical resistance[95]. Many studies neglect the water balance all together, concluding its effect is minimal after observing a small change in the reservoir volume. Both forms of water transport will be faster at higher concentrations, since the salinity gradient is steeper, and the ion transport rate can be higher. It is also a phenomenon that can erroneously be accounted for by modification of the transport number.

Channel material balance model.

There are three main types of model that are used as the basis for ED channels: well mixed, fully differential and a discretised model, which uses a finite series of well mixed cells. This is akin to modelling the channel as a CSTR, PFR, or finite series of CSTRs, respectively. It should be noted that well mixed is only in the direction of flow, and not necessarily across the width of the channel, and so concentration polarisation can still be considered, as seen in the work by Galama et al. [87]. All three kinds of models have been used extensively, with well-mixed being algebraically simpler than differential models and thus easier to solve. However, the assumption that the change along the length of the stack is negligible is often not valid in practice. This is especially true at the beginning of experiments when the concentrate stream has a low concentration and transport is fast since both diffusional and electrophoretic flux act in the same direction. For low concentration streams, even small absolute changes in concentration have large relative effects on the electrolyte resistance. The inability for well-mixed models to account for this restricts their use to moderate concentrations in very short stacks with low current densities and would be unlikely to achieve accurate results at industrial scale. Discretised models are an improvement and approach the full differential solution as the number of cells approaches infinity. It can be easier to implement this type of model in explicit modelling programs without the use of differential equation solvers.

Electrode potentials.

Electrode potentials are often neglected when calculating the cell voltage from the total stack voltage. It is often assumed that for industrial scale stacks, the electrode potential (order of 1 V) is negligible when compared to the total stack voltage (order of 100 V), which is reasonable. However, validation of these models is often caried out on experimental stacks where the total voltage is much lower (~10 V), and so neglecting it may cause



significant error. Further, the electrode overpotential (η) is a function of current density, and so is not constant for batch systems. The electric potential drop between the electrodes and solution can be contained in empirical non-ohmic resistance terms to force agreement with experimental data. Inclusion of the electrode potentials can be handled through the Tafel equation, for which data for the exchange current density (i_0) and Tafel slope (b) parameters is readily available in published literature.

$$\eta = b \ln \left(\frac{i}{i_0}\right) \tag{2.17}$$

Donnan Potential.

The Donnan potential is the sharp change in voltage at the interface between membranes and solutions, resulting from the exclusion of co-ions [69], and the formation of an electric double layer [68] (Eq. 2.6). It is neglected by most models, however Qasem et al. [83] state that it is important for an accurate prediction of the electric potential. Their model under-predicted the voltage when Donnan potential was excluded, and over-predicted when it was included, showing that the underlying phenomena are highly complex and are still not fully understood. Since the electric double layer is extremely small (a few ions thick) and there are rapid changes in concentration and electric potential, modelling is not trivial. The drop in potential can be accounted for through an increase in resistance, allowing models to maintain accuracy without its direct inclusion.

Molar Conductivity Model.

To calculate the solution conductivity from the ion concentration, a molar conductivity is typically used as a proportionality constant. However, the method through which the value of the molar conductivity is derived varies between studies, and typically requires complex non-linear empirical models at high concentrations. At low concentrations, a constant value of the molar conductivity is sufficient. This is the most common approach and is either found in literature or calculated through the Nernst-Einstein equation (Eq. 2.9). Moderate to high concentrations require the use of the Falkenhagen equation, or other empirically derived model. The issue with simply using a fixed molar conductivity is a lack of globality, with the model valid for a dilute concentration only. Since there can be large changes in the concentrations of solutions over the course of ED, the accuracy of certain models may significantly decrease. Generally, higher concentrations require more sophisticated models for the molar conductivity, requiring greater computational expense [72]. However, ED is typically only operated at low to moderate concentrations since it is not economical at higher concentrations. As such, molar conductivities or the Nernst-Einstein equation are usually sufficient. Inaccuracies in solution conductivity can also be accounted for by nebulous resistance terms.

Summary

Modelling ED is very complex and involves consideration of a range of variables and phenomena which are deeply interconnected. The design space over which certain phenomena are important is not fully understood, which can either lead to over-simplification or a very high complexity. The wide use of empirical fitting parameters can account for both these errors where certain phenomena are exaggerated to compensate for deficient ones



across the myriad of confounding variables. As such, when compared against a limited data set, model inaccuracies are often obscured while still attaining good agreement between the model and experimental data. It has been shown that modifications to the current efficiency through the membrane transport numbers and ancillary resistance terms are able to compensate for inaccuracies in nearly all phenomena. For circuit-based models, these parameters directly relate the only experimentally measured values of the voltage, current, and concentration, through Ohm's law and Faraday's law (Figure 2.4). As such, sophisticated models with a high enough complexity can always be tuned ensure a good fit with concentration and current profiles, compromising the verisimilitude to these studies. Accurate representations and conclusions about specific phenomena are thus difficult to ascertain. Further, increasing the complexity of a model does not increase its value when additional fitting parameters are introduced. Instead, the model can become 'overfit' where distinct permutations of parameter values can achieve equally good fits at differing local minima. Consequently, the fit values lose their physical representation and deep analysis of the model results to compare different phenomena is not possible.

The wide use of fitting parameters in ED modelling explains why all published models show 'good agreement' with experimental data, despite having a wide variety in formulation and complexity. As such, the general predictive capabilities of a model are restricted to the data range it was trained on. One of the core strengths of ED as a separation technology is that it has a very broad range of applicability across different industries. This is not generally reflected in the published literature of ED models.

Most modelling publications have a similar format: A new model is presented which varies slightly from existing models or is applied to a new application; it is fit to experimental data where close agreement is achieved; nothing more is concluded other than that the model developed is accurate. This formula arguably adds limited value, especially since many works of this type already exist. Greater value from a model comes from analysis into details that are not experimentally accessible. Through this, the relative importance of different phenomena may be identified and future research to improve the technology or modelling efforts may be directed.

2.3.2 Further established model commonalities

Despite the wide variety of models that exist in the published literature, there are assumptions that nearly all models follow. Because of their ubiquity, these assumptions receive far less scrutiny than the ones already mentioned. In this section, these commonalities are investigated to ascertain their impact and validity.

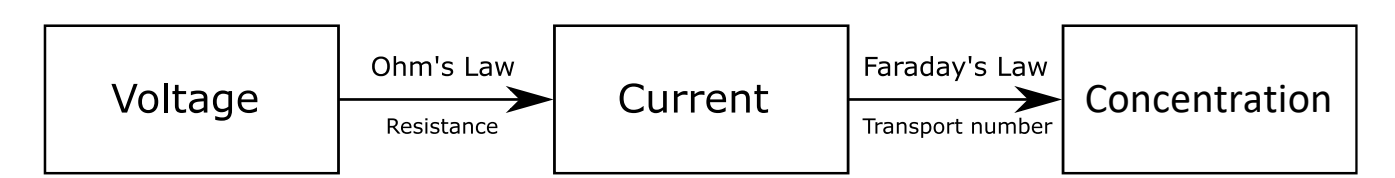


Figure 2.4: A schematic representation of an overview of most circuit-based models. Known/measured variables are in boxes and the links between them are shown with the arrows. This demonstrates how virtually any model deficiency can be accounted for through modifications to the electrical resistance and membrane transport number.



Due to the repetitive geometry of an ED stack, researchers tend to simplify models to a single cell and impose either a periodic boundary condition or a fixed boundary flux at the edges of the unit cell. From here, the results of a single cell may be extrapolated to an arbitrary number of cell pairs when modelling a full ED process. The assumption of channel equivalence is thereby implicitly used. At present, no multi-channel ED model has been developed, owing to the high computational demand it would require, and the belief that channels are equivalent. However, this assumption has not been confirmed. The geometry of a plate-and-frame heat exchanger (PFHEX) is analogous to an ED stack. A non-uniform distribution of flow is well established in PFHEX, and so it is possible that this is present in ED as well. A study of the flow maldistribution in ED is therefore an important area to investigate, and one explored in Chapters 3 and 4 of this thesis.

Another observed trend is that models are typically based on a batch system. This is as expected since laboratory scale stacks are almost exclusively small-scale batch units, and modelling as such facilitates direct comparisons to be drawn to experimental results. However, batch mode is rarely used in industry where either continuous or feed-and-bleed steady state systems are preferred. Some useful information can be ascertained about continuous operation from batch-models including estimates for the specific energy consumption and transport numbers. However, due to the many confounding variables in ED which obfuscate the underlying phenomena through fitting parameters, it is uncertain that the true phenomena are accurately captured. Therefore, models derived for batch systems are likely not valid for large-scale continuous operation due to the differences in concentration, hydrodynamics, and geometry. The values of the non-ohmic resistance and transport numbers may have produced accurate data on a small-scale stack, but the correlations used will not apply in the same way at a larger scale. Consequently, the models developed in Chapters 5 and 6 of this thesis intentionally avoid the use of empirical fitting parameters in an attempt to accurately capture the underlying phenomena. Further, the structure of the model was designed such that a direct conversion between a batch and continuous process is built in.

By far the most popular application of ED studied is that of the desalination of brine or brackish water to produce potable water [23,64,67,69,71,73,74,76,77,80,83,86,87,89,90]. This is due to its simplicity and strong presence in the modern sustainability zeitgeist. Many such works specifically focus on a pure NaCl system for simplicity and derive a model which fits well with experimental data. Further, NaCl is very well characterised with well-defined diffusivities and lack of acid-base equilibria, making modelling far easier. However, the principal barriers that must be overcome before ED can become viable for desalination include the abundance of other ionic species (importantly Mg²⁺ & Ca²⁺) and colloidal particles which can cause severe membrane scaling [23]. Beyond studying desalination, a pure NaCl system is useful for troubleshooting a new ED unit or testing the accuracy of a new model when no fitting is used. This is because it is one of the simplest salts possible yet still captures the fundamentals present in all ED systems. However, the fitting of models to training data of a pure NaCl system does not offer much value since those models cannot be extended to a realistic process as there is no guarantee the foundational phenomena have been captured accurately.



Nearly all physical applications of ED operate with more than one cation or anion present, but models designed for multicomponent systems are rare [88,96]. Those that do almost exclusively neglect interactions between ions since it is challenging to capture mechanistically and results in more experimental fitting. However, interactions between ions can be significant when considering multivalent ions in a system with monovalent ions at a high concentration. Van der Stegen et al. [84] accounted for the interactions between competing ions through the modification of the diffusivities of each of species. This proved effective but still required experimental parameter fitting to accurately match data. An alternate method involves employing membrane selectivity parameters to segment the current between different counterions to determine their relative fluxes. Again, this is ultimately simplifying the differing degrees of electrostatic interaction between fixed charges and transported ions into a single number. Any selectivity parameter determined this way would be bespoke only to the exact system and thus can add to the over-parameterisation of models. Greater fundamental theoretical work on membrane selectivity is clearly needed.

Related to selectivity is the effect of specific electrostatic interactions between the membrane and ions. Luo et al. [79] claim that traditional models begin to fail when these interactions grow in strength. This could be handled by an additional diffusion coefficient model as Van der Stegen et al. [84] did for selectivity, however, would result in the same kind of model fitting and detracting from fundamental understanding of the ED process.

A common justification for why models are created is that it can be used for the design and improvement of industrial scale units. This justification employs an implicit assumption that models will remain accurate for scaleup. However, it is very rare that these models are tested on a range of unit sizes, or anything larger than laboratory scale. Wright et al. [80] are the exception to this where a robust circuit-based model was created without fitting to experimental training data and was tested on both a lab-scale and commercial-scale stack with reasonable accuracy. Further, this model employs no prior system characterisation demonstrating that the use of empirical fitting parameters is not necessarily required. However, this model is tested on a very simplified case of pure NaCl, at concentrations close to those used when manufacturers characterised the membranes and assumed that transport numbers were equal to unity. Therefore, the model was validated using the best-case scenario, and under different conditions it could possibly lose accuracy. This limitation was identified within the study and tested by applying the model to and ED unit processing groundwater, where much greater deviations between predicted and observed results were seen. This demonstrates that although it is possible to avoid parameter fitting in models, it requires the use of existing experimental data, which exist only for certain cases and have limited applicability to different scenarios. The success of this study and the ways in which it can potentially be improved were considered when developing the models of Chapters 5 and 6. This study also acknowledged the limitations of the model, which is uncommon among published ED models.

Membrane fouling is an important consideration for industrial ED use as it increases the overall electric resistance and power consumption. Resultantly, membrane cleaning is conducted at regular intervals. This leads to process down-time and additional costs for commercial operations, and so effectively modelling membrane fouling can be used to optimally schedule cleaning cycles. A few studies have attempted to derive mechanistic



models for the process of fouling [97–99], but rely on fitting against experimental data, and so have limited general predictive capabilities. Pawloski et al. [100] developed a statistical linear regression model to predict the long-term behaviour of RED with seawater and river water over a month using data from 2D fluorescence spectroscopy. Although this was able to accurately account for the effects of fouling, the requirement for real-time data hinders the predictivity of the model. De Jaegher et al. [60] developed a model for colloidal membrane fouling which combines an adapted Nernst-Planck model with an artificial neural network to account for fouling. The fouling model considers the rate of collision of colloidal particles with the membrane and probability of attachment. As before, good agreement with experimental data was achieved. However, neural networks inherently require a large and complete data set to perform well and so are only useful for the most established applications.

In summary, there are several issues with how ED is currently modelled. Extensive parameter fitting of confounding variables leads to a lack of globality and an obfuscation of the underlying phenomena. The interactions of behaviours are very complex and multifaceted, and this must be acknowledged when models are created. The fact that a model has good agreement with experimental data it was fit to does not reveal any understanding of the fundamental behaviours of ED. It is when models do not fit data that our understanding is questioned, and areas of valuable investigation and insight are found. The conclusions drawn from the literature were used as guiding principles for the development of the models presented in Chapters 5 and 6 as well as the initial spark for investigating maldistribution (Chapters 3 and 4).

2.4 Computational fluid dynamics simulations

2.4.1 Overview

2.4.1.1. Software packages used

Fluid dynamics plays a key role in ED and is intrinsically linked with mass transfer processes [101]. For at least the last decade, several groups have devoted considerable research efforts to the multi-dimensional simulation of ED [66,91,93,96,101–125] in three different software packages. These are: COMSOL Multiphysics, Ansys (both Fluent and CFX), and OpenFOAM. Published studies which use CFD packages fundamentally differ from stipulated-equation models by considering the fluid flow either in isolation or in conjunction with mass transfer and electric field calculations. All three programs use a similar hierarchy: selecting governing physics, defining and meshing geometry, implementing boundary conditions, implicitly solving partial differential equations, and processing the results. They differ in the means of user input and the solver method used (Table 2.2).

The most popular package is COMSOL, primarily due to the presence of an inbuilt ED application module. This allows users to input system-specific parameters into a graphical user interface (GUI) and solve the Navier-Stokes, Nernst-Planck, and Poisson equations sequentially or concurrently. Further, the presence of a pre-existing model significantly reduces the developmental overhead from researchers. Further, the fact that COMSOL uses the finite element method over the finite volume method is key, the relevance of which is discussed in greater detail below. However, the use of an inbuilt ED model restricts the applicability and diversity of CFD research



Table 2.2: Comparison of different CFD software used to model ED

| | COMSOL | Ansys Fluent/CFX | OpenFOAM |
|------------|------------------------------|-----------------------------------|--------------------------|
| Studies | [91,96,102,103,107,110,111,1 | [66,101,109,112,114,120,121,123,1 | [93,106,108,118] |
| | 13,115,117,119,124,125] | 26] | |
| Number of | 14 | 9 | 4 |
| Studies | | | |
| Solver | Finite element method | Finite Volume/element method | Finite Volume method |
| method | | | |
| User input | Graphical user interface | Graphical user interface (GUI) | Directly coded text user |
| | (GUI), all in one | across several application. User | interface (TUI) |
| | application. | defined function coded in C | |
| | | programming language | |
| Inbuilt ED | Yes | No | No |
| module | | | |

and leads to 'plug-and-play' studies where researchers use the pre-defined model, change the values of the input parameters, and publish the results with little novel value [113]. The lack of variety results in a polarising view of Nernst-Planck CFD models where only one formulation is seen. The field would therefore benefit from greater representation of different model forms.

Despite the domination of COMSOL for CFD models of conventional ED, models of RED are seen in Ansys Fluent and OpenFOAM. These models are far easier to solve because the non-linear coupling of the potential field and mass transport equations can be neglected. The primary difference between conventional ED and RED which facilitates this difference is that in RED, salt transport is driven by convection and diffusion, and the electric field is formed as a result of ion transport. As such, the governing transport equations can be simplified and the flow, concentration, and electric potential fields can be solved sequentially in that order.

OpenFOAM is an opensource, code based CFD software used by one research group to investigate fluid dynamics [108,116] and RED mass transfer [106,118]. Although the text user interface (TUI) is considerably less user friendly than a GUI, it gives a greater understanding of how the program is operating and how the equations interact.

Despite the lack of inbuilt mass transfer models, Ansys Fluent and Ansys CFX are popular for other aspects of ED modelling. For Fluent, focus is given to pure fluid dynamics modelling [66,109,114,120] and reverse electrodialysis mass transfer [101,123,126] and CFX has been used to study membrane deformation resulting from trans-membrane pressure differences [112,121,122]. Since these are the only applications of Ansys CFX in modelling ED, they are not discussed here further. Like COMSOL, Ansys programs are based on a GUI and so are relatively user-friendly. Ansys Fluent has the added capability of implementing user defined functions (UDF), which are scripts written in the C programming language and directly interface with solvers. They can be used to manipulate aspects of the simulation and for implementing additional constraints, such as ensuring electroneutrality, by setting a cell zone condition requiring the overall charge density to be zero everywhere.



2.4.1.2. Finite element and finite volume methods

The main difference between Fluent and COMSOL is that while Fluent uses a finite volume method, COMSOL uses a finite element method. These two methods differ in the route taken to the solution and thus are effective for different problems. Both methods compute a solution on nodes of a discretised meshed geometry with the values of the dependent variables (i.e. concentration and electric potential) computed at either the centroids of the cells of the mesh (finite volume) or at the points of intersection (finite element).

Fundamentally, the equations of a model are constraints on the values that the dependent variables and their gradients can take. A well-defined model should have one distinct solution where the values of the dependent variables at each spatial and temporal point on a meshed geometry balance the governing equations. Since the number of nodes of a simulation mesh can be of the order of many millions, finding this solution can be challenging. Both the finite element and finite volume methods start by initialising the values of the dependent variables at each node using an initial guess or a simplified (usually uniform) solution. The 'residuals' of the model, which are metrics of how far the equations are from being balanced, are then calculated. Advanced solvers are then implemented to iteratively adjust the values of the dependent variables at each node to reduce the residuals to below a threshold set by the user. There are several solvers implemented by both methods, but usually use some form of iterative gradient decent and are derived from Newton's method. Here, the effect that adjusting the dependent variables at each node has on the residual is probed, and a step is taken in the direction which leads to the greatest decrease in the residual. This process is then repeated until the residual is below the tolerance threshold.

The difference between the finite element method and the finite volume method is in how the model equations are interpreted and how the relationships between dependent variables at neighbouring nodes are considered. In the finite volume method, variable values are stored in the cell centroids, and 'fluxes' are calculated across the faces of cells from the variable gradients (Figure 2.5). Ultimately, the finite volume method looks to balance the fluxes in and out of cells and is the epitome of the classic engineering equation: Accumulation = In - out + generation. In Fluent, a standard general transport equation is used which can be adapted for a specific application.

$$\frac{\partial c_i}{\partial t} + \nabla (B_i c_i - \Gamma_i \nabla c_i) = S_i$$
 [2.18]

From left to right these terms represent accumulation, convection, diffusion, and a source/sink term, with general parameters B_i , Γ_i and S_i , to scale the convection, diffusion, and source respectively. The variable c_i represents the value of a scalar or vector dependent variable. From this general equation, many continuum mechanics problems can be derived. For example, the heat equation (Fourier's law) can be derived by setting c_i as the temperature, B_i and S_i as zero, and Γ_i as the thermal conductivity. Extensions to account for additional phenomena can be implemented through modifications to the three parameters (e.g. resistive Joule heating by modifying S_i). Implementing the Nernst-Planck and Poisson equations in this general transport model is also



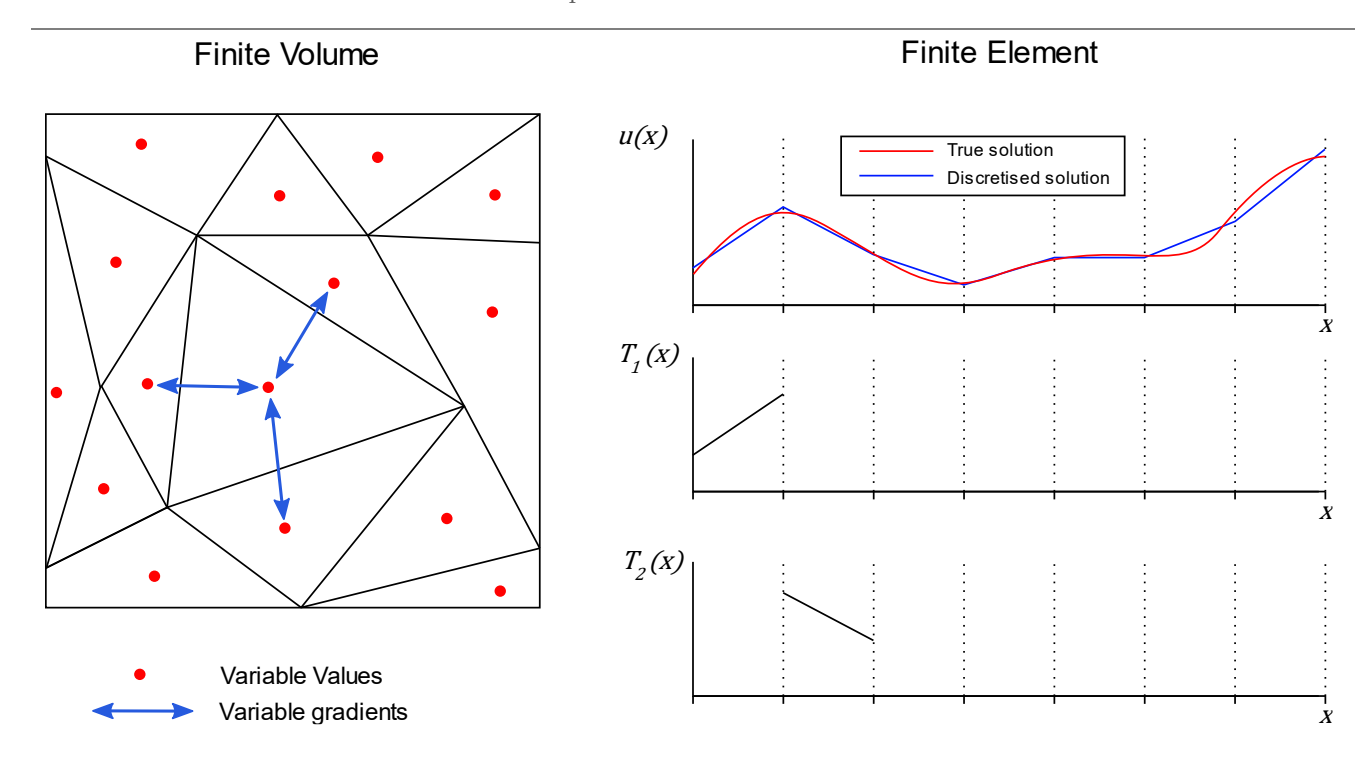


Figure 2.5: A representation of the difference between the finite volume and finite element methods of CFD modelling. For finite volume modelling, variable values are stored at the cell centroids, fluxes are calculated between them, and used in a standard transport equation. For finite element modelling, the solution is represented as a set of piecewise polynomial functions and the governing PDE is sampled in each subdomain using a set of test functions equal to the solution within a small region. An integration reduces the order of continuity by 1.

possible. For the Nernst-Planck equation, B_i is the sum of convection and electromigration, and Γ_i is the diffusivity. Any reactions can be handled by the source term. The benefit of using a standard equation format is that solvers can be optimised for it.

The finite element method takes a more general approach where any form of PDE can be implemented, not just those which can be adapted from a standard equation. To lessen the computational burden, the PDE is converted to a 'weak form'. The primary goal of this is to integrate the PDE to remove a higher order derivative. Second order and higher derivatives are computationally difficult to handle for large problems, and so this conversion greatly expedites the simulations. Consider the following one-dimensional second order PDE:

$$u''(x) = f(x)$$
 [2.19]

A solution to this would be to compute the value of u(x) over the domain of interest (\mathcal{D}) . The obvious way to remove one derivative order would be to integrate PDE over a small domain d which is a narrow subset of the overall solution domain \mathcal{D} $(d \in \mathcal{D})$.

$$\int_{d} u''(x) = \int_{d} f(x)$$
 [2.20]

This could then be repeated over the myriad sub-domains to find a set of new first-order PDEs which are much easier to handle. The solution to this PDE set would then give a discretised solution where the average value of u(x) within each sub-domain is computed. However, handling the large number of integrals individually is



computationally cumbersome. Instead, some mathematical wizardry is implemented through the use of a set of 'test functions'. These test functions, T(x), are a set of functions of x, each defined to be zero everywhere except for within a small domain. The form of the test functions used is entirely arbitrary, and thus can be selected advantageously. The only requirement is that it is convenient to differentiate within the domain where it is active, and so polynomial functions are typical. For each test function, corresponding to one element of the domain, both sides of the PDE are multiplied by the test function and it is integrated over the entire domain.

$$\int_{\mathcal{D}} T(x) \ u''(x) = \int_{\mathcal{D}} T(x) f(x)$$
 [2.21]

$$T(x) = \begin{pmatrix} T_1(x) \\ T_2(x) \\ \dots \\ T_n(x) \end{pmatrix}$$
 [2.22]

This method essentially samples the PDE at a finite set of discretised locations and thus has the same effect as just integrating over a subset of the domain as per Eq. 2.20. Using integration by parts, the weak form of the PDE becomes

$$[u'(x) T(x)]_{\mathcal{B}} - \int_{\mathcal{D}} T'(x) u'(x) = \int_{\mathcal{D}} T(x) f(x)$$
 [2.23]

where \mathcal{B} is the boundary of \mathcal{D} . Hence, the highest order derivative that u must be evaluated to (order of continuity) is reduced from two to one. It is also useful to discretise the solution (u) into a piecewise-polynomial function which can use the same discretisation (mesh) as the test function. In fact, since the choice of the set of test functions is arbitrary, it is convenient to set the test function equal to the solution in the domain where it is not trivial (Figure 2.5). Since the value of $T_n(x)$ is zero everywhere except for a small region, computing the terms of Eq. 2.23 becomes trivial.

The simplest form of test function is linear, but any conveniently differentiable function is suitable. A linear test function is determined by just two parameters. Discontinuities between neighbouring test functions can be disallowed when a continuous solution is required, which subsequently reduces the degrees of freedom per node to just one. As such, the solution to the problem involves manipulating the values of the parameters which define the linear functions such that all the resultant PDEs of Eq. 2.23 (one per element) balance. As with the finite volume method, the 'balance' of the equations is quantified by a residual which must be reduced below a threshold tolerance.

In summary, the primary difference between and inherent strengths of the finite element and finite volume methods comes from their opposite approaches to specificity. In the finite volume method used in Ansys Fluent, all problems must be related to a standard transport equation. For nearly all continuum mechanics problems faced by engineers, this is sufficient to describe the governing equations. As such, sophisticated solvers that are purpose built for handling equations of that type can improve computation expediency even for second order derivatives. The finite element method used in COMSOL Multiphysics takes a much more general approach where any PDE can be implemented as long as it is converted to the weak form. This may increase the algebraic



overhead in developing the model but comes with several additional benefits. The ability of COMSOL to handle complex boundary conditions far exceeds that of Fluent. For ED, this is vital for modelling the membrane-solution interface where rapid changes in the concentration and electric potential fields occur. There are two approaches to deal with this: i) model discontinuities in the solutions using the Donnan equations. ii) Relax electroneutrality by using the Poisson equation and a very fine mesh at the membrane-solution interface to accommodate for the rapid variable changes. The former is generally preferred as it hugely decreases computational expense without overly sacrificing accuracy. The issue with this is that Fluent does not handle discontinuities well. Since it is ultimately based on balancing fluxes in and out of cells, accounting for discontinuities interrupts how Fluent works at the basic level. However, implementing discontinuities in the finite element method is trivial by simply breaking the discretised solution function and adding an additional parameter. Consequently, while Fluent performs well for most problems encountered in engineering (fluid/solid dynamics, heat transfer, electromagnetism, reaction kinetics etc.), applications beyond these, especially those with complex boundary conditions, are better left to COMSOL. This fundamental advantage, along with the pre-existing application module, is why studies employing Nernst-Planck CFD models of conventional ED exclusively use COMSOL.

2.4.2 Applications of CFD in ED modelling

Simulations in CFD software are powerful tools used to visualise and predict phenomena such as flow-patterns, concentration profiles and limiting current densities under many conditions and often concurrently. After the construction of a model, an enormous amount of data about a wide range of phenomena may be generated rapidly. Further, CFD models are used to isolate and investigate ED governing phenomena and methods of leveraging them. Here, CFD models have been classified into three categories: Turbulence promotion, parameter studies, and novel models for bespoke studies (Table 2.3). In this section, a discussion of these classes will be presented, along with the common shortcomings associated with each.

2.4.2.1. Turbulence Promotion

Altering the design of ED stacks to encourage greater turbulence is commonly studied using CFD. In ED, the primary role of the netted membrane spacers is to define the geometry of the channel, prevent membranes

Table 2.3: Classification of CFD models into three different topics, along with which software is used with each in CFD studies

| | Turbulence Promotion | Parametric studies | Novel Models |
|-------------|---------------------------|-------------------------|---------------------------------------|
| Description | Assess flow profiles and | Investigate | Models built for a specific |
| | modifications to increase | performance under | purpose or application |
| | crossflow. | changing operating | |
| | | conditions. | |
| Typical | Navier-Stokes | Navier-Stokes / Nernst | Navier-Stokes, (Nernst- |
| Equations | | Planck | Planck), Darcy's Law |
| | | | |
| COMSOL | [89,110,125] | [91,96,102,103,113,124] | [91,107,111,117,119] |
| Ansys | [66,109,114] | - | $[101,\!112,\!120,\!121,\!123,\!126]$ |
| OpenFOAM | [93,108] | [106,118] | - |

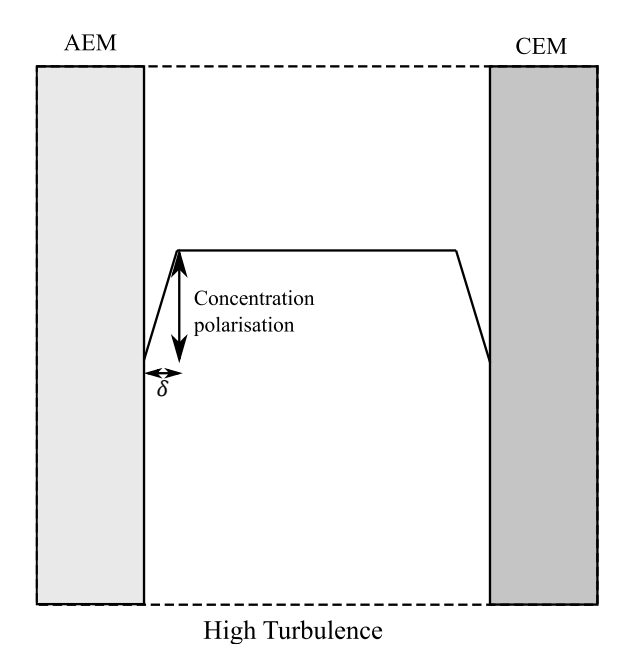


touching, and generating turbulent mixing. Increasing the degree of turbulence encourages bulk mixing and crossflow perpendicular to the membrane, thereby thinning diffusional boundary layers. This increases the diluate-membrane interfacial concentration and thereby reduces concentration polarisation, electrolyte resistance, and back-migration, as well as increasing the LCD (Figure 2.6). The study of turbulence promotion using CFD is therefore of great interest.

The geometry of the spacer net has a large influence on the degree of turbulence which cannot be predicted analytically. Circumventing the time-consuming and costly process of designing and manufacturing spacers through simulation allows rapid testing and optimisation. Experimental validation can then be conducted on the most promising candidates.

Increasing turbulence reaches an optimum economic trade-off between reduced electricity consumption for the separation, and increased pumping power arising from a greater pressure drop [89]. The latter is often neglected in studies on lab-scale stacks, however becomes significant at industrial scale where the fluid path length may be orders of magnitude longer. This was highlighted by Chandra et al. [110] who investigated the effect of in-line flow-promoters as an alternative to traditional woven-mesh spacers. Like many researchers who investigate turbulence promotion, local dimensionless numbers were used to represent mass transfer rather than simulating it directly. Sherwood and Power numbers are commonly used to represent mass transfer effectiveness and pumping power, respectively. This greatly reduces computational requirements and allows for easy and rapid comparison of designs across scales but may overlook fundamental phenomena.

Kim et al. [105] found that adjusting the position of the spacer in the channel can have a positive impact on overall mass transfer. Positioning the spacer closer to the membrane where the counterion with the lower diffusivity is transported increases the overall mass transfer coefficient. Doing this ensures that the mass transfer coefficient is the same for both species and minimises concentration polarisation. Through optimal placing of the



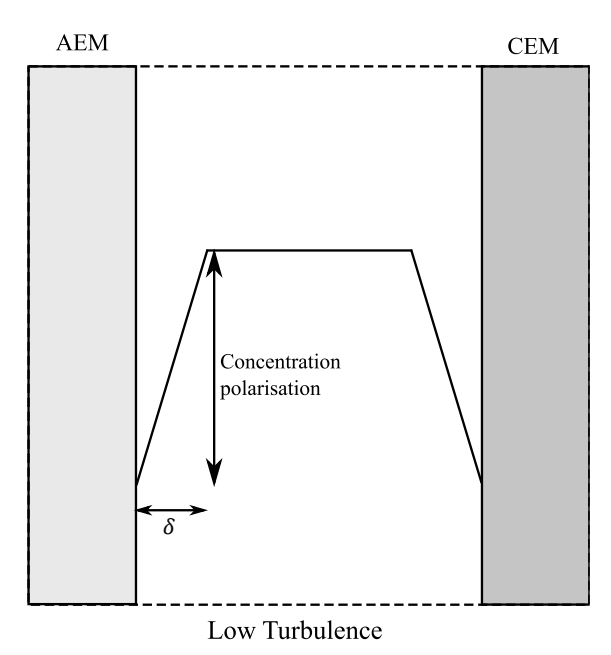


Figure 2.6: A schematic representation of how the degree of turbulent mixing affects concentration polarisation. A high degree of turbulence (left) leads to thinner boundary layers (δ) and lower concentration polarisation, whereas the converse is true for low turbulence (right).



spacer, a 30-40% reduction in power consumption was seen with a negligible increase in flow resistance. This was then validated by experiments and demonstrates a significant benefit that can be achieved with the insights gained through CFD simulations.

Profiled membranes use a 3D membrane surface structure to promote turbulence directly at the membranesolution interface and thereby remove the need for netted spacers. When simulated in CFD, it was found that
profiled membranes consume a similar electrical power for transport to netted spacers but have a much lower
pressure drop since the bulk flow remains unobstructed [109,114,125,127]. Another benefit is the removal of the
'shadow-effect' from non-conductive spacers. This is a reduction in the area through which current flows due to
the presence of the non-conducting spacer, which increases the electrical resistance of stacks. Multiple studies
[93,106,109] have reported that triangular (chevron) shaped profiled membranes offer the best compromise
between increased mass transfer and a larger pressure drop both at laboratory and industrial scale over the
alternatives (waves, pillars, ridges) [109]. It was also found by Pawlowski et al. [93] that chevron shaped profiles
have a reduced fouling tendency due to the specific path taken by the fluid. The depth and breadth of these
studies would not be possible experimentally due to the challenges associated with measuring flow profiles on a
small scale as well as the design and manufacturing of the spacers and membranes. However, since correlations
are used to determine mass transfer, rather than direct calculation using the Nernst-Planck equation, the claims
about mass transfer for profile membranes may lack accuracy. The definition of local mass transfer coefficient can
take on unrealistic and even negative values for complex geometries [128].

In studies concerning turbulence promotion, laminar CFD solvers [89,105,109,110,114,125] are used more commonly than turbulent solvers [66,93]. The simplification of the Navier-stokes equations greatly reduces computation time and avoids the use of somewhat nebulous parameters such as the turbulent viscosity. The use of a laminar solver is justified by researchers based on low Reynolds numbers (as low as 30) typically observed in channels. However, for complex geometries (which are always seen for these studies) other sources of turbulence such as cross flows are the direct target of the study, and so a Reynolds number justification is inappropriate. Koutsou et al. [129] determined critical Reynolds numbers for the onset of unsteady flow for spacer filled channels could be as low as 35-45. Further, this justification does not extend to industrial scale stacks, where flow velocities are typically much higher, and pressure drops are far more significant.

2.4.2.2. Parametric Studies

Parametric CFD studies [91,96,102,103,111,113,118,124] take a different focus from those of turbulence generation, in that researchers seek to understand how mass transfer is affected when operating conditions are varied. These simulations are used to investigate underlying phenomena such as concentration polarisation, which is exceedingly difficult to measure experimentally. However, the results are only as good as the model itself, and so caveats must always be kept in mind. Models exclusively use the Nernst-Planck equation (Section 2.2.1) for mass transfer. For the fluid dynamics, two approaches are used; either the Navier-Stokes equations are solved, or a uniform or parabolic flow field is pre-defined. The effect of temperature has also been explored by Fazlali et al. [124] which requires the addition of an energy balance. The conclusions of parametric studies tend to focus on the effects that



changing ED operating parameters (electrolyte flow rate, cell voltage, solution concentrations, temperature) has on the ion transfer rate and specific power consumption.

All literature CFD models which present concentration profiles simulate the same inlet concentration in both the concentrate and diluate streams, with the exception of one [111]. This makes the simulation considerably more tractable since the final solution more closely resembles the initial conditions which are almost always a uniform concentration everywhere. However, the result is less realistic since a key degree of freedom in the design of ED stacks is lost. Further, models in COMSOL which generate concentration profiles frequently use the inbuilt ED application, where system-specific properties are entered through a GUI. This results in a distinct lack of variety.

2.4.2.3. Novel Models

Novel CFD models [101,104,107,111,112,117,119,120,123,126] are defined as those which do not fall into the other categories, but instead investigate some aspect of ED via the creation of a new model. For example, Battaglia et al. [112,121,122] investigated membrane deformation as a result of trans-membrane pressure differences and the subsequent redistribution of flow. Hatzel & Logan [107] investigated the effect of the channel aspect ratio on fluid dynamics and bubble removal. Each of these models uses well established principles of fluid and solid mechanics to attempt to gain novel insights into ED. These models are occasionally pushed further to investigate the effect on operation through the mass transfer and the LCD. The goal of these simulations is to improve operational efficiency or equipment lifetime.

As with stipulated-equation models, the complexity of ED requires that certain phenomena are neglected when defining new models. Water transport and concentration polarisation are the most common to be assumed negligible. Justification for these assumptions is sparse and tends to stem from the fact that other models have done the same. Explanations generally focus on the behaviour of the system studied, rather than the operating conditions, which has a considerable effect on phenomenon negligibility. Because of this, models tend to focus solely on the investigated phenomenon in isolation, rather than considering ED operation holistically.

The myriads of confounding variables in ED generally results in incomplete conclusions as researchers consider only a narrow subset of phenomena. For example, this occurred when Battaglia et al. [121] described the effects of membrane deformation on mass transfer. Compressions and expansions in channels lead to increased or reduced mass transfer, respectively, as the channel width changed. It is mentioned that the LCD and resistance will be affected, but it is not discussed in what way or how severe it would be. Furthermore, compressions were found to lead to an increase in pressure drop and expansions to a reduction, although to a lesser degree, resulting in the conclusion that there would potentially be an overall increase in pressure drop. Quantification of the potential problems arising is not given, and so the question is raised as to whether this issue needs addressing or if it just leads to a negligible decrease in performance.

This is an issue which is common in novel CFD models. Engineering problems are discovered and the severity of it is quantified under various conditions, but an analysis of the impact is lacking. The resulting suggestions on how to improve performance are subsequently vague. For example, Battaglia et al. [112] suggested that the



stiffness of membranes should be increased to limit deformation. However, this would have the adverse consequence of increasing membrane electrical resistance. Whether membrane stiffness should be increased and by what degree depends on the magnitude of the effects on both deformation and resistance. It is therefore important that the consequences of identified wasteful phenomena be quantified. This principle was considered when performing the work outlined in Chapter 3 concerning the impact that flow maldistribution may have on ED performance.

A further novel use of CFD is in the development of coupled models [101,120]. These models use the predictive power of CFD to find parameters to be used in simplified stipulated-equation models. Concentration polarisation, Sherwood numbers, friction loss coefficients and area electrical resistances are computed from concentration profiles predicted in CFD models. These are then used directly in simplified models to determine overall performance through the power density or overall rate of mass transfer. Through this, coupled models are able to take advantage of the granular and broad predictive capabilities of CFD along with the rapidity of simplified models for process-scale predictions. Coupled models go some way to addressing the problem of a lack of impact of quantification by linking localised and global phenomena. However, they suffer the same deficiencies as other types of models in that they only account for the phenomena directly considered and suffer from trade-offs between insight, expediency, and accuracy due to the use of fitting parameters. Errors and assumptions taken in either of these models will accumulate and so this type of model can end up being less accurate than other types. Therefore, although these models gain additional insight through combining CFD and stipulated-equation models, they are not able to obtain any greater inherent accuracy.

The modelling of bipolar membrane ED (BPMED) in either stipulated-equation models or CFD is not common [130]. The limited models that do exist are explored further in the introduction to Chapter 6. However, the modelling of monovalent selective membranes is more common in CFD. Monovalent selective membranes are similar in form to bipolar membranes (having two ion exchange layers) but are different in function. Golubenko et al. [131] modelled monovalent selective ED in COMSOL while also including the phenomenon of water splitting. This model will have the same formulation as a CFD model for BPMED but will be used for a different purpose.

2.4.3 Model validation

A common problem with all classes of CFD models is the lack of experimental validation. Many studies do not mention it at all, while others do basic validation on a few bulk performance metrics (reservoir concentration or power density) or compare to a small number of previous literature results. For studies that focus on turbulence promotion, validation was present in only two papers where the limiting current density was measured for profiled membranes and compared to netted spacers [114,125]. When a preferred geometry of spacer or profiled membrane is concluded, no experimental validation is presented on either global performance or concentration profiles. This is generally because the small intermembrane distances used of around 1 mm mean that direct measurements inside channels are prohibitively challenging.



A single-cell flow field pattern model was validated experimentally by Enciso et al. [119] on a transparent single channel using dye-based digital image analysis. This is a powerful tool for discovering flow dead-zones, which become depleted of ions very quickly, leading to a high local resistance and water splitting. However, single cell experimental studies such as this are not able to directly consider effects on mass transfer, or how the study of a single cell is scaled to that of a whole stack.

Parametric studies on ED are just as poorly validated as turbulence models, with two studies measuring the electrolyte concentration and reservoir volume over time for a batch experimental stack [102,111]. However, the model parameters of one of these [111] were determined though fitting to experimental data, and so close resemblance to that data is expected and not indicative of model accuracy. What is more common is to validate against existing literature experiments, most notably the concentration profiles measured by Shaposhnik et al. [132] through interferometry. The shape of the curves is similar to those obtained in COMSOL mass transfer simulations, which lends confidence to the use of the Nernst-Planck equations for ED modelling. However, only a single system was studied, and at only three current densities, limiting its applicability. This study was published in the year 2000, and no other studies of concentration polarisation using interferometry or otherwise have been found at the time of writing.

For new models, validation is more common, however tends to be on a limited number of global variables such as concentration or current density over time. It is clear that CFD simulations would benefit from greater validation, especially for flow and concentration fields. Developing new methods of concentration profile determination at different inlet concentrations, operating current densities, and flow rates would be a potentially valuable area of study.

The CFD studies presented in Chapter 3 are novel and their conclusions are based solely on numerical evidence. As such, the purpose of the work presented in Chapter 4 is to experimentally validate the most important conclusions drawn.

2.5 Conclusion

There is a wide variety of stipulated-equation ED process models that exist in the published literature, all of which demonstrate reasonable agreement with experimental data. Variety primarily stems from ED being a highly multifaceted technology with a myriad of phenomena occurring simultaneously at a wide range of scales. Each of these phenomena are either included or neglected from the formulation, leading to many permutations of model existing in the published literature.

The challenge behind accurately predicting ion transport is that micro and nanoscopic phenomena such as electrostatic interactions, ion hydration, and acid-base equilibria of fixed charge groups all influence each other and are only adequately described by simplified and empirical equations. Further, it is always assumed that ions don't interact with each other, only that the charge density of cations and anions at any spatial point must be equal or else is modelled using the Poisson equation. Systems are also often simplified by, for example, ignoring additional ion species present in seawater beyond sodium and chloride and their interactions.



There is a knowledge gap in the understanding of the assumptions taken by researchers in developing their models. In particular, under what circumstances they are valid, and what the consequences are when they are not. It has been identified that invalid assumptions may be obfuscated by confounding variables under certain conditions. One assumption of interest is that of channel uniformity and forms the basis of some of the research undertaken in this project presented in Part I of this thesis.

Increasing model complexity results in a more comprehensive model formulation, but also requires a greater number of model parameters. For example, concentration polarisation modelling requires accurate knowledge about the degree of turbulence, the thickness of the boundary layers, flow profiles, and ion diffusivities at changing concentrations. Each of these come with uncertainties and will aggregate and affect the model output data. Additionally, each new phenomenon presents additional empirical parameters which may be tuned to guarantee a better fit or can be accounted for through confounding variables such as a transport number or non-ohmic resistance. The introduction of system specific parameters reduces model globality and increases the experimental burden needed to independently resolve their values. The added value from greater model complexity is therefore questionable.

Despite the variety in model formulation, all published literature concerning ED modelling claims good agreement with experimental data. This is primarily due to the multifaceted nature of ED and the large number of confounding variables and interacting phenomena. The high complexity leads to the use of empirical parameters which are then tuned to ensure a good fit with experimental data. Therefore, it is possible for phenomena to be neglected, but their effect considered by adjusting the contributions of others. Resultantly, many published models can be summarised by the following: a slightly modified model formulation is presented, parameter manipulation is able to achieve a good fit to a limited data set, it is concluded that this is an accurate model. This is a serious issue and greatly detracts from the model's verisimilitude. Process modelling and optimisation become very difficult as extrapolation becomes infeasible.

As a result of these observations, Part II of this thesis involves developing novel models of conventional ED and BPMED which explicitly avoid the use of empirical fitting parameters. Through this, it is hoped that these models will avoid the common pitfalls detailed in this literature review. Model validation has also been conducted throughout this work and attempted in such a way so as to test model performance over a range of conditions rather than achieving the closest possible fit.

Fluid dynamics plays a key role in ED and is partly responsible for ion removal efficiency. Therefore, models of ED which implement CFD have a significant advantage over stipulated-equation models, in that they can identify and account for non-standard flow patterns. They are also able to identify spacer design improvements to generate more turbulence, as well as study limiting phenomena. These simulations have also shown that CFD is a powerful tool for studying the flow profiles in ED, a technique employed in Chapters 3 and 4. However, experimental validation of CFD models is lacking, as is exploration into limiting phenomena and simulations of an ED stack in 3D. Further, the field would greatly benefit from better techniques to measure concentration profiles. Overall, the multifaceted nature of ED is seen clearly when performing CFD simulations.





Part I:

Maldistribution in electrodialysis

Chapter 3: Maldistribution though simulation

Chapter 4: Experimental validation of maldistribution

Flow maldistribution is pervasive in process units such as plate and frame heat exchangers which utilise a parallel flow distribution pattern. In Part I of this work, the presence and impact of maldistribution in electrodialysis is investigated using both computational and experimental studies. In Chapter 3, three-dimensional computational fluid dynamics simulations of a standard lab-scale ED stack geometry were conducted to explore the presence of maldistribution in comparable experiments. Simulations of modified geometries were also performed to investigate what factors impact maldistribution. An analytical maldistribution model, originally developed for a plate-and-frame heat exchanger, was used to quantify the degree of maldistribution using a single dimensionless number. The impact that maldistribution has on two important variables – the electrical resistance and the limiting current density – was determined though numerical modelling. In Chapter 4, the conclusions drawn about the presence and impact of maldistribution were empirically tested. Particle image velocimetry was used to measure the velocity distribution within each channel and a statistical model used to further validate this. Transport experiments on a real ED stack were conducted where the degree of maldistribution was varied and the limiting current density measured.





Chapter 3:

Maldistribution though simulation

NB: this chapter has been adapted from the following published work.

Ledingham, J., Campbell, K.L.S., in 't Veen, B., Keyzer, L. and Campbell, A.N., 2022. Barriers to electrodialysis implementation: Maldistribution and its impact on resistance and limiting current density. Desalination, 531, p.115691.



3.1 Introduction*

A ubiquitous assumption in both Electrodialysis (ED) modelling and experimental data analysis is that of channel uniformity. This allows for simplification of models to consider only one channel or cell pair consisting of two membranes and two channels defined by membrane spacers (Figure 3.1a & b), the results of which can be scaled to infer conclusions about global stack performance. In the case of computational fluid dynamics (CFD) models which utilise the Nernst-Planck equation, this greatly decreases computational expense. However, the validity of this assumption has seldom been explored. Gurreri et al. [133] simulated a 50 cell-pair stack in two dimensions (2D) with 0.2 mm thick channels and 0.5 mm width manifolds and found significant flow maldistribution. It was concluded that a more homogeneous distribution can be obtained by increasing channel pressure drop, decreasing manifold hydraulic losses, and reducing total flow rate. While these insights are valuable, the geometry of the manifold and distributors cannot be accurately represented in 2D, and so conclusions about 3D ED operation are extrapolations. Cruz-Diaz et al. [134] investigated the effect of the manifold on flow distribution in a single threedimensional (3D) channel through tracer-based residence time distribution (RTD) experiments and CFD modelling. It was found that assuming homogeneous flow with dispersion did not accurately predict RTD results, but a segregated flow laminar model did. These studies identified that flow distribution both between channels and within a single channel is not uniform, and that the geometry of the stack has a significant effect on maldistribution for simplified cases. This study aims to expand this to a more accurate representation of an ED stack and study the effects of maldistribution in greater depth.

Significant insight into the flow distribution in ED stacks is found by considering investigations into plateand-frame heat exchangers (PFHEX) due to their analogous geometries. The study of flow maldistribution in
PFHEX and fuel cells is frequently studied [135], often using CFD, to also understand its effects on operation
[136–143]. One useful result from these studies is an analytical flow distribution model developed by Bassiouny
and Martin [143]. A dimensionless number, m, is used to quantify the extent of maldistribution and to recreate
the channel velocity distribution given appropriate geometrical and operating parameters. The details of the
model are found in Section 3.2.2.

Analysing the effect of maldistribution on ED is crucial to ascertain the extent to which operational efficiency is impacted. One key performance metric is the limiting current density (LCD). In ED, transport is fastest in the IEMs due to the high ion concentration, and so ions deplete at the diluting side of the membrane and accumulate at the concentrating side through a process known as concentration polarisation [144] (Figure 3.1c). The magnitude of concentration polarisation grows as the applied voltage and ion flux are increased. A point is reached where the concentration at the diluting side of the membrane vanishes, and the flux of ions cannot be increased further. This is referred to as the LCD and is associated with a large increase in electrical resistance. Increasing the voltage beyond this point induces water-splitting to provide additional ion flux, leading to wasted energy and undesired changes in the pH of streams. It is therefore imperative to operate below the LCD, with any reduction

^{*} The first three paragraphs of the article have been removed. These provided a basic outline of ED and current state of research that is covered in greater depth in Chapters 1 and 2.



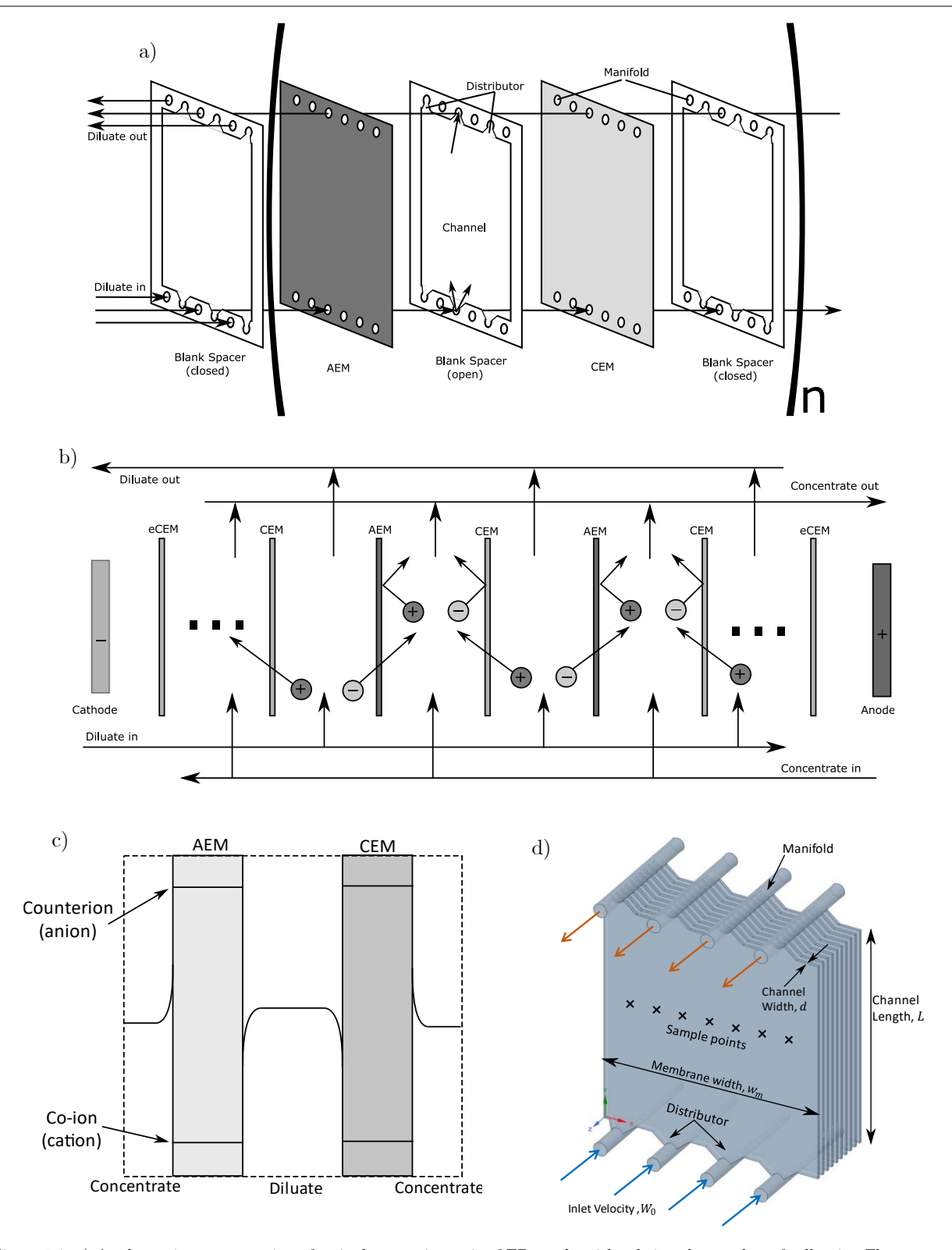


Figure 3.1. a) A schematic representation of a single repeating unit of ED stack, with n being the number of cell pairs. Flow enters and exits from the left-hand side and is distributed to every other channel through open spacer distributors. For simplicity, the concentrate stream is not shown, this would enter through the right-hand side. b) A schematic of ion transport in ED, indicating the repeating pattern of cation and anion exchange membranes as well as the electrodes and end cation exchange membranes (eCEM). Dark shades show positive charges (cations, AEMs, anode) and light shades show negative charges (anions, CEMs, cathode). c) A schematic representation of concentration polarisation. Lines represent the concentration at a given horizontal point, and the vertical height represents the concentration. d) The geometry of a typical lab scale geometry which was used in Fluent CFD simulations. This is the flow region of one stream only, the second being rotationally symmetric to the first. Also shown are the named domains, dimensions and the locations of centreline velocity sample points.



in it having significant consequences for process intensification. The LCD is reached when the interfacial concentration anywhere vanishes, which occurs first in the slowest channel where the residence time and ion depletion are the greatest. The effect of maldistribution on LCD was studied by Tanaka [145–147], assuming a normal distribution of the stack velocity. The standard deviation was used as a quantification of maldistribution when calculating the LCD, and the minimum velocity was assumed to be three standard deviations below the mean. This approach is, however, at odds with the maldistribution model of Bassiouny and Martin [143], which suggests a hyperbolic-cosine distribution. The strengths of these two approaches to maldistribution will be combined in this study to provide a dimensionless measure for maldistribution in ED, which is then used as a more rigorous metric when determining the impact on the LCD.

Variation in residence times between channels has the potential to be detrimental to ED performance and thus demonstrates the value of this research. Beyond the studies mentioned, the presence and consequences of maldistribution have been neglected in published ED models. This study aims to quantify flow maldistribution in an ED stack using a dimensionless number, as well as how it is affected by geometrical and operating parameters. Crucially, quantification of the effect maldistribution has on overall stack resistance and limiting current density is also investigated. Three-dimensional fluid dynamics simulations in ANSYS Fluent were conducted on a representative lab-scale ED stack (Figure 3.1d). Several aspects of the flow geometry including channel width, manifold area, distributor angle and the number of cell pairs were varied independently to investigate the effect on maldistribution. The inlet stack flow rate was also varied. An analytical model adapted from Bassiouny and Martin [143] is used to quantify and compare the extent of the maldistribution through a dimensionless number, with centreline channel velocities used as the basis of comparison. Furthermore, the effect of maldistribution on ED operation through the LCD and overall stack resistance is determined though a one-dimensional model.

3.2 Model development

3.2.1 Ansys Fluent CFD model

ANSYS Fluent 2020 R2 was used in this study to generate 3D flow profiles for an ED stack while varying the flow rate and geometry to study the flow maldistribution between channels. A bench-scale ED stack with ten cell pairs was selected as this is the most common studied in published literature. It is also the simplest geometry that can be simulated while still being representative of what is practically used at larger scales. Analogies will be drawn to pilot and industrial scale stacks, which tend to have much higher flow rates, a smaller number of large manifolds, a much greater size, a length to width (L/D) ratio of 2.0 (bench scale is typically 1.0) and many more channels, on the order of 50-200. However, different scale stacks do have a similar intermembrane spacing of 0.8 mm to 1.0 mm. A typical lab-scale ED geometry (Figure 3.1d) consists of cylindrical manifolds used to distribute the fluid feed to the channels (bottom) and collect the treated streams (top). Distributors at the bottom and top of the channel connect it to the manifold and tend to vary significantly in shape. It should be noted that only one of the two streams was simulated, as the two flow regions are rotationally symmetrical. The standard



case geometry used in simulations (Figure 3.1d) has channel dimensions of 1 mm by 80 mm by 80 mm, a distributor angle of 90°, and four manifolds, each of diameter 5 mm. The standard inlet flow rate was 45 L/h, equivalent to an inlet velocity of 0.159 m/s, and liquid water was chosen as the simulated fluid. These values were chosen to represent the geometry of that used in lab-scale ED stacks commercially manufactured for academic research.

To generate the flow profiles, Fluent solves the Navier-Stokes and continuity equations to account for conservation of momentum and mass, respectively.

$$\rho \frac{\partial \boldsymbol{v}}{\partial t} + \rho \, (\boldsymbol{v} \cdot \boldsymbol{\nabla}) \boldsymbol{v} = \rho \boldsymbol{g} - \boldsymbol{\nabla} P + \mu \boldsymbol{\nabla}^2 \boldsymbol{v}$$
 [3.1]

$$\frac{\partial \rho}{\partial t} + \nabla(\rho v) = 0 \tag{3.2}$$

Here, \boldsymbol{v} is the vector velocity, $\boldsymbol{\rho}$ and $\boldsymbol{\mu}$ are the fluid density and viscosity, respectively, \boldsymbol{g} is the gravitational acceleration vector, and P is the pressure. The flow was assumed to be steady and laminar to decrease model complexity. Reynolds numbers were calculated post-simulation and were found to be approximately 30 in channels and a maximum of 1000 in the manifolds, which quickly drops as flow is distributed to the channels. Critical Reynolds numbers for spacer-filled channels have been reported at between 140 and 1800 [129,148]. Since the channels simulated in this study are spacer-free, the transitional Reynold's number is likely much higher. Manifold flow is analogous to pipe flow, and so the critical Reynolds number is 2300. Simulations using k-epsilon turbulence modelling gave near-identical flow fields to ones using laminar solvers. The assumption of laminar flow is therefore likely valid.

Boundary conditions of a given inlet velocity, zero wall velocity and zero outlet gauge pressure were applied:

$$\boldsymbol{v}|_0 = \widehat{\boldsymbol{n}} W_0 \tag{3.3}$$

$$\mathbf{v}|_{w} = 0 \tag{3.4}$$

$$P|_e = 0 ag{3.5}$$

Here, W_0 is the stack inlet velocity, $\hat{\boldsymbol{n}}$ is the unit vector normal to the inlet surface, and the subscripts 0, e, and w refer to the inlet, outlet, and wall boundaries, respectively. Channel velocities were obtained by sampling a distribution of seven points across the centreline of the channel at 10 mm intervals on rake surfaces. The mean of these seven points gave a value for the average channel centreline velocity. Table 3.1 shows the geometrical

Table 3.1. The operating and geometrical parameters independently varied for the simulations. The range of variation is given along with the nominal value at which a parameter is set while others are adjusted.

| Parameter | Range | Nominal | |
|-----------------------|-------------|---------|-----|
| Inlet velocity | 0.04 - 0.32 | 0.16 | m/s |
| Channel Width | 0.2 - 1.8 | 1.0 | mm |
| Distributor angle | 0 - 180 | 90 | 0 |
| Number of manifolds | 2 - 6 | 4 | |
| Number of cell pairs | 10 - 45 | 10 | |
| Length-to-width ratio | 1,2 | 1 | |



parameters varied independently. Where appropriate, the inlet velocity was adjusted to maintain a constant average flow rate across all channels of 4.5 L/h. Fluent auto-meshing was used to construct the simulation mesh with 2.4 million polyhedral cells used for the standard case. This was found to be appropriate by conducting simulations on a range of mesh densities and selecting the smallest number of cells (*i.e.*, the least computationally demanding) which showed a minimal difference to meshes with higher densities.

3.2.2 Dimensionless maldistribution model

Determining the flow distribution in ED through CFD simulations is computationally demanding, with the nominal case simulation taking approximately 1.5 hours to solve. Therefore, an analytical model which uses a single, predictable dimensionless number to describe the maldistribution is desirable. A model for the distribution of flow in ED was adapted from one developed by Bassiouny and Martin [143] for a PFHEX. The model is based on mass and momentum balances, taken around junctions between the channels and the feed and exhaust manifolds (Figure 3.2a). It is assumed that the (vertical) z-component of the channel velocity is equal to the manifold velocity for the feed, and zero for the exhaust. For the PFHEX, the impact of this assumption was tested by comparing the results of models which did and did not consider it. Both approaches gave similar answers, demonstrating that this assumption is appropriate.

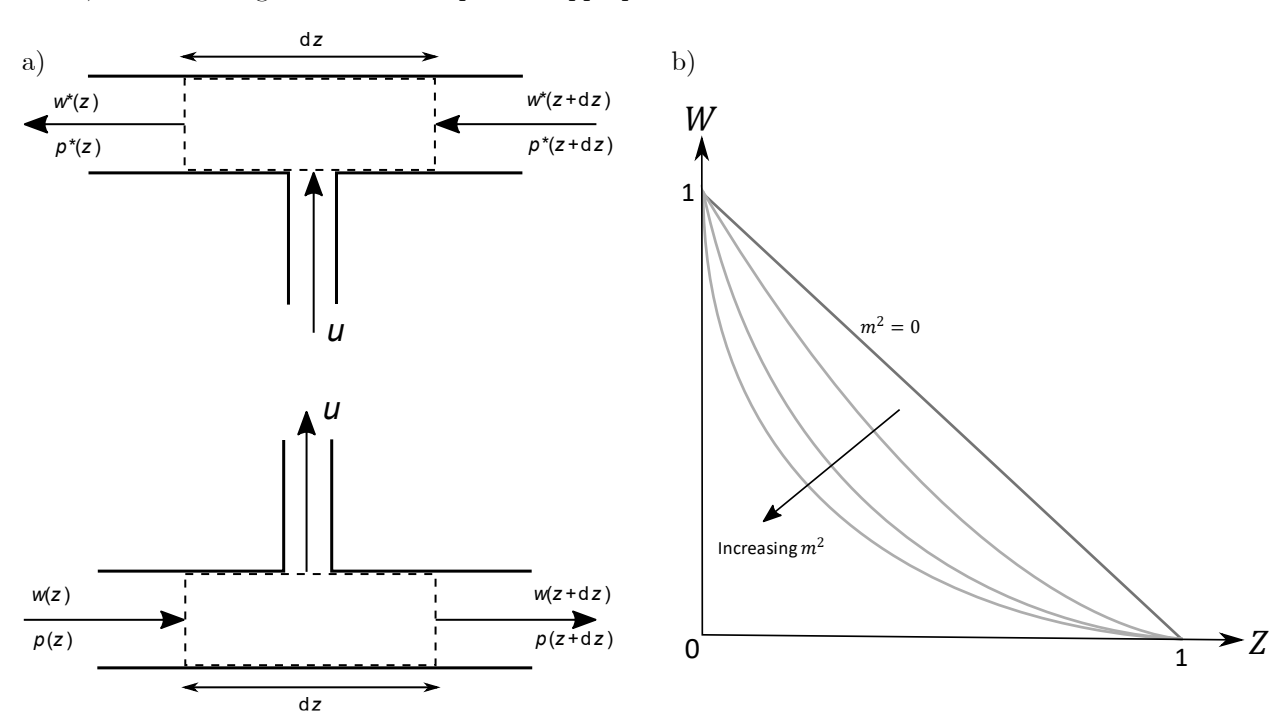


Figure 3.2.a) A schematic representation of the control volumes used in the derivation of the maldistribution model. The feed (bottom) and exhaust (top) manifolds are shown. Based on a schematic from Bassiouny and Martin [143] b) A graphical representation of how the dimensionless axial manifold velocity (w) is affected by the maldistribution number, m. The boundary conditions are w(z=0) = 1 and w(z=1) = 0 for the inlet manifold velocity and zero flow at the end of the manifold, respectively. The channel velocity for a given value of z is proportional to the negative of the gradient of the curve.



Combination of the mass and momentum balances and subsequent conversion into dimensionless form results in the following second order differential equation.

$$\frac{d^2w}{dz^2} - m^2w = 0 ag{3.6}$$

Here, w is the dimensionless manifold axial velocity, normalised to the inlet velocity (W_0) , z is the dimensionless axial coordinate, normalised to the manifold length (L), and m is the maldistribution number. The following equation defines m:

$$m^2 = \left(\frac{nA_c}{A_m}\right)^2 \frac{1}{\zeta} \tag{3.7}$$

Here, n is the total number of channels, A_c and A_m are the cross-sectional areas of the channel and manifold, respectively, and ζ is the general friction coefficient, which is found through the mean channel pressure drop (ΔP_{mc}) and velocity (U_{mc}) [141].

$$\zeta = \frac{2\Delta P_{mc}}{\rho U_{mc}^2} \tag{3.8}$$

The general friction coefficient is related to the Darcy friction factor (f_D) through the channel length (L) and the hydraulic diameter (d_h) .

$$f_d = \zeta \cdot \frac{d_h}{L} \tag{3.9}$$

The boundary conditions used to solve Eq. 3.6 are the non-dimensional inlet velocity (w(0) = 1) and the fact that the flow at the far end of the manifold is zero (w(1) = 0). The value of m^2 determines the curvature of the profile connecting the two boundary points, with higher values leading to greater curvature (Figure 3.2b). This is related to the distribution of channel velocities through the dimensionless mass balance

$$u_c = -\left(\frac{A_m}{n A_c}\right) \frac{dw}{dz} \tag{3.10}$$

where u_c is the dimensionless channel velocity, normalised to the manifold inlet velocity (W_0) . A higher value of m leads to greater curvature of the axial velocity profile, which leads to a wider distribution of u_c and hence more maldistribution.

Eq. 3.6 can be solved analytically, assuming m^2 is positive. The equation for w(z) can then be differentiated once obtain $u_c(z)$ using Eq. 3.10, and dimensional variables can be reintroduced to give an equation for the channel velocity.

$$u_c = \frac{U_c}{W_0} \tag{3.11}$$

$$z = \frac{Z}{L} \tag{3.12}$$

$$w = \frac{W}{W_0} \tag{3.13}$$



$$u_c = \left(\frac{A_m}{n A_c}\right) \frac{m \cosh(m(1-z))}{\sinh(m)}$$
 [3.14]

$$U_{c} = W_{0} \left(\frac{A_{m}}{nA_{c}} \right) \frac{m \cosh \left(m \left(1 - \frac{Z}{L} \right) \right)}{\sinh(m)}$$
[3.15]

Eq. 3.15 gives a simple analytic expression for the distribution of flow between channels. The ratio between the velocity of the fastest channel $(Z = 0 \mid z = 0)$ and the slowest channel $(Z = L \mid z = 1)$, is determined from Eq. 3.15 to be simply $\cosh(m)$, further highlighting the power of m to describe maldistribution.

The strength of this model is that it allows for a single non-dimensional number to quantify flow maldistribution which has a well-defined and rigorous physical basis. Further, m retains enough information to reconstruct velocity distribution profiles using minimal geometric data and the inlet velocity. Below, the model will be fit to a simulation of a 3D ED stack for the first time to test the applicability of this potentially powerful model and then to quantify the extent of maldistribution. Importantly, m can be used in ED process design or targeted models to calculate the LCD and resistance as the independent variable. This is superior to other maldistribution metrics such as the standard deviation or percentage-difference between the fastest and slowest channels, which do not have a physical basis and are therefore of limited practical use.

The centreline channel velocities are calculated in Fluent (Section 3.2.1) and exported to MATLAB R2020b. The function 'Isquantian', a least-squares non-linear optimisation tool was used to obtain a best fit of the model to the flow profiles, tuning the values of m and W_0 . Fitted velocity distribution profiles could then be compared those simulated in Fluent, and the value of m used as a non-dimensional metric for the degree of maldistribution.

3.2.3 Limiting current density model[†]

The limiting current density is an important operational parameter in ED as it represents a practical upper bound for ion flux. Transport is fastest in the membranes and is significantly slower in diffusional boundary layers. Consequently, ion depletion and accumulation occur at the diluting and concentrating sides of the membrane, respectively (Figure 3.1c) [144]. Concentration gradients form adjacent to the membrane surfaces through a phenomenon known as concentration polarisation. As the current density is increased, concentration polarisation is exacerbated and the dilutate interfacial concentration decreases until it vanishes. This point is referred to as the LCD and coincides with a steep increase in electrical resistance. A further increase in the current density would initiate water splitting, leading to wasted energy, unwanted pH changes of streams, and in the most severe cases, membrane damage. It is therefore desirable to operate below the LCD; thus, the LCD is a key parameter for the design and operation of ED stacks. It is therefore crucial for the wider deployment of ED that the effect maldistribution has on LCD is evaluated.

[†] The limiting current density model that was originally presented in the ESI of the publication has been included in the main body of this chapter for convenience.



This work utilises mass transfer coefficients and linear representations of diffusional boundary layers to compute an estimate for the LCD. It is assumed that the LCD will be reached at the point where the concentration in any channel vanishes [145] which will first occur at the exit of the slowest diluate channel since it has the greatest residence time.

The exit concentration of a channel can be calculated from the flux by the following equation, assuming flux is constant over the whole membrane

$$C_0 - C_e = \frac{\dot{N}L}{ud} \tag{3.16}$$

Here, C_e and C_0 are the exit and inlet concentrations, respectively, \dot{N} is the ion flux, L is the membrane length in the direction of flow, u is the channel velocity and d is the intermembrane spacing. Faraday's law is used to relate the ion flux to the current density (i).

$$\dot{N} = \frac{i\phi}{z_q F} \tag{3.17}$$

$$C_e = C_0 - \frac{i\phi L}{z_q F du} \tag{3.18}$$

Here, z_q is the ion charge, F is the Faraday constant, and ϕ is the current efficiency, defined as the fraction of current density which results in useful ion transfer from the diluate to the concentrate. Eq. 3.18 can be rearranged and expressed in terms of a dimensionless group E_T which represents the ratio of inlet convective flux to electromigration flux

$$\frac{C_e}{C_0} = 1 - \left(\frac{L}{d}\right) E_T \tag{3.19}$$

$$E_T \equiv \frac{i\phi}{z_q F C_0 u}$$
 [3.20]

A mass transfer coefficient (k) is used to relate the concentration of the bulk (C_b) to the concentration at the membrane surface (C_i) for the diluate stream

$$\dot{N} = k(C_h - C_i) \tag{3.21}$$

Faraday's law (Eq. 3.17) can then be implemented along with the fact that the LCD (î) is achieved when the interfacial concentration is zero and the bulk concentration is equal to the outlet to find

$$\frac{\hat{i}\phi}{z_a F} = k C_{e,10}$$
 [3.22]

where $C_{e,10}$ is the outlet concentration of the slowest channel. Using Eq. 3.19 to relate $C_{e,10}$ to C_0

$$\frac{\hat{\iota}\phi}{z_q F} = k C_0 \left(1 - \frac{L}{dE_T}\right)$$
 [3.23]

into which, Eq. 3.20 can be substituted and solved for E_T



$$E_T = \frac{1}{\frac{u}{k} + \frac{L}{d}} \tag{3.24}$$

In order to compute the mass transfer coefficient, the following correlation is used [80]

$$Sh = 0.29 Re^{\frac{1}{2}} Sc^{\frac{1}{3}}$$
 [3.25]

where the Sherwood, Reynolds and Schmidt numbers are defined as follows

$$Sh = \frac{kd_h}{D}$$
 $Re = \frac{\rho u d_h}{\mu}$ $Sc = \frac{\mu}{\rho D}$ [3.26, 3.27, 3.28]

Here, D is the diffusivity and d_h is the hydraulic diameter, which is approximated to twice the intermembrane spacing:

$$d_h = 4 \times \frac{A_{flow}}{p_{wet}} = \frac{4 d w_m}{2 (d + w_m)} \approx \frac{4 d w_m}{2 w_m} = 2 d$$
 [3.29]

Here, A_{flow} is the flow area, p_{wet} is the wetted perimeter, and w_m is the width of the membrane, which is about 100 times greater than the intermembrane spacing

Using the above definitions, Eq. 3.25 is simplified to

$$k = \beta \sqrt{\frac{u}{d}}$$
 [3.30]

where β is a parameter of fluid physical properties

$$\beta \equiv \frac{0.29}{\sqrt{2}} \, \sqrt[6]{\frac{\rho}{\mu}} \, D^{\frac{2}{3}} \tag{3.31}$$

This is then substituted into Eq. 3.24 to give an equation for E_T in terms of the channel velocity

$$E_T = \frac{\beta}{\sqrt{ud} + \beta \frac{L}{d}}$$
 [3.32]

Or, in terms of the limiting current density

$$\hat{i} = \frac{F}{\phi} \frac{C_i \ u_{10} \ \beta}{\sqrt{u_{10}d} + \beta \frac{L}{d}}$$
 [3.33]

In this case, u_{10} is the velocity of the slowest channel. For the configuration considered, this is at the far end of the manifold, where z = 1, and so can be found from the maldistribution model:

$$U_c = W_0 \left(\frac{A_m}{nA_c}\right) \frac{m \cosh\left(m\left(1 - \frac{Z}{L}\right)\right)}{\sinh(m)}$$
 [3.34]

$$u_{10} = \left(W_0 \frac{A_m}{n A_c}\right) \frac{m}{\sinh m}$$
 [3.35]



Therefore, this is a model that can estimate the LCD as a function of the maldistribution number, m. Equations 3.33 and 3.35 were solved directly in MATLAB R2020b for a range of m between 0 and 6 for the nominal geometry and inlet flowrates defined in Table 3.1.

3.2.4 Resistance model[‡]

The overall stack resistance is an important consideration as it directly impacts both the operating cost through the energy consumption and the capital cost through overall membrane area required. It is therefore important to investigate how the stack resistance changes with the degree of maldistribution. Ohm's law shows how, for a given overall charge transfer rate (*i.e.*, current, often process fixed), a higher resistance (R in $[\Omega \text{ m}^2]$) must lead to either a higher voltage (V), or greater membrane area (A).

Charge transfer rate =
$$iA = \frac{VA}{R}$$
 [3.36]

Voltage is the work done per unit charge, and so is proportional to the specific energy consumption of separation. Hence, an increase in resistance will ultimately lead to an increase in either the capital costs through greater membrane requirements, or operating costs through a greater energy consumption.

To evaluate the stack resistance, a circuit-based model is used. The stack is imagined as a set of resistors in series, the total resistance of which is used to relate variables such as the voltage and current density to the ion flux through Ohm's law and Faraday's law. In this model, it is assumed that the cell voltage (V_{cell}) is fixed at 1.2 V. It is imagined that an infinitesimal slice is taken across the stack, where variables are constant. The channel is therefore treated like a plug flow reactor (PFR) with a surface reaction occurring. The rate of ion depletion in the diluate is found directly from the flux.

$$\frac{dC}{dx} = -\frac{1}{u d} \dot{N}$$
 [3.37]

The ion flux is related to the current density through Faraday's law

$$\dot{N} = \frac{i\phi}{z_a F} \tag{3.38}$$

The current density is related to the cell voltage and cell resistance (R_{cell}) though Ohm's law

$$iA = \frac{V_{cell}}{R_{cell}}$$
 [3.39]

Finally, the cell resistance is calculated assuming that the infinitesimal slice is made of a series of four resistors, accounting for the concentrate (R_{con}) , diluate (R_{dil}) , CEM (R_{cem}) and AEM (R_{aem}) .

$$R_{cell} = R_{dil} + R_{con} + R_{gem} + R_{cem}$$
 [3.40]

[‡] The resistance model originally presented in the EDI of the publication has been included in the main body here for convenience.



The membrane resistance is assumed to be constant, and the electrolyte resistances are calculated through the conductivity, which is modelled as being proportional to the ion concentration [149] using the molar conductivity (m_{κ}) .

$$R_{dil} = \frac{d}{\kappa_{dil}} = \frac{d}{m_{\kappa} C_{dil}}$$
 [3.41]

$$R_{con} = \frac{d}{m_{\kappa} C_{con}}$$
 [3.42]

This is extended by considering diffusional boundary layers as well. It is assumed that the channel consists of a bulk layer where the concentration is constant, and two boundary layers each of thickness δ .

The resistance of the bulk (R_b) can be calculated as

$$R_b = \frac{d - 2\delta}{m_\kappa C_b} \tag{3.43}$$

The resistance of the boundary layer (R_{BL}) is found via integration, assuming that the concentration profile is linear, and the interfacial concentration known. It is also assumed that the boundary layers adjacent to the AEM and CEM are symmetrical.

$$R_{BL} = \frac{2\delta}{m_{\kappa} (C_b - C_i)} ln \left(\frac{C_b}{C_i}\right)$$
 [3.44]

The interfacial concentration is found using a mass transfer coefficient model (Equations 3.21 - 3.30), and the boundary layer thickness is calculated directly from the mass transfer coefficient (k) and the diffusivity (D).

$$\delta = \frac{D}{k} \tag{3.45}$$

To determine the effect maldistribution has on overall resistance, the calculations are run for each channel, with the velocity determined by the maldistribution model. Since the cell pairs are themselves considered resistors in series, the resistances of the cell pairs are summed to compute the overall resistance for a given value of m.

This system of algebraic and differential equation was solved in MATLAB R2020b using the function ode45[§] which utilises the Runge-Kutta method. Sodium bicarbonate was used as the species of study, specified by using value of 1.36 S m⁻¹ (mol/m³)⁻¹ for the molar conductivity. It should be noted that very similar results may be obtained with alternate species, specified through using the appropriate value of the molar conductivity.

3.3 Results – quantifying maldistribution

This section explores and quantifies the extent of inhomogeneous flow distribution observed in the simulated flow profiles. Maldistribution results are presented in graphs of channel number versus channel velocity. A numbering convention is taken here representing the channel's distance from the inlet and outlet ports. 'Channel n' is the

[§] The differential solver ode45 was used throughout this thesis since the problems encountered were very non-stiff. That is, variables change very gradually. Further, the difference between the solution using ode45 and a stiff solver (ode15s) was negligible. In general, non-stiff solvers do less work per solution step, but struggle when there are large changes between steps, leading to long solving times and numerical errors.



nth closest to the inlet, with channel 1 being the closest. The points on the distribution profile graphs (typically part b in figures) represent the magnitude of the centreline velocity averaged over several points (shown in Figure 3.1d), simulated in Fluent. Unless otherwise stated, the lines represent the maldistribution model (Eq. 3.15) fit to the Fluent distribution using the MATLAB function Isquonlin.

3.3.1 Maldistribution model validation

To determine the applicability of the maldistribution model derived for a PFHEX to that of ED, it was compared to a standard-case simulation using the nominal conditions described in Table 3.1. This simulation was also used to confirm the existence of maldistribution in typical ED systems.

A value for the maldistribution number, m, was determined in two different ways: calculation using channel data and Eqs. 3.7 and 3.8, and by fitting the model (Eq. 3.15) directly to the flow distribution profile (Figure 3.3a). This was done to evaluate both the applicability of the model and how representative the calculated value of m is. To calculate m, values for ΔP_{mc} and U_{mc} were computed directly from the Fluent simulation results and

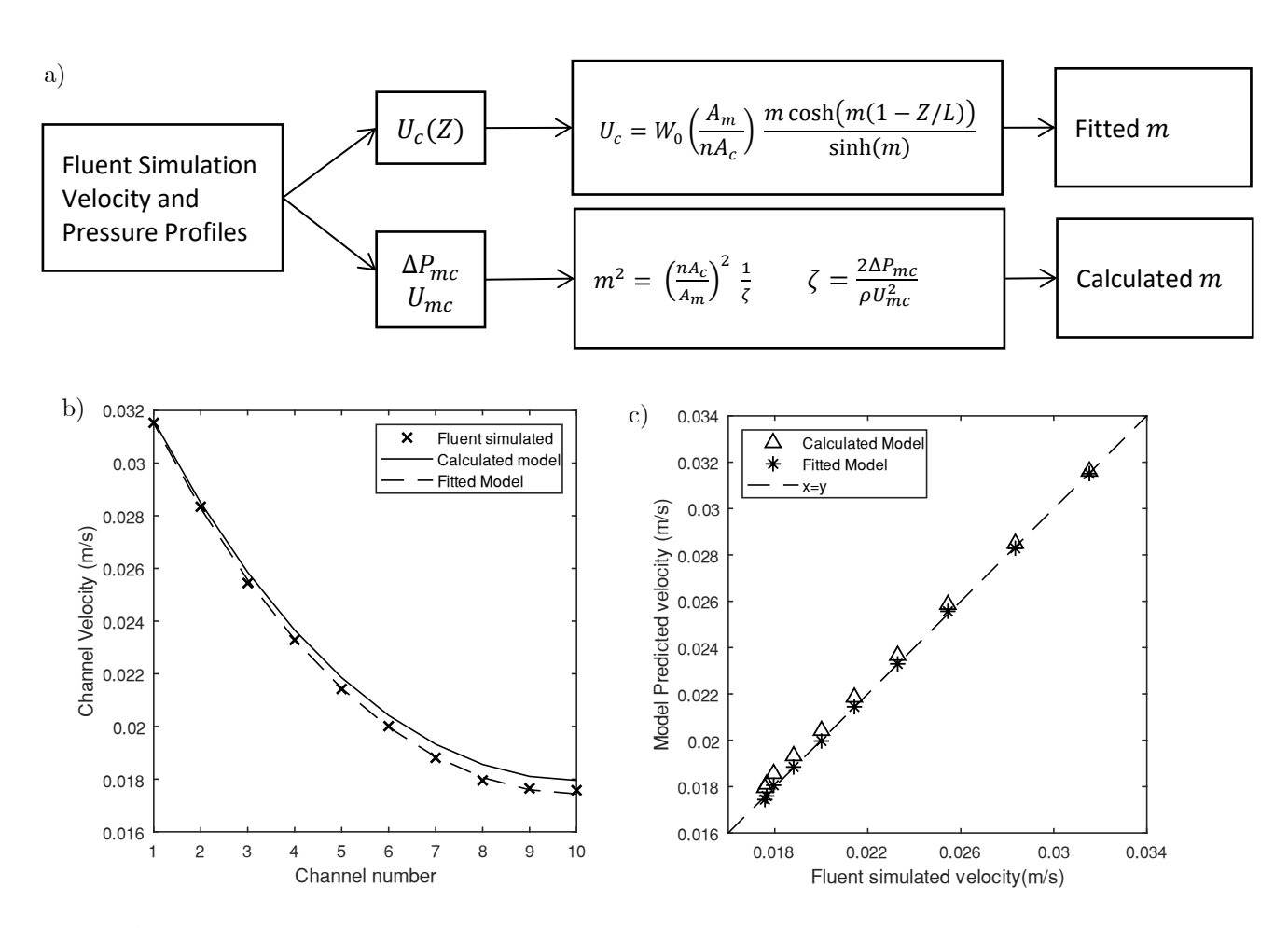


Figure 3.3. a) A flow chart showing the process through which the calculated and fitted values of the maldistribution number are determined using Fluent simulation data. b) The distribution of velocity between the ten channels of the standard-case stack with the calculated model (equation 3.15) and the fitted model predictions shown. Channels are numbered with one being the channel closest to the inlet and outlet, and ten being the farthest. c) the model predicted velocity plotted against the fluent simulated velocity for both the calculated and fitted models.



subsequently used to find m to be 1.30. To fit the maldistribution model (Eq. 3.15) to the velocity distribution, a MATLAB non-linear least-squares fitting tool (Isqnonlin) was used to find optimum values of W_0 and m. These were determined to be m = 1.33 and $W_0 = 0.157$ m/s. The closeness of the fitted and calculated values (Table 3.2) shows that Eq. 3.7 is a good representation of the maldistribution number for ED. It also shows, for the first time, that this model is a powerful tool for predicting the distribution of flow in an ED stack.

The simulated flow profile reveals that the velocity is greatest in channel one and decreases in each subsequent channel at a decreasing rate (Figure 3.3b). Significant maldistribution is seen, with the greatest average channel centreline velocity nearly twice that of the slowest. Channel one will therefore have just over half the residence time of channel ten, and so the performance between channels will vary significantly. It can therefore be concluded that maldistribution is significant in the simulated standard ED stack under reasonable operating conditions with a flow rate of 45 L/h (average of 4.5 L/h per channel).

Maldistribution is pronounced because there is a higher flow rate in the manifolds nearer to the stack entrance and exit. The flow rate subsequently decreases along the manifold (and the z-coordinate) as fluid is distributed to the channels. Therefore, a greater momentum is transferred to lower numbered channels and the flow takes the path of least resistance.

For the model using the calculated value of m, a better fit is seen for lower numbered channels with higher flow rates (Figure 3.3c), with the model over-predicting high-channel velocities. This could be partly due to the assumption of negligible wall friction. The effect would be small for channels close to the entrance but lead to a non-negligible reduction in momentum for late channels.

Both the calculated and fitted models show good qualitative and quantitative agreement with the simulated data and very low root-mean-square (rms) relative errors (Table 3.2). This gives confidence that the maldistribution model provides an accurate representation of the overall flow distribution. Fitting of the model to the flow profiles gives an accurate representation of the flow distribution. Comparison of the trend in m to what is expected from Eqs. 3.7 and 3.8 is useful in determining the underlying causes of these trends. This model will be used for quantification of maldistribution in simulations and used to recreate flow profiles for the LCD and resistance models below.

For comparison, Kumar and Singh [141] computed m to be 0.54 for a PFHEX with 27 plates. It would be expected that m would be significantly less for PFHEX than for ED due to the much larger manifolds used and thus much greater value of A_m . However, a similar order of magnitude result gives further confidence in the applicability of this result.

Table 3.2. The calculated and fitted values for the maldistribution number (m) and inlet velocity (W_0) , as well as the relative root mean square (rms) error between the maldistribution model and simulated velocities.

| | Calculated | Best fit |
|----------------------|------------|----------|
| m | 1.30 | 1.33 |
| $W_0~(\mathrm{m/s})$ | 0.159 | 0.157 |
| rms relative error | 2.1% | 0.4% |



3.3.2 Inlet flow rate

The inlet flow rate to the ED stack is an important parameter as it determines the total process throughput. For a given process, the overall throughput is typically fixed by other unit operations, and so instead can be altered by using multiple stacks in parallel and splitting the flow between them.

A stack with the standard geometry (Figure 3.1d) was simulated, and the manifold inlet velocity was varied between 0.04 m/s and 0.32 m/s. It is shown in Figure 3.4 that increasing inlet flow rate increases the degree of flow maldistribution between channels. Higher flow rates can be seen to increase the value of m, but at a decreasing rate, and the distribution of velocity can be seen to broaden (Figure 3.4a). The velocity in individual channels appears to increase linearly (Figure 3.4b), suggesting that the velocity of each channel is proportional to the inlet flow rate. This agrees with the prediction of Eq. 3.15.

The increase in maldistribution can be explained using the analytical model by combining Eqs. 3.7 and 3.8:

$$m \propto \frac{U_{mc}}{\sqrt{\Delta P_{mc}}}$$
 [3.46]

The inlet flow rate is approximately proportional to the mean channel velocity, U_{mc} . However, accompanying the increase in mean channel velocity is a non-linear increase in the channel pressure drop, resulting in a non-linear relationship between the inlet flow rate and maldistribution number.

The consequences of this are that the flow maldistribution may be significantly reduced by decreasing the inlet flow rate. Industrial scale stacks tend to have flow rates three orders of magnitude higher $(10 - 100 \text{ m}^3/\text{h})$, and so from this effect it would be expected that they would experience greater maldistribution.

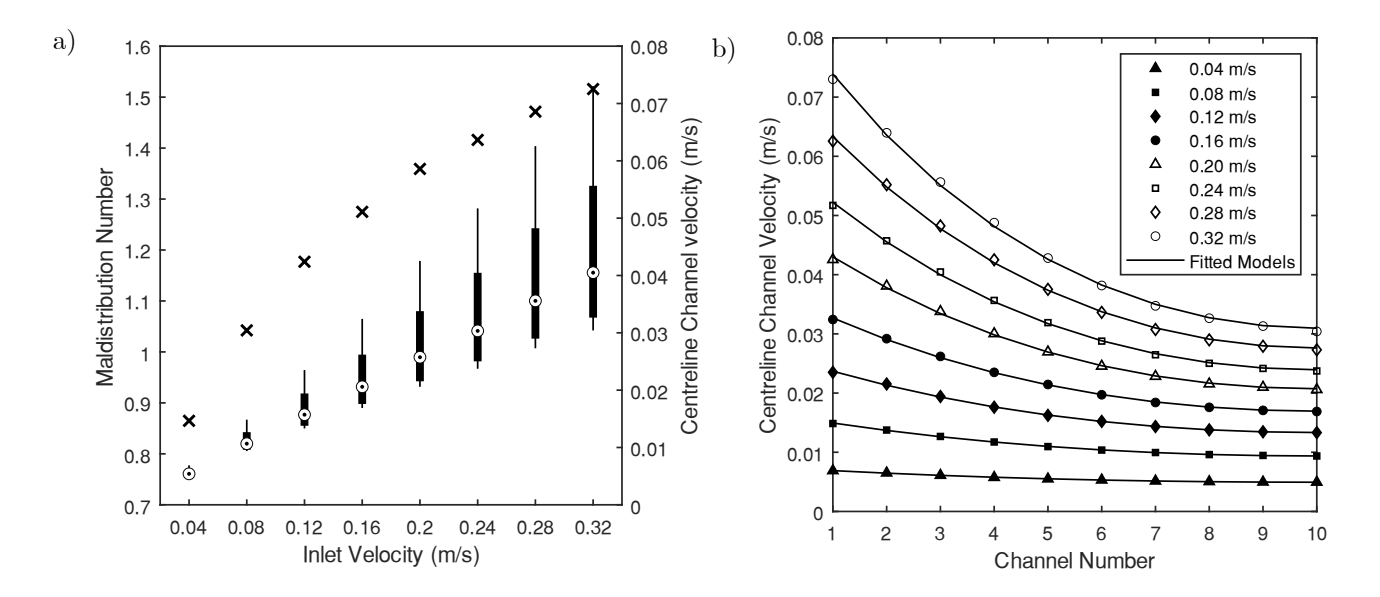


Figure 3.4.a) Fitted values of the maldistribution number (**x**, left y-axis) and a box-and-whisker diagram showing the distribution of the velocity across the stack (right y-axis) for simulations where the inlet velocity was changed. Targets (**②**) give the median velocity, boxes represent the interquartile range, and lines show the overall range of velocity. b) The distribution of flow between channels for a varying inlet flow rate with channel one being the closest to the stack inlet. Also shown is the fitted maldistribution model for each flow rate (equation 3.15)



3.3.3 Channel width

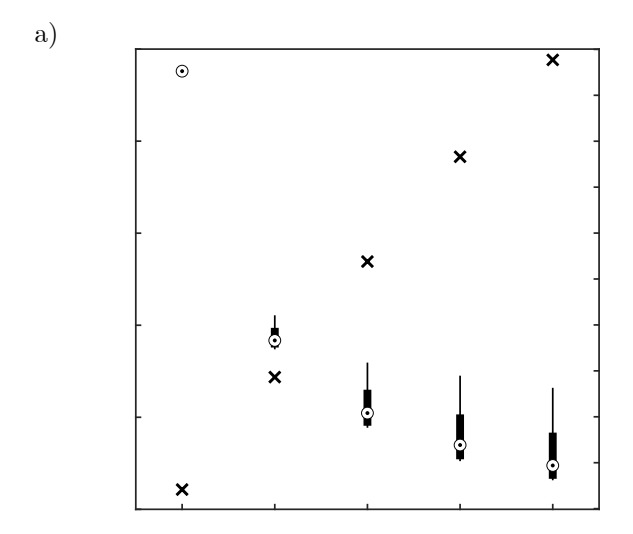
A series of simulations were run where the width of the channel was varied between 0.2 mm and 1.8 mm to determine the effect of this geometric parameter on maldistribution. The manifold inlet flow rate was maintained at 45 L/h, and so the velocity in each channel should increase as the intermembrane distance decreases. The intermembrane distance determines the channel width and is directly controlled by the geometry of the spacer. Both bench-scale and industrial-scale stacks tend to have a very thin channels on the order of 1 mm. This is because the electrolyte resistance is proportional to its length in the direction of the electric field. Hence, thinner channels should theoretically have lower electrical resistances, all else being equal. Thinner channels do, however, have a higher flow resistance, requiring greater pumping power and increasing the risk of solution leakage. Further, the risk that membranes will touch and short-circuit is increased.

Increasing the channel width increases the degree of maldistribution (Figure 3.5). Wider channels have a lower velocity since inlet flow rate is held constant. A greater maldistribution is seen from the broader distribution of velocities between channels. This is confirmed by the trend in m which increases substantially as channel width is increased. The 0.2 mm thick channel experienced very little maldistribution and with a value of m of only 0.10, but this increased to 2.44 as the channel width is increased to a maximum of 1.8 mm.

The relationship between m and channel width appears to be near-linear with only slight convex curvature over the range studied. A proportional relationship would be expected from Eq. 3.7 since

b)

$$A_c = d \times w_m \tag{3.47}$$



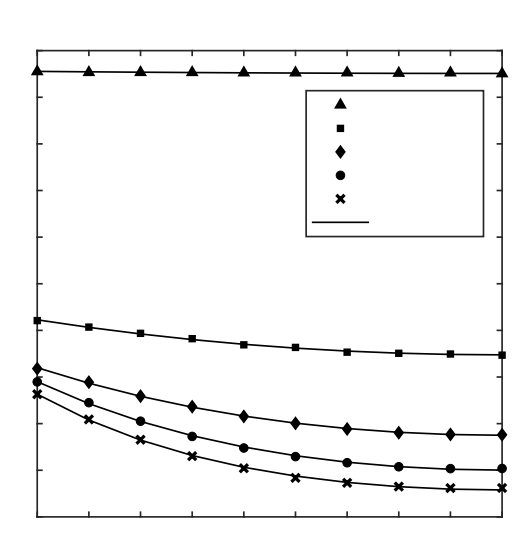


Figure 3.5. a) Fitted values of the maldistribution number (\mathbf{x} , left y-axis) and a box-and-whisker diagram showing the distribution of the velocity across the stack (right y-axis) for simulations where the channel width was changed. Targets ($\mathbf{\Theta}$) give the median velocity, boxes represent the interquartile range, and lines show the overall range of velocity. b) The distribution of flow between channels for a varying channel width with channel one being the closest to the stack inlet. Also shown is the fitted maldistribution model for each channel width (equation 3.15).



For this to hold, the friction coefficient must be constant. For laminar flow, the friction coefficient is found from the Reynolds number correlation for the Darcy friction factor as a consequence of Poiseuille's Law:

$$f_d = \frac{64}{Re} \tag{3.48}$$

$$\zeta = f_d \cdot \frac{L}{d_h} = \frac{64}{Re} \cdot \frac{L}{d_h}$$
 [3.49]

The mean channel Reynolds number is proportional to the product of the velocity and the channel width (assuming d_h is twice the intermembrane space).

$$Re \propto u \cdot d$$
 [3.50]

The channel volumetric flowrate, Q_c is held constant and is the product of u and A_c . Therefore, the Reynolds number is expected to be constant

$$Re \propto \frac{Q_c}{W_m}$$
 [3.51]

Thus, if laminar Poiseuille flow is assumed, the friction coefficient would be expected to be inversely proportional to d_h (Eq. 3.49). This would result in m having the following relationship with d_h

$$m \propto d_h^{\frac{3}{2}} \tag{3.52}$$

and Figure 3.5a showing a non-linear trend, which is not the case. It can therefore be concluded that the fluid dynamics deviates significantly from ideal Poiseuille flow, with phenomena such as entrance effects having a significant effect.

It has been shown by the results that a reduction in the channel width can reduce the degree of maldistribution. This would, of course, contend with other factors such as the pressure drop which would affect the mechanical stability, pumping power, and solution leakage.

3.3.4 Distributor angle

The geometry of the distributor connecting the manifolds to the channels varies widely across ED applications. It is controlled by the spacer design, and so any feasible geometry can be easily created. This study looks at the effect of the distributor geometry on maldistribution by changing the angle the distributor makes with the horizontal manifold centreline. To do this, two points on the horizontal diameter of the manifold were set, each 0.5 mm away from the centre (Figure 3.6a). From these, two lines were drawn up to the channel with a specified angle made to the vertical. The angle recorded is that of intersection between the two lines, equivalent to twice the angle the lines make with the vertical. All other aspects of the geometry were maintained at the nominal values, and the inlet flow rate was held at 45 L/h.

It is suggested by the results that wider distributors, with a larger angle, lead to greater maldistribution. Profiles from simulations with wider distributor angles have a broader velocity distribution (Figure 3.6b & 6c). This observation is repeated in the trend of the maldistribution number, which shows a smooth curve with a



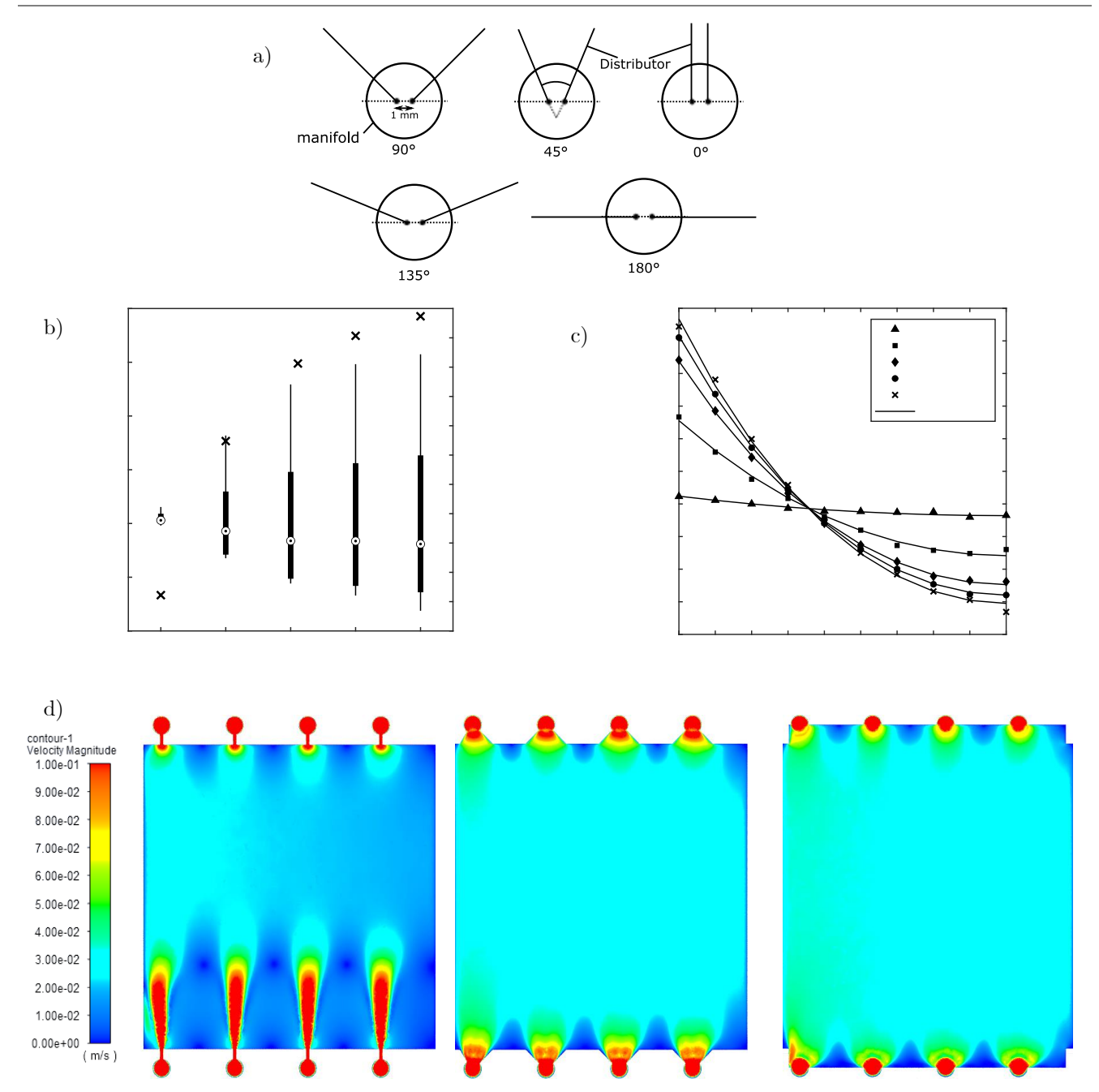


Figure 3.6. a) A schematic representation of the distributor geometry and how the angle is defined. b) Fitted values of the maldistribution number (**X**, left y-axis) and a box-and-whisker diagram showing the distribution of the velocity across the stack (right y-axis) for simulations where the distributor angle was changed. Targets (**②**) give the median velocity, boxes represent the interquartile range, and lines show the overall range of velocity. c) The distribution of flow between channels for a varying distributor angle, with channel one being the closest to the stack inlet. Also shown is the fitted maldistribution model for each distributor angle (equation 3.15). (d) A contour plot showing the centreline velocity profile in the fastest channel for three distributor angles, 0°, 90° and 180° from left to right

positive but decreasing gradient. It is seen from the results that the increase in the maldistribution slows at higher angles. There is a difference in the value of m of 0.57 between the 0° and 45° simulations, but only 0.07 between 135° and 180°.

The geometry of the distributor is not directly accounted for in the maldistribution model since a twodimensional approximation is taken in its derivation (Section 3.2.2). This is one of the key limitations of simulating



ED in 2D as the distributor geometry clearly has a significant effect on flow distribution. However, the effect on maldistribution number is captured through the channel pressure drop. It can be seen from Eqs. 3.7 and 3.8 that m is inversely proportional to the square root of the pressure drop.

$$m \propto \frac{1}{\sqrt{\Delta P_{mc}}}$$
 [3.53]

Narrower distributors will have a larger associated pressure drop, and so would be expected to have less maldistribution. A physical interpretation of this is that due to the higher pressure drop of the distributor, a lower proportion of the manifold flow momentum is transferred to the channels nearer the entrance and exit, and so the fluid is distributed more uniformly. The flow is essentially held back in the manifold due to the restrictive distributor. The consequence of this is that maldistribution may be reduced by changing the spacer geometry to have narrower distributors. However, this also comes with an increase pressure drop and thus increased pumping power and greater solution leakage between channels. Spacers used at both the bench and industrial scales have very varied geometries from narrow groves in the spacer to wide-open distributors. Therefore, this may be an important lever when it comes to reducing maldistribution. This may also present a potential solution to maldistribution in ED. The angle of the distributor be increased in subsequent channels to artificially restrict flow in early channels and manipulate individual pressure drops. This may be tuned to counteract the effect of a higher manifold flowrate in early channels. The exact nature of this solution is, however, not trivial to determine, and would lead to an overall increase in the pressure drop. The latter increases the pumping power required, and the probability of solution leakage. An additional important caveat to reducing distributor angle is the appearance of jetting effects at the channel inlet (Figure 3.6d). They arise due to the increased velocity present in the distributor because of the reduced flow area, and lead to stagnant flow regions either side of the distributor. Ion depletion occurs rapidly in these stagnant zones, and results in a reduction in the effective membrane area and other negative effects of operating beyond the limiting current density (pH changes, wasted energy and potential membrane damage from an extreme pH).

3.3.5 Number of manifolds

The number of manifolds in a bench-scale stack is typically between four and six, but it is common for large-scale instillations to have only one. The number of manifolds is built into the stack design, and so is not as easily manipulated in practice as other parameters. These simulations were run by changing the geometry of the simulated stack to increase the number of equally spaced manifolds and reducing their spacing. The manifolds were moved off-centre, so that if the manifolds of the other stream were present, the stack would be symmetrical. The inlet velocity was subsequently scaled to maintain the same overall flow rate to the stack. All other parameters including the distributor geometry and channel width remained unchanged.

It is shown by the results that a greater number of manifolds leads to a lower degree of maldistribution (Figure 3.7). Increasing the number of manifolds from two to six reduces the maldistribution number from 1.62



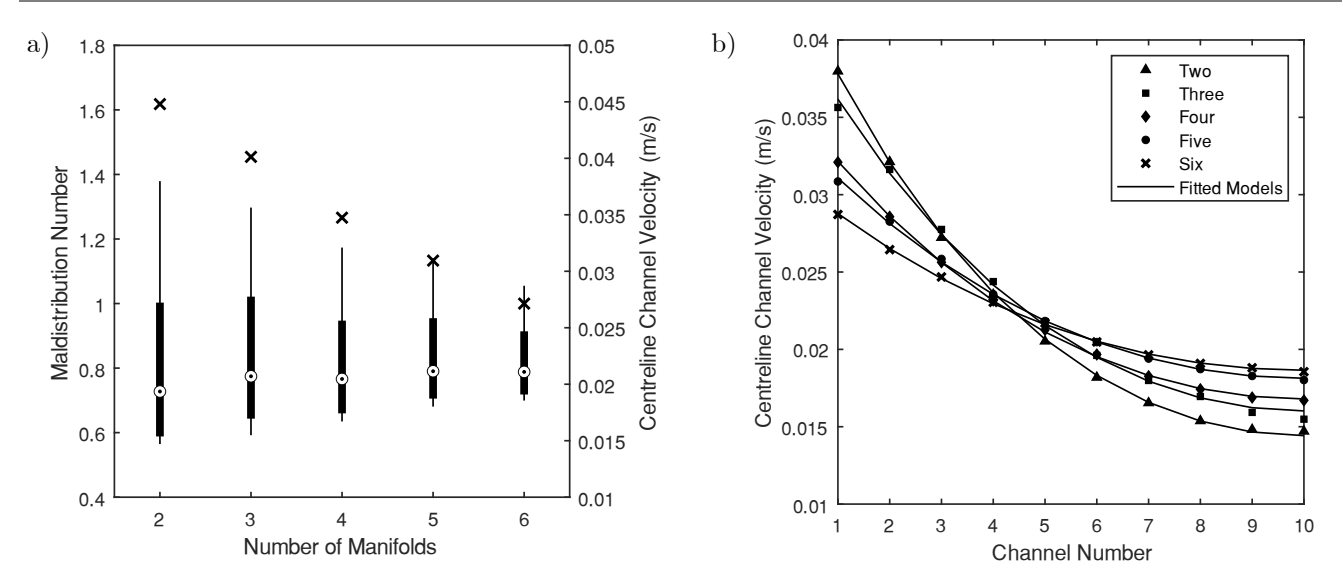


Figure 3.7. a) Fitted values of the maldistribution number (\times , left y-axis) and a box-and-whisker diagram showing the distribution of the velocity across the stack (right y-axis) for simulations where the number of manifolds is changed. Targets (\odot) give the median velocity, boxes represent the interquartile range, and lines show the overall range of velocity. b) The distribution of flow between channels for a varying number of manifolds, with channel one being the closest to the stack inlet. Also shown is the fitted maldistribution model for each case (equation 3.15).

to 1.00. This is expected from the maldistribution model (Eq. 3.7), where m is inversely proportional to the manifold area.

An explanation for why maldistribution worsens with a lower number of manifolds is due to the higher velocity present in the manifold. The manifold inlet flow rate is constant, so reducing the manifold area leads to an increase in the velocity. Similar to the case of increasing flow rate (Section 3.3.2), the fluid in the manifolds has a higher momentum, and so will transfer a greater proportion of it to the channels nearer the entrance, with less left over for those farther away.

3.3.6 Number of cell pairs

A repetitive geometry is one of the key strengths of ED, making it modular and easily scalable. It allows for relatively consistent designs of stacks to be used for different throughputs, with the number of cell pairs being scaled to maintain a consistent residence time. Bench-scale stacks tend to use between ten and twenty cell pairs, whereas pilot-scale can reach 50, and industrial-scale can be over 200 pairs.

A set of simulations was carried out, varying the number of flow channels between 10 and 45. Attempts at simulations with a greater number of cell pairs failed to converge, presumably due to the high velocity gradients in manifold-channel junctions close to the entrance and exit. It was revealed by the simulations that increasing the number of cell pairs significantly increased maldistribution (Figure 3.8a). The value of m ranged from \sim 1 when ten cell pairs were used, to more than 9 with 45 cell pairs. The effect of the number of cell pairs on maldistribution was significantly more than any other parameter investigated.

It is indicated by Eq. 3.7 that m is directly proportional to the number of cell pairs, and so the trend observed in Figure 3.8a is expected. The strong dependence of m on the number of cell pairs is notable due to the very



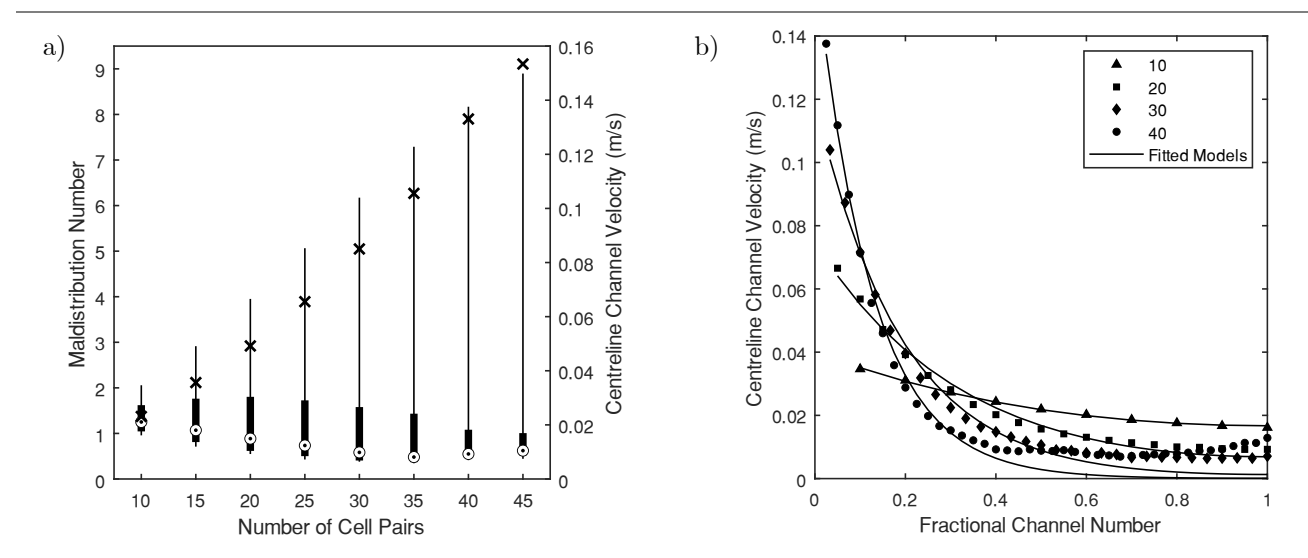


Figure 3.8. a) Fitted values of the maldistribution number (**x**, left y-axis) and a box-and-whisker diagram showing the distribution of the velocity across the stack (right y-axis) for simulations where the simulated number of cell pairs was changed. Targets (②) give the median velocity, boxes represent the interquartile range, and lines show the overall range of velocity. b) The distribution of flow between channels for a varying number of cell pairs with channel one being the closest to the stack inlet. Also shown is the fitted maldistribution model for case (equation 3.15).

high number used at an industrial scale. Maldistribution is expected to be worse when more cell pairs are used, and so this shows the importance of leveraging the other parameters mentioned to prevent it becoming unmanageable.

A caveat is revealed by these results; the goodness of fit of the model is reduced for simulations of a high number of cell pairs in the slower channels (Figure 3.8b). The maldistribution model predicts that the velocity should tend to zero in this case, but the Fluent model shows that instead a steady value of around 0.01 m/s is reached, or that the velocity increases in further channels. Therefore, there is inaccuracy in either the Fluent simulation or the maldistribution model. Simulating a high number of cell pairs in Fluent is very computationally demanding, as the volume of the domain increases, and denser meshes are required around junctions to account for the very steep velocity gradients between early channels and the manifolds. The total number of mesh cells therefore increases at an increasing rate. The velocity profile can be seen to oscillate slightly, indicating numerical instabilities. Additionally, the validity of the assumption of negligible wall friction would decrease as a higher number of cell pairs are considered.

3.3.7 Length-to-width ratio

All previous simulations were carried out on an L/D of 1 since this is typical for lab-scale stacks. However, pilot and industrial stacks typically have an L/D of 2 to increase channel residence time and reduce the impact of localised effects such as stagnant regions. A comparative flow simulation was conducted on two stacks, identical except for one having double the channel length (16 cm) of the other.

It is shown by the results that the maldistribution is slightly less for the longer flow path (Figure 3.9), with an L/D of 1 and 2 resulting in a maldistribution number of 1.20 and 0.99, respectively. The reasoning of this is



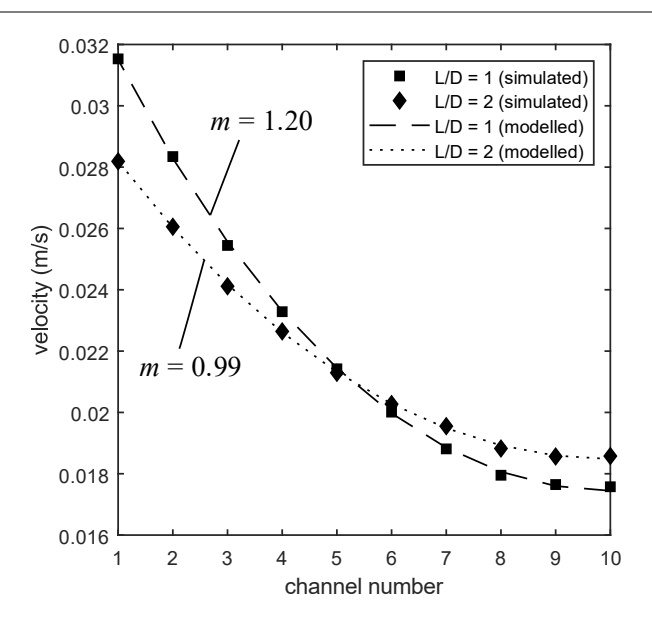


Figure 3.9. The velocity distribution for simulations where the length-to-width ratio (L/D) was changed. The simulated velocities are shown as points. Also displayed are the results of the fitted maldistribution model, shown as lines.

the same as that of the distributor angle, where longer flow paths lead to higher pressure drops and thus a lower proportion of the momentum of the manifold flow is transferred to the channel.

As a result, the higher L/D used at industrial scale would go some way to reducing the maldistribution, but the effect is relatively low compared to other parameters studied. A similar effect would be expected from the presence of a netted spacer, which can, on average, increase the pressure drop by about 55% [93]. Eq. 3.53 shows how m is inversely proportional to the square root of the mean channel pressure drop. It can therefore be estimated that the presence of a spacer would reduce the value of m by about 20%.

3.4 Consequences of maldistribution

It has been shown in Section 3.3 that maldistribution exists in ED and that it is affected by stack geometry and inlet flow rate. It can be shown from the maldistribution model that the ratio of the velocity of the fastest channel to the slowest channel is $\cosh m$. A value of m of 1.3, which could be considered moderate, would lead to twice the flowrate through the fastest channel compared to the slowest, and thus the fluid would have half the residence time. Understanding the effect this has on ED operation is vital as it raises the question 'to what degree maldistribution is an issue that needs addressing?' It is expected that performance decreases as maldistribution worsens; this section investigates to what degree this is true. Two operational metrics were chosen for this investigation, the LCD and stack resistance, as these represent local and global effects, respectively.

3.4.1 Limiting current density

The LCD is a practicable upper bound for ion flux, and thus reductions in LCD are detrimental for process intensification purposes. The one-dimensional model outlined in Section 3.2.3 was used to determine the change in LCD with maldistribution. It is clear from the results that the limiting current density decreases significantly



as maldistribution worsens (Figure 3.10a). The LCD as a function of m is plotted, where the LCD has been scaled to a case of uniform flow distribution (m = 0). This non-dimensionalisation was done to remove the effects of variables such as the inlet concentration, channel residence time, and current efficiency. Hence, the y-axis represents the LCD as a fraction of that for a uniformly distributed case. As m increases, the scaled LCD rapidly

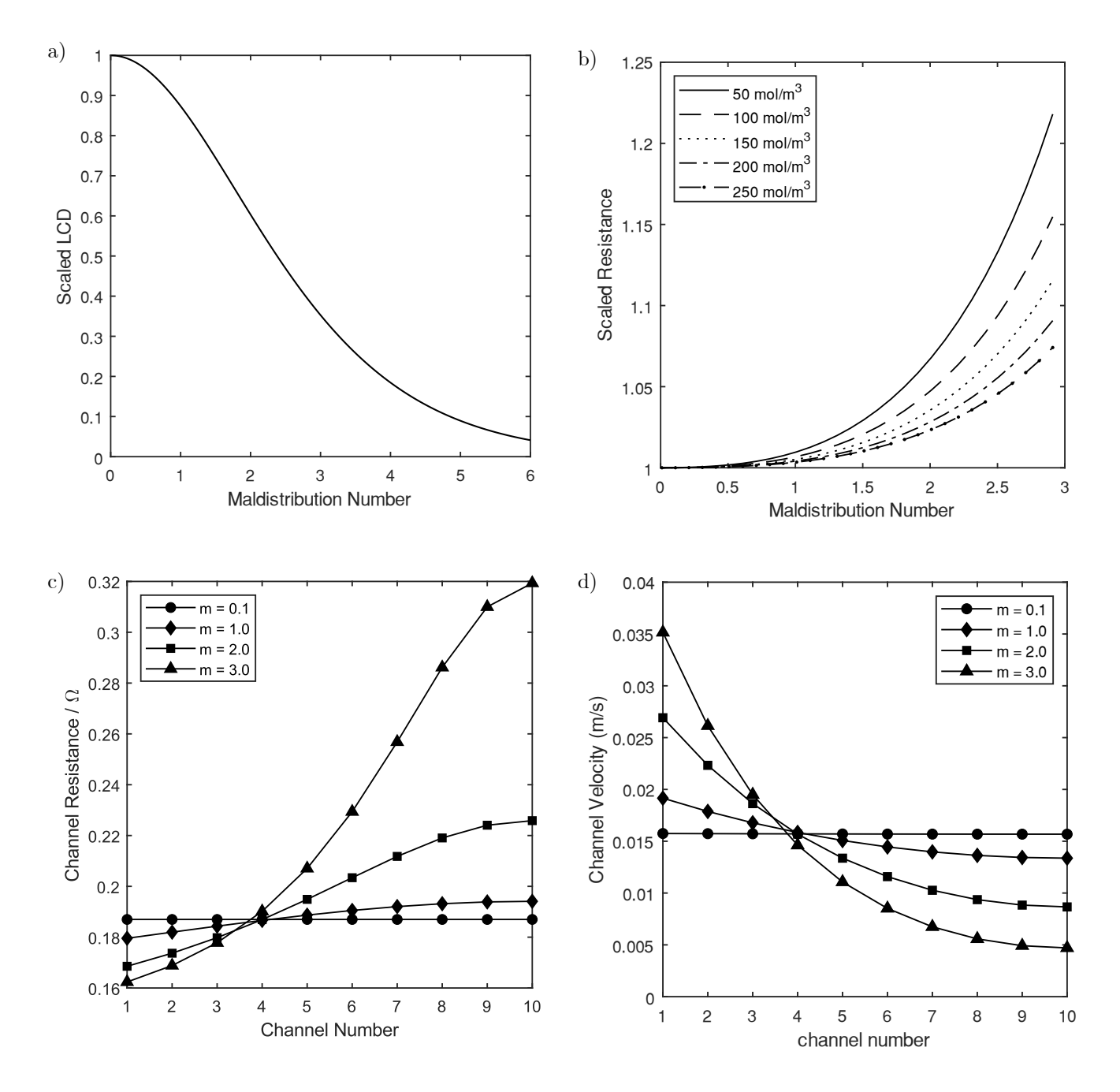


Figure 3.10. a) A graph of the scaled limiting current density (LCD) as a function of the maldistribution number. The LCD is normalised to a case of uniform flow distribution (m = 0) to remove the effects of confounding variable such as inlet concentration and current efficiency. b) The calculated resistance of a multi-channelled one-dimensional stack as a function of the maldistribution number for different inlet concentrations. The resistance is normalised to a case of uniform distribution (m = 0). c) The profile of channel resistance for different values of the maldistribution number. d) the velocity profile for different values of the maldistribution number. Low numbered channels are closer to the entrance and exit of the stack.



drops before asymptotically approaching zero. An inflection point is seen at m = 1.63, where the LCD has fallen to 67% of the uniform distribution value.

The reason LCD decreases as maldistribution worsens is because it is reached first when the membraneelectrolyte interfacial concentration for the slowest channel vanishes. Concentration polarisation is always greatest at the end of the slowest diluting channel, since it has the longest residence time, and thus the greatest amount of salt removed. As m increases, the velocity in the slowest channel decreases, the residence time increases, and hence the outlet concentration decreases. Therefore, a zero interfacial concentration is reached with a lower flux, and the LCD is lower. It can be seen from Eq. 3.35 that the velocity of the slowest channel decreases as mincreases.

$$u_{10} \propto \frac{m}{\sinh m} \tag{3.54}$$

The $\sinh m$ term grows much faster than m, leading to an overall decrease in the slowest channel velocity which tends to zero as m gets large. This is expected from the broadening of the velocity distribution. The residence time subsequently increases and so a lower flux is needed to achieve a zero interfacial concentration.

The magnitude of the reduction in LCD resulting from maldistribution is large, with a 'moderate' maldistribution of m = 1.3 leading to a 23% reduction in the LCD. This has significant consequences for process intensification. Generally, it is desirable to operate just below the LCD since a higher current density results in a higher ion flux. There is a subsequent reduction in required membrane area and unit size, leading to lower costs. A reasonable increase in maldistribution leads to a marked reduction in the LCD, significantly hindering performance.

The effect that maldistribution has on LCD is not one that has been studied much before, despite its apparent prevalence. Tanka [146,147] modelled how the LCD decreased as the standard deviation of the stack velocity increased. It was assumed that the slowest flow path has a velocity three standard deviations below the mean. While this was useful to show the effects of maldistribution, the velocity distribution in a stack is far from normal, and so the application of a dimensionless maldistribution number gives a more realistic depiction.

It is suspected that the lack of research into maldistribution in published literature may be because of the large number of confounding variables in ED. The LCD is typically accounted for in both modelling and experimental papers as an empirical power law, with the inlet concentration and occasionally the velocity as variables. All contributing phenomena to the LCD are therefore lumped into a single model, the effects of which are subsequently obscured. Many phenomena that are difficult to quantify have been identified as leading to a reduced LCD including solution leakage [93] and ionic shortcuts [94]. The degree of turbulence in the channel also significantly affects the thickness of the laminar boundary layers, which alters the LCD in a non-linear way. It is therefore reasonable that maldistribution and its effects have gone unnoticed, as it is challenging to measure experimentally, and its effects may be obscured by many confounding variables.



3.4.2 Stack resistance

The stack electrical resistance is important to the overall performance of ED. An increase in resistance will lead to an increased cost either in terms of a greater required membrane area or higher voltage to achieve the same charge transfer rate (Eq. 3.36).

Figure 3.10b shows the scaled resistance as a function of m for a series of different inlet concentrations. Like the analysis performed for the LCD (Figure 3.10a), the y-axis gives the ratio of the resistance to a case of uniform flow distribution (m = 0). This is again to remove the effect of confounding variables. Maldistribution leads to an increase in overall resistance, which grows rapidly as m is increased. It can also be seen that the increase in resistance is greater for lower inlet concentrations. The effect on resistance is less severe than the effect on LCD. A moderate maldistribution with m = 1.3 has a 23% reduction in the LCD, however experiences only a 2% increase in overall stack resistance for a 50 mol/ m^3 inlet concentration.

Figure 3.10c and d show the corresponding velocity and channel resistance profiles, respectively. It is shown by these figures that the lower the channel velocity, the higher the resistance. The electrolyte resistance is inversely proportional to concentration, and so a reduction in average channel concentration from a longer residence time leads to a large increase in absolute resistance. Due to the reciprocal nature of the relationship, the effect of decreasing concentration has a larger relative effect than increasing it. Hence, higher numbered channels are seen to deviate in resistance more from the uniformly distributed case, and so the sum of the channel resistances is higher. When m is increased, the velocity distribution broadens, and so the resistance distribution broadens also. These two effects combined show why resistance increases with maldistribution. The greater increase in resistance for lower inlet concentrations is also because electrolyte resistance is inversely proportional to concentration. The same absolute change at a lower concentration has a much greater proportional effect.

The effect on resistance is less severe than the effect on LCD because resistance is global whereas LCD is local. The channels slower than the average lead to increase in resistance, but this is partly counteracted by the faster channels having lower resistances. The slowest channel in the case where m = 3 (severe maldistribution) has about 70% higher resistance than the average channel (Figure 3.10c & 10d), but the faster channels balance this out and lead to an overall increase in resistance of only 20%. The effect on LCD only considers the slowest channel and so the effects will always be more extreme. In the case of m = 3, the LCD is reduced by about 75%.

This highlights that the effects of maldistribution may be more of a localised problem than a global one. It also further explains why ED maldistribution has not had much attention historically. The issues of lower LCD and increased localised concentration polarisation can be explained by many confounding phenomena and obscured in empirical modelling. Whereas a significant increase in resistance is one that is less likely to go unnoticed.

One caveat with the resistance model is that although it accounts for concentration polarisation, there is no consideration for the LCD or associated phenomena such as water-splitting. As a result, as interfacial concentrations approach zero, boundary resistances blow-up to infinity. The resistance would significantly increase only until water-splitting occurs. It is therefore implicitly assumed that these simulations occur below the LCD.



3.5 Maldistribution of Z-configuration stacks**

The work presented in this chapter has been performed on the so-called U-type geometry, where the entrance and exist of a given stream are on the same side of the stack. However, many commercially available ED stacks operate in the Z-configuration, where the entrance and exit are on opposite sides (Figure 3.11a). A question arises as to how the degree of maldistribution differs between these two configurations. To investigate this, CFD simulations of both a U and Z-configuration stack were performed over a range of inlet flow rates using the standard lab-scale stack geometry. The degree of maldistribution was quantified by fitting the maldistribution models of Bassiouny and Martin [143,150] and computing dimensionless maldistribution numbers.

Figure 3.11b shows the centreline velocities for a U- and Z-configuration ten-cell pair stack operated at 45 L/h (4.5 L/h per cell pair). While the shapes of the flow distributions are very similar, their directions are opposite. It can be seen that from channel 1 to channel 10, the velocity for the U-type geometry decreases whereas for the Z-type it increases. As such, for both configurations, the channel closest to the stack outlet has the greatest flow rate. This is also seen in the maldistribution models for the dimensionless channel velocity, $u_c = U_c/W_0$:

U-type:
$$u_c = \left(\frac{A_m}{n A_c}\right) \frac{m \cosh(m(1-z))}{\sinh(m)}$$
 [3.55]

Z-type:
$$u_c = \left(\frac{A_m}{n A_c}\right) \frac{m \cosh(mz)}{\sinh(m)}$$
 [3.56]

with the notable difference being the hyperbolic cosine function of the dimensionless manifold axial distance, z = Z/L. This function decreases with z for the U-type geometry but increases for the Z-type. The reason for this difference can be found in the derivation of the models, and in particular from the pressure drop. Combination of the mass and momentum balances around the manifold-channel junctions reveals the relationship between the dimensionless pressure, p, and manifold velocity, w for the inlet manifold:

$$\frac{dp}{dz} = -w\frac{dw}{dz} \tag{3.57}$$

and the outlet manifold:

$$\frac{dp^*}{dz} = -2 w^* \frac{dw^*}{dz} \tag{3.58}$$

The factor of two arises from the turning losses incurred and the asterisks (*) indicate variables for the outlet manifold. For the U-type configuration, dw/dz and dw^*/dz are equal and are both negative. Flow in the manifold is greatest nearest to the entrance/exit and decreases away from it as z increases Therefore, pressure increases along the manifold in the direction of increasing channel number for both the inlet and outlet. However, the pressure in the outlet manifold increases more than for the inlet due to the factor of 2 present. Hence, the manifold pressures are converging, reducing the pressure drop of higher numbered channels and thus, decreasing

^{**} This section was not present in the original publication. It presents work that was performed in collaboration with undergraduate student Lauren Hodgson under the supervision of JL. All results present here are the original work of JL



76

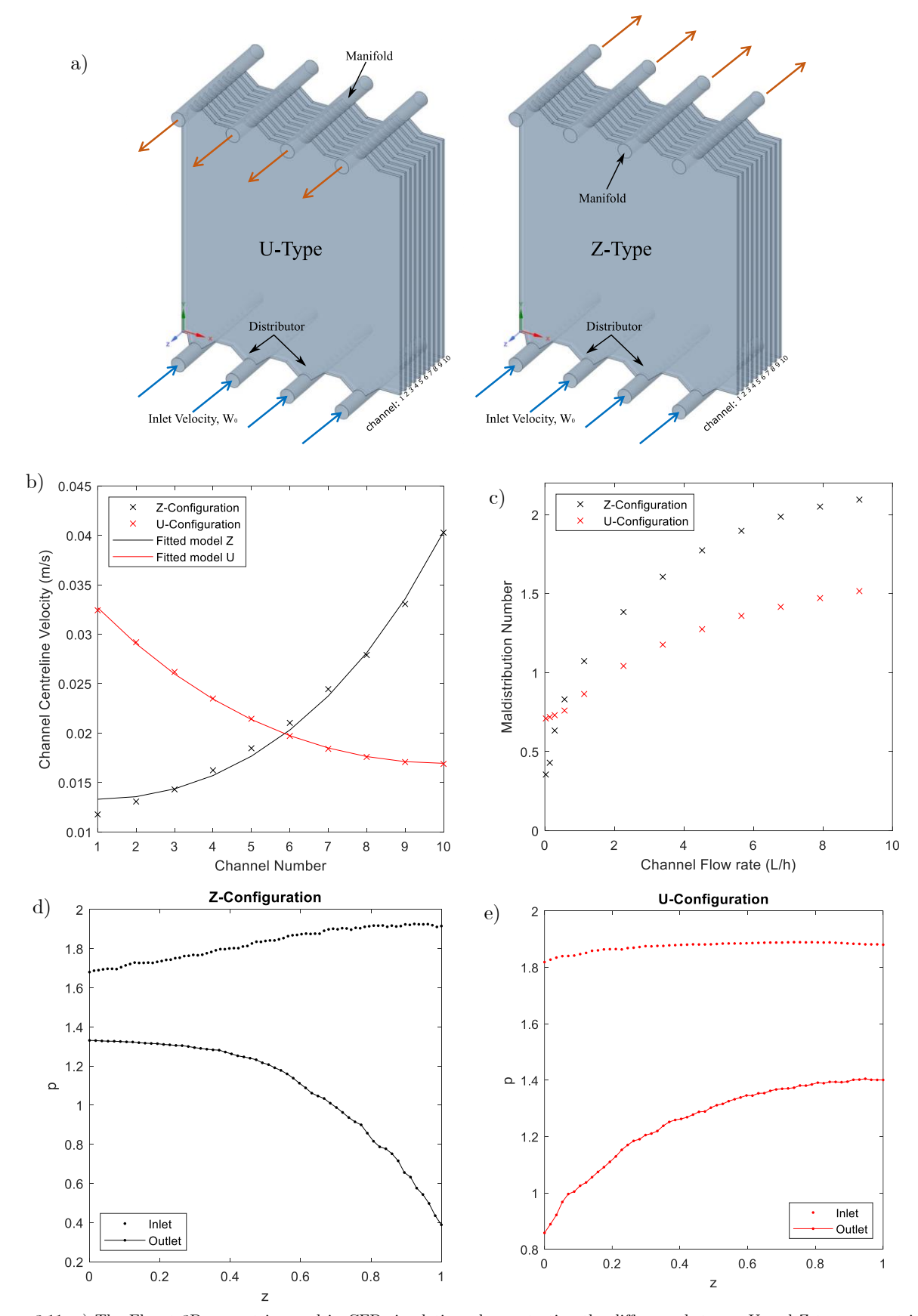


Figure 3.11: a) The Fluent 3D geometries used in CFD simulations demonstrating the difference between U and Z type geometries. b) the distribution of centreline velocities for a U and Z-configuration stack. c) The dimensionless maldistribution number, m, as a function of the average channel flow rate for both U and Z-type geometries. e) The manifold pressure profile calculated in Fluent for the Z-configuration geometry. e) The manifold pressure profile calculated in Fluent for the U-configuration geometry.



their flow rate. For Z-type geometries, dw/dz and dw^*/dz have opposite signs. For the inlet manifold, w decreases in the direction of increasing channel number but for the outlet manifold w^* increases. Thus, while dp/dz is positive, dp^*/dz is negative, and the manifold pressures diverge. This increases the pressure drop of channels with higher channel numbers (closer to the outlet) and thus increases their flow rates. The inlet and outlet manifold pressures measured in Fluent at a flow rate of 4.5 L/h per cell pair are shown in Figure 3.11e and Figure 3.11f for the Z-type and U-type geometries. A diverging and converging pressure drop is clearly seen for the Z and U-type geometries, respectively.

Figure 3.11c shows that the degree of maldistribution for a Z-type geometry is greater than for U-type at higher flow rates and smaller at lower flow rates. Further, for very low flow rates, the maldistribution number appears to tend to a lower value for the Z-type geometry (0-0.4) than the U-type (about 0.7). This leads to a situation where the Z-configuration is preferred at low flow rates and the U-configuration is preferred at high flow rates. A classical approach to predicting the degree of maldistribution using the Darcy friction and equation 3 factor can be used to directly predict the maldistribution number from system parameters.

$$\xi = \frac{64}{Re} \frac{L}{d_h} \tag{3.59}$$

$$m^2 = \left(\frac{nA_c}{A_m}\right)^2 \frac{d_h^2}{L} \frac{\rho u_m}{\mu}$$
 [3.60]

Here, Re is the Reynolds number (proportional to velocity), L is the channel length, d_h is the hydraulic diameter (twice the intermembrane distance), μ is the solution viscosity, and u_m is the mean channel velocity. Using Eq. 3.60 would suggest that as overall flow rates tend to zero, m should also tend to zero. This may be the case for the Z-configuration but is certainly not true for the U-type. The disparity may be explained by comparing the lengths of the flow paths taken in the manifolds. In the Z-type geometry, flow travels exactly one manifold's length regardless of the channel selected. However, for the U-type geometry, the manifold length travelled varies from very short for channel one up to two manifold's length for channel ten. At low flow rates, the friction encountered in the manifolds begins to be the dominating discriminating factor driving maldistribution in the U-type geometry.

At higher flow rates, when the manifold friction is not dominating, the maldistribution in Z-type geometries is greater than that of the U-type geometry. This arises due to the relative flow rates in the inlet and outlet manifolds at the same axial position in z. For the Z-type geometry, close to the inlet adjacent to channel 1, w is at its greatest value, whereas w^* is at its lowest value. Conversely, for channel 10, w approaches zero and w^* achieves its highest value. However, for the U-type geometry, w and w^* are always of an equal magnitude. The imbalance of the velocities in the manifolds leads to a greater difference in the pressure drops between the inlet and outlet of different channels. The result of this is a much more dramatic decrease in the outlet manifold pressure at the outlet for the Z-type geometry (right has side of Figure 3.11d) than the U-type geometry (left hand side of Figure 3.11e).



3.6 Conclusion

Maldistribution in ED was investigated through CFD simulations of a stack with varying geometrical and operating parameters. It was determined that the distribution of flow between channels is far from uniform. Therefore, the ubiquitous assumption of channel uniformity in ED modelling has been shown to be inaccurate. Further, a rigorous analytical model was found to accurately capture the distribution of flow between channels and represent the degree of maldistribution using a dimensionless number, m. The strong physical basis of this model allowed for the clarification of observed trends in simulations and provided a useful metric of maldistribution for use in one-dimensional models.

The simulations revealed that changes which increased the manifold velocity (reducing the number of manifolds, increasing the number of cell pairs, and increasing the inlet flow rate) increased maldistribution. This is because channels nearer to the entrance are adjacent to a higher velocity in the manifold, and so a greater amount of momentum is transferred to those channels. This increases the proportion of flow to the channels closer to the entrance and subsequently reduces the channel velocity of those farther away. Additionally, alterations which increase the channel pressure drop (reducing the width of the distributor, reducing the channel width, and increasing the L/D ratio) were found to reduce maldistribution by encouraging flow to remain in the manifold. From these conclusions, it can be extrapolated that maldistribution will likely worsen at larger scales due to the much higher number of membranes and larger flow rates. However, this must be confirmed either experimentally or through simulations due to the large number of confounding influences present. This shows that maldistribution in ED is likely ubiquitous, and so this research is important for all applications.

The impact of maldistribution on ED operation was investigated through two performance parameters. The LCD was chosen as a representation of localised effects, and the stack resistance to represent global impacts. The effect of maldistribution, through m, on these parameters was determined using a one-dimensional model. The results showed that although the resistance was increased slightly, the impact on the LCD was significant. The maldistribution of the standard geometry led to a 23% reduction in LCD, relative to a case where no maldistribution is present. This highlights that the issues caused by flow maldistribution manifest at a localised level rather than a global one. It further shows that maldistribution is an important phenomenon which significantly reduces the performance of ED by limiting process intensification.

Flow maldistribution in ED has not had particularly much attention because the most significant effects, on LCD, can be obscured by modelling it empirically and the presence of many confounding variables. This study has shown that maldistribution in ED exists and that its effects are significant. Maldistribution should therefore be investigated further, both experimentally and computationally across many scales to fully explore its prevalence and effects.





Chapter 4

Experimental validation of maldistribution

N.B.: The work in this chapter has been submitted to The Journal of Membrane Science on the 24th of July 2024 under the name 'Experimental validation of the presence of maldistribution in electrodialysis and its effect on the limiting current density'. At the time of submission of this thesis, this paper is in review.



4.1 Introduction*

In Chapter 3, the phenomenon of maldistribution within electrodialysis (ED) was investigated. A ubiquitous assumption in ED process models is that of channel uniformity, where every channel behaves identically. From this, only one channel need be modelled, and the overall stack operation found by considering an arbitrary number of channels in parallel. However, in previous work (Chapter 3, [151]), it was determined that this is not a justified assumption. Computational fluid dynamics (CFD) simulations of a typical lab-scale stack geometry demonstrated that there is a significant degree of maldistribution between channels in ED. It was shown that in a standard lab scale stack with ten cell pairs and a flowrate of 45 L/h, the flowrate in the channel closest to the inlet and outlet was twice that of the channel furthest away. Several aspects of the design including the channel width, distributor angle, number of channels, number of manifolds, and overall flow rate were varied to investigate the effect on maldistribution. An analytical maldistribution model, developed initially for a plate and frame heat exchanger by Bassiouny and Martin [143,150], was applied to the velocity distribution results for the ED stack due to the analogous geometry. This model considers the geometry and flowrate of the stack and represents the degree of maldistribution in a single dimensionless number, m. A model for the flow velocity in each channel (U_c) is derived from mass and momentum balances around the junction between the manifold and channels. For a U-type geometry (where the entrance and exit are located on the same side of the manifold) this model is the following

$$U_c = W_0 \left(\frac{A_m}{nA_c}\right) \frac{m \cosh(m (1 - Z/L))}{\sinh(m)}$$
 [4.1]

Here, W_0 is the inlet velocity, A_m is the flow area of the manifold, n is the number of channels, A_c is the flow area of the channel, L is the length of the manifold, and Z is the axial distance along the manifold (varies from zero to L). The dimensionless maldistribution number (m) is defined as

$$m^2 = \left(\frac{nA_c}{A_m}\right)^2 \frac{1}{\zeta} \tag{4.2}$$

$$\zeta = \frac{2\Delta P_{mc}}{\rho U_{mc}^2} \tag{4.3}$$

where ζ is the general friction coefficient. Here, ΔP_{mc} is the mean channel pressure drop, ρ is the fluid density, and U_{mc} is the mean channel velocity. This model was found to represent the maldistribution well and explained the trends observed in the case study investigations where the geometrical design was altered. The case studies demonstrated that maldistribution was worsened when the channel pressure drop was lowered, or the manifold velocity was increased. Consequently, it is expected that maldistribution in ED will be worse upon scaleup. Two significant contributors to this conclusion are the overall flowrate and the number of cell pairs. A larger flow rate led to a wider distribution of flowrates between channels and consequently a higher maldistribution number (Figure 3.4). The number of channels is directly proportional to m (Eq. 4.2), and thus more cell pairs is associated with a greater degree of maldistribution (Figure 3.8).

^{*} The beginning of the paper has been reduced in length as it provides an outline of ED and a recap of the work presented in Chapter 3



The impact that maldistribution has on operation was numerically investigated through the stack electrical resistance and LCD. The resistance was computed using a circuit-based, one-dimensional model of ED, aggregating the resistances of many channels with distinct flow rates. To compute an estimate for the LCD, the concentration profile was modelled as having a bulk mixed region and boundary layers adjacent to the membranes.

It was found that the impact on the resistance was not significant, with the maldistribution contributing to only a 2% increase for a standard lab scale stack where m is around 1.3. However, the impact on the LCD was substantial. There is a significant decrease in the LCD as m is increased (Figure 3.10a), where the standard lab-scale case which had a computed m of 1.3 is associated with a 23% decrease in the LCD relative to a stack with no maldistribution. The disparity between the resistance and LCD is because the electrical resistance is a function of the environment across the entire stack, whereas reaching the LCD is a localised phenomenon. The faster and slower channels mostly balance each other out when it comes to resistance, but the LCD is always dependent on the slowest channel. Greater maldistribution means a lower flowrate in the slowest channel (velocity proportional to $m/\sinh(m)$) and thus a lower current density is required to achieve ion depletion.

The conclusions reached in the previous work concerning the existence and impact that maldistribution has on the LCD have significant consequences for the future of ED development. However, these conclusions were based solely on numerical models, and thus require experimental validation. In this work, both the existence and the impact that maldistribution has on the LCD are experimentally investigated.

The presence of maldistribution within a standard laboratory ED stack geometry with a 45 L/h water flowrate is evaluated experimentally using red-blue particle image velocimetry (PIV). The velocity of each channel is determined by measuring the distance travelled by particles flowing through the channel between a red and blue pulse of light with a known time delay. These results are then analysed to identify maldistribution and compared to the CFD simulations.

To investigate the impact of maldistribution, the LCD is measured as a function of the degree of maldistribution within the ED stack. Maldistribution is manipulated by changing the overall flow rate and the number of cell pairs while maintaining a constant average salt flow rate within each channel to eliminate any confounding effects. This ensures that if no maldistribution is present, all experimental results will show the same LCD. However, if maldistribution is present, the LCD should decrease as the flowrate and number of cell pairs is increased. The magnitude of this decrease is then compared to model predictions.

One important distinction between this and the previous work is the variation between the U and Z-type geometries. The flow cell used in Section 4.2 was built in the U-configuration, where the inlet and outlet are on the same side of the stack and designed to match the geometry used in CFD simulations. However, the commercial ED stack used to measure the LCD was a Z-type geometry where the inlet and outlet are on opposite sides of the stack. This distinction does not dramatically affect the degree of maldistribution and relevant simulations of the Z-type geometry were completed using the same method as in the previous work and new maldistribution numbers were computed.



4.2 Validating the presence of maldistribution using red-blue PIV

4.2.1 Method

The core experimental method employed in this section is red-blue PIV [152]. This method allows for visualisation of a flow velocity field within a single image, using equipment which is inexpensive relative to traditional PIV. Reflective spherical particles are introduced to a flow which then pass through a transparent flow cell. A region of interest is focused upon by a camera with a short focal depth. This ensures that only the particles within a narrow plane are in focus, circumventing the need for a laser light sheet, as in traditional PIV. It is essential that the density of the spheres is close to that of the carrying fluid to minimise buoyancy and ensure the particles track the flow.

During the experiment, all sources of background light are removed, and a single long-exposure photograph is captured. During this exposure, red and blue light emitting diode (LED) light sources are briefly sequentially pulsed, with a known time delay between them. For each particle captured by the camera, this leaves two bright impressions on the image, one for each light pulse. Due to the Bayer filter present over the CCDs in modern digital cameras, the red and blue images are effectively captured on different sensors, and their brightnesses are recorded separately. Therefore, they can be separated and processed as two temporally distinct images. The distance between the particles on the red and blue images can be measured using image processing software and divided by the pulse time delay to compute a velocity.

4.2.1.1. Experimental setup

Photographs of the experimental setup can be found in Section 4.2.3. A glass flow-cell with the same geometry as the domain used in CFD simulations (Figure 4.1a) was constructed by layering 1 mm thick glass sheets. The cell has ten channels, each of which has dimensions of 8 cm by 8 cm by 1 mm. Distributors of angle 90° connect the channels to four 5 mm diameter manifolds. As with the CFD simulations this work is attempting to replicate, the geometry was designed to be representative of a PCCell ED 64004 stack with 1 mm wide blank channels. The flow cell was constructed by cutting the various layers out of 1 mm thick glass with a water jet cutter and joining them with UV-activated glue. This had the unforeseen effect of slightly increasing the width of each channel above the desired 1 mm to about 1.15 mm. Despite this, the resultant flow cell had geometrically uniform channels and was transparent. For simplicity, channels will be referred to hereafter by number, with channel one being that closest to the inlet and outlet, and channel ten being farthest away.

White polyethylene microspheres of diameter 45-53 µm and density 1.00 g/cm³ (Cospheric) were used for particle tracking. Their size was optimum as it meant they would be clearly visible within the camera's region of interest (imaged spheres have a ~18-pixel diameter) without being so large as to significantly affect flow patterns. Their white colour and opaque nature were ideal for this PIV application as they were highly reflective of both the red and blue light. A precise diameter sphere was not crucial for this work. A particle concentration of 0.01 g/L was found to work well as it resulted in just a single particle being captured in most photographs. This corresponds to ~150 particles per mL.



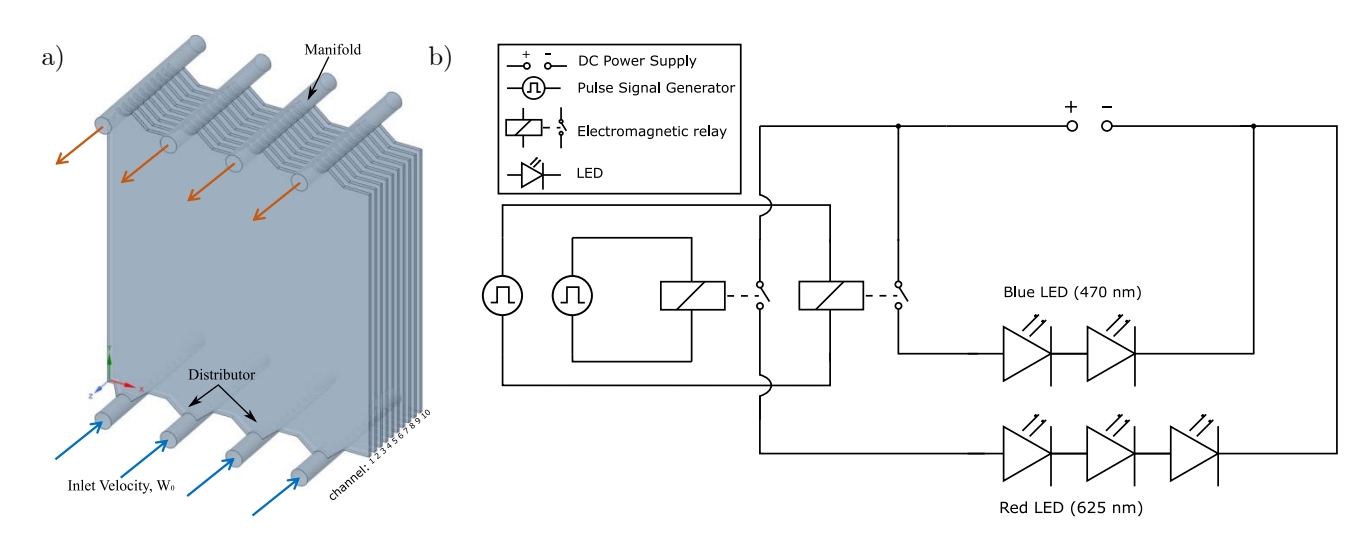


Figure 4.1: a) The CFD geometry, representative of an experimental ED stack, and is what the glass flow cell design is based on. Flow enters the manifolds at the bottom of the stack and is distributed to the ten channels before collecting in the top manifolds and exits the stack. Channels are numbered as shown, with one being closest to the entrance and exit, and ten being farthest away. b) A circuit diagram for the pulsed LED light sources, showing red and blue LEDs in parallel, each of which operated by solid state relays and a pulsed signal generator.

The flow was pumped around a circuit by a water strider centrifugal pump and the flowrate controlled by a rotameter (Georg Fischer) to be 45 L/h. A Pixelink digital camera with Navitar Resolv4K zoom lens and fixed 4X magnification microscope lens (Nikon) was employed for capturing the images. A calibration image found a distance conversion factor of 326 pixels per millimetre. The camera was mounted on a unidirectional translation stage with micrometer thread to accurately adjust the focal plane and ensure it was set to the middle of each channel.

The focal length of the lens is ~18 mm. This is less than the total width of the flow cell, and so not all channels can be imaged from the same direction. To overcome this, channels one through six are imaged from the top (the same side as the inlet and outlet), and then ten through four are imaged from the bottom. The overlapping of channels four, five, and six allow for comparison between the data to demonstrate that the orientation of the stack does not affect the maldistribution. The coinciding data taken from both ends of the stack were similar, demonstrating that gravitational body forces do not significantly affect maldistribution.

A circuit diagram for the LED setup can be seen in Figure 4.1b. Three red LED arrays and two blue LED arrays (each with four LEDs, from Intelligent LED Solutions) were used for the illumination. The different number of LED arrays for each colour ensures that each parallel branch has a similar electric resistance and therefore similar current as they are powered with the same power supply (Keysight technologies).

A two-channel signal generator (AIM-TTI Instruments) was configured to send two 2 ms pulsed signals with a delay of 15 ms between them. Each of these pulses activates a solid-state relay (Omron), closing one branch of the circuit and activating one colour of LED for the duration of the pulse. A short pulse width is desirable as this prevents captured particles turning into streaks. However, a short pulse also produces a smaller amount of light, increasing the proportion of noise in the image. Excessively short pulses can also be hampered by the 'turn on time' of the relay.



The focal depth of the lens used was ~500 µm. This meant that there were particles in focus that were not in the channel centreline, nor could their distance from the channel wall be discerned to determine what the centreline velocity would be. Resultantly, a more stochastic approach was taken where several hundred images of each channel were taken to capture the distribution of the velocity. The maximum particle velocities seen (which would be present in the centre of the channel) could then be compared to the CFD computed channel centreline velocities. Images taken were initially screened to remove those with no particles present or where particles were out of focus, and the remaining images were processed automatically to discern their velocities.

4.2.1.2. Image processing

Over six thousand images were generated, of which approximately 1500 were appropriate for measuring particle velocities. An automated image processing method was developed to determine the velocities of the captured particles for a batch of raw images. A program in MATLAB R2023a was written to remove all background noise and the presence of stationary particles that had become stuck to a wall. Further, the program automatically recognises the difference between multiple transiting particles and calculates their individual velocities. The details of this program are outlined below, and an example is shown in Figure 4.2.

First, all the raw images from a single image batch are imported. These bitmap images are stored as 2048 by 2448 by 3 three-dimensional matrices. Each element is a value between zero and 255 and denotes the brightness of a single colour (red, green, or blue, the third dimension of the matrix) of each pixel of the 2048 by 2448 image. The matrices are looped over with the following procedure applied to each:

Background subtraction is performed by simply subtracting the RGB values of the background image (an image with no particles which otherwise would have been discarded in the pre-screening) from the image being processed. This leaves just the transitory particles and a small amount of noise. The image is then separated into its red and blue counterparts (The green image is not used any further) which are then processed individually.

The 'imadjust' function is used to increase the brightness and contrast of the red and blue images. This removes most of the low-brightness noise remaining after the background subtraction and makes the particles clearer. The images are then segmented based on their morphology to remove any regions too small to fit a circle with a radius of 7 pixels. Large, connected regions with an area greater than 1200 pixels are then removed. This takes care of any out of focus particles in neighbouring channels which were captured in the image. Example processed images can be found overleaf.

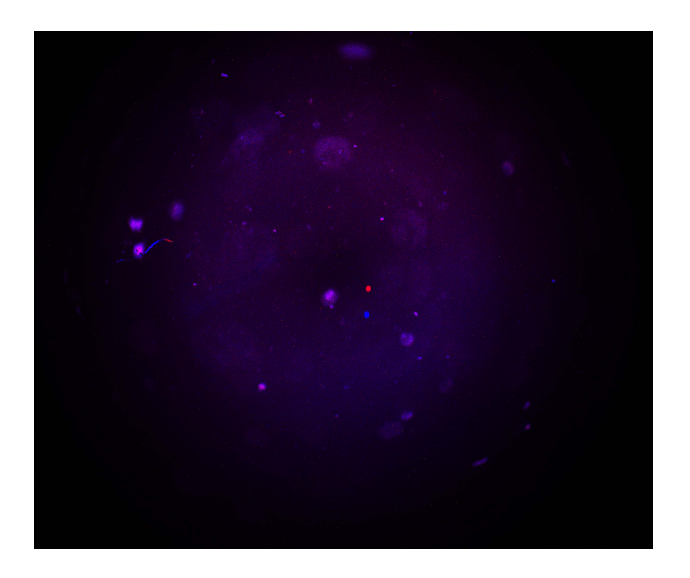
The resultant processed red and blue images are binary and contain only transiting particles. The 'regionprops' function is used to discern the particle centroids. These centroids are recorded, and the displacement vectors between all red and blue particle pairings are stored in an array, where the columns and rows are different red and blue particles. When multiple transiting particles are present, the correct pairings between the red and blue images can be found by filtering using the magnitude and phase angle of the displacement vector. This process is then repeated for all images within the batch, after which the transit distances are converted into real distances using a conversion factor of 326 pixels per millimetre, and then to a velocity by dividing by the pulse delay time of 15 ms.



Raw, unprocessed image.

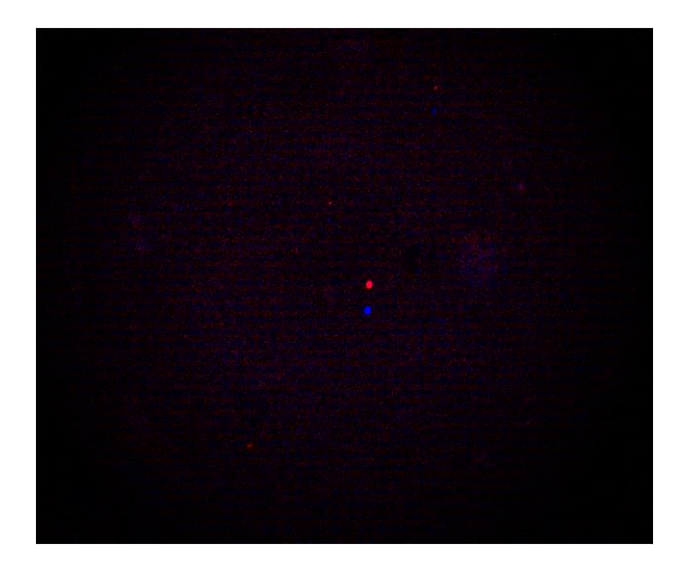
A significant amount of background noise can be seen. Blurry purple circles are particles that have become stuck to the walls of the flow cell. A purple hue is the result of reflection of the LED pulses off the surface of the flow cell.

A single transiting particle can be seen from the red and blue circles. The red pulse occurred 15 ms after the blue pulse, and thus the particle is transiting vertically up the image



After background subtraction and contrast adjustment.

Most of the noise has been removed. A few transiting particles that are out of focus can be seen that will be removed in the next processing step.



The final image

Following segmentation and masking, two binary images of the particle at each time step remain. These are stitched back together to form the final image. The distance between the centroids of the remaining regions is computed and represented here with a white line.

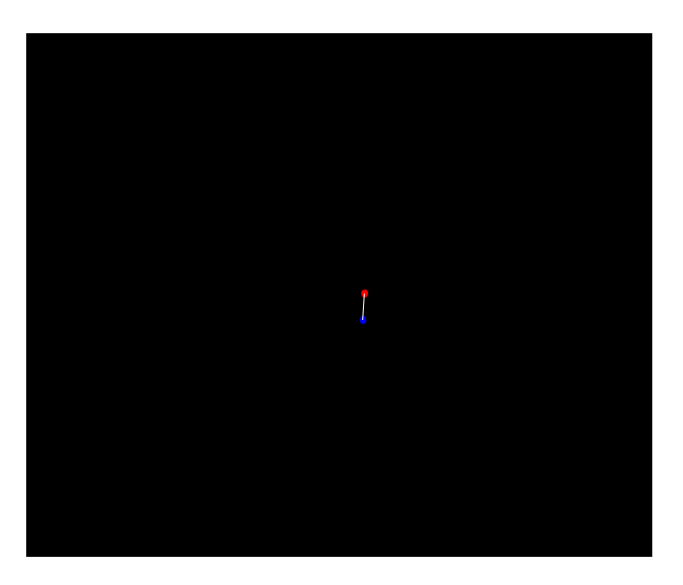


Figure 4.2: An example of the image processing procedure.



4.2.1 Results and discussion

In this section, the velocities of measured particles are compared to CFD simulation results. Figure 4.3 shows the centreline (maximum) velocity measured in CFD simulations as horizontal blue lines. The maldistribution of flow is clearly visible, with the flow rate of channel one (closest to the inlet and outlet) being almost twice as fast as that of channel ten. Individual experimentally measured velocities are shown as white points within the same column, and the black bars indicate the maximum experimentally measured velocity. A perfect validation result would be one in which the black bars and blue lines match. In total, over 1000 velocities were measured and populate this graph.

Clear maldistribution can be seen in the experimentally measured maximum velocities, showing a similar qualitative trend to that of the simulated results. However, an important disparity can be seen, where there is a lower-than-expected velocity for all channels. A lower velocity with the same volumetric flow rate is characteristic of an increased flow area. It is believed that the channels are slightly wider than the expected 1 mm as a result of the UV activated glue used to bind glass sheets together during the flow cell construction. The channel expansion was measured by placing a micrometer across the entire flow cell width. It was hence concluded that the channel widths were increased by ~ 15 % and explains the lower-than-expected velocities.

The desired width of 1 mm was initially selected to coincide with existing simulations. A re-calculated distribution of velocities can be seen in Figure 4.3a where Eq. 4.1 was implemented with a channel width of 1.15 mm. A significantly better agreement between experimental and simulated results is seen, with an average relative difference of only 4.5%.

The remaining disparity can be attributed to the sources of error in the experiment, the largest of which is likely that of the volumetric flow rate. This was measured and set using a rotameter with a precision of 5 L/h and validity at only 20 °C. Increases in temperature over the experiment would reduce the viscosity of the water and thus a higher actual flowrate would be required to maintain the float at the same level. The temperature was

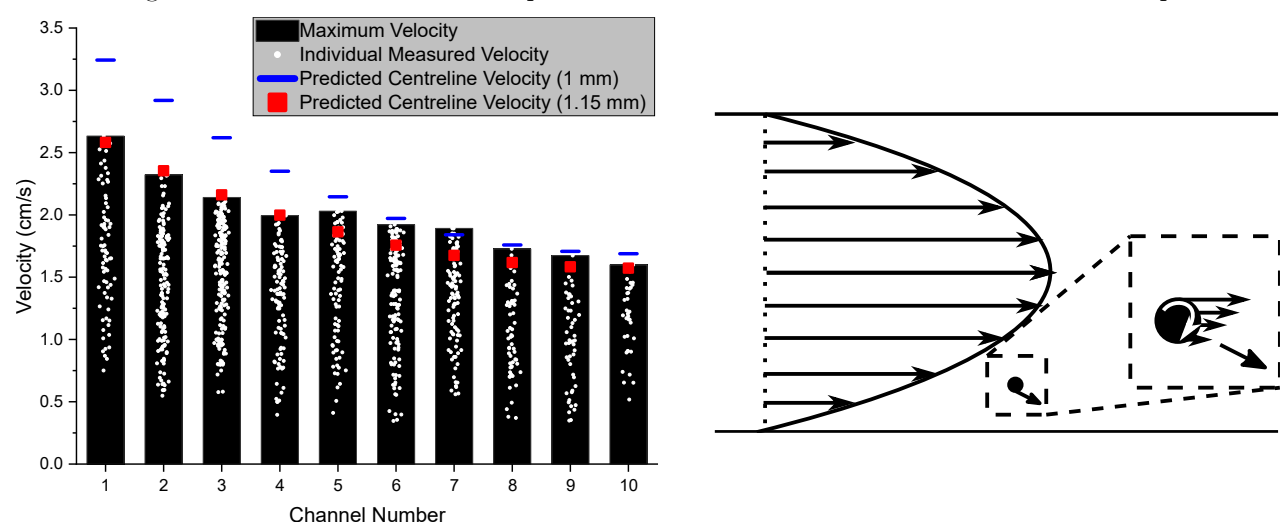


Figure 4.3: a) A graph showing the simulated and experimentally measured channel velocities. Individual measured particle velocities are shown as white points, and the maximum velocity in each channel is represented as the black bars. Simulated channel velocities for a channel width of 1 mm and 1.15 mm are shown with blue and red markers, respectively. b) A schematic representation of the lift force experienced by particles which may be driving them to the wall and be responsible for the lack of particles seen at low velocities.



seen to increase by ~4 °C over the experiment time. This rise in temperature corresponds to a 10% reduction in the viscosity which could be responsible for the discrepancies seen [153]. The heat produced from the pump is the likely source of this temperature increase. Further, it can be seen that the channels of greatest disparity are 5, 6, and 7. These channels would have been the ones imaged last during each experiment and so greater increases in the temperature could have transpired.

There is a distinct lack of particles encountered with low velocities, made apparent by the gap in the black bars between zero and the lowest measured velocity. Although its presence does not affect the comparison to the centreline velocities, it should be investigated, nonetheless. Due to the parabolic velocity profile of the laminar flow within the channel, the particles moving slowest will be those closest to the wall. Therefore, they are farthest away from the focal plane and will be more out of focus, and thus more likely to be removed during image processing.

A potentially impacting phenomenon that warrants investigation is the lateral lift forces experienced by particles, well known in the field of inertial microfluidics. The first of these forces arises due to the parabolic flow profile imposing a shear gradient on the particles, causing them to migrate towards the wall (Figure 4.3b) [154]. A further 'wall effect' force can provide lift in the opposite direction, driving particles away from the wall. As such, in microfluidics systems, particles can be seen to migrate to 'equilibrium positions' where these forces balance. The channel length required for particles to migrate to equilibrium positions can be calculated using a method outlined by Di Carlo [154] and was found for this work to be ~ 3 m. This far exceeds the channel length used in this work of 8 cm (or 4 cm to where the particles where photographed), and so it can be concluded that particles do not significantly migrate laterally from streamlines due to these forces. However, if the shear gradient force dominates the wall effect force it could be responsible for causing particles near to the wall to migrate on to the wall where they become stuck.

Despite the imperfections seen in the experimental results, this study has demonstrated that maldistribution between channels exists within ED. Further, it corroborates evidence from previous work that both CFD and a simple analytical model can accurately capture the degree of maldistribution within ED.

4.2.2 Statistical analysis[†]

The evidence presented for the presence of maldistribution in the previous section is a velocity distribution collected in a method comparable to a Monte Carlo simulation, and thus is inherently subject to a certain amount of randomness. Many data points were collected to achieve an accurately represented distribution. However, a question remains as to whether enough particles were captured to ensure accurate representation or if any bias was present in the data collection method. Here, a statistical model of the data collection procedure based on the Poisson distribution is presented and used to compare the expected velocity distribution to the one experimentally measured. In these experiments, particles flowing through rectangular channels were photographed with one long-

[†] The derivation of this section was present in the supplementary information of the publication



exposure photo and two pulses of light with a known time delay. A probability density function (PDF) of the velocity distribution of a captured particle is derived.

In this model, it is assumed that particles behave as point masses and travel with the same velocity as the surrounding fluid flow. Further, it is assumed that the path (streamline) taken by any one particle is random, and thus the depth coordinate (y) is a random continuous variable and is uniformly distributed across the width of the channel (Figure 4.4a). The low flowrate leads to a channel Reynolds number on the order of 10, and the flow pattern is laminar. Therefore, the velocity distribution u(y) within the channel is parabolic and can be described by

$$u(y) = \frac{3}{2}\bar{u}\left(1 - \left(\frac{2y}{\bar{d}}\right)^2\right)$$
 [4.4]

where y is the distance coordinate along the width of the channel (intermembrane distance) with the zero-point being the centre of the channel, \bar{u} is the superficial channel velocity (channel volumetric flow rate divided by the flow area), and \bar{d} is the channel width. Variables are converted to dimensionless form for simplicity as any

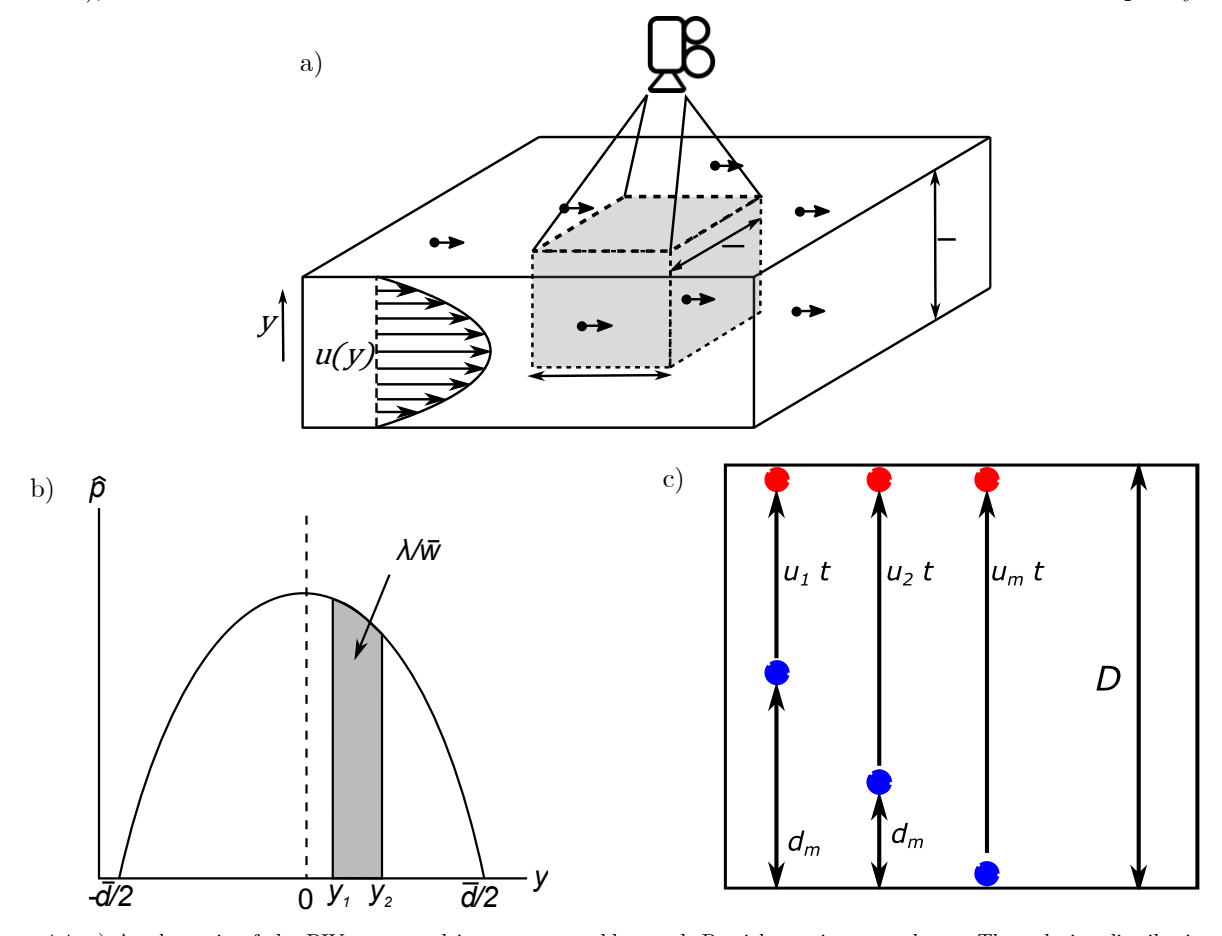


Figure 4.4: a) A schematic of the PIV setup and important variables used. Particle motions are shown. The velocity distribution (u(y)), channel width (\bar{d}) , distance across photographed area (\bar{w}) are shown. b) A schematic representation of the profile of the particle flux (\hat{p}) as a function of the position within the channel width (y). The expected particle observation frequency (λ) within a given depth can be found by integrating between two depths (indicated by the shaded region) and multiplying by the width of the camera's area of interest (\bar{w}) . c) A representation of the marginal distance for particles travelling with a certain velocity $(u_2 > u_1)$. This is used to calculate the probability that a particle is captured in both red pulses, given that it has been captured in one. Faster moving particles have a shorter marginal distance and thus are less likely to be captured with the second pulse. Also illustrated is the maximum transit velocity (u_m) .



constants are factored into a probability normalisation factor when forming the final PDF. Further, since the parabolic velocity distribution is symmetric, only the range of y between zero (the channel centreline) and one need be considered.

$$u = 1 - y^2 ag{4.5}$$

The desired PDF is the probability density of an encountered particle having a velocity of u. To properly encounter a particle, it must be within the photographed region when both pulses of light occur. For the development of this model, a simplified case of a single pulse of light is considered first, and the impact of the second pulse is considered after. The probability distribution to be implemented in this work is the Poisson distribution. Here, the probability of witnessing an event (X) a given number of times (x) is calculated given an average occurrence rate (λ) and an observation time (t)

$$P(X = x) = \frac{(\lambda t)^x}{x!} e^{-\lambda t}$$
 [4.6]

The time between pulses gives the parameter t (there is some further complexity regarding this below) and λ is the flowrate of the particles. The parameter λ , with units of particles per second, is a function of the velocity. The velocity can be translated to a particle flux $(\hat{p}, \text{particles/mm}^2/\text{s})$ by multiplying by the number concentration of particles (C_{part} , particles/mm³)

$$\hat{p} = C_{part} u(y) \tag{4.7}$$

Then, by multiplying by the distance across photographed region (\overline{w}), this can be translated into a particle density function (particle/mm/s), where integrating the region under the curve would find the number of particles passing through a region per second, equivalent to λ (Figure 4.4b).

$$\lambda(y) = \bar{w} \int_{y_1}^{y_2} \hat{p}(y) \, dy$$
 [4.8]

The event of interest for capturing a particle (\mathcal{C}) on a given streamline (with depth y) with a single pulse is the probability of photographing at least one particle given a certain streamline. This is equal to one minus the probability of photographing no particles:

$$P(C|y) = P(X \ge 1) = 1 - P(X = 0) = 1 - e^{-\lambda(y)t}$$
 [4.9]

This can then be converted to a PDF through differentiation with respect to y

$$f(C|y) = \frac{d}{dy}P(C|y) = \frac{d}{dy}\left(1 - e^{-\lambda(y)t}\right) = t \,\lambda'(y) \,e^{-\lambda(y)t} \tag{4.10}$$

The derivative of λ with respect to y is

$$\lambda'(y) = \overline{w} \,\, \hat{p}(y) \tag{4.11}$$



For a specific value of y, the value of λ is zero as the region under the curve in Figure 4.4b is zero. Thus, the exponential term in Eq. 4.10 is equal to one. It should also be noted that since PDFs require normalisation, all constants can be factored into a normalisation parameter, η . Hence, the PDF becomes

$$f(C_1|y) = \eta u(y) \tag{4.12}$$

This represents the probability of capturing a particle given it is on a particular streamline with distance y from the centreline. The desired PDF is the opposite of this: the probability a particle is on a particular streamline (with a particular velocity) given that it has been captured with a single pulse $(f(y|C_1))$. For this conversion, Bayes' theorem is used

$$f(y|C_1) = f(C_1|y) \frac{f(y)}{f(C_1)}$$
 [4.13]

The probability density of capturing a particle $(f(C_1))$ is constant. It was assumed that the streamline taken by a particle was a random continuous variable. Hence, y is uniformly distributed and f(y) is equal to unity. The PDF of Eq. 4.13 becomes:

$$f(y|C_1) = \eta \, u = \eta \, (1 - y^2) \tag{4.14}$$

Thus, the probability of encountering a particle on a given streamline is proportional to its velocity, where a particle with twice the velocity will be encountered twice as often. A change of variable is required to convert from position to velocity. Using the appropriate theorem, the PDF can be converted:

$$f(u|C_1) = f(y|C_1) \cdot |y'(u)|$$
 [4.15]

$$y(u) = \sqrt{1 - u}$$
 [4.16]

$$y'(u) = -\frac{1}{2\sqrt{1-u}}$$
 [4.17]

$$f(u|\mathcal{C}_1) = \eta \frac{u}{\sqrt{1-u}} \tag{4.18}$$

The value of η can be computed by integrating with respect to u over the domain of 0 to 1 and setting this value equal to unity (the total probability). From this, η is found to be $\frac{3}{4}$. According to this equation, the probability of seeing a particle with a certain velocity increases faster than linearly with the velocity. This is expected since due to the parabolic flow profile, a greater proportion of particles travel at a higher velocity. While the probability of witnessing a particle on a certain streamline is proportional to its velocity, there are fewer streamlines with a low velocity and so the probability of recording a higher velocity is increased.

One further aspect must be considered. The PDF in Eq. 4.18 is the probability density that a particle that passes a certain point having a velocity of u and is captured with one light pulse. For a particle to be captured accurately in the experiment, an additional condition is required since two pulses of LED light occur. For a good capture, both pulses of light must occur when the particle is within the photographable region (event denoted C_2). Faster particles are more likely to have the pulses straddle the boundary of the photographed region and thus must be penalised.



If the length of the whole photographed region in the direction of travel for the particle is D, the peripheral distance (length of the region available to the particle where if the first pulse occurs, the second pulse will be in the photographed region, Figure 4.4c), d_p is:

$$d_p = D - u t ag{4.19}$$

The probability of the particle being in the photographed region for the second particle given it was for the first and has a velocity u $(C_2|(C \cap u))$ is proportional to d.

$$f(C_2|(C_1 \cap u)) = \eta_2 d_p = \eta_2 \left(1 - \frac{u}{u_m}\right)$$
 [4.20]

Here, u_m is the maximum particle velocity that could still result in both flashes occurring while the particle is in the photographed region and is equal to D/t. A particle travelling at a velocity of u_m would have a peripheral distance of zero and only be successfully captured if the first pulse of light occurred as the particle entered the region and the second occurred as it left (Figure 4.4c). It should be noted that despite the photographs themselves being rectangular, the actual region in focus is a circle. As such, the parameter D is a function of the perpendicular distance from the captured particles path to the path taken by a particle passing through the centre of the photographed region. Thus, u_m is found from the average length of the photographed regions, \overline{D} , which is the circle diameter multiplied by $\pi/4$.

The intersection between the PDFs of Eqs. 4.18 and 4.20 is computed, which can be derived using the threeevent intersection probability formula. It should be noted that C_2 is a subset of C_1 ($C_2 \cap C_1 = C_2$), and that $f(C_1)$ and $f(C_2)$ are constants that are factored into η .

$$f(u \cap C_1 \cap C_2) = f(u \cap C_2) = f(C_1) f(u | C_1) f(C_2 | (C_1 \cap u))$$
[4.21]

$$f(u|C_2) = \frac{f(u \cap C_2)}{f(C_2)} = \frac{f(C_1)}{f(C_2)} f(u|C_1) f(C_2|(C_1 \cap u))$$
 [4.22]

$$f(u|C_2) = \frac{f(C_1)}{f(C_2)} f(u|C_1) f(C_2|(C_1 \cap u))$$
 [4.23]

$$f(u|C_2) = \eta \frac{u}{\sqrt{1-u}} \left(1 - \frac{u}{u_m} \right)$$
 [4.24]

The derivation and final form of Eq. 4.24 reveals that there are three influences on the velocity PDF, captured in the three terms of the equation. The first term, simply u, is illustrative of the fact that particles that travel faster are photographed more often. The second term, $1/\sqrt{1-u}$ is representative of the parabolic flow profile associated with laminar flow. There are a greater proportion of streamlines that have faster flow rates, and thus it is more likely to see a particle on a faster streamline. The final term accounts for the fact that very fast flowing particles are more difficult to capture because of the higher risk that one of the two pulses will be outside of the photographed region. The parameter u_m is an upper bound on the velocity, as a particle travelling this speed could only be captured with one pulse as it barely enters the photographed region and the other pulse as it barely



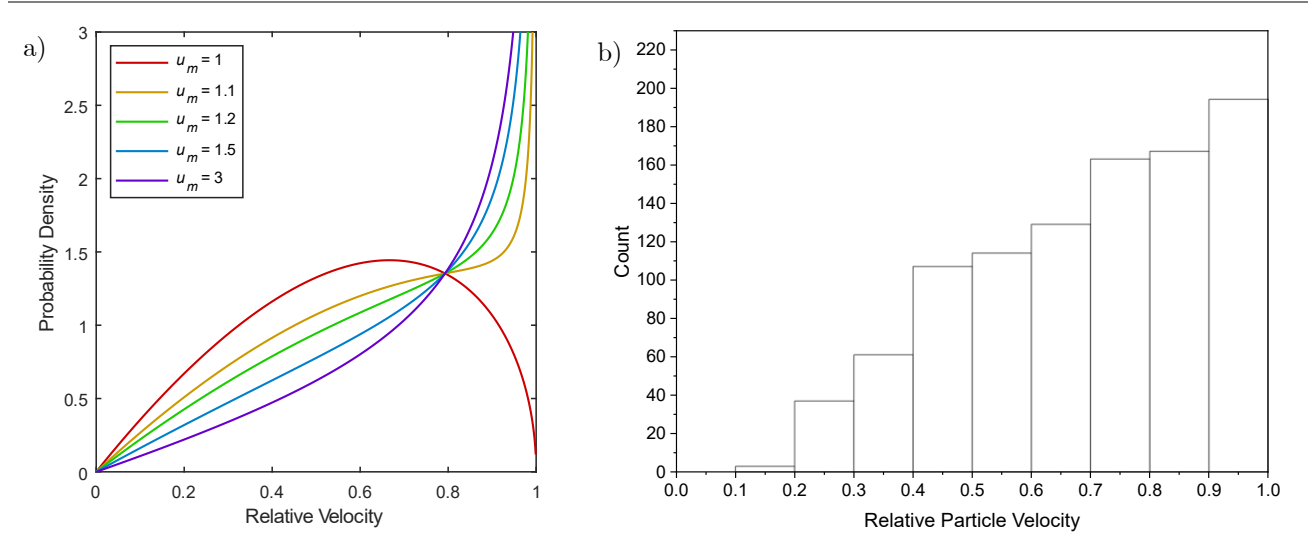


Figure 4.5: A histogram showing the distribution of the velocities of measured particles. Velocities are relative to the maximum velocity of a channel.

leaves. As with the dimensionless velocity, it is scaled relative to the maximum velocity in each channel and thus the minimum practical value is one.

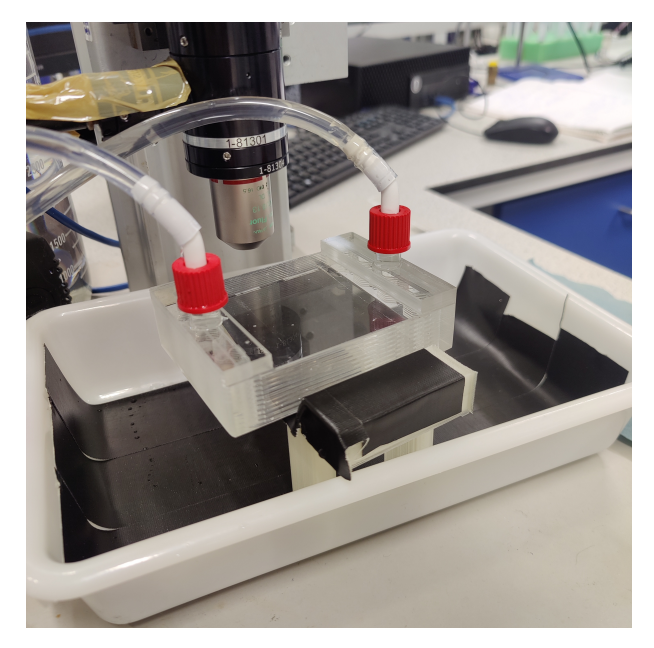
Figure 4.5a shows the dimensionless velocity PDF for a range of values of the maximum transit velocity parameter, u_m , from 1 to 3. Further changes to the shape of PDF above a u_m of 3 are negligible. In this figure, all PDFs have been scaled using the η parameter to ensure a total integrated area of unity. It can be seen that the probability density for all u_m blows up to infinity as the dimensionless velocity approaches one (i.e. the maximum velocity in the channel) except for $u_m = 1$. Mathematically, this arises from the $1/\sqrt{1-u}$ term and is not an issue as the bounded area (total probability) remains finite. It indicates that high velocity particles are significantly preferred as the PDF is localised around u being 1. However, as u_m is decreased, the probability of encountering very high velocity particles decreases in favour of lower velocity ones as the chances of a fast particle straddling the boundary of the photographed region increases.

The overall distribution of normalised particle velocities is shown in a histogram in Figure 4.5b. Here, as with the PDF, velocities on the x-axis are normalised relative to the maximum velocity seen in each channel to eliminate the effect maldistribution has. In the limit of infinitesimally thin bins and an infinite number of data points, a histogram approaches an empirical form of the PDF, and thus the two graphs in Figure 4.5 can be compared based on their shape. The experimental histogram does show a similar trend to the predicted PDF for a low value of u_m (~1.2). More particles of a higher velocity are captured, but the increase in the height of the bars decreases for faster particles. An up-tick in the height of the final bar is also seen, which is reflected in the calculated PDF. A notable caveat is that there are far fewer particles of a low velocity (< 0.4) relative to what is predicted. However, this is not unexpected due to the issues with those particles being out of focus and interacting with the channel wall.

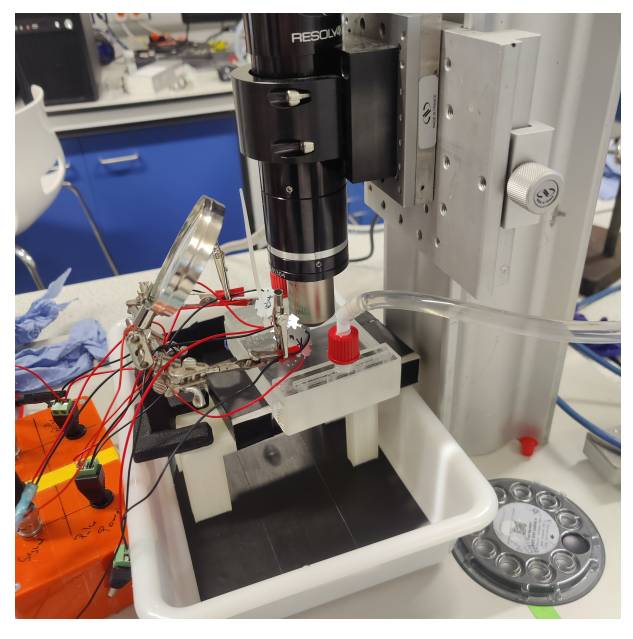
The expected value of u_m based on the actual size of the photographed region is ~1.8, slightly higher than the value of 1.2 seen in the closest matching PDF. Nevertheless, the trend observed demonstrates that the experimental methodology accurately captures the velocity distribution, and thus no bias is present.



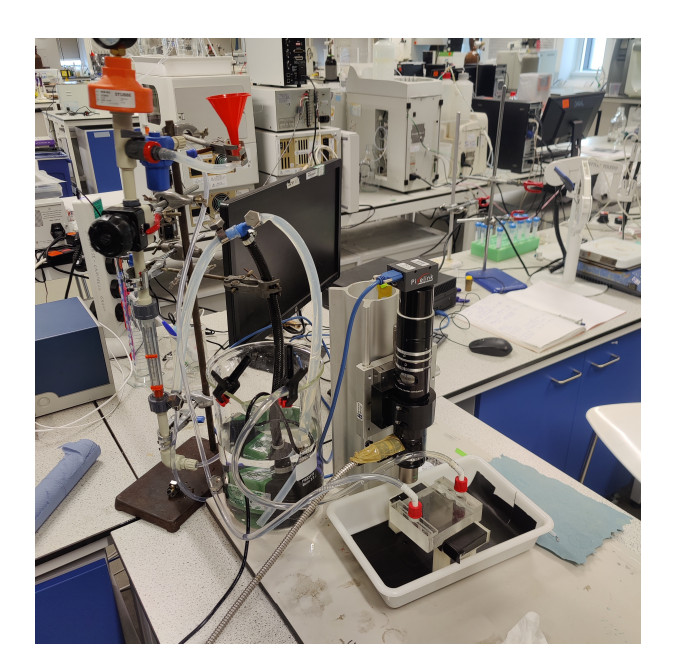
4.2.3 PIV experimental setup



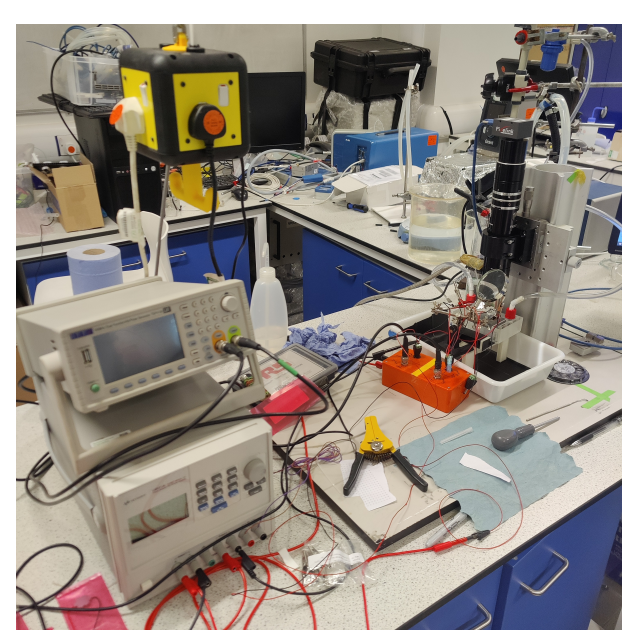
The glass flow cell positioned under the microscopic camera. Tubing connectors are also shown.



A setup showing the LED arrays held close to the glass flow cell. The orange box contains the circuitry for the solid-state relays for switching the LEDs on and off.



The pump, reservoir, flow meter and control valve are shown connected to the glass flow cell. A T-junction to allow for a flow bypass is present to prevent the pump from over-pressurising.



The two-channel signal generator and power supply are shown connected to the orange signal box.



4.3 Validation of the effect of maldistribution on the limiting current density

4.3.1 Method

4.3.1.1. Overview

The fundamental aim of the work presented in this section is to experimentally discern whether maldistribution in ED leads to a reduction in the LCD. One problem when devising an experiment to investigate this is that maldistribution itself cannot be directly influenced. Instead, the degree of maldistribution is a function of the geometric design and hydrodynamic environment of the ED stack, and so must be indirectly influenced by changing various experimental parameters. In previous work it was numerically established that maldistribution is affected by the geometry of the channel through the distributor angle, intermembrane distance, and length-to-width ratio. These are set by the geometry of the membrane spacer and are not simple to control precisely experimentally. Further, since they impact the degree of maldistribution through the channel pressure drop, quantifying the maldistribution of individual experiments is prohibitively difficult. Consequently, these geometric parameters were not changed in this study. However, the solution flow rate and number of cell pairs were also identified as key drivers of the degree of maldistribution. Controlling these accurately is much easier and thus are used in this study to affect the degree of maldistribution.

The number of cell pairs and volumetric flowrate were varied over a range where the expected difference in the degree of maldistribution is significant (m varies from 1 to 4.5). The average flow rate within one channel is varied over the range of 1-9 L/h for both a stack of ten and twenty cell pairs. It was vital to ensure that these changes would have no confounding effect on the LCD which is influenced primarily through the salt molar flowrate. To achieve this, when the number of cell pairs was increased from ten to twenty, the overall flow rate was doubled. This maintains the same average channel volumetric flow rate and thereby guarantees the same LCD if no maldistribution is present. However, a more complex approach is required when varying the flow rate. If no other variables were manipulated, increasing the flow rate would increase the LCD as the amount of salt removed in a single pass is reduced, and thus a higher current density is required to achieve ion depletion. To offset this, as the flow rate is increased, the salt concentration is reduced. This is done in such a way that it maintains a constant salt flow rate and thus should maintain a constant LCD if no maldistribution is present.

In summary, if no maldistribution exists, or if it has no impact on the LCD, then all experiments should show the same LCD. Conversely, since increasing the flow rate and the number of cell pairs have been shown to increase the degree of maldistribution, it is expected that the LCD should consequently decrease. The LCD was measured by gathering current-voltage response data and identifying the point at which the electric resistance significantly increased.



4.3.1.2. Experimental setup

All experiments were performed on the MEGA P EDR-Z/4x1_17 (MemBrain) electrodialysis unit with ED 64004 stack (PC Cell). Fuji-12 AEM and CEM membranes (Fujifilm) and spacers of width 1000 µm with the net cut out were used to comprise the membrane stack. This ensured that the conditions of the experiments were as similar as possible to the CFD simulations. Solution flow rates were controlled automatically using the unit's inbuilt pumps and control system, ensuring a constant volumetric flow rate was maintained. A sodium chloride solution was used, the concentration of which was varied with the solution flow rate. Experiments at the median flowrate of 4.5 L/h per cell pair used a salt concentration of 46.5 mol/m³, resulting in a salt flowrate of 0.21 mol/h per cell pair. This molar flow rate was constant throughout all experiments when the number of cell pairs or solution volumetric flow rate was changed so as to remove confounding effects on the LCD.

The flow configuration was setup to ensure a steady state operation (Figure 4.6a). Here, the outlet of the diluate stream was fed into the concentrate reservoir and *vice versa*. As such, the fluid travels in a loop through both the diluate and concentrate channels. Consequently, there is no overall change to either the diluate or concentrate concentration, and a steady state is established. Conductivity probes (Endress+Hauser) are present on the inlets and outlets of each stream and are monitored to establish when a steady state has been achieved.

The built-in power supply of the MEGA unit was used to control the voltage applied over the entire stack (V_{ap}) and measure the current (Figure 4.6b). Platinum probe electrodes were inserted into the end chambers either side of the stack, held against the end membranes and used to measure the potential drop across the membranes and channels only (V_{mem}) . This removed the confounding current-voltage behaviour of the electrode reactions and overpotential, making discerning the LCD much easier.

The experimental procedure is as follows. The solutions are loaded into the (cleaned) diluate and concentrate reservoirs and the pumps are activated. Once a desired steady flow rate has been achieved, the power supply is activated, and the applied voltage set to 3 V. This corresponds to a measured membrane voltage of ~0.5 V. Once

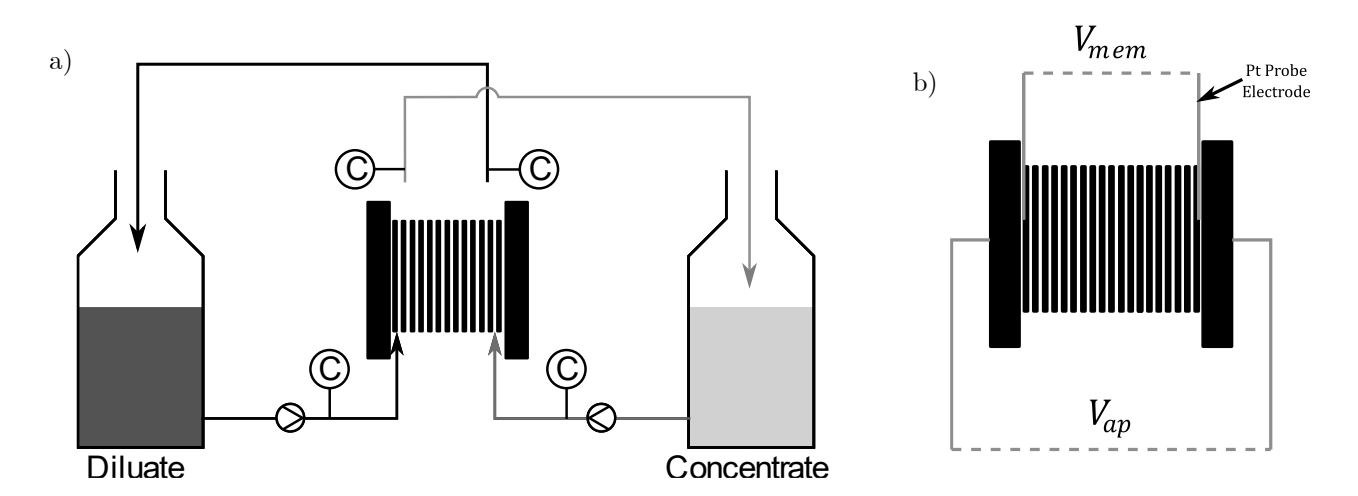


Figure 4.6: Experimental schematics. a) The stream configuration of the ED stack and reserviours. The diluate outlet stream is fed to the concentrate reserviour and *vice versa*. Pumps and conducivity measurement probes are shown also. b) The different voltages measured. The stack voltage is set by the power supply over the entire stack. The membrane voltage is measured by platinum probe electrodes inserted into the end chambers in contact with the end CEMs.



a steady state has been achieved, the power supply voltage, measured membrane voltage, and current are recorded, and the voltage increased by 0.5 V. This procedure is repeated for applied voltages up to ~30 V, or until a very clear over-limiting region is seen in the current-voltage response curve. After an experiment, the solutions are drained, and the reservoirs flushed with the next experiment's solution to remove any residual fluid.

To measure the LCD from the current-voltage response curve, the Isaacson and Sonin method [155] was employed. Linear regression was performed on the underlimiting and overlimiting regions of the current-voltage polarisation curve, and the LCD was calculated from the intersection of these lines.

4.3.2 Results and discussion

An example of the current-voltage polarisation curves used to find the LCD can be seen in Figure 4.7 where current density is plotted against both the stack voltage and membrane voltage. A clear decrease in gradient is seen in both data trends at a current density of about 60 A/m^2 , corresponding to the LCD. This decrease in the gradient is equivalent to an increase in the electrical resistance associated with achieving ion depletion. However, this change is seen much more clearly when current density is plotted against membrane voltage than against stack voltage. For a given current density, the difference between these two voltages is a summation of the electrode equilibrium potential, electrode overpotential, and the voltage drop across the end chamber. While the equilibrium potential is constant (1.2 V), the overpotential and end chamber voltage increase as a logarithmic (Tafel equation, $^{\sim}1$ V) and linear (Ohm's law, resistance = 0.01 Ω m²) function of the current density, respectively. The additional resistances associated with these potential drops reduces the proportional increase in the resistance when transitioning above the LCD, making the change in gradient more difficult to see. Further, while the current-membrane voltage curve intersects the origin, the current-stack voltage data does not. This is attributed to the

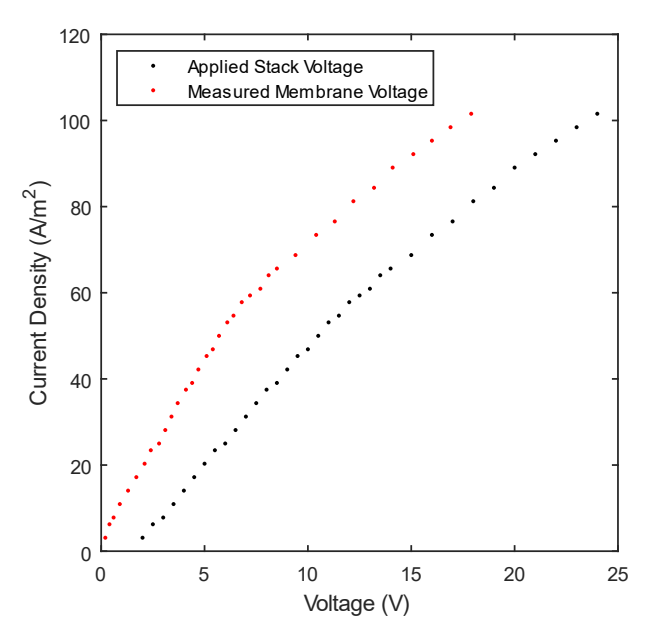


Figure 4.7: An example of a current-voltage plot used to discern the LCD. Shown are the current densities plotted against the membrane (measured) voltage and applied stack voltage, with a change in gradient indicating the LCD.



electrode equilibrium potential (~1.2 V) which must be exceeded for electrode reactions to occur and current to flow. This again makes linear regression less accurate making it harder to discern the LCD.

Consequently, plotting current density against stack voltage obfuscates the increase in resistance associated with operating above the LCD. As such, in this work it is the membrane voltage data that was used for linear regression and to discern the LCD.

The dimensionless maldistribution number, m, determined through simulation, for the different experimental conditions can be seen in Figure 4.8a. As expected, the value of m and the degree of maldistribution increases with a higher flow rate and a greater number of cell pairs. The measured LCD as a function of the flow rate for both the ten and twenty cell pair stacks can be seen as points in Figure 4.8b. If maldistribution did not affect the LCD, it would be expected that all points lie on a horizontal line at about 90 A/m². However, it is very clear that this is not what is seen in the experimental results. The LCD decreases as the flow rate increases for the experiments performed on both the ten and twenty cell-pair stacks. Since the molar flowrate of the salt was held constant, the only phenomenon which changes with flow rate is the degree of maldistribution. Since maldistribution is predicted to worsen at a higher flow rate, this is a clear qualitative validation of the impact of maldistribution on the LCD. However, the quantitative agreement between the predicted and measured LCD is limited. The predicted decrease in the LCD is somewhat higher than experimentally measured, although the magnitude of the measured and calculated LCD values is similar. This is probably due to the simplicity of the model used to calculate the LCD. The model considers only a bulk mixed region and linear concentration gradients within boundary layers adjacent to the membrane. The predicted LCD is very sensitive to the thickness of these boundary layers, which is computed using a Sherwood number correlation for plate flow. The validity of this correlation for the specific geometry used is unknown and so errors may be introduced here. Nevertheless, the

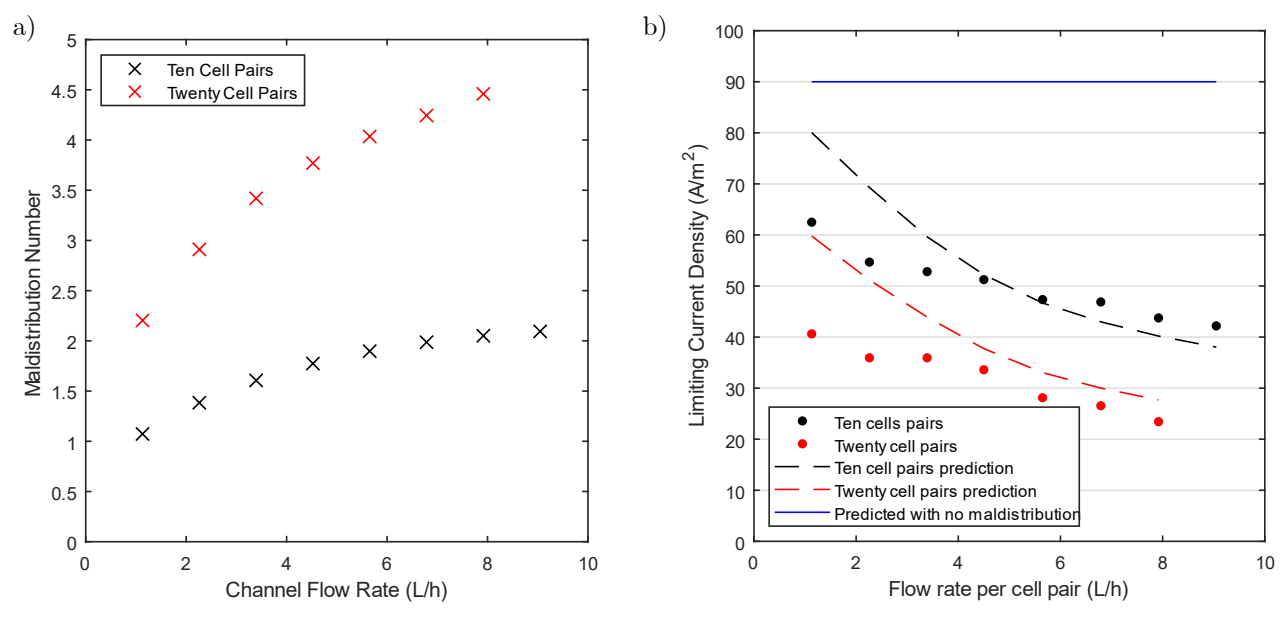


Figure 4.8: a) The calculated maldistribution number against average channel flow rate for a CFD simulated stack of both ten and twenty cell pairs. b) The experimentally determined and mathematically predicted limiting current density as a function of average channel flow rate for both a stack of ten and twenty cell pairs. If maldistribution does not impact the LCD, then a horizontal straight line is expected.



observed trend of a decrease in LCD with greater maldistribution from an increased flowrate is clear and validates previous work.

When changing the flowrate, there is an inherent source of error present arising from the method of reducing the salt concentration while increasing the flowrate to negate the effect on the LCD. The LCD is notoriously difficult to predict as there are many confounding phenomena which obfuscate the transport processes occurring at and above the limiting point. Therefore, it is possible that the impacts of increasing the flowrate and decreasing the concentration did not fully negate the confounding impact on the LCD, reducing the reliability of the results already mentioned. However, the difference between the results on ten and twenty cell pairs does not suffer from this uncertainty.

The LCD measured on the twenty cell-pair stack is consistently lower than that measured on the ten cell-pair stack for all flowrates. For two points on the graph at the same horizontal position, the experiments have the same average flow rate per cell pair and the same salt concentration. That is, the overall flowrate for the twenty cell-pair stack is twice that of the ten cell-pair stack, a variable that is trivial to control with the unit's built-in pump control schemes. Therefore, the number of cell pairs and the degree of maldistribution is the only distinction between the points. As such, the observed trend of a reduction in the LCD at an increased number of cell pairs is a very strong indication that the presence of maldistribution reduces the LCD. Further, the quantitative agreement between the model and experimental results is stronger, showing a very similar ratio of 1.3-1.5 for the LCD between the ten and twenty cell pair stacks.

One potentially confounding phenomenon from increasing the number of cell pairs comes from parasitic currents, also known as shunt currents [156]. Parasitic currents are current paths which bypass the membranes and flow through the distributors and manifolds instead. This reduces the apparent current efficiency, the ratio between the useful current which results in a transfer of salt from the diluate to the concentrate, and the total current measured. However, for lab-scale ED stacks, the major contributor to a non-ideal current efficiency comes from back-migration of salt from the concentrate to the diluate resulting from an imperfect membrane permselectivity. Nevertheless, it has been reported that an increasing number of cell pairs increases the amount of parasitic current as there are more conductive pathways for the current to take. A lower current efficiency from an increased parasitic current would result in an increase in the measured LCD. This is because the LCD is dependent on the concentration polarisation which results from the transmembrane current. Parasitic current increases the measured current without affecting the transmembrane current, and thus will increase the apparent LCD. This is the opposite of the expected effect from increasing the degree of maldistribution. Therefore, any parasitic currents would reduce the difference between the ten cell-pair and twenty cell-pair measured LCD, appearing to offset the effect of maldistribution. Since the difference between the ten and twenty cell pair measurements is stark, it is apparent that the effect of maldistribution is much greater than that of parasitic currents.



4.4 Conclusion

In this work, the presence and impact of maldistribution within electrodialysis are experimentally validated. Redblue particle image velocimetry was undertaken to investigate whether maldistribution exists within electrodialysis. These experiments were designed to confirm observations made in CFD simulations. Particles present in water flowing at 45 L/h through a flow cell with an internal geometry based on that of an ED stack simulated in CFD were imaged twice in a single exposure photograph with two sequential pulses of light (red and blue). The velocity of this particle was then determined by measuring the distance between the two differently coloured particle images and dividing by the time between the pulses. This procedure was repeated for all channels and in total over 1500 particles were imaged. A velocity distribution of each channel was effectively measured.

In the experimental results, the highest velocities measured in each channel (corresponding to the centreline velocities) demonstrated clear maldistribution. The velocities seen in channel one, closest to the inlet, were significantly higher than those seen in the ones further away, and higher than those expected from a uniform distribution. The opposite is true for channel ten, farthest from the inlet. However, the velocities seen were consistently lower than predicted, explained by a slightly wider flow-cell channel. After this was accounted for, experimental centreline velocities closely matched calculated ones. Further, the overall distribution of velocities did not significantly deviate from a statistical model that was derived based on the experimental procedure.

The effect of maldistribution on the LCD was evaluated by varying the number of cell pairs and the average flow rate per cell pair independently to manipulate the maldistribution and measuring the effect on the LCD. The confounding impact on the LCD when varying the flow rate was offset by changing the solution concentration to maintain a constant salt molar flow rate per cell pair. The LCD was measured by constructing current-voltage polarisation curves and applying linear regression to the under and over-limiting regions, identifying the LCD as the intersection between these lines.

It was found that increasing the maldistribution through increasing the flow rate leads to a significant reduction in the LCD. Furthermore, increasing the maldistribution by increasing the number of cell pairs also led to a reduction in the LCD. The only confounding factor when doubling the number of cell pairs was entirely offset by doubling the overall flow rate, which was precisely controlled by a pump and control feedback loop. Therefore, this is very strong evidence that a greater degree of maldistribution leads to a lower LCD. However, it was made clear that more advanced LCD models are required.

Together, these experiments successfully confirmed the presence of maldistribution within ED and its effect on the LCD. This validates previous work, demonstrating that the CFD simulations of maldistribution are accurate, and validating the analytical model of maldistribution within ED. Further, this work conclusively demonstrates that maldistribution in ED leads to a reduction in the LCD, in line with what was predicted numerically. As a result of this work, maldistribution is solidified as an important phenomenon in ED which requires further investigation with the focus of abatement and elimination.





Part II:

Modelling Electrodialysis

Chapter 5: A model of conventional ED

Chapter 6: A model of bipolar membrane ED

It was identified in Chapter 2 that models of ED vary widely in their formulation and that almost all lack appropriate experimental validation. In Part II, a model of ED is developed with the intention of overcoming many of the issues identified in the literature review. Two guiding philosophies of this model were that it should be flexible and avoid reliance on empirical fitting parameters and training data. This way, the model can be applied to a range of applications where additional features can be added as appropriate while remaining plausibly verisimilitudinous. In Chapter 5, the 'base' ED model is developed and experimentally tested. Notable advances include a novel transport number model and a membrane resistance model. Model performance was tested against experimental data in two orthogonal ways: Over a range of concentrations where the voltage was fixed and streams were recirculated in a batch system, and over a range of voltages where the inlet concentration was fixed. In Chapter 6, The base ED model is adapted to one for bipolar membrane electrodialysis. Additional resistive elements were added for the extra stream and membrane, along with considerations for the acid-base equilibrium. One notable addition is the consideration of neutralisation reactions within the membranes and their effect on 'freeing up' additional current. The same form of empirical model testing was conducted here as in Chapter 5.





Chapter 5

A Model of conventional ED

N.B.: this chapter has been adapted from the following published work:

Ledingham, J., Campbell, K.L.S., in 't Veen, B., Keyzer, L., Yip, N.Y. and Campbell, A.N., 2024. The development and validation of a novel, parameter-free, modelling strategy for electromembrane processes: Electrodialysis. Desalination, 576, p.117386.



5.1 Introduction

5.1.1 Background and motivation*

As global water scarcity worsens, it is becoming ever more imperative to conserve natural freshwater resources and unlock new sources [2]. Demand for water has increased by an order of magnitude in the last century due to a combination of rapid population growth and societal development [4]. Meanwhile, freshwater resources are rapidly declining due to the discharge of untreated sewage and industrial wastewater [9]. Without rectification, the world will face an estimated water deficit of 40% by 2030, likely worsened further by climate change [7]. Failure to correct this will result in environmental and humanitarian disasters in the form of ecological collapse and widespread famine. Reusing water in both municipal and industrial settings is key to water conservation, and brackish water and brine desalination are the most promising pathways to novel freshwater sources.

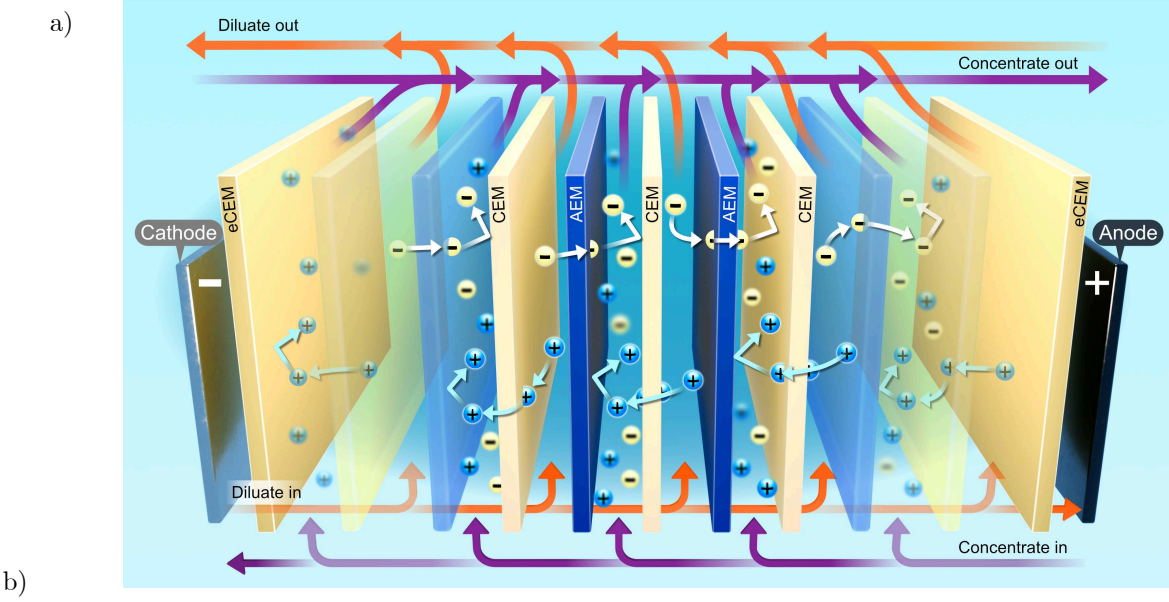
Electromembrane processes are uniquely positioned as effective and adaptable technologies for the treatment of aqueous ionic solutions [157]. In general, electromembrane processes use an electric field to drive the transport of ions between different streams through ion exchange membranes (IEMs). Membranes are typically either anion selective or cation selective and are layered in a repeating pattern with the solutions flowing between. One repeating unit is known as a 'cell' and when an arbitrary number of cells are placed between two electrodes, the engineering unit of a 'stack' is formed. The electrostatic interactions between the membrane fixed charges and free ions in solution greatly inhibits the transport of like-charged co-ions while promoting the migration of opposite-charged counterions. Anion exchange membranes (AEMs) contain positive fixed charge groups bound to a polymeric backbone which are typically quaternary amine groups. This gives the membrane an overall positive charge which theoretically only permits the transfer of anions. The positive charge of cation exchange membranes (CEMs) typically results from fixed sulfonate or carboxylate groups and thus are selective towards cations.

The quintessential electromembrane process is electrodialysis (ED) [18]. In ED, a unit cell is composed of one AEM and one CEM, with two separate solutions flowing between: a diluate and a concentrate. An electric field is imposed perpendicular to the flow by electrodes housed in end-compartments. These electrodes are washed by an electrode rinsing solution to carry away electrode reaction products and are separated from the rest of the stack by end cation exchange membranes (eCEM). The electric field drives ion transfer from the diluate channel, through the appropriate IEM and into the concentrate channel (Figure 5.1a). They are theoretically blocked from migrating further by the oppositely charged IEM bounding the other side of the channel. However, an imperfect permselectivity results in some of the ions migrating back to the diluate, wasting energy, and reducing the efficiency. Nevertheless, this process results in an overall transfer of salt from the diluate to the concentrate, effectively separating the salt from a process stream and recovering the separated salts in a second highly concentrated stream.

One of the greatest strengths of electromembrane technologies is the ability to change elements of the unit cell to adapt the functionality to different processes [32]. These modifications can be used to increase the

^{*} A comparison of the different electromembrane processes has been removed from this section as it is present in Chapter 1.





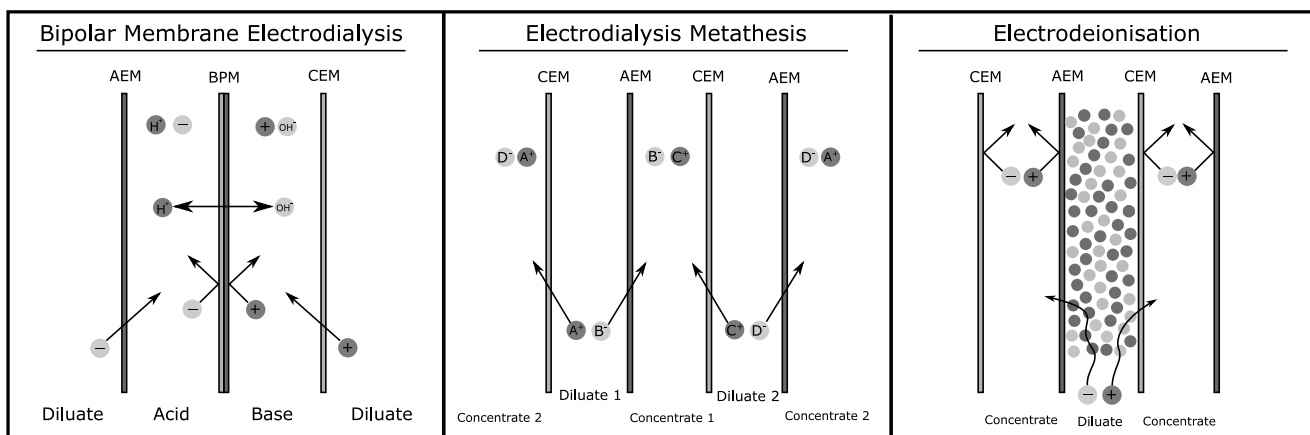


Figure 5.1 a) A schematic presentation of ideal transport pathways within ED. b) Schematic representations of other electromembrane processes. Positively charged entities are darker and negatively charged entities are lighter.

effectiveness of ED under different circumstances or to change the chemical environment of the streams. The main forms of electromembrane processes are outlined in Chapter 1, Section 1.5.

At present, reverse osmosis (RO) and nanofiltration (NF) dominate commercial membrane separations due to their maturity and reliability [21] and are a direct competitor to ED for desalination processes. However, there are many inherent advantages that all electromembrane processes, and especially ED, have over RO arising from their fundamental principles and design. A lot of inherent safety concerns are removed by operating ED at ambient pressure rather than the very high pressures required for RO and NF. Membrane fouling is much lower in ED because the salt is transported perpendicular to the direction of flow rather than in RO and NF where the membrane acts as a dead-end filter where foulants are brought to the membrane surface. A greater membrane lifespan, higher recovery ratio, and greater controllability result from the transfer of the minority species (the salt) instead of the majority species (the solvent). The tunability of electromembrane processes are a crucial benefit, where the transport rate is directly controlled by the applied voltage. This makes startup times very low, and process control much easier. Further, the unit size of ED may be reduced by operating at a higher voltage,



making it attractive when using expensive membranes or in locations where space comes at a premium. The similarity of electromembrane processes as well as its modularity allows for the reuse of components (membranes, electrodes, housings) for completely different applications.

Current research into electromembrane processes principally focuses on proof-of-concept studies for novel applications [151]. However, very few of these can be implemented at industrial scale due to uncertain performance at this scale and significant uncertainties around process economics. This is, in part, due to the lack of reliable and scalable models that can traverse scales from lab to industry. Therefore, to bridge this gap between the promising research and industrial implementation, process modelling and optimisation is vital. Furthermore, an accurate and general model of electromembrane processes would be able to indicate areas of most beneficial to technological advancement, helping to direct future research and provide a boon for industrial development. Hence, in this work a modelling strategy applicable to all electromembrane processes is presented. The desired model should capture macroscopic behaviour during both steady state and batch modes to model industrial processes as well as laboratory experiments. Further, no empirical fitting parameters are to be used to ensure that the model is valid over a wide range of process conditions. This will ensure that process modelling and optimisation over a range of conditions can be accurate.

Conventional ED is the most fundamental electromembrane process, and all others mentioned are built on its foundations. Consequently, a valid model of EDI, BPMED or EDM must be built on a phenomenologically robust and adaptable model of ED. As such, the model presented herein will focus directly on ED but be flexible enough to be expanded to any electromembrane process.

5.1.2 Modelling strategies for electrodialysis[†]

Modelling of ED, and all electromembrane processes, is especially challenging due to the multitude of concurrent phenomena at the macro, micro, and nano scale which all interact to affect the overall behaviour. A wide range of ED modelling is presented in existing literature, but, in general, all aim to translate the controlled input variables (inlet concentration and applied voltage) into a measurable outlet concentration (or concentration profile) and current density. Important process performance indicators such as the current efficiency and power consumption can then be obtained. Models of ED can broadly be divided into three categories:

1. **Nernst-Planck Models** [65,68,74,76,85–87]. Here, the Nernst-Planck equation is solved to generate a multi-dimensional concentration field by summing contributions to the overall flux from diffusion, convection, and electromigration[158]:

$$\boldsymbol{J}_{i} = D_{i} \boldsymbol{\nabla} C_{i} + \boldsymbol{u} C_{i} + \mu_{i} z_{i} C_{i} \boldsymbol{\nabla} \Phi$$
 [5.1]

$$\nabla \cdot \boldsymbol{J}_i = 0 \tag{5.2}$$

Here, J is the overall flux vector of component i, D_i is its diffusivity, C_i its concentration, μ_i its mobility, z_i its charge number, \boldsymbol{u} is the velocity vector, F is the Faraday constant, and $\boldsymbol{\Phi}$ is the electric potential.

[†] N.B. The ideas presented in this section are explored in greater depth in Chapter 2, however this section has been left here as it provides a useful summary and justification of the choices made in this chapter.



108

An additional charge condition is required for closure which either comes from assuming electroneutrality (the sum of all charges at a point, including that provided by the membrane, is zero) or implementing the Poisson equation [159]:

$$\sum_{i} z_{i} C_{i} = -\varepsilon_{r} \varepsilon_{0} \nabla^{2} \Phi$$
 [5.3]

where ε_r and ε_0 are the relative permittivity of the media and the permittivity of free space, respectively. Due to the multitude of coupled partial differential equations, these models are often solved using the finite element method or finite volume method in computational fluid dynamics (CFD) software such as COMSOL Multiphysics, Ansys Fluent, or OpenFOAM. These models can achieve high resolution on a small scale and thus are useful for investigating localised phenomena such as concentration polarisation and the effect of a space charge region [160]. However, the small-scale focus results in extrapolation to full-scale process modelling being inefficient, and thus is not appropriate for the desired modelling strategy.

- 2. Semi-empirical models [58,75,78,89,99,100] take a basis in ED mass transfer theory but simplify equations, only considering necessary variables and lumped empirical parameters. The parameters are then tuned to ensure model predictions fit existing experimental data. A subset of these models are irreversible thermodynamic models [161] which take their basis in thermodynamic relations rather than mass transfer. Semi-empirical models generally capture process behaviour well but require many experiments to be trained initially, and many more to ensure accuracy over a range of conditions. Semi-empirical models also lack globality, meaning models validated on experimental lab-scale systems will not be applicable at industrial scale. Further, the lumping of empirical parameters obfuscates the effect individual phenomena contribute to overall behaviour, limiting insight and inhibiting process improvement. Since a globally valid model is desired, semi-empirical models are not appropriate.
- 3. Equivalent Circuit models [64,66,67,69,71,73,77,80,82,83,90]: The transport of ions perpendicular to the direction of flow in an ED stack is analogous to electrons moving in a direct current circuit with solutions and membranes comprising resistive elements. Equivalent circuit models use fundamental theories such as Ohm's law and Faraday's first law to link the variables of ion flux, current density, electrical resistance, and voltage. These models are very flexible in terms of what phenomena they include as additional phenomena can be accounted for through contributions to the resistance and a modification to the material balance. As such, they vary widely in their formulation. Consequently, they are an effective compromise between the two aforementioned modelling methods. A high-level view of an ED system may be taken, while also accounting for essentially any small-scale phenomena deemed important. The most common variations in model aspects are:
 - Whether a fixed voltage or current is assumed
 - Whether a plug flow reactor (PFR) or continuous stirred tank reactor (CSTR) model is used for the channel material balance
 - Whether boundary layers adjacent to the membranes are included
 - Whether transport by diffusion is considered
 - Whether water transport is present
 - Whether electrode reactions and end compartment effects are considered,
 - How membrane selectivity is represented (perfect, fixed, or a transport number model)



Each of these phenomena introduces additional intermediate confounding variables to the model (Figure 5.2). Due to the complexity of the phenomena considered, most existing models in literature contain empirical parameters which are tuned to fit the model to experimental data. As such, there is an incentive to include as many phenomena and empirical parameters as possible as each addition increases the ability to achieve a good fit to experimental data. This is especially true given the confounding nature of the intermediate variables on the few output variables measured. For example, the rate of diffusion, rate of water transport and membrane selectivity are all solely impacted by the inlet concentration and impact only the outlet concentration. They are not impacted by the applied voltage, nor do they impact the current density. Their impacts are brought about through different intermediate variables which are not measured, and thus cannot be isolated in an empirically driven circuit-based model. This has the additional effect of converging the model onto a single specialised system, reducing globality and the insight that can be gained. Although this is not as problematic as for semi-empirical

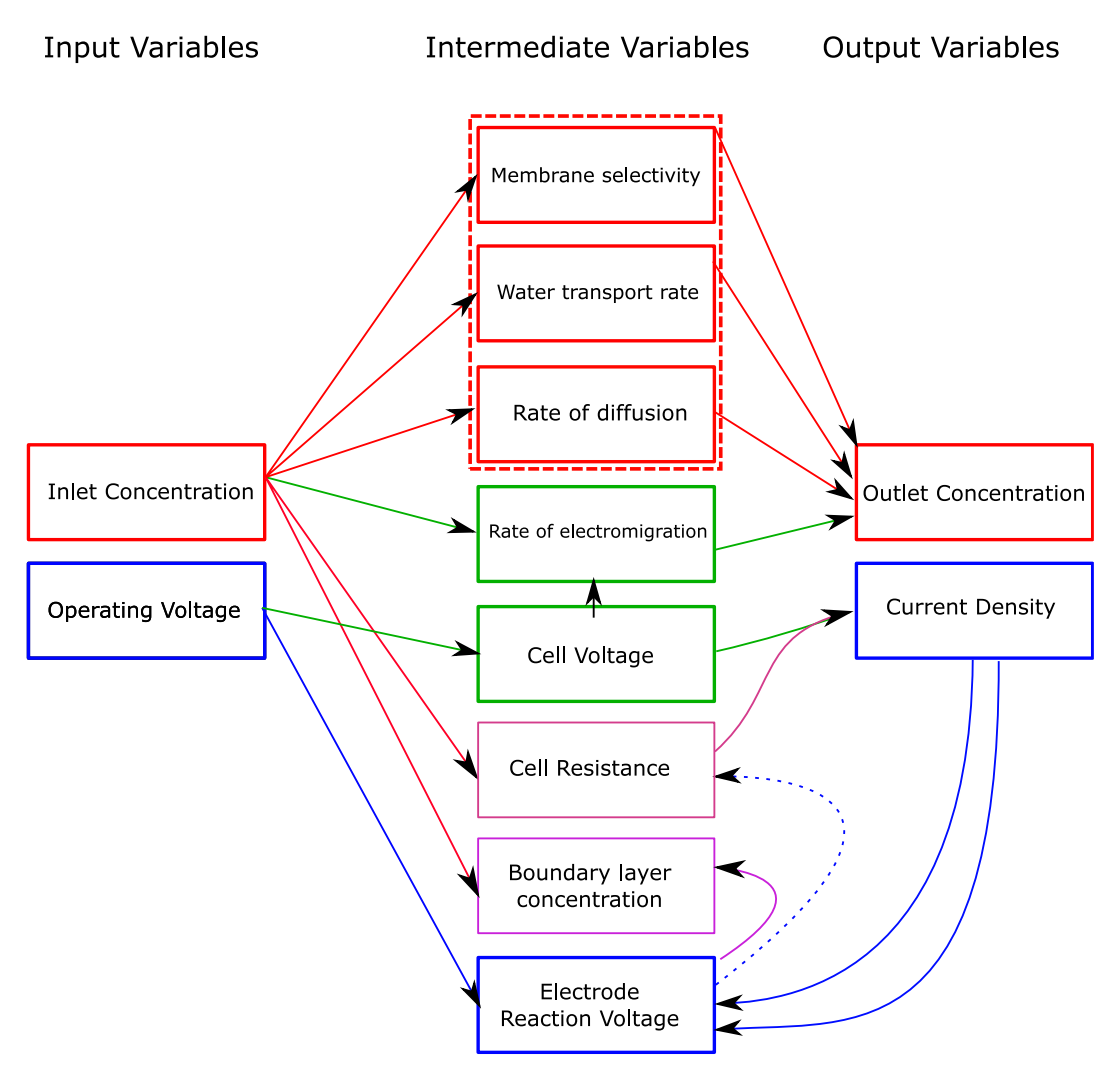


Figure 5.2: A flow diagram of common analogous circuit models of ED. The objective of these models is to compute output variables (which may be measured experimentally) from input variables (which are controlled) via intermediate variables which are not measured but represent key phenomena occurring within ED transport processes. The core ED variables are shown in green; the effect of inlet concentration is shown in red, and the effect of the operating voltage is shown in blue. Variables shown in purple are significantly impacted by both the inlet concentration and operating voltage.



models due to the stronger basis in physical laws, it still greatly limits the translation of models to other systems and full process scale. The only way to avoid this result without the direct measurement of intermediate variables (extremely challenging, if not presently impossible) is to ensure that there are no empirical parameters present in the model.

In circuit-based models, membranes are typically treated as a 'black box', where simplified empirical parameters are used to attempt to mathematically characterise the membrane. This is required due to the complexity of the myriad electrostatic interactions between all charged species within the membrane. For circuit-based models, these need to be simplified to a membrane selectivity and electrical resistance.

A circuit-based model presented by Wright, Shah, and Winter [80] avoids the use of empirical parameters and was validated against both laboratory and industrial scale batch systems. The agreement between the model and experimental data was initially excellent, but tended to diverge as a more extreme difference in concentration between the diluate and concentrate was encountered. One potential reason could be the assumption of perfect permselectivity. Manufacturer data provided a membrane transport numbers (selectivity) of over 90%, leading to the seemingly reasonable assumption of ideal permselectivity. However, over the course of the experiment, the concentration difference between the diluate and the concentrate grows, increasing the driving force on co-ions in the concentrate to migrate back to the diluate and reduce the current efficiency. Consequently, a more rigorous approach to defining membrane selectivity may be required to accurately capture ED behaviour over a wide range of concentration differences. As such, to improve model globality, a membrane transport number model will be implemented in this work.

The membrane electrical resistance is also typically treated as a fixed empirical parameter. Membranes make up approximately 25% of the cost of a small-scale ED unit [162] and make up a significant proportion of the cost at industrial scale [23]. There is an inherent trade-off between the membrane area required and specific power consumption of an ED stack as they are inversely proportional for a given overall salt transfer rate. Since cost is one of the greatest barriers to widespread ED commercialisation and membrane properties and performance vary widely, there is a great need for accurate representation of the membranes. Typically, literature models consider the membrane resistance to be fixed. The value is either provided by the membrane manufacturer, measured experimentally, or calculated from the fixed charge concentration. It is desirable to move away from this approach and towards integrating an advanced membrane resistance model such as the one presented by Fan et al. [163].

In this work, a novel equivalent circuit model of conventional ED is presented containing no empirical tuning parameters so as to minimise the inaccurate confounding of variables. This model can straightforwardly be validated against a laboratory scale ED unit and is directly applicable to full industrial scale for process design and optimisation. Notable novel aspects include a transport number model which considers trans-membrane concentration differences, and the adaptation of a membrane transport model which accounts for electrostatic interactions between fixed and mobile ions. Although derived principally for ED, this modelling strategy may be adapted to any electromembrane process, primarily by altering contributions to the electrical resistance and material balance.



5.2 Model development

5.2.1 Model overview

Laboratory experiments of ED (and other electromembrane processes) for proof-of-concept studies are almost exclusively conducted on recirculating batch systems (Figure 5.3b). Separate concentrate and diluate reservoirs hold solutions, the concentrations of which vary over time. Conversely, industrial applications of ED are continuous and operate in steady state. The modelling approach presented herein allows for the direct translation of experimentally validated batch model to a full continuous process model. To achieve this, the presented model consists of several layers, a flow diagram of which is presented in Figure 5.3c.

The inner-most layer is where the Tafel equation and Ohm's law are solved iteratively on a differential volume slice of a cell pair perpendicular to the direction of flow to compute a current density (Figure 5.3a). This is then passed to a middle layer and converted to an ion flux using Faraday's first law and a current efficiency model. It is in this layer that the electrical resistance of the differential volume is computed and passed to the inner layer. The ion flux is then integrated across the length of the flow path within the membrane stack in a spatial material balance to determine the outlet conditions. This is sufficient for modelling a continuous process, as the steady-state inlet concentration is fed as an initial condition, and the internal profiles of concentration and resistance, as well as the overall current density and power consumption are computed. However, for batch-mode operation, the inlet conditions are continuously changing. Therefore, an outer layer is present which, for each time step, passes an inlet concentration to the middle layer, returning an outlet concentration. A delayed differential temporal material balance is then used to compute how the reservoir and inlet concentrations vary with time while accounting for the dead time within the pipes.

In this model, it is assumed that water transport and ion diffusion are negligible. These transport phenomena are at least two orders of magnitude smaller than transport by electromigration under normal conditions, and only become important for a low applied voltage [54]. The channel material balance model is that of a PFR, with differential material balances solved along the internal flow path. Membrane boundary layers are not considered, as these require empirical models and are only impactful at high voltages and currents approaching the limiting current density (LCD) where this model is not valid. Electrode reactions and end chambers are considered for their contribution to the overall stack voltage. The model primarily considers stack voltage as a fixed input variable rather than the current, as this is what is controlled in typical ED experiments. This model was built and solved in MATLAB version R2022b. The flow of information within the layered approach allows for easy implementation in explicit programming solvers such as MATLAB and Python. However, an implicit solution approach in software such as COMSOL Multiphysics or gPROMS may be preferable. A reformulated model of balanced differential and algebraic equations is presented in Section 5.6.



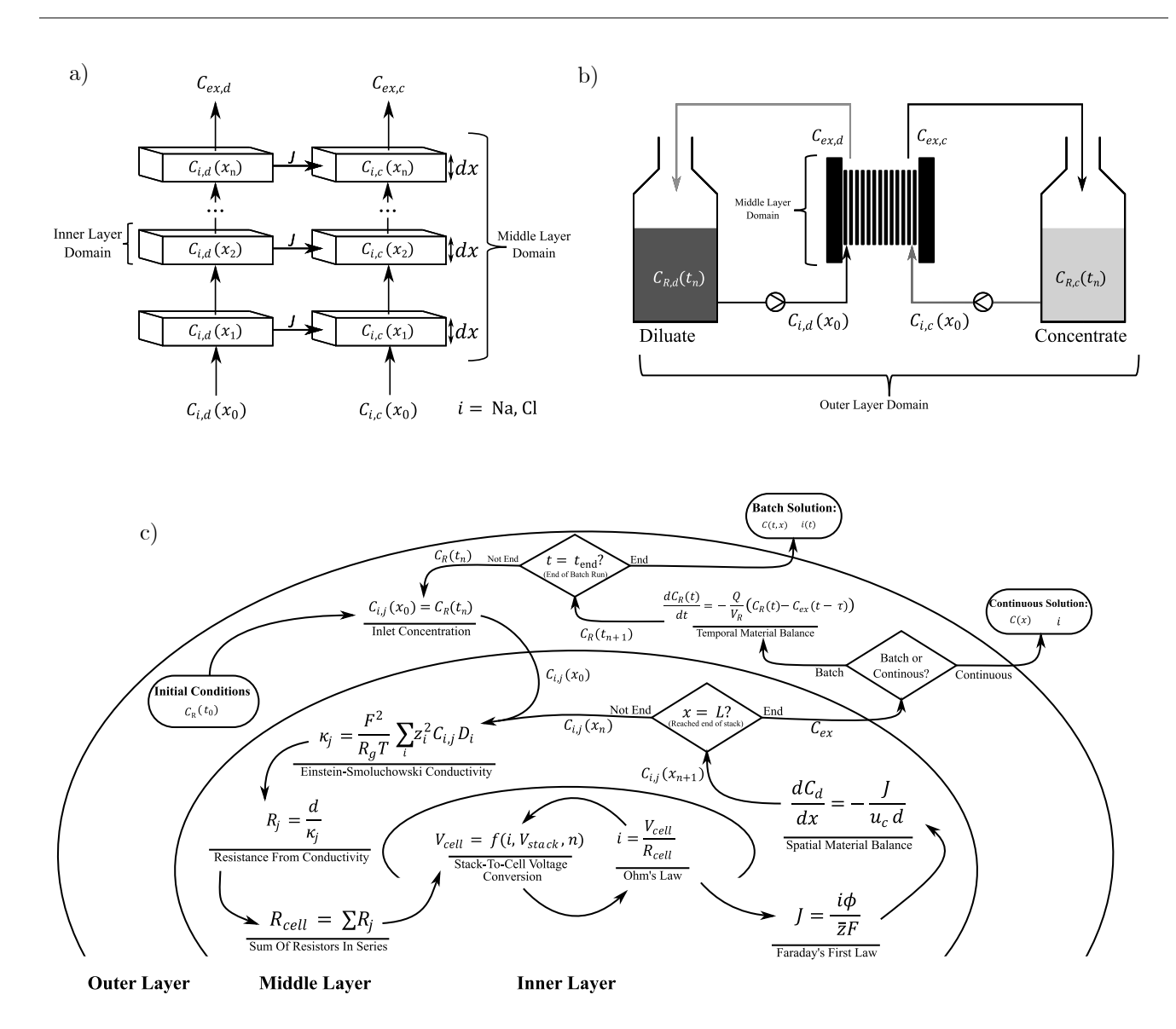


Figure 5.3: Schematic representations of various sections of the model. a) A diagram of the differential volumes over which the material balance is conducted (inner layer) and how they are related to find a concentration profile over the path length of the stack (middle layer). b) A schematic of a recirculating batch experiment. Solutions are contained within reservoirs and pumped in a loop though the ED stack and back to the reservoir. The middle layer and outer layer domains are also shown c) A flowchart representation of the overall layered equivalent circuit model. Arrows show the variables passed between different physical laws within the model. The adaptability of the model to both continuous and batch systems can also be seen through the decision point where the outer layer is engaged or not.

5.2.2 Inner layer: computing current density

In this layer, the cell resistance for the differential volume is passed as an input argument and the associated current density is returned. All other required parameters are unchanging. The current density (i) is computed from the resistance (R_{cell}) and voltage (V_{cell}) of a single repeating cell pair through Ohms law.

$$i = \frac{V_{cell}}{R_{cell}} \tag{5.4}$$



In order to calculate the voltage of a single cell from the voltage imposed over the whole stack, several potential drops beyond those over the cell pairs must be accounted for. These are the electrode reaction equilibrium potentials (V_{eq}) and overpotentials (η) , and the voltage drops over the electrolyte end chambers (V_{ec}) . The cell voltage is found by subtracting each of these potential drops from the stack voltage and dividing by the number of cell pairs (n)

$$V_{cell} = \frac{1}{n} \left(V_{stack} - V_{eq} - \eta - V_{ec} \right)$$
 [5.5]

The overpotential and end chamber potential drops are functions of the current density. The end chamber resistance is calculated using Ohm's law and a fixed end chamber resistance (R_{ec}) based on the unchanging concentration of the electrode washing solution.

$$V_{ec} = i \left(R_{anolyte} + R_{catholyte} + 2 R_{m,ec} \right)$$
 [5.6]

$$R_{anolyte} = R_{catholyte} = \frac{d_{ec}}{\kappa_{m.ec} C_{ec}}$$
 [5.7]

Here $R_{m,e}$ is the electrical resistance of the membrane separating the end chambers from the rest of the stack, d_{ec} is the perpendicular distance from the electrode to the end chamber membrane, $\kappa_{m,e}$ is the molar conductivity of the electrolyte, and C_e is the unchanging electrolyte concentration. The overpotential is computed using the Tafel equation [164]

$$\eta = A_a \log \left(\frac{i}{i_{0,a}}\right) + A_c \log \left(\frac{i}{i_{0,c}}\right)$$
 [5.8]

where A and i_0 are empirical parameters found in literature and are dependent on the electrode and electrolytic reactions occurring. The two terms correspond to the overpotentials and the anode and cathode and are summed to compute an overall overpotential. It can be seen in these equations that the overpotential is a function of the current density, but also that the current density is a function of the overpotential. Since only the former is a logarithmic function, this cannot be solved analytically and so must be iterated. The MATLAB function 'fzero' is used iterate over the equations and find a solution. Using this method, the current density for the infinitesimal slice across the stack can be computed and passed to the middle layer.

5.2.3 Middle layer: electrical resistance and spatial material balance

The middle layer has two primary functionalities: (i) compute the cell resistance to pass to the lower layer, and (ii) to convert the current density returned by the lower layer into an ion flux to be integrated in the spatial material balance.

5.2.3.1. Cell resistance

An analogous circuit method allows the cell resistance to be calculated by summing the resistances of an arbitrary number of constituents. In this model, four resistive elements are considered: the diluate (R_D) , the concentrate (R_C) , the AEM (R_{AEM}) , and the CEM (R_{CEM}) .



Electrolyte resistance

The electrolyte resistances of channel j (R_j) is computed from the conductivity of each channel (k_j) and the intermembrane distance (d)

$$R_j = \frac{d}{\kappa_i} \tag{5.9}$$

The solution conductivity is related to the concentration (C_i) , charge number (z_i) , and ion mobility (μ_i) of each species, i [158]

$$\kappa_j = F \sum_i |z_i| C_{i,j} \mu_i$$
 [5.10]

The ion mobility can be substituted out using the Einstein-Smoluchowski equation [165,166]

$$\mu_i = \frac{F}{R_g T} |z_i| D_i$$
 [5.11]

Consequently, an equation is found for the solution conductivity as a function of the ion concentration, charge number and diffusivity

$$\kappa_{j} = \frac{F^{2}}{R_{g}T} \sum_{i} z_{i}^{2} C_{i,j} D_{i,s}$$
 [5.12]

where F is the Faraday constant, R_g is the ideal gas constant, T is the operating temperature, and $D_{i,s}$ is the diffusivity of ion i in solution.

Membrane resistance

The resistance of the membranes is determined using a method developed by Fan *et al.* [163]. In this method, electrostatic interactions between all transported ions (both co-ions and counterions) and fixed charge groups are accounted for and an effective membrane ion diffusivity $(D_{i,m})$ is computed from the diffusivity in free solution.

$$D_{i,m} = D_{i,s} \left(\frac{f_w}{2 - f_w}\right)^2 exp(-Az_i^2)$$
 [5.13]

Here, f_w is the volume fraction of water in the membrane, and A is a collection of membrane parameters and physical constants, defined as follows

$$A = \frac{\theta e^4 N_A^{2/3}}{16 \pi^4 \varepsilon_R^2 k_P^2 T^2} C_{fix}^{2/3}$$
 [5.14]

where θ is a coefficient arising from the summation of infinite vectors (5.48 if fixed charges are assumed to be point charges, refer to the supporting information of [163] for more detail on this), e is the charge of an electron, N_A is the Avogadro constant, ε_m is the permittivity of the membrane matrix, k_B is the Boltzmann constant, and C_{fix} is the membrane fixed charge concentration. The membrane diffusivity can then be used to compute the conductivity (κ_m) of membrane m using the ion mobility and Einstein-Smoluchowski relationship, as in Eq. 5.12

$$\kappa_m = \frac{F^2}{RT} \sum_{i} z_i^2 C_{i,m} D_{i,m}$$
 [5.15]



To find the counterion and co-ion concentrations inside the membrane $(C_{i,m})$, the Donnan equilibrium equation is utilised with a charge balance to compute the concentration equilibrium present at the membrane-solution interface [167].

$$\prod_{i} C_{i,s}^{\nu_i} = \prod_{i} C_{i,m}^{\nu_i}$$
 [5.16]

$$\sum_{i} C_{i,s} z_{i} = \sum_{i} C_{i,m} z_{i} + z_{m} C_{fix}$$
 [5.17]

Here, v_i is the stoichiometric coefficient (number of ions contributed to the salt) of ion i, $C_{i,s}$ and $C_{i,m}$ are the ion concentrations in the solution and membrane, respectively, and z_m is the charge number of the membrane fixed charges (+1 for AEM, -1 for CEM). For two-component salts with a charge of unity (e.g., NaCl), this relation simplifies to the following

$$C_{ct,m} = 0.5 \left(C_{fix} + \sqrt{C_{fix}^2 + \frac{4C_s^2 \gamma_s^2}{\gamma_{an,m} \gamma_{ca,m}}} \right)$$
 [5.18]

$$C_{co,m} = C_{fix} - C_{ct,m}$$
 [5.19]

where the subscripts ct and co refer to counterions and co-ions, respectively, C_s is the total concentration of solution s, γ_s is the overall salt activity coefficient, and $\gamma_{ca,m}$ and $\gamma_{an,m}$ are the activity coefficients of individual anions and cations inside the membrane, respectively. Since the membrane is adjacent to both solutions, the concentration of an ion within the membrane would be different depending on which solution was considered for the equilibrium. One solution could be to take a simple average of the conductivities computed with either. However, this is not sufficient due to the reciprocal relationship between the conductivity and resistance. Instead, a linear concentration profile between the two membrane-solution interfaces is assumed, and the overall resistance of membrane m (R_m) is found through the integration of this profile. This approach essentially divides the membrane into an infinite number of resistors in series along its width and sums their contributions.

$$R_m = \int_0^{d_m} \frac{dy}{\kappa_m(y)}$$
 [5.20]

$$\kappa_m(0) = \kappa_{m1} \qquad \kappa_m(d_m) = \kappa_{m2} \tag{5.21}$$

$$\kappa_m(y) = \kappa_{m1} + (\kappa_{m2} - \kappa_{m1}) \frac{y}{d_m}$$
 [5.22]

$$R_m = \frac{d_m \ln\left(\frac{\kappa_{m2}}{\kappa_{m1}}\right)}{\kappa_{m2} - \kappa_{m1}}$$
 [5.23]

Here, κ_{m1} and κ_{m2} are the membrane conductivities at the membrane-solution interfaces on either side of the membrane and y is the distance coordinate through the membrane, ranging from zero to the membrane thickness, d_m . Finally, the cell resistance can be found by summing the membrane and electrolyte resistances and passed to the inner layer



$$R_{cell} = R_{AEM} + R_{CEM} + R_C + R_D ag{5.24}$$

It is here where the flexibility of the model to be applied to other electromembrane processes is demonstrated. Different electromembrane technologies can be deconstructed into their individual resistive elements which can then be calculated by sub-models and aggregated. For example, an electrodeionisation (EDI) model would have additional contributions to the resistance from the ion exchange resin within the channels. For BPMED, the resistance of the BPM and voltage drops from splitting water at the bipolar junction must be accounted for.

5.2.3.2. Spatial material balance

Once a current density is returned from the inner layer, a differential spatial material balance can be solved to compute a concentration profile. Faraday's first law is used to convert the current density passed from the inner layer into an overall ion flux (I).

$$J = \frac{i\phi}{\bar{z} F}$$
 [5.25]

Here, ϕ is the current efficiency and \bar{z} is half the sum of the charge magnitudes of the salt ions (e.g., 1 for NaCl, 2 for CaCl₂ and CaO, 6 for Al₂(SO₄)₃). This equation can be extended to allow for consideration of diffusion through the addition of a diffusive flux term (a simplified one would be: $D_m(C_C - C_D)/d_m$). However, the rate of diffusion is typically at least two orders of magnitude lower than the rate of electromigration for most ED applications and its impact is often exaggerated through confounding with back migration. Therefore, diffusion is neglected here.

The current efficiency, ϕ , is the ratio of useful current (resulting in salt transfer from the diluate to the concentrate) to the total current. As such, it accounts for the non-ideal permselectivity of membranes resulting in ions transported from the concentrate back to the diluate. The current efficiency is related to the transport number, \bar{t}_m of each membrane, which is defined as the ratio of the counterion equivalent flux to the total equivalent flux

$$\bar{t}_m = \frac{z_{ct} J_{ct}}{z_{ct} J_{ct} + z_{co} J_{co}}$$
 [5.26]

$$\phi = \bar{t}_{CEM} + \bar{t}_{AEM} - 1 \tag{5.27}$$

A value of \bar{t}_m of unity is representative of perfect permselectivity, whereas a value of 0.5 signifies no discrimination between co-ions and counterions. A value of less than 0.5 would indicate selectivity towards co-ions over counterions.

In ED, it is often assumed that transport numbers are constant (often unity) and not a function of the electrolytic environment. However, this is not realistic, especially for large trans-membrane concentration differences. Herein, a novel transport number model is presented.

Membrane manufacturers often provide an experimental value for the membrane transport number, measured when the trans-membrane concentrations are equal. This value is used in the model and will be considered the 'intrinsic' transport number, \bar{t}_0 , and has associated counterion and co-ion equivalent fluxes



$$\bar{t}_0 = \frac{|z_{ct}| J_{ct,0}}{|z_{ct}| J_{ct,0} + |z_{c0}| J_{co,0}}$$
 [5.28]

The migratory flux of ionic species $(J_{m,i})$ is proportional to the ion concentration, according to the Nernst-Planck equation (Eq. 5.1)

$$\boldsymbol{J}_{m,i} = z_i \, C_i \, \mu_i \, \boldsymbol{\nabla} \Phi \tag{5.29}$$

The diffusive flux across membranes for conventional ED is typically a few orders of magnitude below the migratory flux and is thus neglected. Convective flux is not applicable since current is not transported through this method and there is no fluid convection inside the membrane. From this, the ratio between the ion flux at an arbitrary concentration and when the transmembrane concentrations are equal is as follows

$$\frac{J_i}{J_{i,0}} = \frac{C_i}{C_{i,0}} \tag{5.30}$$

To yield the final model for the transport number of membrane j, equations 5.28 and 5.30 are substituted into Eq. 5.26 along with the fact that $C_{co,0}$ and $C_{ct,0}$ are equal (by definition) to find the final equation:

$$\frac{1}{\bar{t}_m} = 1 + \frac{|z_{co}| C_{co}}{|z_{ct}| C_{ct}} \left(\frac{1}{t_{0,m}} - 1\right)$$
 [5.31]

The current efficiency can then be found by aggregating the transport numbers through Eq. 5.27 and used in Eq. 5.25 to find the ion flux. For conventional ED, counterions are transported from the diluate and co-ions from the concentrate, and thus can be substituted appropriately. For a two-component salt such as NaCl, the final transport number equation becomes:

$$\frac{1}{\overline{t}_m} = 1 + \frac{C_c}{C_d} \left(\frac{1}{t_{0,m}} - 1 \right)$$
 [5.32]

As expected, when the concentrate (co-ion) concentration is much larger than the diluate (counterion) concentration $(C_c \gg C_d)$, the transport numbers approach zero. In this scenario, the current efficiency becomes negative one as essentially all current is carried by co-ions back-migrating to the diluate. Conversely, when $C_d \gg C_c$, the current efficiency approaches unity. In practice, the transport numbers would not be able to be reduced below 0.5, where the current efficiency would be zero and an equilibrium would be established where the fluxes of co-ions and counterions would be equal and no overall transport would take place.

After the current efficiency and ion flux are calculated, the concentration differential for the concentrate and diluate streams can be computed:

$$\frac{dC_c}{dx} = \frac{J}{u_c d} \tag{5.33}$$

$$\frac{dC_d}{dx} = -\frac{J}{u_c d} \tag{5.34}$$

where u_c is the flow velocity. Only one of these differential equations needs to be solved to find the concentration in one channel, as the other can be found from a material balance. Boundary conditions of the stack inlet



concentrations for both streams are passed by the outer layer of the numerical scheme, and integration generates concentration profiles along length of the stack. The function 'ode45' was used to solve the differential equation and compute spatial concentration profiles. Variables of interest such as the voltage over a single cell, current density, overall current efficiency, resistance, and power consumption were then extracted. This model may be directly used as a unit process model or in conjunction with full process simulations in software such as Aspen or gPROMS.

This material balance can be adapted to other electromembrane processes as is required. For BPMED, a series of differential equations is required, one material balance for each species in each channel. This is because there are now multiple different co-ions and counterions, and the current must be split between them. Therefore, accounting for the membrane selectivity between like-charged ions in Eq. 5.25 is necessary for BPMED and multi-component ED where it is not for conventional ED with only one salt. Reactions taking place in BPMED and EMR are captured through the material balance as well.

An implicit assumption of cell uniformity has been taken throughout this model, principally arising in equations 5.5, 5.30, and 5.33. However, due to the analogous circuit approach of this method, extension to account for inefficiencies such as maldistribution [151] can be accounted for. Cells may be treated individually when computing their resistance with different velocities assigned, and an overall stack resistance computed. This flexibility also allows for potential consideration of a very broad range of phenomena such concentration polarisation and space charge regions.

5.2.4 Outer layer: temporal material balance

Experimental validation of ED models almost exclusively occurs on recirculating batch units. In these systems, the stack voltage is typically held constant, and salt is transferred from the diluate to concentrate reservoirs. Over time, variables such as the stack inlet concentration, current density, and resistance will change in response to the salt transfer. As such, this model requires an additional temporal material balance as an outer layer to compute how these variables change. This aspect of the model translates the fundamental transport phenomena of the middle layer up to the level of a real batch process. It is not necessary to include this model section for modelling a steady state continuous unit but is essential for a recirculating batch process. This is because in the latter the stack inlet concentration changes over time and so the entire middle and inner layers must be re-solved for each time step.

For a given time, t, the outer layer passes a value of the diluate and concentrate inlet concentrations, C_{d0} and C_{co} , respectively, to the middle layer. For each stream, the outlet concentration (C_{ex}) is returned by the middle layer and used in the temporal material balance on the reservoir concentration (C_R) . It is assumed that the reservoirs are well mixed. If pipe dead-time is assumed to be negligible (and thus material transfer from the reservoir to the stack is instantaneous) the inlet concentrations are equal to reservoir concentrations and the temporal material balance for each reservoir is



$$\frac{dC_R}{dt} = -\frac{Q}{V_R}(C_R - C_{ex})$$
 [5.35]

where Q is the volumetric flow rate, and V_r is the reservoir volume. During ED experiments, measurements of pH and conductivity in flow cells are common. The additional dead-volume that tubing and flow cells contribute is often around 0.5 L. This is not negligible compared to the solution reservoirs which typically have a maximum volume of 2 L, and so the dead-time associated cannot be ignored. As such, a time-delayed differential equation is utilised for the temporal material balance. A time delay, τ , is defined as the time taken for a parcel of fluid to travel from the reservoir outlet and back to the reservoir. It is equal to the dead volume divided by the volumetric flow rate. What is essentially happening is that the flow leaving the reservoir is being replaced by the treated fluid which had left the reservoir a time τ in the past. Hence, the delayed differential temporal material balance is as follows.

$$\frac{dC_R(t)}{dt} = -\frac{Q}{V_R} \left(C_R(t) - C_{ex}(t - \tau) \right)$$
 [5.36]

Initial reservoir concentrations are provided as boundary conditions and the stack exit concentration is computed using the middle layer of the model. Using the MATLAB delayed differential equation solver dde23, temporal reservoir concentration profiles are generated. It should be noted that when comparing experimental data obtained at different positions in the flow circuit, their individual delays must be accounted for. For instance, the current measured at the stack in will not mathematically match with the concentrations present in the reservoir in real time due to the delay between flow exiting the reservoir and entering the stack. The same is true of conductivity measured in flow cells. This will create a mismatch in validation data sets unless it is accounted for, which can be done by shifting the time series experimental data to a standard time or adjusting predicted data to 'real time'. In this work, the latter was performed.

The current density varies along the internal pathlength, but only a single value is measured at a given time. To compute this 'overall' or 'stack' current density, a simple average of the spatially varying current density is sufficient. This is essentially equivalent to summing contributions from an infinite number of resistors in parallel, one for each differential volume. An extension can be added here to consider parasitic currents (also referred to as 'shunt currents') which bypass the membranes and pass through the solutions in the manifolds. This can be done by multiplying the stack current density by an additional efficiency term defined as the ratio of transmembrane current to total current (sum of trans-membrane current and parasitic current). A resistors-in-parallel approach with resistive elements for the membrane stack and parasitic pathways can be implemented to compute this efficiency [94,156]. However, parasitic currents are typically negligible in ED unless high salt concentrations are present, a scenario where an alternative process such as RO may be preferable. For that reason, parasitic currents are neglected for this model.



5.3 Model validation

5.3.1 Validation methods

The inclusion of novel aspects in this model and avoidance of fitting parameters demand experimental validation. All experiments were conducted on a PC BED 1-4 unit (PCCell GmbH) and a PC Cell stack (ED 64004) with ten cell pairs (AEM: PC Acid 60, CEM: PC MV, eCEM: PC MTE). The conductivity and pH of both streams were measured before and after the stack using JUMO CTI-500 inline conductivity probes and JUMO digiLine pH sensors, respectively. The pH has not directly been used in the model validation but was used to ensure that operation was consistently below the limiting current density, where this model would be valid. An SP-300 potentiostat (Biologic) was used to apply a stack voltage and record the current.

Two orthogonal methods were used for validation, both of which used sodium chloride due to its simplicity and prevalence in ED desalination applications. The first of these methods, temporal validation, is a typical recirculating-batch experiment. The initial concentrations of the diluate and concentrate reservoirs are chosen to be equal and the stack voltage is fixed well below the LCD. The solutions are circulated at a constant flow rate and reservoirs are jacketed to maintain a constant temperature.

The other form of validation involves measuring the current and solution conductivities at steady state over a range of voltages and comparing to model predictions. To achieve steady state, the outlet streams from the diluate and concentrate are mixed to 'undo' the separation performed inside the stack and split again before returning to the reservoirs. This ensures that the feed concentrations of both streams remain consistent throughout the experiment. The stack voltage is increased stepwise, holding constant until a steady current is achieved. This steady current and outlet concentration is recorded before the voltage is increased. The use of a potentiostat for these experiments ensures very high accuracy and control over the measured current and applied potential.

The two validation methods undertaken were chosen because they test the validity of the model over a range of concentrations and a range of voltages. These are the most common input variables of ED models and have a large impact on behaviour through confounding phenomena (Figure 5.2). Validity over a wide range of concentrations and voltages without the use of tuning parameters demonstrates that individual confounding phenomena are accurately captured. Membrane properties such as innate current efficiency, thickness, and ion exchange capacity were taken from manufacturer data. These can also be independently measured to guarantee accuracy.

5.3.2 Temporal experimental validation

Experimental settings and physical parameters for the temporal validation can be found in Table 5.1. The combination of 10 V stack voltage and 0.05 mol/L NaCl initial reservoir concentration ensured that the current density was below the LCD (independently measured to be ~1.5 A and 18 V) and upper detection limit of the potentiostat (2 A, 36 V). Experiments began with circulating the fluids and applying the potential at time zero.



Table 5.1: Experimental settings and system parameters used in the temporal validation.

| Parameter | Symbol | Value | Unit | Source |
|---------------------------------|-------------------------------|------------|---------------------------------------|------------------------------------|
| Applied Stack Voltage | V_{stack} | 10 | V | Measured/Set |
| Initial reservoir concentration | $C_R(0)$ | 0.05 | m mol/L | Measured/Set |
| Reservoir volume | V_R | 1.0 | L | Measured/Set |
| Intermembrane distance | d | 0.8 | mm | Stack Characteristic |
| Membrane area | A_m | 64 | $ m cm^2$ | Stack Characteristic |
| Recirculation flowrate | Q | 20 | ${ m L/h}$ | Measured/Set |
| Temperature | T | 297 | K | Measured/Set |
| Time delay | $	au_c$, $	au_d$ | 59.1, 47.6 | S | Measured/Set |
| Diffusivity | D_{Na}, D_{Cl} | 1.33, 2.03 | $\times 10^9 \mathrm{m}^2/\mathrm{s}$ | [168] |
| Membrane thickness | d_m | 0.1 | mm | Membrane data from manufacturer |
| Membrane water fraction | f_w | 0.22 | - | Membrane data from manufacturer |
| Fixed charge concentration | C_{fix} | 0.8 | m mol/L | Membrane data from manufacturer |
| Intrinsic transport number | $ar{t}_{0,cem},ar{t}_{0,aem}$ | 0.99, 0.96 | - | Membrane data from manufacturer |

Dead volumes were measured to be 0.41 L and 0.33 L for the concentrate and diluate, respectively. This weak measured by filling the fluid circuit with water and measuring the volume.

Experimental and modelling results can be seen in Figure 5.4a and Figure 5.4b for the solution conductivity and current density, respectively. As expected, over time the conductivity of the diluate decreases and the conductivity of the concentrate increases as salt is transferred from the diluate to the concentrate. It can also be seen that the inlet diluate conductivity is consistently higher than the outlet, showing that salt has been removed from the diluate when passing through the stack. The inlayed graph in Figure 5.4a shows the conductivities of the concentrate and diluate very early on in the experiment. Here, the outlet conductivity of the diluate decreases sharply, and before any change in the inlet diluate conductivity is seen. The sharp decrease to outlet diluate conductivity is seen soon after the voltage is activated, and the delay to the response in the inlet diluate conductivity is because of the time taken for the low conductivity solution to flow back to the reservoir, mix with the solution there, and flow out to the conductivity meter. The presence of these delays demonstrates how vital the use of a delayed differential material balance is for these batch ED systems.

The current density is initially high, decreasing over time with a sigmoidal behaviour (Figure 5.4b). The decrease in current density is expected due to the increase in the electrical resistance (~20X) while the voltage across a cell only increases slightly (~1.1X, Figure 5.4c). The electrical resistance of the solutions is what is primarily driving the increase in overall resistance (Figure 5.4d). Since the electrolyte resistance is inversely proportional to the salt concentration (equations 5.9 & 5.12), the minimum overall electrolyte resistance (diluate+concentrate) occurs when the two solutions have the same concentration. As salt is transferred from the diluate



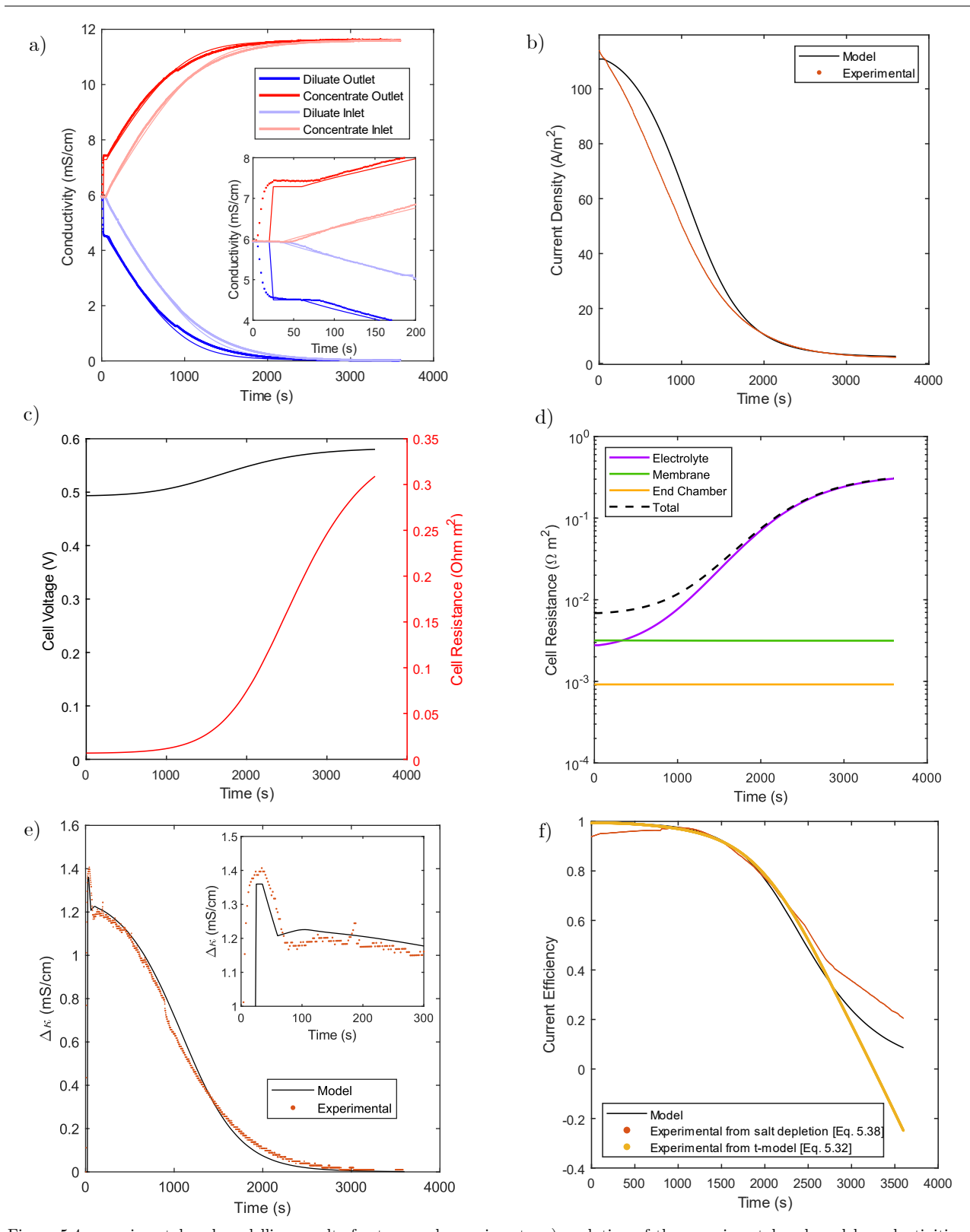


Figure 5.4: experimental and modelling results for temporal experiments. a) evolution of the experimental and model conductivities over time for the inlet and outlet of diluate and concentrate steams. Model predictions are solid lines and experimental data points are shown as crosses b) The current density evolution over time for both the experimental and model-predicted series. c) a graph showing the evolution of the calculated cell voltage and cell resistance over time. d) A graph showing the constituent electric resistances which comprise the overall stack resistance. It should be noted the y-axis is on a logarithmic scale. e) The time evolution of the difference in conductivity between the inlet and outlet of the diluate stream. f) The calculated current efficiency over the validation experiment, as well as the smoothed experimentally determined current efficiency calculated from both the rate of salt depletion and through the transport number model.



to the concentrate, the increase in resistance of the diluate is higher than the decrease in the resistance of the concentrate, increasing the overall electrolyte resistance. The slight increase in cell voltage can be explained through Eq. 5.5. The electrode overpotential is the only quantity that changes as it is a function of the current density. Since this is a logarithmic function (Eq. 5.8), the overpotential decreases by only 0.95 V despite the fall the current density by over an order of magnitude. This is then further offset by the fixed reaction equilibrium potential and end chamber potential drop, reducing the relative impact of the falling overpotential to only a 13% increase in cell voltage.

The difference between the diluate inlet and outlet conductivities can be seen in Figure 5.4e, with the inlayed graph showing the behaviour very early on. In both the model and experimental results, the conductivity difference spikes initially, remains constant for a short while, drops slightly, and then increases slowly, all in the first 60 seconds of the experiment. After this, the conductivity difference decreases over the rest of the experiment, ending in a very low value (0.0015 mS/cm). The initial erratic behaviour is a direct result of the delays incurred from the pipe dead time. The original spike occurs because the outlet conductivity falls long before a change in the inlet conductivity is seen. Since the inlet concentration is constant during this time, the outlet concentration is as well. Once the response is detected by the inlet conductivity probe, it takes time for this to be measured by the outlet probe, as they have a relative delay of about ten seconds between them. This is what causes the rest of the odd behaviour. Once again, this demonstrates the importance of the use of a delayed differential temporal material balance.

The current density can be seen to fall to a non-zero value (~3 A/m², 2.6% of the initial amount) as the solution conductivity falls to a very low value (0.01 mS/cm, 0.16% of the initial amount) and the single pass conductivity difference nearly vanishing (0.0014 mS/cm). This can be explained through having a low current efficiency, calculated to be ~20% (Figure 5.4f). At this point, only 20% of the current results in a net transfer of salt from the diluate to the concentrate. Approximately 40% of the current is used to transport salt from the concentrate back to the diluate, effectively cancelling out part of the 60% of current driving salt in the useful direction. The current efficiency decreases because the concentrate concentration increases far above that of the diluate, steepening the transmembrane electrochemical potential gradient and the driving force on co-ions in the concentrate. This clearly demonstrates the need for an accurate current efficiency model when large concentration differences are present. The intrinsic transport number provided by manufacturers is above 99%, which could, seemingly reasonably, lead to the assumption of perfect permselectivity. However, it is clear that this assumption becomes increasingly erroneous throughout the experiment.

The goodness of fit between model and experimental results was quantified using the average absolute difference (AAD) metric:

$$AAD = \frac{1}{N} \sum_{o=\text{observation}} |\chi_o - \bar{\chi}_o|$$
 [5.37]

Here, N is the total number of data points in an experiment, χ_o is a certain experimentally observed data point, and $\bar{\chi}_o$ is the associated model predicted observation. The AAD values of the experimentally measured quantities



are shown in Table 5.2 alongside the values of each variable at the beginning of the experiment. Excellent agreement between the experimental results and model can be seen, with all AAD values around two orders of magnitude below the initial variable values. These low difference values demonstrate the high accuracy of the model and is significant as no fitting parameters were utilised which would ensure a good fit.

The divergence of a temporal experiment from model predictions are expected to be much larger than with a single steady-state measurement. This is because small errors compound over time, feeding back between the concentration and current density. The greatest sources of error within the experiments stem from control of the volumetric flow rate and the total volume of fluid within each circuit. These are difficult to control accurately and have a large effect on the measured data. Despite best efforts to fix them precisely, it is likely that remaining errors stem principally from these parameters. Nevertheless, the close resemblance of the model and experimental results for all concentrations demonstrates that the model is valid over a range of concentrations and fluxes.

The novel transport number model presented in this work appears to accurately capture both the trend of the current efficiency and the phenomenon driving it. The current efficiency can be found directly from the single pass concentration difference for a stream (ΔC_i) and the current density through the following equation:

$$\phi = \frac{\Delta C_j \ Q_j \ F}{i \ A_m \ n} \tag{5.38}$$

Here, A_m is the area of one membrane. The equation expresses the ratio of useful current ($\Delta C Q/n F$) to total current ($i A_m$). This value can be calculated from experimental data and is shown in orange in Figure 5.4f. A similar trend between the model and experimental results is seen for this validation but diverge significantly at later times. It should be noted that the experimental data curves have undergone smoothing using a moving mean method. Towards later times, the solution conductivity approaches the detection limit of the probe, and so the uncertainty increases to over 100%. Consequently, the data towards the end of the experiment is unreliable. Nevertheless, the qualitative agreement for the current efficiency data and the excellent quantitative agreement for both the current density and conductivities demonstrates that the current efficiency is accurately captured in the model. However, this is not sufficient to fully validate the transport number model.

The underlying cause of the reduction in current efficiency was assumed to be the increase in the transmembrane concentration difference. The transport number model may be isolated and independently validated using the measured conductivities. Eq. 5.32 was used to calculate an experimental transport number for each

Table 5.2: Values of the average absolute difference (AAD) between experimental and model values for measured quantities, along with their initial values for temporal experiments

| Measured Variable | AAD | Initial Value | |
|--------------------|------------------------|-------------------------|--|
| Current Density | $2.563 \; { m A/m^2}$ | $111 \mathrm{\ A/m^2}$ | |
| Diluate Inlet | $0.051~\mathrm{mS/cm}$ | $5.95~\mathrm{mS/cm}$ | |
| Diluate Outlet | $0.105~\mathrm{mS/cm}$ | 5.95 mS/cm | |
| Concentrate Inlet | $0.055~\mathrm{mS/cm}$ | $5.95 \mathrm{\ mS/cm}$ | |
| Concentrate Outlet | $0.063~\mathrm{mS/cm}$ | $5.95~\mathrm{mS/cm}$ | |



membrane using the measured conductivities converted into concentrations. These transport numbers are then aggregated into a current efficiency through Eq. 5.27. The results of this are shown in yellow in Figure 5.4f. Excellent agreement is seen with the model for much of the experiment which breaks down towards the end as the uncertainty in the conductivity grows to over 50%. Overall, Figure 5.4f demonstrates that the transport number model accurately describes not just the effect on the current efficiency, but the underlying phenomenon as well. This is crucial because it shows that a simple model which uses only manufacturer data can be used to capture the current efficiency up to extreme concentration differences where the selectivity falls to very low levels.

5.3.3 Steady-state validation

Current-voltage curves are used prevalently in ED research to determine the limiting current density as well as the ohmic resistance of the stack. These values are essential for process modelling and used to compute the power consumption and membrane area which are vital for cost optimisation. For a given desired outlet concentration and flowrate, the power consumption per unit volume of treated water is proportional to the stack voltage. Conversely, the total membrane area is inversely proportional to the stack voltage. Therefore, an optimum voltage can be found through minimisation of the overall cost. As such, it is important that the model presented herein is valid over all voltages below the LCD.

Figure 5.5a shows the controlled voltage and measured current over time for the steady state experiments. After each step increase in voltage, the current experiences a step increase as well, before asymptotically decreasing to a new steady state value. The initial surge of current could potentially be caused by the transient thickening of the electric double layer or increasing concentration polarisation adjacent to the membrane. Additional current would flow to cause these effects which would dissipate over time. As the model presented is not designed to consider these transient migratory behaviours, only the steady state current is used for validation.

The inlet and outlet conductivities of the diluate and concentrate streams over time are shown in Figure 5.5b. The inlet concentrations for both the concentrate and diluate streams are constant throughout the experiment, demonstrating that a steady state was achieved using the experimental method described in Section 5.3.1. The outlet conductivities of the diluate and concentrate are seen to decrease and increase stepwise, respectively. These steps coincide with the step increases in the applied voltage and show a greater amount of salt is removed in a single pass when a higher voltage is applied, as is expected. After the end of the experiment, at ~3500 seconds, the outlet conductivities fall immediately back to being the same as the inlet conductivities, again demonstrating that an effective steady-state environment has been achieved.

The experimental and model current-voltage curves are shown in Figure 5.5c. For low voltages (0-1V), the current density is zero. This is because the applied voltage is lower than the equilibrium voltage (1.23 V), and without electrode reactions, no current can flow. Above this value, the current-voltage curve is near-linear. A linear relationship is characteristic of an unchanging electric resistance, the calculated values of which can be seen in Figure 5.5e. The electrolyte resistance is the only resistive element which changes with the applied voltage. It decreases because despite the inlet salt concentration being constant, a higher voltage results in a greater amount



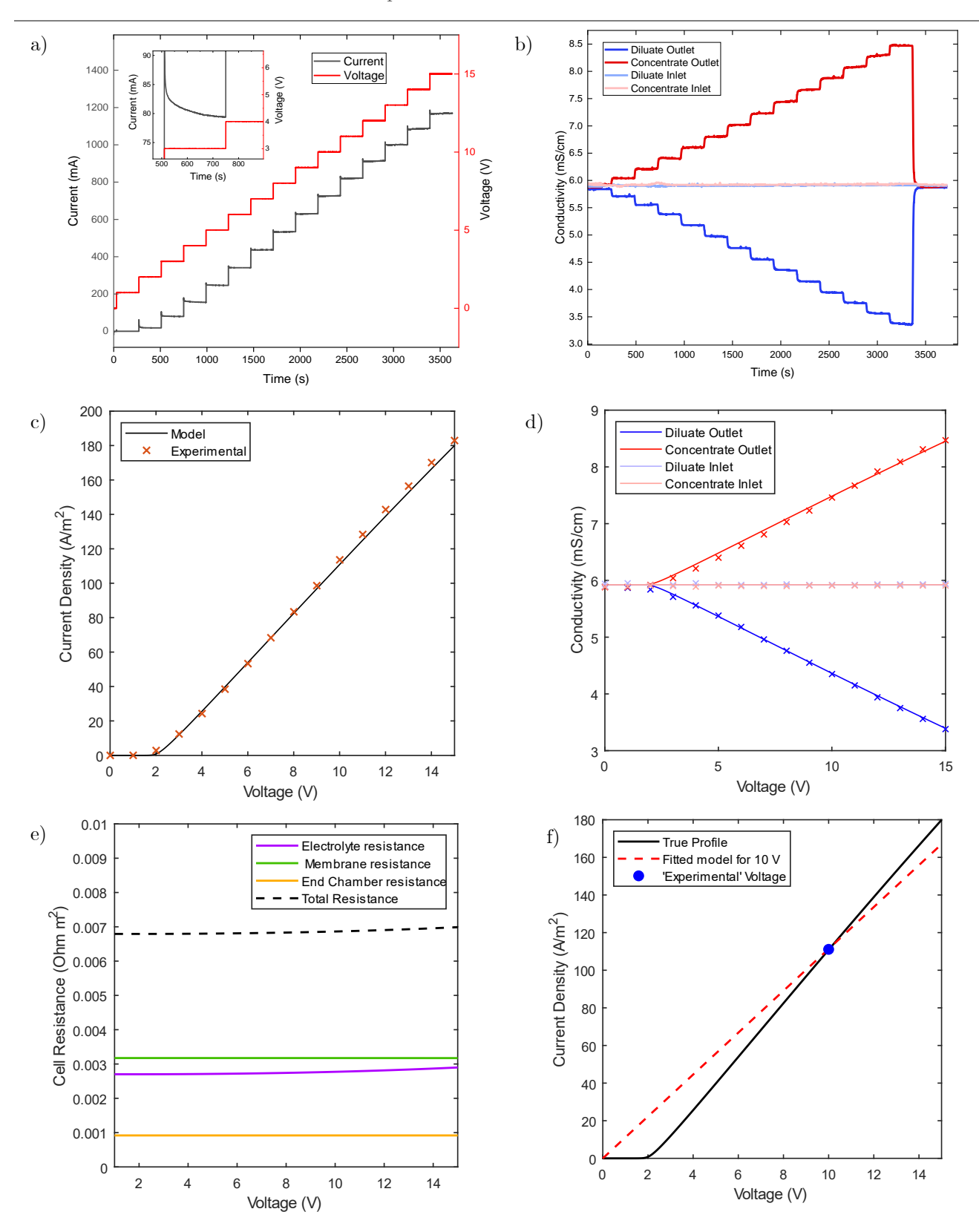


Figure 5.5: figures showing the results of the steady-state validation experiments. a) The temporal evolution of the applied voltage and measured current showing the step increases in voltage and the transient behaviour of the current. b) The temporal evolution of the inlet and outlet conductivities of the diluate and concentrate streams. c) The current voltage curve for both the experimentally measured data (crosses) and model prediction (line). d) The voltage-conductivity plot for experimentally measured data (crosses) and model predictions. e) Variation of the constituents of the resistance of a single cell with the applied voltage. f) A current voltage plot showing the 'true' modelled profile, and a generic model which excludes the overpotential and equilibrium potential, empirically fit to experimental data at 10 V.



of salt transferred from the diluate in a single pass. This decreases the concentration of the diluate and increases the concentration of the concentrate by the same amount. Since the resistance is inversely proportional to the salt concentration, the increase in the diluate resistance is larger, resulting in an overall increase in resistance. Nevertheless, the outlet diluate concentration only decreases by about 40% at the highest voltage and so the increase in resistance is very low. This effect is further reduced due to the other fixed contributors to the resistance and the fact that the electrolyte resistance is averaged over the entire path length inside the stack.

The model predicted and experimentally measured conductivities are seen in Figure 5.5d. As with the current density, there is no response for voltages below the equilibrium voltage. Above this, the diluate and concentrate decrease and increase linearly with voltage, respectively. At these concentrations, the current efficiency remains relatively constant at above 0.99. As such, over this voltage range the current density and inlet-outlet salt concentration difference is directly proportional (Eq. 5.38) and so the outlet conductivity trends are expected to be linear.

As with the temporal validation, the AAD was used to quantify the goodness of fit of the models (Table 5.3). Once again, excellent agreement is seen between the model and experimental results over the entire range of voltages, shown by AAD values two orders of magnitude below the range of experimental data. Consequently, it is shown that that the model accurately captures ED behaviour over a wide range of voltages. This is vital to ensure that the model is globally valid, and to ensure that ED voltage optimisation will be accurate. Further, it demonstrates that modelling the electrode reactions using the equilibrium potential and overpotential (using the Tafel equation) is necessary for global accuracy. A model without these potentials would only be able to capture a single temporal experiment using a resistance fitting parameter, and the equivalent current-voltage curve would be a straight line through the origin (Figure 5.5f). Although this method would suffice for one design at a single voltage, it is apparent that at all other voltages, the model would not be accurate. Optimising the voltage is a key aspect of the design of all electromembrane processes, and so accurately capturing the behaviour over a wide range of voltages is paramount.

The membrane resistance hardly increases over both time the temporal experiments (Figure 5.4f) and voltage in the steady-state experiments (Figure 5.5e). This is primarily due to the low range of concentrations that are present in the validation experiments, chosen to ensure that the current and voltage were well below the upper detection limits of the potentiostat (2 A, 30 V) and that the LCD was not reached. The low NaCl concentrations result in a high electrolyte resistance relative to the membrane resistance. The impact of the membrane resistance at a wider range of concentrations is evaluated in Section 5.4.

Table 5.3: Values of the average absolute difference between experimental and model values for steady-state experiments.

| Measured Variable | AAD | |
|--------------------|------------------------|--|
| Current Density | $1.956 \; { m A/m^2}$ | |
| Diluate Inlet | $0.020~\mathrm{mS/cm}$ | |
| Diluate Outlet | $0.024~\mathrm{mS/cm}$ | |
| Concentrate Inlet | $0.009~\mathrm{mS/cm}$ | |
| Concentrate Outlet | $0.045~\mathrm{mS/cm}$ | |



5.4 Exploration of novel model aspects

The model presented herein contains several novel aspects, most notably the membrane resistance model and transport number model. In this section, the impact of these two aspects is investigated for their impact on the modelling results.

The full details of the membrane resistance model can be found in a recent publication by Fan et al. [163]. Typically, fixed membrane electrical resistances are considered constant in ED models, but realistically it varies with the salt identity and its concentration in the concentrate and diluate streams. Membrane resistances are often provided by manufacturers, but these will be only valid for a certain salt and concentration (typically 1 M NaCl). Membrane resistance can be accurately measured experimentally through electrochemical impedance spectroscopy (EIS) using a potentiostat [169]. However, this will still only be valid at that experimental concentration. The method presented by Fan et al. (equations 5.11-5.17) allows the membrane resistance to be modelled as a function of the external solution identity and concentration. Furthermore, the membrane model has been validated for bivalent and trivalent ions, ensuring that the electromembrane modelling strategy presented herein has global applicability across a range of salts and concentrations.

Figure 5.6a shows how the membrane electrical resistance varies with NaCl solution concentration. The membrane resistance is relatively constant at very low solution concentrations, but decreases by an order of magnitude as the electrolyte concentration increases from zero to 2 mol/L. This is because at low concentrations, the internal membrane counterion concentration is almost equal to the membrane fixed charge density and the co-ion concentration is negligible. However, as the external solution concentration increases, the solution concentration inside the membrane pores increases, resulting in an increase of the conductivity (Eq. 5.15). As the external solution concentration approaches the range of the fixed charge density, co-ions become significant charge carriers, further reducing the resistance. This demonstrates why an advanced membrane resistance model which varies with electrolyte identity and concentration is important for model globality. The membrane resistance provided by the manufacturer (6 Ω cm²) intersects the curve at around 1 mol/L, which is likely to be the conditions at which the resistance was measured.

Membrane transport numbers are also provided by membrane manufacturers and are considered constant in most ED models. The transport numbers for each membrane in the model presented herein are a function of the transmembrane concentration difference (Eq. 5.32). Figure 5.6b shows how the transport numbers for each of the membranes varies with the transmembrane concentration ratio (concentrate to diluate), along with the intrinsic transport numbers and current efficiency. Transport numbers are equal to the intrinsic transport number when the concentration ratio is one (by definition). At concentration ratios lower than this, the transport numbers and current efficiency tend to unity as counterion transport dominates. At higher concentration ratios, the transport numbers decrease and asymptotically tend to zero. The current efficiency tends to negative one as co-ion transport dominates. The current efficiency is zero when the concentration ratio is about 42. This represents an equilibrium where the flux of counterions and co-ions are equal, resulting in no overall transfer between the concentrate and



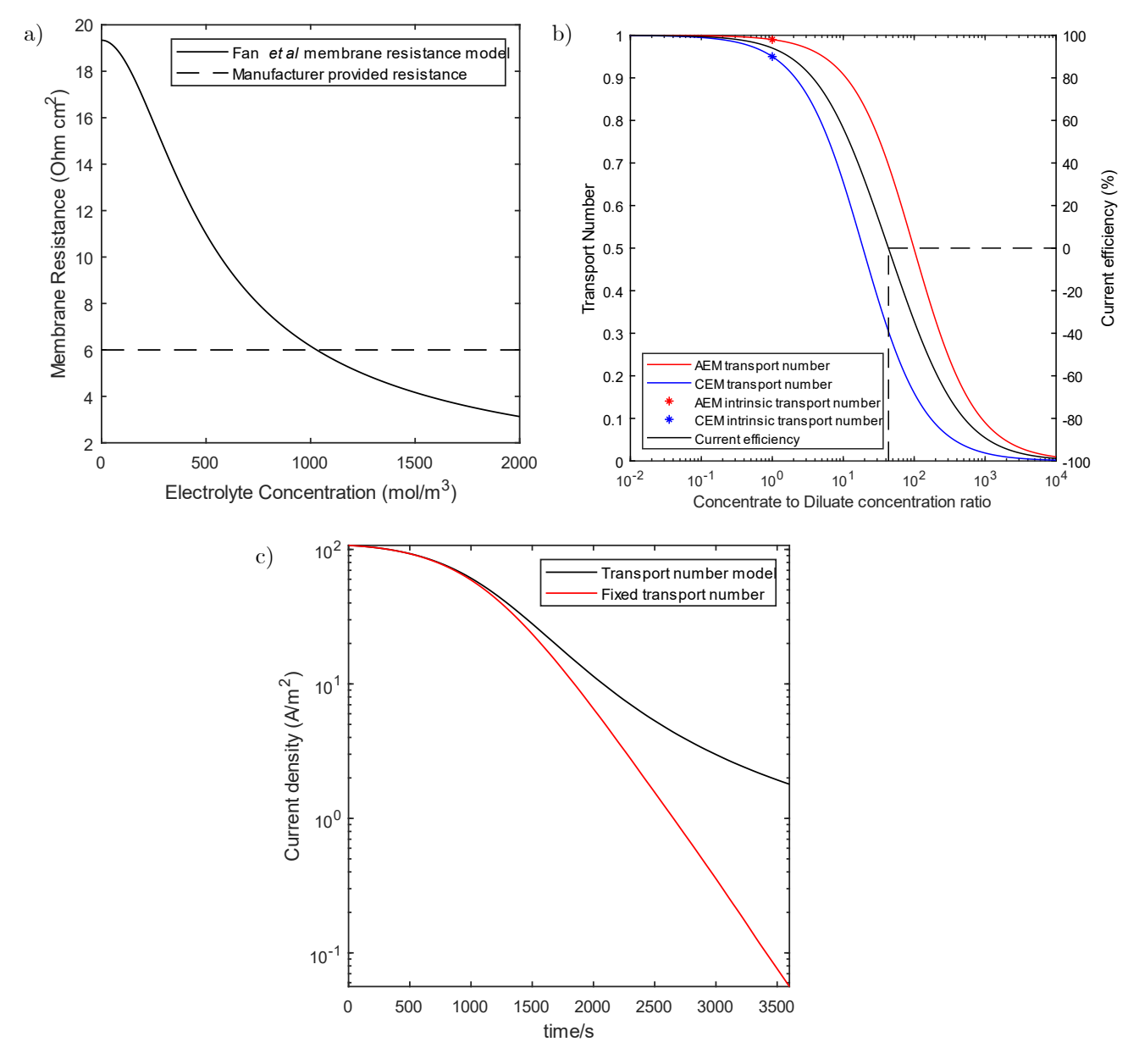


Figure 5.6: a) a graph of how the membrane resistance changes with the electrolyte concentration as well as the resistance provided by the membrane manufacturer. b) results of how the transport number model (left y-axis, equation 5.32) and current efficiency (right y-axis, equation 27) vary with the ratio of the concentration of the concentrate to the diluate. Also shown are the intrinsic transport numbers provided by the membrane manufacturer and the maximum separation ratio. c) time evolution of the calculated current density with a transport number fixed at the intrinsic value and the with a varying transport number

diluate. As such, this is the effective separation limit for the ED stack. It is dependent only on the intrinsic transport numbers of the membranes and can be calculated by the following equation.

$$\left(\frac{C_c}{C_d}\right)_{max} = \sqrt{\frac{1}{\left(\frac{1}{t_{0,aem}} - 1\right)\left(\frac{1}{t_{0,cem}} - 1\right)}}$$
[5.39]

which is derived by combining equations 5.32 and 5.27 and setting ϕ equal to zero. The importance of membrane selectivity on high degrees of separation is made apparent through this equation. Further, the maximum



concentration ratio serves as an important design parameter as it would instruct what degree of separation would be attainable.

Figure 5.6c shows a comparison of the temporal evolution of the current density when the transport numbers are fixed at the values provided by the membrane manufacturer and vary with the concentration as per Eq. 5.32. Initially, the current densities are very similar as the concentration ratio is close to one, and thus the transport numbers are close to their intrinsic values. However, the current density in the fixed transport number model drops to a very low value much faster than in the varied transport number model due to the much higher current efficiency when there is a large transmembrane concentration difference. The difference in these values at the end of the time series would result in an underprediction of the power consumption by a factor of 32 if fixed transport numbers were used. As with the membrane resistance model, this demonstrates how crucial a transport number model is for model globality over a range of concentrations.

5.5 Conclusion

A robust layered circuit-based model of conventional ED is presented herein, the fundamental strategies of which may be applied to a wide range of electromembrane processes. The innermost layer of the model uses Ohm's law to compute the current density within a differential volume tangent to the direction of flow for a given cell electrical resistance. This is passed to the middle layer which converts the current density into a flux through the Faraday constant and current efficiency, which is then integrated to generate a spatial concentration profile. At this point, key variables for process design and optimisation including outlet concentration, overall current density, and power consumption can be extracted. An outer layer utilises a time-delayed differential material balance to compute how reservoirs in a recirculating batch system vary over time while accounting for the pipe dead time, which can be significant in laboratory systems.

This model was validated on a standard recirculating batch experiment and through how the steady-state behaviour varies with applied voltage. Both methods showed excellent agreement between model results and experimental data, with values of the average absolute difference being two orders of magnitude below the range of values measured. This is noteworthy since no parameter fitting was conducted. Further, it demonstrates that the model is valid over a wide range of concentrations and voltages and has not been undermined by confounding phenomena.

To ensure model globality, a membrane resistance model and novel transport number model have been utilised. These were shown to have a significant impact on the model behaviour and were crucial to accurately capture ED behaviour over a wide range of salts and concentrations. The impact of the transport number model was found to be particularly strong when the diluate concentration is far lower than the concentrate concentration, as this leads to a very low current efficiency resulting from excessive back-migration. The membrane resistance model was found to be more impactful when the overall concentration varies over multiple orders of magnitude. Although the membrane resistance may not have a significant impact over a single batch experiment, it is important for extending the results to processes with different concentrations or different salts.



The modelling strategy presented is inherently flexible due to the presence of the multiple layers and analogy to an electrical circuit. As such, additional features can be added to the model with ease through modifications to the material balance and the consideration of auxiliary resistive elements. Examples of process units which can be modelled using this strategy include bipolar membrane electrodialysis, electrodialysis metathesis, electrodeionisation, and electromembrane reactors. Kinetic or equilibrium contributions to the material balance can account for any reactions present which is vital for BPMED. Membrane fouling can also be accounted for through an additional electrical resistance term. Concentration gradients within boundary layers can be considered using mass transport coefficients and Sherwood number correlations. This will be particularly impactful for low concentration ED and may be taken further to model behaviour of ED at or above the LCD by accounting for the potential drop over a space charge region and the mixing resulting from electroconvection. This is becoming ever more important as industrial operation of ED at overlimiting conditions is explored.

Membranes were characterised in the model through only their thickness, fixed charge concentration, and intrinsic transport number (when the transmembrane salt concentrations are equal). These are all fixed fundamental properties of a membrane which are either provided by membrane manufacturers or can be measured through simple experiments. Consequently, they will remain fixed as process conditions change and thus the models should be globally valid. As such, an ideal membrane may be chosen for a given application through optimisation using this model.

Fundamentally, this model was designed to contain no empirical parameters and be globally valid. Further, the model is applicable to both a recirculating batch system and a steady-state continuous process. As such, any model developed with this strategy may be validated on laboratory-scale batch system and then used in process modelling software for full scale design and optimisation. Therefore, this represents a powerful tool for both researchers and industrial electromembrane process designers.



5.6 Tabulated model[‡]

| Equation | Unknown variables | # Variables | # Equations |
|--|--|-------------|-------------|
| $\frac{\partial C_d}{\partial x} = -\frac{J}{u_c d}$ | $C_d(t,x),J$ | 2 | 1 |
| $\frac{\partial C_c}{\partial x} = \frac{J}{u_c d}$ | $C_c(t,x)$ | 1 | 1 |
| $J = \frac{i\phi}{\bar{z} F}$ | i,ϕ | 2 | 1 |
| $\phi = \bar{t}_{CEM} + \bar{t}_{AEM} - 1$ | $ar{t}_{CEM},ar{t}_{AEM}$ | 2 | 1 |
| $\frac{1}{\overline{t}_m} = 1 + \frac{z_{co} C_c}{z_{ct} C_d} \left(\frac{1}{t_{0,m}} - 1 \right)$ | - | | 2 |
| $i = \frac{V_{cell}}{R_{cell}}$ | V_{cell} , R_{cell} | 2 | 1 |
| $V_{cell} = \frac{1}{n} (V_{stack} - V_{eq} - \eta - V_{ec})$ | η , V_{ec} | 2 | 1 |
| $\eta = A_a \log \left(\frac{i}{i_{0,a}} \right) + A_c \log \left(\frac{i}{i_{0,c}} \right)$ | - | | 1 |
| $V_{ec} = i \left(R_{anolyte} + R_{catholyte} + 2 R_{m,ec} \right)$ | $R_{anolyte}, R_{catholyte}$ | 2 | 1 |
| $R_{anolyte} = R_{catholyte} = \frac{d_{ec}}{\kappa_{m,ec} C_{ec}}$ | | | 2 |
| $R_{cell} = R_{AEM} + R_{CEM} + R_c + R_d$ | $R_{AEM}, R_{CEM}, R_c, R_d$ | 4 | 1 |
| $R_j = \frac{d}{\kappa_j}$ | κ_c, κ_d | 2 | 2 |
| $\kappa_j = \frac{F^2}{R_g T} \sum_i z_i^2 C_j D_{i,s}$ | | | 2 |
| $R_{m} = \frac{d_{m} \ln \left(\frac{\kappa_{m,c}}{\kappa_{m,d}}\right)}{\kappa_{m,c} - \kappa_{m,d}}$ | $\kappa_{CEM,d}, \kappa_{CEM,c}, \ \kappa_{AEM,d}, \kappa_{AEM,c}$ | 4 | 2 |
| $\kappa_{m,j} = \frac{F^2}{RT} \sum_{i} z_i^2 C_{i,m,j} D_{i,m}$ | $\mathcal{C}_{i,m,j}$ | 8 | 4 |
| $D_{i,m} = D_{i,s} \left(\frac{f_w}{2 - f_w}\right)^2 exp(-Az_i^2)$ | $A, D_{i,m}$ | 5 | 4 |
| $A = \frac{\theta e^4 N_A^{2/3}}{16 \pi^4 \varepsilon_m^2 k_B^2 T^2} C_{fix}^{2/3}$ | | | 1 |
| $\prod_i C_j^{\nu_i} = \prod_i C_{i,m,j}^{\nu_i}$ | | | 4 |
| $\sum_{i} C_{j} z_{i} = \sum_{i} C_{i,m,j} z_{i} + z_{m} C_{fix}$ | | | 4 |
| $\frac{dC_{R,j}(t)}{dt} = -\frac{Q}{V_R} \Big(C_{R,j}(t) - C_d(L,t-\tau) \Big)$ | $C_{R,c}(t), C_{R,d}(t)$ | 2 | 2 |
| | Total | 38 | 38 |

 $^{^{\}ddagger}$ This section has been taken from the electronic supplementary information of the publication mentioned at the beginning of this chapter



| Initial Conditions | Number of Conditions |
|------------------------------|----------------------|
| $C_{R,j}(t=0)=C_{R,j,0}$ | 2 |
| $C_j(t, x = 0) = C_{R,j}(t)$ | 2 |

5.7 Nomenclature

| Latin Symbol | Meaning |
|---------------------|--|
| AAD | Average absolute difference |
| A | Membrane physical parameter collection |
| A_a A_c | Tafel slope parameters |
| A_m | Area of one membrane |
| С | Concentration |
| C_{fix} | Membrane fixed charge concentration |
| d | distance |
| D | Diffusivity |
| е | Elementary charge |
| F | Faraday Constant |
| f_w | Membrane water volume fraction |
| i | Current density |
| $i_{0,a}$ $i_{0,c}$ | Tafel exchange current density parameter |
| J | Ion flux |
| k_B | Boltzmann's constant |
| n | Number of repeating cells |
| N | Total number of experimental data points |
| N_A | Avogadro's constant |
| Q | Volumetric flow rate |
| R | Electric resistance |
| R_g | Gas constant |
| t | Time |
| Ē | Transport number |
| u | Velocity |
| u_c | Channel velocity |
| V_{cell} | Cell Voltage |
| V_{ec} | End Chamber voltage drop |
| V_{eq} | Equilibrium Voltage |
| V_{stack} | Stack Voltage |
| x | Spatial coordinate |
| у | Distance coordinate through the membrane |
| Z | Ion charge number |



| Greek Symbol | |
|-----------------|---|
| ε_0 | Permittivity of free space |
| ε_r | Relative permittivity |
| Ф | Electric potential |
| γ | Activity coefficient |
| η | Overpotential |
| θ | Coefficient of the summation of infinite vectors |
| κ | Conductivity |
| μ | Ion mobility |
| ν | Ion stoichiometry |
| τ | Time delay |
| φ | Current efficiency |
| χ | Experimentally measured data point |
| $\bar{\chi}$ | Model predicted data point |
| | |
| Subscript | |
| 0 | Referring to conditions when the concentrate and diluate are of equal concentration |
| AEM | Anion exchange membrane |
| С | Concentrate |
| an | Anion |
| ca | Cation |
| со | Co-ion |
| ct | Counterion |
| CEM | Cation exchange membrane |
| D | Diluate |
| ec | Referring to the end chamber domain |
| ex | Referring to the stack exit conditions |
| i | Ion Species |
| j (= C, D) | Solution Channel |
| m (= CEM, AEM) | Membrane |
| 0 | Observation |
| R | Referring to reservoir domain |
| S | solution |





Chapter 6:

A model of bipolar membrane ED

N.B.: this chapter has been adapted from the following published work:

Ledingham, J., Campbell, K.L.S., Keyzer, L., Yip, N.Y. and Campbell, A.N., 2024. The development and evaluation of a parameter-free circuit-based model of bipolar membrane electrodialysis for process design and optimisation. Chemical Engineering Journal, 497, p.154895.



6.1 Introduction

In recent decades, there has been a substantial and enduring decrease in the cost of renewable electricity from solar and onshore wind farms, primarily resulting from huge reductions in their construction costs [170]. Consequently, the levelised cost of electricity (LCOE) from wind and solar farms is now lower than from fossil fuels. Further, between 2021 and 2022, the LCOE of onshore wind and solar fell by 5 % and 3 %, respectively, suggesting that costs will continue to decrease. Globally, industrial processes account for more than a third of energy consumption [171] and more than a fifth of greenhouse gas emissions [172]. As such, the electrification of industrial processes has the potential to provide myriad benefits both in terms of process economics and sustainability [173]. However, there are several challenges inhibiting the widespread adoption of electrified process units including the availability of suitable replacement technologies, the high capital costs of these less mature technologies, and the risk averse nature of industry [174]. Much of the focus of electrification revolves around process heat as this consumes a substantial amount of energy and has relatively mature replacement technologies. Separation processes and chemical reactors have historically been much more challenging to electrify. Electromembrane processes will be instrumental in the electrification of many industries as they have a wide range of capabilities in both mass transfer and electrochemical reactions. This makes them excellent as both reactors and separators, often concurrently. Further, the direct transfer of the electrical energy to the unit's functionality makes electromembrane processes highly tuneable and easily controllable.

The desire to manipulate pH is ubiquitous in chemical processes both to optimise process unit conditions and to neutralise waste effluents prior to discharge. At present, the most common industrial method of pH control involves dosing chemical additives, such as NaOH and HCl in a 'feed-and-bleed' configuration. Sophisticated control loops are required due to the logarithmic nature of pH and its sensitivity to strongly acidic or alkaline substances. Chemical dosing is simple and effective, but involves complex supply chains, increasing the economic and environmental burden. Here, electromembrane processes are uniquely poised to offer an advantageous alternative.

Bipolar membrane electrodialysis (BPMED) is an emerging electromembrane technology which provides an electrochemical alternative to existing pH manipulation process units [130]. The unique structure of BPMED systems allows for the treatment and valorisation of industrial wastewaters by concurrent resource recovery and pH adjustment. In BPMED, an electric field is simultaneously used to drive the transport of ions across ion exchange membranes (IEMs) between flowing streams and to induce water splitting into protons and hydroxide ions. The structure of a BPMED unit, known as a stack, is essentially an extension of conventional electrodialysis (ED) with the addition of a bipolar membrane (BPM).

The functionality of a BPM is to induce water splitting, which is achieved by laminating two oppositely charged IEM layers together with a catalyst at the interface [175]. These layers are a cation exchange layer (CEL) and anion exchange layer (AEL), which are permeable only to cations and anions, respectively. Theoretically, no ions can permeate through the BPM between the acid and base streams due to its composition. Only neutral species, such as water molecules, may diffuse into the BPM domain. However, to maintain continuity of current,



ions must flow through the BPM. When a strong enough electric field is applied (on the order of 1 V per BPM), water splitting is initiated at the bipolar interface and protons and hydroxide ions are transported through the CEL and AEL of the BPM, respectively.

As with ED, the BPMED stack consists of many repeating unit cells which are comprised of streams and membranes (Figure 6.1). The standard repeating unit of a BPMED stack consists of three membranes: an anion exchange membrane (AEM), a cation exchange membrane (CEM), and the BPM. Three different saline streams flow tangentially between these membranes in channels created by spacers. The stream between the AEM and CEM is known as the diluate or salt. Anions and cations within the diluate streams are driven by the electric field in opposite directions through the AEM and CEM, respectively. The acid stream receives the anions from the diluate stream and protons from the BPM. Conversely, the base stream receives the diluate's cations as well as hydroxide ions from the BPM. As such, the salt initially present within the diluate is converted into an acid and a base in different streams. To exemplify this, an NaCl feed can be converted into highly concentrated NaOH and HCl product streams. The limiting factors controlling how concentrated the acid and base can become are the membrane selectivity, the membrane stability, and the diluate feed concentration.

At present, there are a great number of publications which explore potential applications of BPMED in industry [176]. One of the most prevalent is for the electrochemical recovery of CO₂ capture solvents [34]. The regeneration of capture solutions is an energy intensive process which typically involves heating the solution in a stripper column until the chemical equilibrium is thermally driven to the gaseous form of CO₂. With BPMED, the same equilibrium can be electrochemically driven by acidification of the stream. Further, BPMED has also been demonstrated to be practicable in the recovery of deep eutectic solvents (DES) used to pre-treat lignocellulosic biomass to increase digestibility prior to fermentation [37]. Here, the BPMED unit cell consists of

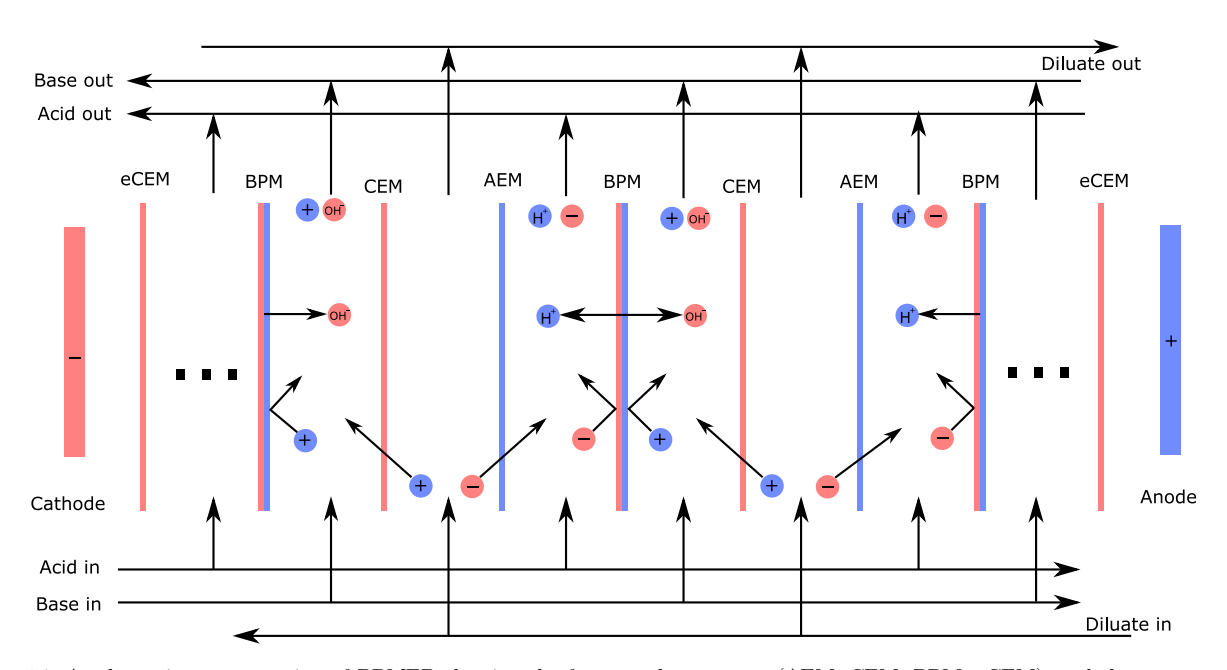


Figure 6.1: A schematic representation of BPMED showing the four membrane types (AEM, CEM, BPM, eCEM), and three stream types (acid, base, diluate) as well as an ideal representation of how ions are transferred. A repeating element of two cell triplets is shown between the electrodes. Positive charges are shown in blue and negative charges in red.



only a BPM and AEM and is used to concurrently separate the DES and control its pH. Beyond solvent recovery, BPMED has been demonstrated in the recovery of copper from electroplating sludge [36]. The copper was successfully recovered by using the protons generated by the BPMED to balance the pH in the waste sludge. The current best alternate approach to this involves chemical or biological leaching which are environmentally hazardous and slow, respectively.

Despite the myriad potential applications explored academically, there are very few industrially implemented examples of BPMED [177]. This primarily stems from the risk-averse nature of industry and the fact that tried-and-tested technologies typically benefit from lower costs and greater reliability. Bipolar membranes are also very expensive, on the order of 1000 \$/m². This far exceeds the costs of other IEMs, which are typically between 50 and 100 \$/m² [31]. As such, process intensification to reduce the size of units would greatly improve the commercial feasibility.

A cost optimisation for electromembrane processes exists through variation of the applied voltage. In general, the desired overall current is pre-determined as this is directly proportional to the total amount of ions transferred between the streams. A higher voltage leads to a higher current density (Ohm's law) and thus a lower membrane area and stack size is required, reducing the capital expenditure. However, a higher voltage also increases the specific power consumption, increasing the operating expenditure. Mathematical modelling of BPMED can be used to optimise the size of a stack and consequently de-risk industrial adoption of the technology. However, due to the myriad concurrent phenomena at the nano, micro, and macro scale, electromembrane technologies, and especially BPMED, can be very challenging to model accurately. Herein, a robust mathematical model of a BPMED process is to be developed which can adequately represent phenomena over a wide range of process conditions to allow for comprehensive design and optimisation.

Relative to conventional ED, there are very few published studies concerning BPMED modelling. A recent publication by Culcasi et al. [178] evaluated twelve existing BPMED models, classifying them based on their solution methods and the phenomena considered and neglected. It was made clear that, as with conventional ED, there are a wide range of different BPMED model formulations. Phenomena such as diffusion, osmosis, back-migration, shunt currents, and concentration polarisation are considered by some models but not by others. Despite this, all models show at least a reasonable agreement with validation experiments. The individual phenomena mentioned are generally very difficult to model accurately without the use of empirical fitting parameters. For example, concentration polarisation is highly dependent on the hydrodynamic environment as it determines the thickness of the boundary layers where concentration gradients form. The degree of turbulence provided by the spacer directly influences the boundary layer thickness, which in turn is strongly controlled by the geometry of the spacer. Since modelling this is ambiguous, fitting parameters are employed. Consequently, it is very easy for the complex phenomena included to confound others, leading to them inadvertently compensating for each other's inaccuracies. With more phenomena and fitting parameters included, it becomes ever easier to find local minima when fitting parameters, especially when limited experimental data sets are considered. As such, the model developed in this work will completely avoid the use of fitting parameters and training data. To



achieve this, only phenomena that can be directly modelled and which use readily accessible parameters are included.

For many existing BPMED models, experimental validation is conducted as a means of parameter estimation [178–184]. This is done to either find values of parameters that are otherwise difficult to predict (e.g. membrane diffusivities, transport numbers, temperature dependence of conductivity), or used to gain insight into experimental results (e.g. finding the current efficiency, or membrane resistance). This is useful for improving the accuracy in the range where they are experimentally validated but limits generalisation. Extrapolation is often necessary for process design and optimisation due to the time-intensive nature of experimental studies. Additionally, many existing models use lumped empirical parameters to simplify equations and parameter estimation, further obfuscating the model insights. In this work, experimental and modelling results are collected completely separately, and compared directly, providing a sincere and robust evaluation of the model.

The Nernst-Planck equation is very commonly used to model multidimensional concentration fields in both conventional ED and BPMED. Here, an overall flux is computed by summing contributions from diffusive, electrophoretic, and convective constituents [158]:

$$J_i = D_i \nabla C_i + u C_i + \mu_i z_i C_i \nabla \Phi$$
 [6.1]

$$\nabla \cdot \boldsymbol{J}_i = 0 \tag{6.2}$$

In these equations, J_i is the overall flux vector of component i, D_i is its diffusivity, C_i its concentration, μ_i its mobility, z_i its charge number, \boldsymbol{u} is the velocity vector, and $\boldsymbol{\Phi}$ is the electric potential. A charge condition is required for closure of this model. The most common is the assumption of electroneutrality, where the sum of all charges at each spatial point (including the membrane) is zero. To model the water splitting effect of the Bipolar membrane, an equation for the second Wien effect is used, where the water dissociation constant is a function of the electric field strength [185,186].

$$K_w = C_H C_{OH} ag{6.3}$$

$$K_w = \frac{k_f(E)}{k_r} \tag{6.4}$$

$$k_f(E) = k_{f,0} \left(1 + b + \frac{b^2}{3} + \frac{b^3}{18} + \frac{b^4}{180} + \dots + \frac{b^n}{(n+1)! \, n! \, /2^n} \right)$$
 [6.5]

$$b = 0.09636 \frac{\nabla \Phi}{\varepsilon T^2} \tag{6.6}$$

Here, K_w is the water dissociation constant, k_f and k_r are the forward and reverse reaction rate constants for the dissociation of water, respectively, $k_{f,0}$ is the nominal forward reaction rate constant without the effect of the electric field, E is the electric field strength (negative gradient of electric potential), E is a dimensionless term dependent on the strength of the electric field, E is the domain permittivity, and E is the temperature. The value of E0 will be greatest in locations where there is a large gradient of the electric potential, like at the bipolar junction and membrane-solution interfaces when approaching the limiting current density (LCD). Here, E1 sharply



increases, leading to an increase in the rate of water splitting and the water dissociation equilibrium constant, thereby providing the H⁺ and OH⁻ ions. Water recombination is driven by an excess of H⁺ and OH⁻ ions which are transported in opposite directions due to their opposite charges. Due to this, and the fact that the reactions are fast, recombination typically occurs in a plane. One key strength of Nernst-Planck modelling is that the location of this plane can be discerned. Water dissociation and recombination reactions can either be modelled as dynamic by separately computing the forward and reverse reaction rates, or as an equilibrium which is constantly maintained. The former is much more computationally challenging due to the large reaction terms.

Ortega et al. [187] and Leon et al. [188] used a Nernst-Planck model in COMSOL Multiphysics to compute a two-dimensional concentration field across a three-channel BPMED cell. Wang et al. [189] used the same method but in an unspecified software. Results tend to be very granular, where the concentrations and fluxes of individual species as well as the electric potential, can be evaluated at every spatial point in the domain. As such, this modelling approach is excellent for investigating small scale phenomena which may or may not contribute significantly to overall performance. However, when these concentration profiles are used to calculate full scale performance, errors can aggregate, leading to poor predictability. Further, the 2D electrolyte domains do not account for the turbulent mixing provided by the netted membrane spacer, a key source of mass transfer in real electromembrane systems.

One-dimensional Nernst-Planck models are more common than 2D models due to their greater simplicity [181,189,190]. Here, the dimension perpendicular to the membrane surface is either integrated out or ignored. Other methods of modelling mass transfer in BPMED beyond Nernst-Planck models typically include the incorporation of membrane permeabilities to compute ion fluxes [184,191].

Equivalent-circuit models are often used to model conventional ED but have rarely been applied to BPMED. In an equivalent-circuit model, the analogy between electrons moving in a circuit and the ions flowing in an electromembrane stack is leveraged. Fundamental laws such as Ohm's law and Faraday's first law are used to relate important macroscopic variables such as voltage, current density, electrical resistance, and ion flux. As such, these models are very robust, computationally inexpensive, directly applicable to macroscale processes, and can be very flexible. Additional sub-models are used to incorporate smaller-scale phenomena through the electrical resistance and material balance. Vera et al. [182] used an equivalent circuit model to model the deacidification of fruit juice using BPMED. Despite the high complexity of the media studied, a reasonable agreement between model predictions and experimental results was achieved. However, experiments were conducted to estimate model parameters such as the current efficiency and the membrane resistance, reducing the predictive power and hence generality of the model.

Previous work (Chapter 5, [192]) has demonstrated the efficacy of a one-dimensional circuit-based modelling strategy for electromembrane processes, using conventional ED as a case study. Adaptability was a key driver in model development, where it was claimed that additional phenomena could be accounted for through modifications to the material balance and the cell resistance model. In this work, this claim is evaluated by using a similar modelling strategy for the development of model of BPMED which avoids the use of empirical fitting



parameters. The model developed is then validated against a recirculating-batch experiment, using a moderately concentrated NaCl solution that could be reasonably expected in an industrial operation. Various phenomena such as diffusion, water permeation, concentration polarisation, and shunt currents were neglected due to their low impact at the conditions validated against and the difficulty of modelling them accurately without using empirical parameters. However, the flexibility of the model is such that they can easily be included if deemed necessary. The avoidance of empirical parameters ensures that the model has applicability over as wide a range of concentrations and scales as possible.

6.2 Model formulation

Laboratory experiments of both conventional ED and BPMED are almost exclusively conducted on recirculatingbatch systems (Figure 6.2a). Separate reservoirs for the acid, base, and diluate are present, the conductivity and pH of which are typically measured over time. Conversely, industrial BPMED processes are typically operated in a continuous configuration, either as a once-through process or with a recycle stream. As with the previous work, the aim of the modelling approach detailed herein is to be applicable to all scales and all configurations of BPMED. As such, the presented model consists of three 'layers' (Figure 6.2c), the outermost of which defines the overall BPMED process. Here, initial conditions are defined, overall material balances are solved, and global variables such as the current density and faradic efficiency are computed. In the middle layer, acid-base equilibria, the BPM voltage drop, and differential spatial material balances are computed along the flow path within the BPMED stack. The stack is imagined as many differential slices perpendicular to the direction of flow (Figure 6.2b). Transport between channels is related to the applied voltage and changes in concentration along the flow path are computed from material balances. The electrical resistance of each differential volume is also computed here using the analogy of an electric circuit with different resistive elements for each membrane and electrolyte. The resistance and cell voltage are then passed to the inner layer where the Tafel equation and Ohm's law are iteratively solved to find and return the current density of the differential slice. An 'effective' current density is computed for each transporting membrane which accounts for the current released by species reacting within the membrane domains. Once the effective current density is known, a modified form of Faraday's law which incorporates transport numbers and like-charge selectivities is used to compute the fluxes of each ion permeating each membrane. The fluxes are converted into concentration derivatives, assuming plug flow within the channels, after which the concentration at the next differential volume can be computed. Once internal concentration profiles are found, the stack outlet concentrations are passed back to the outer layer to be used in the overall material balance.

In this model, it is assumed that transmembrane diffusion and osmosis are negligible since they are at least two orders of magnitude slower than transport by electroconvection when operating under normal conditions. Despite this, the flexibility of the model is such that they may be included through modifications to the material balances. This may prove necessary for processes where they cannot be neglected such as when a low voltage is applied and there is a very large trans-membrane concentration difference. Membrane boundary layers and



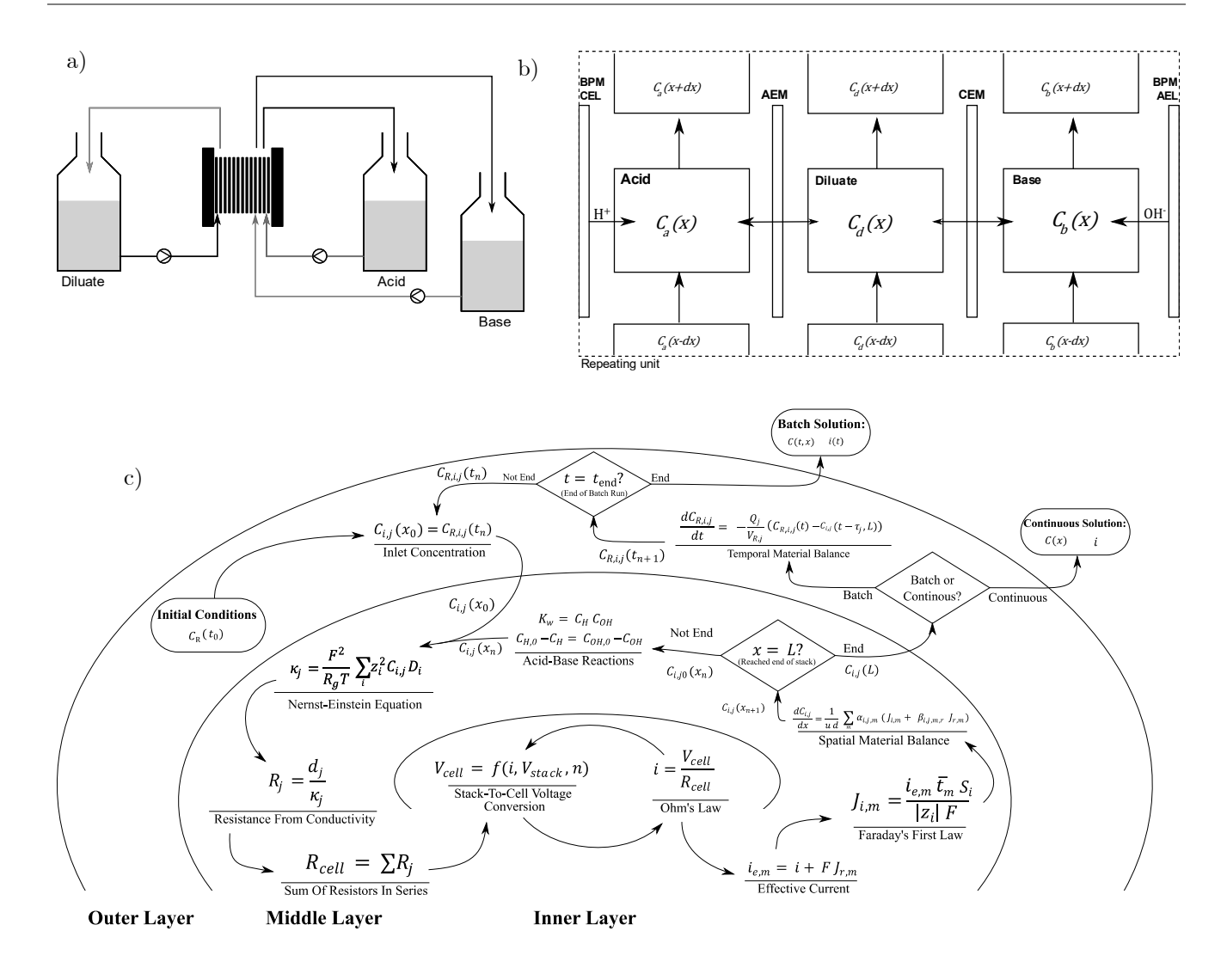


Figure 6.2: a) A schematic representation of a recirculating batch BPMED system. Streams from each of the three reservoirs are pumped around a circuit through the BPMED stack. b) A diagram of the differential volume slice used for the inner and middle layers within the model. Indications of how ions permeate membranes are shown with horizontal lines, and the convective transfer between adjacent differential volumes is shown with vertical lines. c) A flow diagram showing the transfer of information within the layered model and the positioning of the equations. The difference between batch and continuous formulations is also shown.

concentration polarisation are also not considered due to the assumption of plug flow. These are strongly dependent on the hydrodynamic environment and membrane spacer geometry used, and thus require empirical models to capture them accurately. Further, below the LCD of the transporting membranes, where this model is solely applicable, its impact on process scale variables is limited.

This model of BPMED was implemented and solved in MATLAB R2022b. The explicit nature of this modelling strategy makes solving in programmes like MATLAB and Python particularly attractive and facilitates further development and modification. However, some modellers prefer using implicit methods in software such as gPROMS or COMSOL Multiphysics. As such, a generalised form of the model in its entirety has been presented as a system of differential and algebraic equations within Section 6.6.



6.2.1 Inner layer: solving for current density

The goal of the inner-most layer is to determine a current density across a differential volume of a single cell of the BPMED stack given a cell resistance and stack voltage. A single unit cell triplet is here defined as a channel for each of the three streams (diluate, acid, and base) separated by an AEM, CEM and BPM (Figure 6.2b). The analogy of an electric circuit is used, where each of these six constituent domains are resistive elements, and the transported ions are the charge carriers. Thus, the current density (i) perpendicular to the direction of fluid flow can be computed through Ohm's law [193].

$$i = \frac{V_{cell}}{R_{cell}} \tag{6.7}$$

Here, V_{cell} and R_{cell} are the voltage and electrical resistance across the unit cell, respectively. The cell resistance is provided by the middle layer, but the voltage across a cell pair is not yet known. It should be noted that the layout of the cell is chosen such that the voltage drop across the bipolar junction is not included in V_{cell} , making this the voltage which drives ion transport only. A voltage across the entire stack (V_{stack}) is provided by an external power supply and is constant for all differential volume slices. Since its value is typically set by design, it is assumed here to be known. The value of V_{cell} can be computed from V_{stack} by accounting for ancillary voltage drops from the electrode equilibrium potential (V_{eq}) , the electrode overpotential (η) , the water splitting potential at the bipolar interface (V_{bp}) , and the voltage drop over the electrolyte end chambers (V_{ec}) .

$$V_{cell} = \frac{1}{n_c} (V_{stack} - V_{eq} - \eta - V_{ec}) - V_{bp}$$
 [6.8]

Here, n_c is the number of unit cells within the stack which divides the voltages relating to the entire stack between each of the cell pairs. The overpotential can be computed using the Tafel equation [164]:

$$\eta = A_a \log \left(\frac{i}{i_{0,a}} \right) + A_c \log \left(\frac{i}{i_{0,c}} \right)$$
 [6.9]

where A and i_0 are well established empirical parameters found in literature dependent on the electrode material and reactions occurring. The voltage drop over the electrolyte chambers and end membranes is accounted for using Ohm's law

$$V_{ec} = 2 i \left(R_{eCEM} + \frac{d_{ec}}{\sum_{i} C_{ec,i} \kappa_{mc,i}} \right)$$
 [6.10]

Here, R_{eCEM} is the electrical resistance of the end cation exchange membranes, d_{ec} is the width of the end chamber in the direction of the electric field, $C_{ec,i}$ is the end chamber ion concentration of species i and $\kappa_{mc,i}$ is the molar conductivity of species i. A factor of two is present to account for both the analyte and catholyte, which are assumed to provide the same electrical resistance. The resistance of the end chamber is assumed to be constant, but this could be altered.

The voltage drop across the bipolar membrane can be split into an equilibrium potential $(V_{bp,eq})$ and overpotential (η_{bp}) , in the same way as electrode reactions are.



$$V_{bp} = V_{bp,eq} + \eta_{bp} {[6.11]}$$

The equilibrium bipolar splitting voltage is the minimum voltage required across the bipolar junction to overcome the thermodynamic energy barrier and induce water splitting. According to Strathmann *et al.* [194], $V_{bp,eq}$ can be calculated from the Nernst equation, assuming a complete exclusion of co-ions within the BPM.

$$V_{bp,eq} = 2.3 \frac{R_g T}{F} \Delta p H \tag{6.12}$$

Here, R_g is the ideal gas constant, T is the temperature, F is the Faraday constant, and ΔpH is the difference in pH across the bipolar junction. The pH inside the membrane is computed using the Donnan equilibrium and a charge balance, assuming only H⁺ and OH⁻ ions are present inside the bipolar membrane [167].

$$C_{H,BPM} = 0.5 \left(C_{fix} + \sqrt{C_{fix}^2 + 4 \prod_{i} C_{i,a}} \right)$$
 [6.13]

$$C_{OH,BPM} = 0.5 \left(C_{fix} + \sqrt{C_{fix}^2 + 4 \prod_{i} C_{i,b}} \right)$$
 [6.14]

Here C_{fix} is the fixed ion concentration in the membrane and $C_{i,a}$ and $C_{i,b}$ are the concentration of species i in the acid and base chambers, respectively. The bipolar membrane overpotential is typically modelled as proportional to the current density, the proportionality constant of which is of Arrhenius type to account for the effect of temperature. A simple, but tested, relation proposed by Chen et al. [195] is:

$$i = \left(G_0 e^{-\frac{E_{bp}}{R_g T}}\right) \eta_{bp} \tag{6.15}$$

where G_0 and E_{bp} are kinetic parameters analogous to a pre-exponential factor and activation energy for a chemical reaction rate constant, respectively. The exact values of these parameters depend on the composition of the BPM in use. Most notably, they are dependent on the identity and loading of the catalyst employed at the bipolar junction. It should be noted that G_0 varies widely depending on the catalyst loading and can optimally be on the order of 10^{10} S m⁻². The activation energy for water splitting in pure water is 69 kJ mol⁻¹. The presence of the catalyst at the bipolar junction reduces this to around 25 - 30 kJ mol⁻¹. For BPMs operated at 298 K and a current density of 100 A m⁻², the overpotential is only 1.8 mV. Hence, for a well-designed BPM, the bipolar overpotential can often be neglected.

After each ancillary potential has been accounted for, it is possible to compute the cell voltage and current density. However, whilst the cell voltage has a linear dependence on the electrode overpotential, the electrode overpotential has a logarithmic dependence on the current density. Consequently, this set of equations must be solved iteratively. It is primarily for this reason that these computations are separated into their own layer of the model. The MATLAB function 'fzero' was used to loop over the inner layer equations and converge upon a solution for the current density and cell voltage.



Greater computational expediency was gained by selecting appropriate initial guesses for the current density when calling the fzero function. The value of the current density from the previous inner layer solution was used for this, as they would naturally be close in value.

Special consideration was given for the case that V_{cell} was computed as negative in Eq. 6.8. This would indicate that the applied potential was lower than $V_{eq} + V_{BP,0}$ and thus too low to drive any transport. In this case, V_{cell} was forced to be zero, resulting in zero current density and no flux.

6.2.2 Middle layer

The spatial differential material balance within the middle layer computes the concentration profiles of all ion species in each channel along the length of the flow path within the BPMED stack. Ultimately, the derivative of the concentration of species i in channel j with respect to spatial position $\left(\frac{dc_{i,j}}{dx}\right)$ is found from the concentrations in a differential slice across the stack. It is assumed that the channels are in plug flow and that the spacer nets take up a negligible amount of the internal channel volume.

The middle layer can be broken down into three primary functionalities:

- I. Solve the acid-base equilibria and set all concentrations to their equilibrium values.
- II. Compute the electric resistances of the electrolytes and membranes to be passed to the inner layer.
- III. Find the fluxes of all ionic species once the current density is returned from the inner layer using Faraday's first law.

6.2.2.1. Acid-base equilibria

Acid-base speciation reactions are a distinctive characteristic of BPMED, and so must be numerically handled appropriately. Within this model, the effect of these reactions is determined before any other calculations can take place. Due to the rapid rate of water dissociation reactions (rate constant $\sim 10^8$ mol⁻¹ m³ s⁻¹), it is assumed that all reactions are instantaneously brought to equilibrium. For the water speciation reaction within the channels, two equations are required. These are the water equilibrium equation and a material balance which represents the equivalent consumption/production of H⁺ and OH⁻ ions:

$$K_{w} = C_{H} C_{OH}$$
 [6.16]

$$\xi_{H/OH} = C_{H,0} - C_H = C_{OH,0} - C_{OH}$$
 [6.17]

Here, K_w is the water dissociation constant, $\xi_{H/OH}$ is the extent of reaction (assuming the consumption of ions is positive), C_H and C_{OH} are the concentrations of H⁺ and OH⁻ ions in the differential volume after the reaction has occurred, and $C_{H,0}$ and $C_{OH,0}$ are the theoretical concentrations after the ion transfer from the previous step has taken place but before the reaction has occurred. These equations can be combined to compute the extent of reaction within a differential slice as a function of the pre-reaction concentrations:

$$\xi_{H/OH} = \frac{1}{2} \left[\left(C_{H,0} + C_{OH,0} \right) - \sqrt{\left(C_{H,0} - C_{OH,0} \right)^2 + 4 K_w} \right]$$
 [6.18]



Similar equations can be derived for any weak acid or base present in the streams. The post-reaction concentrations are used in the next steps to determine the electric resistances of the streams and membranes.

6.2.2.2. Electrical resistance

The cell electrical resistance is computed from the sum of the electrolyte and membrane resistances using a resistors-in-series approach. An analogy to an electric circuit is drawn with distinct resistive elements used for each of the membranes and electrolyte streams.

$$R_{cell} = \sum_{i} R_j + \sum_{m} R_m \tag{6.19}$$

Here, R_j is the electric resistance of channel j (= d,a,b), and R_m is the electric resistance of the domain of membrane m (= AEM,CEM,BPM). Note that for the BPM, only the resistance across the transporting domains of the CEL and AEL are considered here as the bipolar junction voltage drop is accounted for in Eq. 6.8.

These electric resistances are calculated in the same way as in previous work. Electrolyte resistances are computed from the conductivity (κ_i) and intermembrane distance (d_i) [158].

$$R_j = \frac{d_j}{\kappa_i} \tag{6.20}$$

The electrolyte conductivity can be computed by summing up contributions from individual ions and using the Nernst-Einstein equation [165]:

$$\kappa_j = \frac{F^2}{R_g T} \sum_{i} z_i^2 C_{i,j} D_{i,s}$$
 [6.21]

Here, $C_{i,j}$ is the molar concentration of species i in channel j, and $D_{i,s}$ is its diffusivity in solution.

The membrane resistance is calculated in a similar way to the electrolyte resistance, but with a few key differences. The membrane conductivity (κ_m) is again computed using contributions from individual ions in the Nernst-Einstein equation.

$$\kappa_m = \frac{F^2}{R_g T} \sum_{i} z_i^2 C_{i,m} D_{i,m}$$
 [6.22]

Here, $C_{i,m}$ is the concentration of species i within the membrane, and $D_{i,m}$ is its membrane diffusivity. As in the previous work, the Donnan equilibrium and electroneutrality equations are used to compute the membrane concentrations at the boundary with the electrolyte [196].

$$\prod_{i=1}^{2} C_{i,j}^{\nu_i} = \prod_{i=1}^{2} C_{i,m}^{\nu_i}$$
 [6.23]

$$\sum_{i} z_{i} C_{i,j} = z_{m} C_{fix} + \sum_{i} z_{i} C_{i,m}$$
 [6.24]

Here, ν_i is the stoichiometric coefficient of the ion within the salt and z_m is the charge number of the membrane (-1 for CEM and +1 for AEM). A form of Eq. 6.23 exists for every pairwise combination of ions. An



alternate, non-ideal, formation of these equations exists where activity coefficients multiply each of the concentration terms. Through this, the inherent selectivity of membranes towards certain species may be considered.

Membrane diffusivities are computed using a model outlined by Fan et al. [163] which considers the electrostatic interactions between all transported ions and fixed charge groups. This model incorporates only easily accessible membrane properties such as the swelling degree (f_w) and the fixed charge concentration (C_{fix}) , often provided by membrane manufacturers.

$$D_{i,m} = D_{i,s} \left(\frac{f_w}{2 - f_w}\right)^2 exp(-Az_i^2)$$
 [6.25]

$$A = \frac{\theta e^4 N_A^{2/3}}{16 \pi^4 \varepsilon_m^2 k_B^2 T^2} C_{fix}^{2/3}$$
 [6.26]

Other parameters in this model include a coefficient arising from the sum of infinite vectors (θ , 5.48 if fixed charges are assumed to be point charges, refer to the supporting information of [163] for more detail on this), the charge of an electron (e), Avogadro's number (N_A), the matrix permittivity (ε_m), and the Boltzmann constant (k_B).

For dilute external electrolytes, all parameters in Eqs. 6.25 and 6.26 are constant, and so the membrane diffusivity is invariant. However, in concentrated solutions, osmotic deswelling causes the water content of the membrane (f_w) to decrease and the fixed charge concentration (C_{fix}) to increase, resulting in a reduction of the membrane diffusivity [197]. To account for this effect, additional equations are required to compute the change in membrane volume as a function of bathing solution concentration, such as the one proposed by Kozmai et al. [198]. However, for this application, membrane deswelling is neglected to avoid empirical fitting parameters and because validation was conducted in dilute NaCl solution.

Due to the changing internal concentration across the width of the membrane, the overall resistance is computed by finding the conductivities at both sides of the membrane and integrating, as in previous work:

$$R_m = \frac{d_m \ln \left(\frac{\kappa_{m,1}}{\kappa_{m,2}}\right)}{\kappa_{m,1} - \kappa_{m,2}}$$
 [6.27]

It should be noted that this is not necessary for the two layers of the BPM, which are assumed to have a flat concentration profile, resulting in the following equation for the BPM resistance:

$$R_{BPM} = \frac{R_g T}{F^2} \left(\frac{d_{AEL}}{D_{OH,AEL} C_{OH,AEL}} + \frac{d_{CEL}}{D_{H,CEL} C_{H,CEL}} \right)$$
 [6.28]

After the resistances of the membranes and electrolytes are found, the cell resistance is computed and passed to the inner layer. The current density is then returned and used to find the ion flux.



6.2.2.3. Ion migratory flux

The current density returned by the inner layer is used to compute an ion flux which is ultimately converted into a concentration differential. For consistency, only the magnitude of the fluxes is considered here, and directionality is factored in later when computing the spatial derivative of the concentration. The simplest flux calculation is that for the bipolar membrane. It is assumed that there is total exclusion of external ions from the BPM and thus all current is carried by the water splitting products. Therefore, the water splitting flux (J_{BPM}) is equivalent to the flux of protons from the CEL of the BPM into the acid channel and of hydroxide ions from the AEL into the base channel. It is calculated using Faraday's first law:

$$J_{BPM} = \frac{i}{F} \tag{6.29}$$

A more complex approach is required for the selective transport membranes (AEM and CEM) due to the multitude of species and reactions potentially present. The flux magnitude through each transporting membrane $(J_{i,m}, m = AEM, CEM)$ is computed separately for counterions and co-ions from the current density, again using Faraday's first law:

$$J_{i,m} = \frac{i_{e,m} \overline{t}_m S_{i,m}}{|z_i| F} \qquad \forall \quad i \in ct$$
 [6.30]

$$J_{i,m} = \frac{i_{e,m}(1 - \overline{t}_m) S_{i,m}}{|z_i| F} \qquad \forall \quad i \in co$$
 [6.31]

Here, ct is the set of species which are counterions in membrane m and co is the set of species that are co-ions. Instead of directly using the current density returned by the inner layer, an 'effective' current density (i_e) is used. This is to account for the additional current released by acid-base reactions within the membrane and is discussed further below.

Two important selectivity factors are present in this equation which relate the overall ion flux to that of an individual species. These are the transport number of the membrane (\bar{t}_m) , and the like-charge selectivity of the species (S_i) . The membrane transport number is defined as the ratio of the useful current carried by counterions to the total current carried across the membrane. As such, it varies between zero and unity and is analogous to both a selectivity and current efficiency for a single membrane. Hence, the co-ion flux has the $(1 - t_m)$ term.

In previous work, a transport number model was presented which considers the transmembrane concentration ratio and an 'intrinsic' transport number. The value of the intrinsic transport number is often one provided by membrane manufacturers and is defined as the value measured when the transmembrane concentrations are equal. This model was derived considering the migratory flux term from the Nernst-Planck equation. A similar transport number model is used here which has been adapted to account for multiple competing co-ions and counterions.

$$\frac{1}{\overline{t}_m} = 1 + \frac{\sum_{i \in co} |z_i| C_{i,j}}{\sum_{i \in ct} |z_i| C_{i,d}} \left(\frac{1}{t_{m,0}} - 1\right)$$
 [6.32]

In this equation, the ratio of the trans-membrane equivalent concentrations accounts for the additional electrophoretic driving force when there is a higher normality on one side of the membrane. The channel (j)



indicated in this equation is whichever one counterions are transported *into* across membrane m. For the CEM, this is the base, and for the AEM this is the acid.

The selectivity between like charged ions (e.g., H^+ and Na^+) is defined as the fraction of counterion or co-ion flux corresponding to a single species. This can be computed from their relative electromigration fluxes within the membrane as described in the Nernst-Planck equation (Eq. 6.1). Here, a similar development justification to the transport number model is used. For a single species, the electromigratory flux ($J_{e,i}$) term is calculated by

$$\boldsymbol{J}_{e,i} = z_i \, C_i \, \mu_{i,m} \, \boldsymbol{\nabla} \Phi \tag{6.33}$$

where z_i is the ion charge number, $\mu_{i,m}$ is the ion mobility in the membrane, and $\nabla \Phi$ is the gradient of the electric potential. According to the Einstein-Smoluchowski relationship [165,166], ion mobility is proportional to diffusivity.

$$\mu_{i,m} = \frac{F}{R_g T} |z_i| D_{i,m}$$
 [6.34]

Hence, the proportion of the counterion or co-ion flux carried by a single species can be found from simply summing the contributions of individual ions and taking a ratio. The electric potential gradient, temperature and gas constant conveniently cancel through.

$$S_{i \in ct} = \frac{z_i C_i D_i}{\sum_{i \in ct} z_i C_i D_i} \qquad S_{i \in co} = \frac{z_i C_i D_i}{\sum_{i \in co} z_i C_i D_i}$$
 [6.35, 6.36]

A similar relationship it presented by Roux-de Balmann *et al.* [199]. As with the Donnan equations for computing membrane concentrations, these terms can be modified to account for the inherent selectivity that membranes have for certain species. This can be done with the inclusion of activity coefficients multiplying each concentration.

The necessity of an effective current density arises due to acid-base reactions occurring within the transporting membranes. For example, protons and hydroxide ions which both travel through the transporting membranes would meet at a plane and neutralise each other. Consequently, the trans-membrane current carried by acid-base active species is reduced, releasing additional current to be carried by all species (Figure 6.3). The effective current density can be found from this additional current, which is equal to the reacting flux $(J_{r,m})$ multiplied by the Faraday constant. For the water recombination reaction, this is:

$$J_{r,m} = \min\{J_{H,m}; J_{OH,m}\}$$
 [6.37]

$$i_{e,m} = i + J_{r,m} F$$
 [6.38]

Complete neutralisation is assumed within the membrane rather than an equilibrium forming. This is because any current carried by the reaction limiting species at equilibrium would be vanishingly small, and any small deviations from equilibrium are handled within the electrolyte domains through Eq. 6.18. However, it should be noted that for weak acids and bases this assumption is not sufficient. Through the combination of equations 6.30, 6.31, 6.37, and 6.38, the following relation for the effective current is derived:



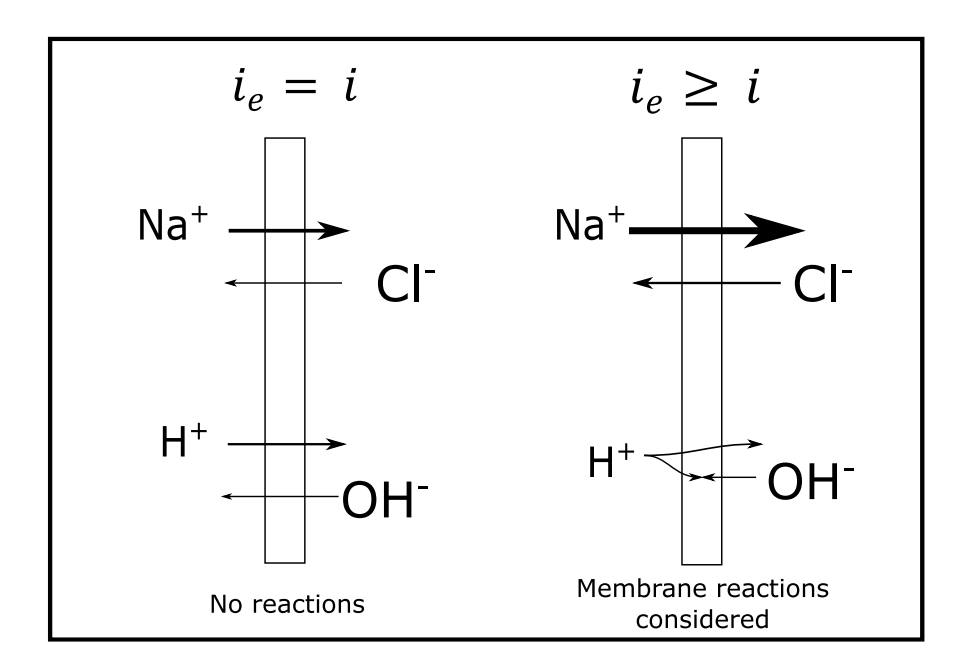


Figure 6.3: A schematic representation of how acid-base reactions within the membrane domain releases additional current which is captured in an 'effective' current density (i_e) . The size of the arrows is representative of the ion flux, but they are not to scale.

$$i_{e,CEM} = \min\left\{\frac{i}{1 - S_{OH,CEM}(1 - \bar{t}_{CEM})}; \frac{i}{1 - S_{H,CEM} \bar{t}_{CEM}}\right\}$$
 [6.39]

$$i_{e,AEM} = \min\left\{\frac{i}{1 - S_{H,AEM}(1 - \bar{t}_{AEM})}; \frac{i}{1 - S_{OH,CEM} \bar{t}_{AEM}}\right\}$$
 [6.40]

In summary, using both a transport number and like-charge selectivity, the total flux, found from an effective current density, can be broken down first by charge identity (co-ion or counterion), and then into individual species. Finally, the membrane fluxes are summed for those adjacent to the appropriate channels and converted into concentration differentials using the flow velocity (u) and channel width (d).

$$\frac{dC_{i,j}}{dx} = \frac{1}{u d} \sum_{m} \alpha_{i,j,m} \left(J_{i,m} + \beta_{i,j,m,r} J_{r,m} \right)$$
 [6.41]

$$\alpha_{i,j,m} = \begin{cases} 1 \text{ if ion } i \text{ is transported though membrane } m \text{ into channel } j \\ -1 \text{ if ion } i \text{ is transported though membrane } m \text{ from channel } j \\ 0 \text{ if membrane } m \text{ is not adjacent to channel } j \end{cases}$$
[6.42]

$$\beta_{i,j,m,r} = \begin{cases} -1 & \text{if ion } i \text{ is consumed in reaction } r \text{ in membrane } m \text{ and } \alpha_{i,j,m} \text{ is -1} \\ 1 & \text{if ion } i \text{ is produced in reaction } r \text{ in membrane } m \text{ and } \alpha_{i,j,m} \text{ is 1} \\ 0 & \text{otherwise} \end{cases}$$
[6.43]

Here, the α factor ensures that the directionality of fluxes is accurately accounted for and only membranes adjacent to channel j are considered. The β factor ensures that reactions are correctly handled in the material balance; a consumed species transported through a membrane should leave with a flux equal to $J_{i,m}$, but arrive at a flux lower by $J_{r,m}$.



For an arrangement of n ionic species and m distinct channels, a system of $n \times m$ differential equations is required. In this work, this system was solved in MATLAB using the ode15s function, which utilises the Runge-Kutta method. The inlet concentrations were provided as boundary conditions from the outer layer, and the model returned the internal concentration profiles of each species in each channel. Other spatially dependent variables such as the total resistance, the fluxes of individual species over each membrane, the current density, and the cell voltage were also extracted.

6.2.3 Outer layer: temporal material balance

The extension of the single-pass model (the middle layer) to that of a real system is crucial for model validation and experimental prediction. This is the function of the outer layer, which in this work involves modelling a recirculating batch system with different reservoirs for the acid, base, and diluate streams (Figure 6.2a). The reservoirs are assumed well mixed and constant in volume. Assuming instantaneous fluid transfer, the temporal material balance for species i in reservoir j is as follows

$$\frac{dC_{R,i,j}}{dt} = -\frac{Q_j}{V_{R,j}} \Big(C_{R,i,j}(t) - C_{i,j}(t,x=L) \Big)$$
 [6.44]

Where $C_{R,i,j}$ is the concentration of species i in the reservoir of stream j, t is experimental time, Q is the recirculation volumetric flow rate, V_R is the reservoir volume, and $C_{i,j}(t,x=L)$ is the stack exit concentration. Before this balance can be solved, $C_{R,i,j}$ is supplied to the middle layer as a boundary condition for the spatial material balance, from which $C_{i,j}(t,x=L)$ is returned.

The validity of this equation in light of the assumption of instantaneous fluid transfer is questionable as there is substantial dead time in the tubing and flow cells where measurements are taken. For the experimental setup in this work, the dead volumes were around 0.25 L for each stream, which is significant relative to the reservoir volume of 1 L. This dead-volume must be included in the parameter V_R to ensure that the overall material balance is accurate. Further, with a flow rate of 20 L/h, the time taken for the fluid to transfer from the reservoir to the stack and then back again is 45 s and thus not negligible. Consequently, the assumption of instantaneous fluid transfer between the reservoir and the stack may not be valid, and so a delayed differential equation is appropriate. Accounting for this delay, the material balance becomes

$$\frac{dC_{R,i,j}}{dt} = -\frac{Q_j}{V_{R,i}} \Big(C_{R,i,j}(t) - C_{i,j}(t - \tau_j, L) \Big)$$
 [6.45]

where the delay (τ_j) is the time for the flowing stream to complete a loop from the reservoir, through the stack, and return. Fluid leaving the reservoir is replaced by material which left a time τ ago, hence the form of this equation. It should be noted that consideration of a series of delays is necessary when comparing measured and computed variables whose domain is not the reservoir. The spatial difference results in a temporal variance, and so failure to account for this would result in a mismatch between data sets. Shifting all data to a relative 'standard time' is required. The MATLAB delayed differential equation solver dde23 was used in solving the temporal material balance.



6.3 Experimental validation

Modelling BPMED is notoriously complex due to the multitude of competing phenomena combining to influence overall mass transfer. Several assumptions were made in the development of this model to avoid reliance on training data and empirical fitting parameters. Consequently, the efficacy of this modelling strategy must be examined through experimental validation.

All experiments were performed on a PC BED 1-4 system (PC Cell) with an ED64004 stack (PC Cell). The four membrane varieties used were the PC Acid 60 (AEM), PC MTE (CEM), PC Bip (BPM) and PC CE (eCEM), all from PC Cell. Eight full cell triplets were used rather than the typical ten to prevent an excessive voltage requirement. A Biologic SP300 potentiostat with 30V/2A booster card was used to accurately control the applied stack potential and measure the current. The conductivity and pH of the three streams were measured close to either the stack inlet or outlet, depending on the experiment, using JUMO CTI-500 inline conductivity probes and JUMO digiLine pH sensors, respectively. Circulation flow rates were maintained at 20 L/h and reservoir volumes were accurately set at 1 L not including dead volume, which was determined independently.

To ensure model accuracy and robustness over a wide range of concentrations and voltages, experimental validation was conducted in two orthogonal ways:

- 1. **Temporal validation:** A typical batch experiment (Figure 6.2a) was performed over the course of an hour with the voltage held constant at 20 V (activated at time zero), and the pH, conductivity, and current measured at two second intervals. The pH and conductivity probes were positioned before the stack for each stream so that conditions were equal to that of the reservoir. The three reservoirs were filled initially with the same concentration of NaCl (0.05 M). Over time, the concentrations would diverge greatly, ensuring that a wide concentration range was tested. A constant stream temperature of 20 °C was maintained by flowing chilled water through the reservoir jackets.
- 2. Steady-state validation: For this form of validation, current-voltage polarisation data was collected. The stack was operated in a continuous steady-state mode by flowing solution through only on a single pass. To achieve this, the outlets of each stream were not connected back to the reservoir, but instead to a waste collection container. The reservoirs which feed the pumps were topped up with fresh 0.05 M NaCl solution frequently to ensure that a constant inlet condition to the stack was maintained. An automatic chronoamperometry programme was set on the potentiostat software where the voltage was periodically stepped up by 1 V. A delay of 10 30 seconds between each step increase in the voltage ensured that any transitory current dissipated and a reasonable steady state was achieved.

For these orthogonal validation methods, model predictions were compared directly to experimental data. The same experimental characteristics and membrane parameters were used in both cases, presented in Table 6.1. All numerical values present here define the modelled system, but crucially were not used for any fitting. These parameters were either set through experimental practice, could be trivially measured, were known *a priori*, or could be found in manufacturer-provided data. As such, it is the model's predictive power that is being validated here.



Table 6.1: parameters and their associated values speficied in the model. Also shown is how their value is obtained.

| Parameter | Symbol | Value | Unit | Provenance |
|---------------------------------|--------------------------------------|---------------|------------------|--------------------------------|
| Applied Stack Voltage | V_{stack} | 20 | V | Set |
| Initial reservoir concentration | $C_R(t=0)$ | 0.05 | $\mathrm{mol/L}$ | Set |
| Reservoir volume | V_R | 1.0 | L | Set |
| Recirculation flowrate | Q | 20 | L/h | Set |
| | | | | |
| Intermembrane distance | d | 0.8 | mm | Known system characteristic |
| Membrane area | A_m | 64 | cm^2 | Known system characteristic |
| | | | | |
| Temperature | T | 293 | K | Measured system characteristic |
| Dead Volume | $V_{D,d}, V_{D,b}, V_{D,a}$ | 251, 248, 224 | mL | Measured system characteristic |
| Time delay | τ_{d} , τ_{b} , τ_{a} | 45, 45, 40 | S | Measured system characteristic |
| | | | | |
| Membrane thickness | d_m | 0.1 | mm | Manufacturer data |
| Membrane water fraction | f_w | 0.22 | - | Manufacturer data |
| Fixed charge concentration | C_{fix} | 0.8 | $\mathrm{mol/L}$ | Manufacturer data |
| Innate transport number | $\bar{t}_{0,cem} \; \bar{t}_{0,aem}$ | 0.99, 0.96 | - | Manufacturer data |

6.3.1 Temporal validation

The evolution of solution conductivity at the stack inlet over time is seen in Figure 6.4a. Here, experimental data is shown with points and model predictions with a solid line. At time zero, all three streams have the same conductivity (~ 5.9 mS/cm) in both the modelled and experimental data. Over time, the diluate conductivity decreases and the acid and base conductivities increase as Na⁺ and Cl⁻ ions are transferred from the diluate to the base and acid streams, respectively. This continues until the diluate conductivity asymptotically approaches a very low value. At this point, the ions are nearly depleted in the diluate, and so the ion flux decreases and the acid and base conductivities level out.

The combined magnitude of the increase in the conductivities of the acid and base streams (~19 mS/cm and 10 mS/cm, respectively) is greater than the decrease in diluate conductivity (~5.9 mS/cm). This is due to the water splitting reaction and generation of additional ions at the bipolar junction. Ideally, one transferred mole of NaCl forms a mole of NaOH and one mole of HCl. It can be seen through the Nernst-Einstein equation (Eq. 6.21) that contributions to the solution conductivity from each ion is proportional to both its concentration and diffusivity. The diffusivities of H⁺ and OH⁻ ions are $9.31 \times 10^{-9} \text{ m}^2/\text{s}$ and $5.27 \times 10^{-9} \text{ m}^2/\text{s}$, respectively; much higher than the $1.33 \times 10^{-9} \text{ m}^2/\text{s}$ of Na⁺ and $2.03 \times 10^{-9} \text{ m}^2/\text{s}$ of Cl⁻. Consequently, a solution of NaCl will have a lower conductivity than an equal concentration of NaOH or HCl. This also explains why the magnitude of the increase in the acid stream conductivity is greater than the increase in the base stream: The diffusivity of H⁺ is greater than the diffusivity of OH⁻.



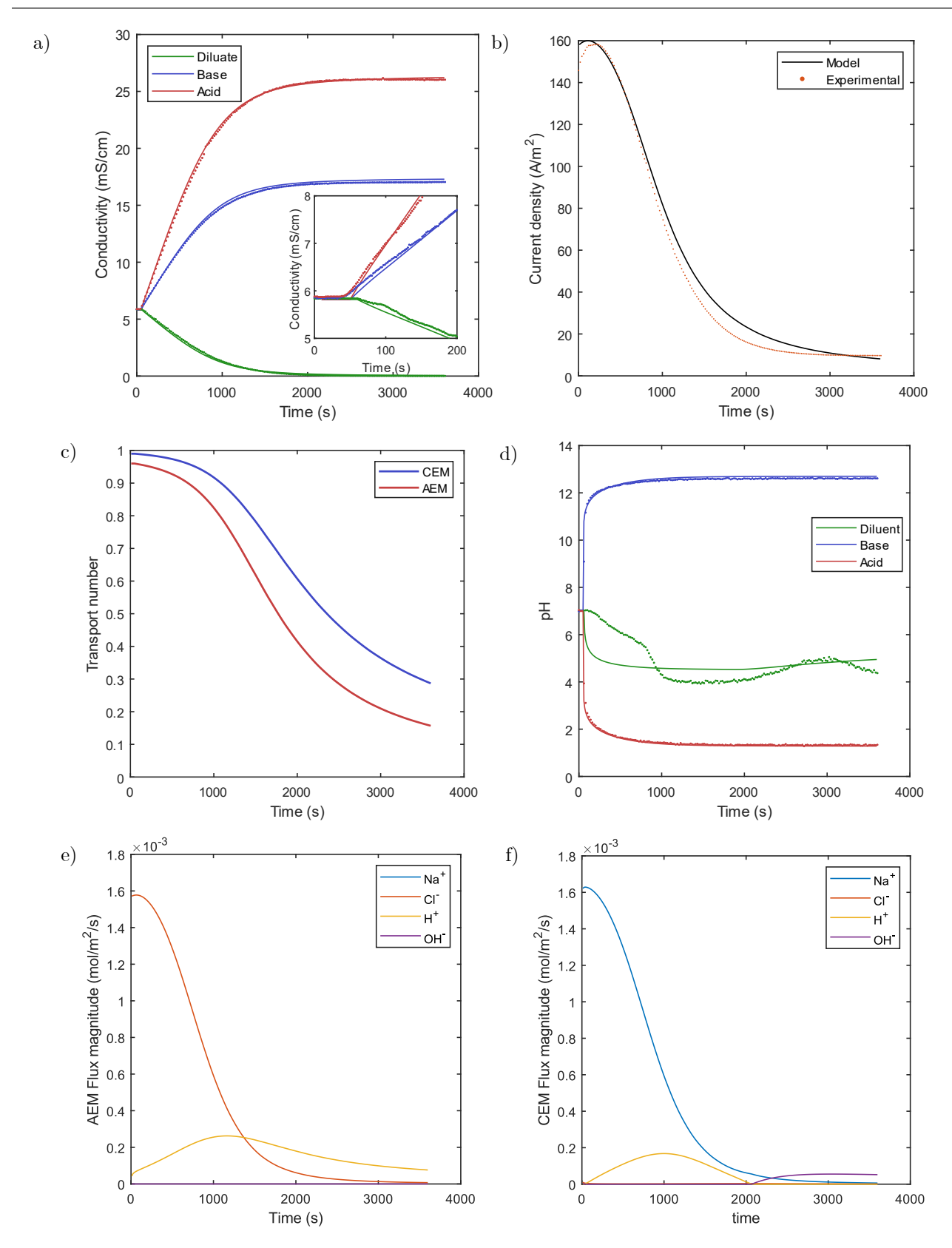


Figure 6.4: results of the temporal validation results. Throughout, modelling results are shown with a solid line and experimental measurements are shown with points. a) The time-evolution of the conductivities of the three streams measured/predicted at the reservoir outlet. The inlayed graph shows the behaviour early on. b) the measured and calculated current density over time. c) The calculated transport numbers for the AEM and CEM over time. d) The time-evolution of the pH of all three streams, measures at the reservoir outlet. e) The calculated flux magnitude of all four species through the AEM over time. f) The calculated time-evolution of the flux magnitude of all species through the CEM.



The inlayed graph in Figure 6.4a shows the system behaviour at the beginning of the experiment, just after the power supply has been switched on. An initial flat region in all conductivity trends can be seen which results from the time delay between fluid leaving the stack, returning to the reservoir, mixing, and then flowing out to the conductivity probe. This delay is represented in the model through a delayed differential equation and is crucial to capture early behaviour accurately.

The temporal evolution of the current density is shown in Figure 6.4b. In both the experimental and model predicted data, there is an initial increase in the current density before it reaches a maximum at $\sim 160 \text{ A/m}^2$ and then decreases. After passing an inflection point at $\sim 760 \text{ s}$ the current density asymptotically decreases to $\sim 10 \text{ A/m}^2$. These trends in the current density can be explained through examining the contributions to the cell resistance from each of the three streams and investigating the evolution of the transport number. As discussed above, the increase in the conductivity of acid and base streams is faster than the decrease in the conductivity of the diluate stream. Since electrolyte resistance is inversely proportional to conductivity, the increase in the resistance of the diluate is initially offset by a larger decrease in the resistances of the acid and the base streams owing to the flood of additional ions. Consequently, the cell resistance decreases and the current density increases. However, the resistance of the diluate soon begins to dominate, again due to the inverse relationship to the conductivity, and the current density falls. As the diluate concentration falls to near-zero, the current, which is related to the gradient of the conductivity curve, would also be expected to fall to near-zero. The fact that it does not is notable and is discussed further below.

The residual current of ~10 A/m² at times greater than 3000 s is significant relative to the rate of change of the stream conductivities. In a model with a constant transport number, the rate of change of the reservoir concentration with time would be proportional to the current density. However, despite the gradient of the conductivity curves falling to 0.5 % of that at the start of the time series, the current only decreases to 5 % of the initial value. This can only be explained by a large reduction in the membrane transport numbers leading to unwanted back-migration and wasted current. This is exactly what is seen in the calculated transport numbers shown in Figure 6.4c. Both membrane transport numbers are initially high at their intrinsic values but decrease to very low values. Additionally, the transport number for the AEM drops to a lower value than for the CEM. This explains the high current density relative to the overall mass transfer. As the concentration of ions in the acid and base streams increase to many times greater than that of the diluate, the rate of back-migration of co-ions increases. This is the dominant source of current across the AEM and CEM later in the experiment.

The transport number for the AEM drops lower than for the CEM because the AEM has a lower intrinsic transport number than the CEM. The overall transmembrane concentration ratios for both membranes remain similar throughout the experiment and thus the only difference in Eq. 6.32 is $\bar{t}_{m,o}$. Hence, the intrinsic transport number is the primary driver and so its value is crucial in establishing the membrane selectivity when extreme concentration gradients are present.

When operating conventional ED, it is usually not possible for the average of the two transport numbers to fall below 0.5. A transport number of 0.5 means that equal amounts of current are carried by both co-ions and



counterions. When this occurs in both membranes for conventional ED, there is no overall ion transport between the streams, and a stable equilibrium is reached. However, at a little after 2000 s in Figure 6.4c, the average transport number for the AEM and CEM falls below 0.5 and towards the end reaches as low as 0.22. After this point, a majority of the current is being carried by co-ions from the acid and base streams into the diluate. Consequently, $\sim 90\%$ of the 10 A/m² of current at the end of the experiment is involved in transporting protons and hydroxide ions from the BPM and across the AEM and CEM as co-ions, respectively, where they recombine. The energy expended in this cyclical process splitting and recombining water molecules is entirely lost.

The flux magnitudes of each ion across the CEM and AEM are shown in Figure 6.4e and f, respectively. The effect of the low transport numbers can very clearly be seen here. The trends of the Na⁺ and Cl⁻ fluxes across the CEM and AEM, respectively, follow a very close trend to the current, with one key difference. They initially increase before decreasing to an inflection point and asymptotically approach a low value. However, while the fluxes of Na⁺ and Cl⁻ approach a flux of zero as ions are depleted in the diluate, the current does not. Proton and hydroxide co-ion transport from the acid and base to the diluate begins to dominate at later times, again demonstrating that the current flowing is being wasted on water splitting followed by recombination. An interesting difference between Figure 6.4e and f is that while proton co-ion flux is present within the AEM for the entire duration, the same is not true about hydroxide ions and the CEM. This will be explored further in Section 6.4.1.

The evolution of the predicted and experimentally measured pH is shown in Figure 6.4d. All three streams start off at a pH of around 7, as expected for a neutral NaCl solution. Soon after the power supply is activated, the pH of the base rapidly increases, and the pH of the acid rapidly decreases, in line with the model results and what would be expected. However, there is a clear difference between the experimental and modelling results for the pH of the diluate stream. The diluate pH decreases slowly relative to what is predicted, before dropping faster and steadily rising again. Several inflection points can be seen in the experimental data which is not present in the model predictions. This trend was seen qualitatively in all experimental repeats performed but differed somewhat quantitatively. The change in the diluate pH is the result of protons and hydroxide ions permeating as co-ions from the acid and base streams, respectively. Hence, if an ideal membrane permselectivity is assumed, the diluate pH would remain more-or-less constant. The flux of protons and hydroxide ions depends very strongly on several parameters which change significantly over the course of the experiment. These are the current density, membrane transport number, and like-charge selectivity. Extreme differences in concentrations across the membranes are present almost immediately, affecting the like-charge selectivities strongly. Further, since pH is a logarithmic function, small changes in the concentration have disproportionate effects on the pH for neutral solutions. Since the diluate pH remains around 5 to 7 and is adjacent to the acid and base streams with concentrations many orders of magnitudes higher, there are likely to be small degrees of ion crossover not accounted for which result in pH fluctuations. Consequently, the fluctuating nature of the pH of the diluate and the lack of predictability is not unexpected.



An implicit model assumption which might also contribute to the poor prediction of the diluate pH is that of instantaneous transfer or the 'hopping' of ions between the bulk mixed regions of the different streams. This is an artifact resulting from how concentrations are handled by the model. For a given differential slice of the stack (position), it is assumed that the ion flux leaving one channel through a given membrane is equal to the flux entering the corresponding channel adjacent to the same membrane. In other words, there is no accumulation inside the membrane, implying steady-state behaviour or that ions 'hop' between channels. Consequently, protons produced within the BPM can be transported from the BPM to the bulk of the acid stream, then across the AEM, diluate, and CEM to the base channel, effectively instantaneously. For a system operating close to steady state, where changes to the inlet concentration happen slowly, this is a reasonable assumption. However, the pH can be seen to change very rapidly in all three streams. If the real time taken for ions to cross the membranes and boundary layers is of a similar or greater order of magnitude to changes to the inlet conditions, the transit time will have a large effect.

The permeation transit time (t_p) for a membrane can be estimated via a permeation superficial velocity (flux divided by membrane concentration), along with the membrane thickness and water (void) fraction:

$$t_{p,m} = \frac{d_m f_w C_m}{I_m}$$
 [6.46]

For dilute electrolytes, the membrane concentration (C_m) is approximately equal to the fixed charge concentration according to the Donnan equilibrium. Hence, t_p is ~ 60 s for both membranes. This is very significant compared to the residence time of the flow within each channel at ~ 4 s and for the changes in inlet conditions to the base and acid streams. Sixty seconds after the stream inlets begin to change, the base and acid have a pH of 11.5 and 2.5, respectively. For a change this drastic, the permeation transit time is significant and thus could be responsible for the sluggish change in the experimentally observed diluate pH. Nevertheless, industrial operations of BPMED will operate a continuous process where long-term changes do not manifest. As such, the overall impact of the poor predictability of the diluate pH is minimal.

To quantify the agreement between the model prediction and experimental data, the average absolute difference (AAD) for each data series was calculated.

$$AAD = \frac{1}{N_o} \sum_{\text{o-observation}} |\chi_o - \bar{\chi}_o|$$
 [6.47]

Here, N_o is the total number of data points recorded, χ_o is an experimentally observed data point at a particular time, and $\bar{\chi}_o$ is the associated model prediction for the same point in time. Table 6.2 shows the calculated values of the AAD for each data series along with their initial values to aid comparison. For almost all variables, the AAD is less than 2 % of the initial value, demonstrating strong agreement between model predictions and experimental results. The diluate pH is the exception to this, the reasons for which have been explained above. The AAD values in this work are slightly larger than those for conventional ED presented in previous work, but not markedly so. This is somewhat expected due to the significantly greater complexity of BPMED and the incorporation of additional phenomena, each of which contributes a potential source of error. Nevertheless,



Table 6.2: A table evaluating the goodness of fit of the model to experimental data, as represented by the average absolute difference (AAD) and calculated using Eq. 6.47. The value of the variable at the start of the experiment is shown to aid comparison.

| Measured Variable | AAD | Initial Value |
|----------------------|------------------------|-----------------------|
| Current Density | $4.51 \; { m A/m^2}$ | $157~\mathrm{A/m^2}$ |
| Diluate Conductivity | $0.097~\mathrm{mS/cm}$ | $5.95~\mathrm{mS/cm}$ |
| Base Conductivity | $0.187~\mathrm{mS/cm}$ | $5.95~\mathrm{mS/cm}$ |
| Acid Conductivity | $0.158~\mathrm{mS/cm}$ | $5.95~\mathrm{mS/cm}$ |
| Diluate pH | 0.56 | 7.0 |
| Base pH | 0.09 | 7.0 |
| Acid pH | 0.06 | 7.0 |

the low AAD values demonstrates the accuracy of the model despite the lack of experimental fitting parameters and training data.

For both the conductivity and current density, there is very good agreement between model predictions and experimental results. Both qualitative and quantitative agreement is seen throughout the entire time of the experiment. This would not be possible without a model for how the transport numbers evolve, as they can be seen to fall by nearly an order of magnitude. A fixed transport number would result in a significant mismatch between experimental results and model predictions. Taking a high fixed transport number would mean underpredicting the current at the end of the experiment and choosing a low fixed transport number would result in the rate of change of the stream conductivities being too slow.

The assumption of negligible diffusion can be scrutinised here. Ion diffusion is greatest relative to electromigration towards the end of the experiment when the transmembrane concentration difference is greatest. The maximum concentration difference attainable is on the order of 100 mol/m^3 . With a membrane diffusivity of $\sim 1 \times 10^{-11} \text{ m}^2/\text{s}$ and membrane thickness of 0.5 mm, this gives a membrane diffusion flux of $2 \times 10^{-6} \text{ mol/m}^2/\text{s}$. At the end of the experiment, the current density is $\sim 10 \text{ A/m}^2$. Dividing this by the Faraday constant gives an electromigratory flux of $\sim 1 \times 10^{-4} \text{ mol/m}^2/\text{s}$. This is two orders of magnitude greater than the diffusion flux. It should be noted that under these circumstances, the rate of diffusion is greatest relative to electromigration. Thus, the assumption that transport by diffusion is negligible relative to electromigration is justified.

6.3.2 Steady-state current-voltage validation

Current-voltage polarisation curves are ubiquitous in the research of electromembrane systems. As such, the ability to accurately model this behaviour is paramount for design and optimisation. When operating an electromembrane unit there is an inherent trade-off between the specific energy consumption and total membrane area, which comprise a large proportion of the operating and capital costs, respectively. The specific energy consumption is proportional to the applied voltage, and the membrane area is inversely proportional to it. Therefore, an optimum voltage and membrane area exists which minimises the total costs of a BPMED operation. Accurate process design and optimisation of units is one of the objectives of this modelling work, and so this form of validation is essential.



Figure 6.5a shows the time series data for the applied voltage and measured current density. After each step increase in the voltage, the current can be seen to spike, before asymptotically decreasing towards a new steady state. This occurs because there is an initial surge of current resulting from the transient thickening of the electric double layer and an increase in the degree of concentration polarisation as a new equilibrium concentration field develops. Additional current resulting from these effects would not be present during steady-state operation, and so is allowed to dissipate before the measurement is taken. The time taken to reach a new equilibrium is demonstrative that transport is far from instantaneous, providing evidence for the claim that this delays changes to the diluate pH. There is much less transient behaviour above 10 V, where the current reaches its steady-state value almost immediately.

Figure 6.5b shows the resulting steady-state current-voltage response curve for both the experimental data and model predictions. At low voltages, below ~5 V, there is essentially no steady-state current seen in either the model or experimental data. This is because there is a minimum operating voltage for current to flow, which results from the reactions that occur within the bipolar membrane and at the electrodes. The electrode reactions have an equilibrium potential of 1.23 V, and the bipolar junction potential drop is proportional to the pH difference across it (Eq. 6.12). Any meaningful current immediately results in a value of ΔpH on the order of 10, and so an effective minimum bipolar potential drop can be calculated to be ~0.5 V. Summing these voltage drops

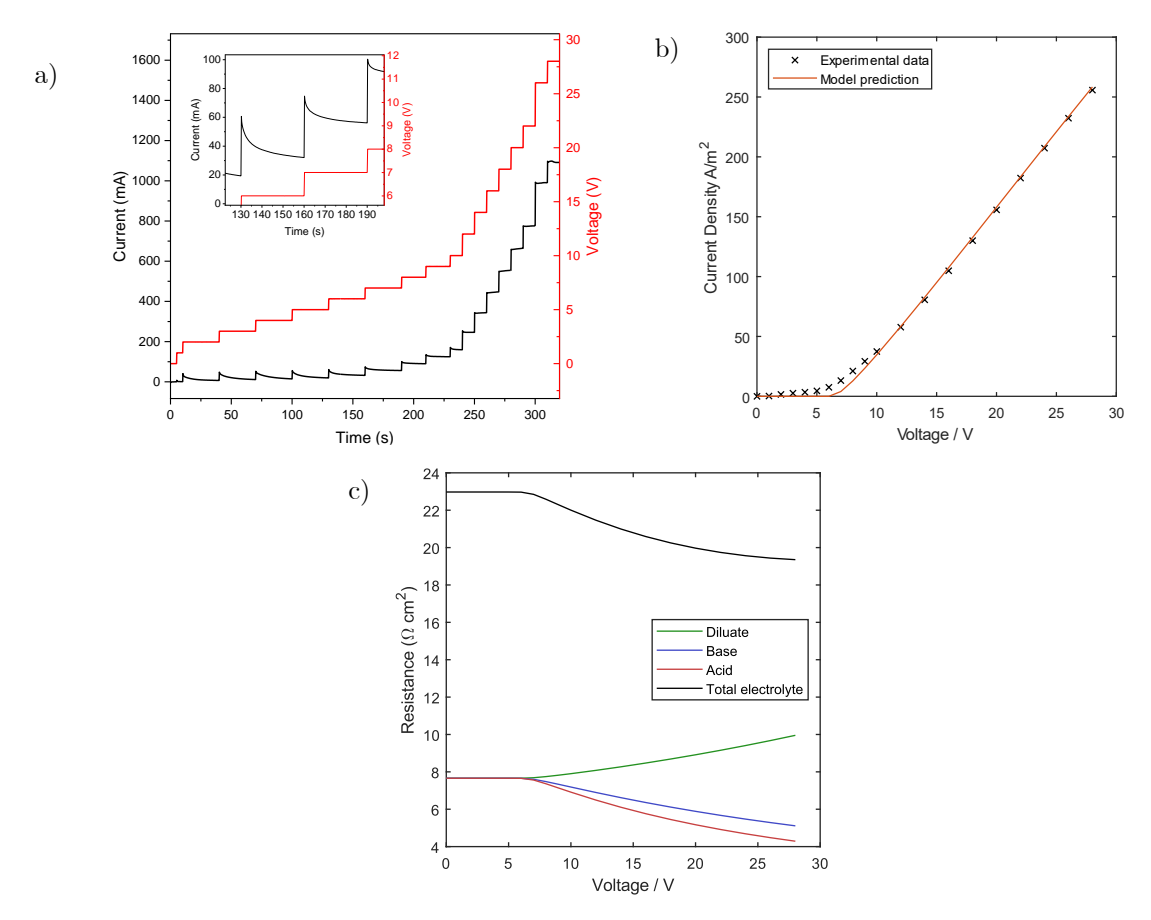


Figure 6.5: Results of the steady-state validation. a) The temporal profile of the current (black) and voltage (red) over the course of the experiment. The inlayed graph shows a magnified area highlighting the assymptotic approach to a steady state. b) The steady state current-voltage response curve. Experimental measurements are shown with crosses and the model is shown with a solid line. c) A graph showing how the calculated resistances for the three streams and the total electrolyte resistance vary with the applied voltage.



for the eight bipolar membranes and the electrode reactions shows that for any current to flow, a minimum voltage of 5.23 V is required. This is reflected in both the model and experimental results.

At higher voltages, above 10 V, the current-voltage response appears to be linear, characteristic of a constant resistance. As voltage increases, the electrolyte resistance is the only resistive element which meaningfully changes. The membrane resistance, bipolar junction potential drop and electrode overpotential do all change as well, but by a relatively low amount due to the form of their equations. The electrode overpotential is a logarithmic function of the current density, whereas the BPM voltage drop, and membrane resistance are both affected by the internal ion concentration. For the dilute solutions used in these experiments, the internal concentration is close to the membrane fixed charge density and does not vary much with the external solution. However, the electrolyte resistances are more directly affected by the applied voltage. A higher voltage will result in a decrease in the diluate concentration and an increase in the acid and base concentrations due to greater salt transfer and water splitting. Resultantly, increasing the voltage increases the diluate resistance and reduces the acid and base resistances (Figure 6.5c). The increase in the resistance of the diluate is greater than the decrease in acid and base resistance since they are inversely proportional to the salt concentration. However, the additional H⁺ and OH- ions to the acid and base streams from the BPM offsets this difference, resulting in a small overall reduction in the total electrolyte resistance. This is the same effect that causes the current density to initially increase in the early stages of the temporal validation experiments (Figure 6.4b). Even so, the overall impact to stream concentrations is relatively low over this voltage range as the inlet concentrations are constant. Consequently, the overall resistance of the stack in the voltage range only slightly increases and so a near-linear trend in the current-voltage curve is seen.

There is a very good agreement between the model prediction and experimental current-voltage polarisation data, with an AAD of 3.11 A/m². This is very low compared to the range of current density that is measured (250 A/m²), demonstrating the close match between the model and the data. The largest divergence occurs during the transition above the minimum splitting voltage around 5 V. Here, experimentally measured currents are somewhat larger than those predicted by the model. One potential reason could be that not enough time was allowed for the transitory current to dissipate after each step-increase in the voltage. The decay of this current was slowest within the transition region, and thus it would have the greatest effect here. This can be evidenced by the tails of the current in Figure 6.5a do not quite reach a steady value. Alternately, the assumption of the exclusion of external ions from the BPM could be responsible. Small amounts of Na⁺ and Cl⁻ ions permeating the BPM at low voltages could provide the low amount of current seen. Nevertheless, the close agreement between the experimental data and model predictions for the current-voltage polarisation curves demonstrates that the model is accurate over a wide range of voltages.

6.4 Model exploration

There are a huge number of individual phenomena comprising BPMED which all aggregate and influence the macroscale variables that are experimentally measured. A core strength of mathematically modelling complex



processes is the ability to extract the profiles of the variables representing those phenomena. This is particularly useful for BPMED and other electromembrane processes where empirical measurement of some phenomena is unfeasible. Understanding which phenomena are limiting allows for conclusions to be drawn about where future research developments can have the greatest benefit. For BPMED, acid-base reactions are one of the most obfuscated phenomena which also has a huge impact on the overall process. In this section, the numerically predicted reaction trends are explored.

Another valuable insight to be gained through model analysis is the impact of the assumptions made during development. Thes can be readily evaluated by directly comparing data from predictions where the assumption is active and inactive. Here, the impacts of using a delayed temporal material balance and an effective current density are assessed to evaluate their underlying assumptions.

6.4.1 The impact of a delayed temporal balance

The inclusion of a delayed temporal material balance was determined to be necessary to account for the significant time taken for the fluid to be transferred from the reservoirs to the stack and back again. Here, the impact of the inclusion of this delay is investigated. The model prediction curves used for experimental validation in section Figure 6.4 for the conductivity and current density are presented in Figure 6.6a and b, respectively. The only difference between the models used to generate the two curves is whether a time delay has been included in the material balance. There is a clear difference between the two predicted trends, where changes in measured variables in the non-delayed predictions occur earlier and faster. The difference cannot be completely removed by simply shifting the predicted data series to a later time. If experimental fitting on training data was used to attempt to match the non-delay predictions to the experimental results (which closely match the delay predictions), then erroneous manipulations would occur. The ion flux would need to be reduced to artificially slow down changes to conductivities while maintaining a similar current density. This could potentially involve artificially reducing the membrane transport numbers, lowering the efficiency and slowing down overall changes. Consequently, the extrapolation of the fitted model to a different system would be greatly hampered.

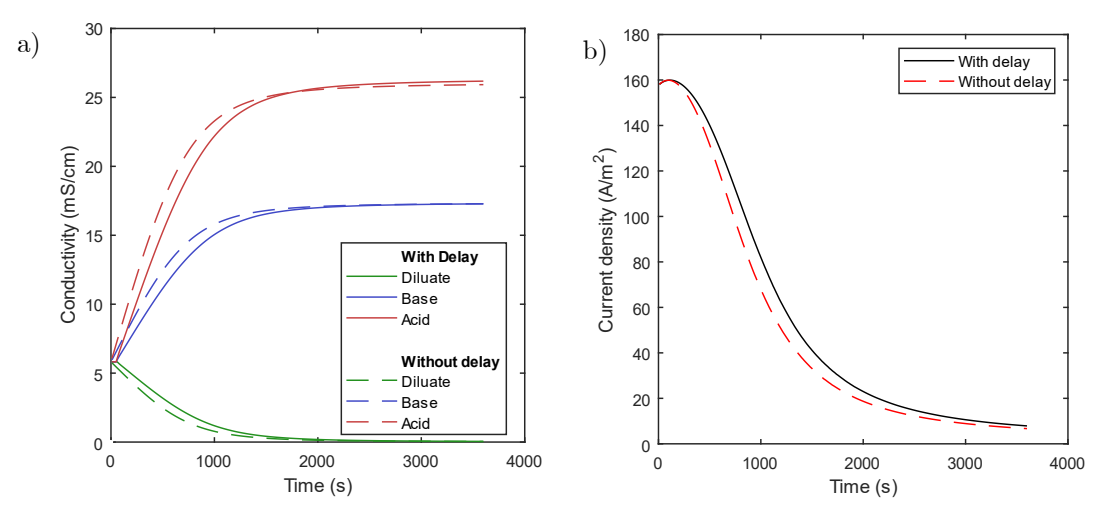


Figure 6.6: The effect of a time-delayed material balance. a) a comparison of the evolution of the calculated conductivity with and without the inclusion of a delay in the material balance. b) A graph showing the effect the inclusion of a delay has on the current density.

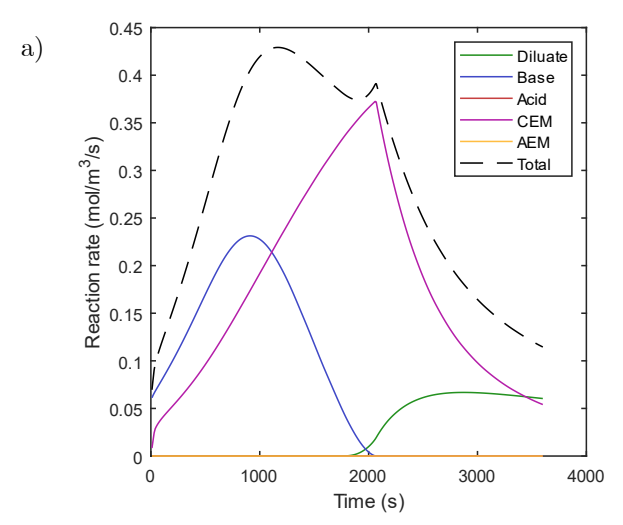


A further impact of including a delay can be seen in a clear difference between the asymptotic limits that the acid conductivity reaches after 2000 s. This is likely due to the delay measured for the acid stream being 5 s lower than for the other two streams. This slight difference on a single pass accumulates over the duration of the experiment producing a meaningful difference. Again, removing this effect by fitting the model to training data would be possible but reduces the model's globality.

6.4.1 Investigating the rate of reactions

The temporal profile for the overall rate of water-recombination reactions in each of the five reacting domains is shown in Figure 6.7a. This data has been extracted from the predicted profiles generated for the experimental validation of Section 6.3.1. Here, the water recombination reaction where H⁺ and OH⁻ ions form water is defined as positive, and the reverse as negative. The reaction rate is always positive, indicating that the recombination reaction is dominant over splitting. This makes intuitive sense, since the ions produced in the bipolar membrane are an excess to the equilibrium already present. Therefore, it is the recombination reaction that is consistently the direction taken back to that equilibrium.

The total rate of reaction can be seen to increase initially before peaking and then decreasing, before reaching a second, sharp peak, at just after 2000 s. This overall profile is the sum of trends in three of the five domains, where the reaction sequentially dominates. Reaction is fastest first in the base stream before the CEM takes over, and then within the diluate, this time tending towards a stable value. The current density is a key driver of the overall reaction trend witnessed (Figure 6.4b). A higher current density results in a greater rate of water splitting in the BPM, a higher migratory flux of protons and hydroxide ions, and thus a greater rate of reaction. However, the rate of reaction peaks at about 1200 s, long after current density does at 120 s. This is because most of the reaction occurs between protons and hydroxide ions that have leaked through the AEM and CEM as co-ions, respectively. As such, the rate of co-ion migration is the greatest driver of the reaction rate. The increasing concentration in the acid and base streams and declining concentration of the diluate stream both reduces the



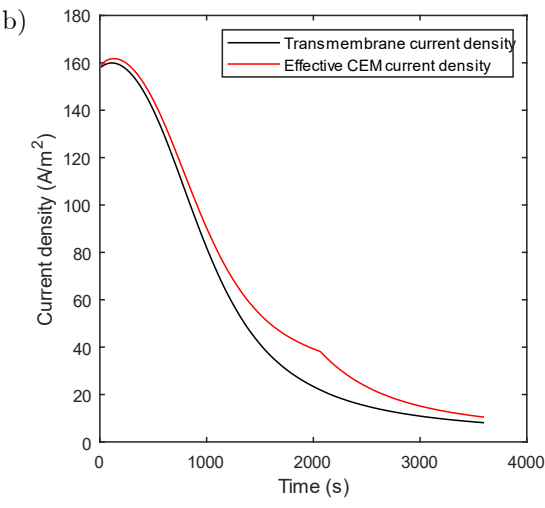


Figure 6.7: a) A graph showing the temporal evolution of the rate of reaction within each of the five domains (three streams, two membranes) where the water recombination reaction is defined as positive. The total reaction rate is shown with a dashed line. b) A comparison of the calculated effective current density and the 'true' or transmembrane current density



transport number of the membranes and increases the like-charge selectivity to protons and hydroxide ions. Both these effects combine to increase the flux of H⁺ and OH⁻ through the AEM and CEM, respectively, even as the current density is decreasing.

The observed successive dominance of reaction within the base, CEM, and diluate is indicative of a shifting reaction plane. The lower intrinsic transport number of the AEM relative to the CEM (0.96 to 0.99) and the higher diffusivity of protons results in the co-ion flux of protons to the diluate from the acid being initially around six times that of hydroxide ions from the base. This is illustrated by the drop in the pH of the diluate. Subsequent transport of protons across the CEM to the base stream is fast since they are now transported as counterions and hence overwhelm hydroxide co-ion transport. Consequently, the reaction is initially dominant within the base stream. Over time as the diluate concentration decreases, the transport numbers of both the transporting membranes decrease. The decreasing CEM transport number along with the increasing like-charge selectivity to hydroxide ions result in the co-ion flux of OH increasing and thus the reaction plane shifts to within the CEM. The peak of the CEM reaction rate at just after 2000 s coincides with when the hydroxide flux matches and then exceeds the proton flux (Figure 6.4f). At the peak, the fluxes of protons and hydroxide ions are equal, leading to complete neutralisation and no transmembrane migration of these ions. After this point, the flux of hydroxide ions exceeds that of protons in the CEM, shifting the reaction plane to within the bulk of the diluate. The sharp peak present in the CEM reaction rate is the result of how the reaction flux is calculated in Eq. 6.37: it is the lower of the H⁺ and OH⁻ fluxes. Since they intersect at a point when hydroxide flux is increasing and proton flux is decreasing, a smooth function is not expected. The approach to a steady current density and rate of reaction in the diluate towards the end of the time series suggests that at this point, a stable situation is arising. Here, protons and hydroxide ions are generated within the BPM and are ultimately both transported to the diluate where they combine once again, wasting energy.

Negligible reaction can be seen in the AEM and the acid streams which results from the transport number of the AEM being lower than the CEM. Hydroxide ions do not get a chance to make it to the acid stream before being neutralised either in the CEM or the diluate. As such, the only reaction in the acid stream is the negligible buffering effect that the existing hydroxide ions have (mostly constant at $\sim 2.7 \times 10^{-3} \text{ mol/m}^3/\text{s}$).

Through these results, a weakness of the circuit-based modelling strategy can be seen. Modelling using the Nernst-Planck equation in software such as COMSOL Multiphysics reveals that due to the rapid kinetics, water recombination reactions essentially occur within a plane. However, in Figure 6.7a, a considerable amount of reaction is occurring concurrently in multiple domains. This results from two features of the circuit-based model: plug flow within the channels (one-dimensional concentration profiles) and instantaneous transfer between the domains. During the early stages of the time series, proton transfer is greater than hydroxide transfer over the CEM, but both are significant, so there is substantial reaction within the CEM. However, because transport is instantaneous and the bulk electrolytes are assumed to be well mixed, the excess protons transported over the CEM then react with the large hydroxide concentration within the base stream. In reality, a reaction plane would be formed, most likely within the CEM or the boundary layer of the base stream.



Despite this inaccuracy, there is no impact on the overall model predictions which would affect process design and optimisation. The overall rate of recombination, in mol/s, is about four orders of magnitude lower than the ion molar flow of the streams passing through the stack. Therefore, while accounting for reactions is important for a long duration experiment, the precise location of where these reactions occur is not. Further, an estimate for the location of the 'true' reaction plane can be discerned from the relative reaction rates in the base, CEM, and diluate domains. It is likely to exist somewhere between the two active domains and depend on their relative rates. Flow boundary layers are not considered within this model but are a likely place for reactions to occur. Again, simply accounting for this excess of ions within the model is sufficient for macro-scale results to be accurate. Deeper insight into the precise location of the reaction plane may be hampered, but the success in achieving the original goal of the model is not affected.

The effect that considering membrane reactions and an effective current density has can be seen in Figure 6.7b, where the effective current density of the CEM is compared to the 'true' current density. The effective current density of the CEM is always greater than the actual transmembrane current density due to the acid-base reactions occurring. The difference between the two curves increases and peaks at just after 2000 s when the rate of reaction within the CEM is the greatest. At this point, the effective current density is ~75% higher than the transmembrane current density. As such, there is a proportional increase in the flux of all ions across the CEM, including sodium and chloride ions. Failure to account for this would result in an inaccurate prediction of the flux. For the set of conditions present in this work, the impact would be limited since the change in the stream conductivities after 2000 s is very low (Figure 6.4a). However, for a different application with a more concentrated feed, this could be very significant.

6.5 Conclusion

In this work, the development, validation, and exploration of a novel circuit-based process model of BPMED is presented. This model was developed without the use of training data or empirical fitting parameters, instead relying on manufacturer provided data only. Consequently, it is hoped that the globality of the model is greatly improved. The model basis uses the analogy of an electric circuit, with different resistive elements for each of the membranes and electrolyte streams. Further, the model was segmented into three layers based on the scale of the domain they consider. In the innermost layer, the current density is found by applying Ohm's law to a differential slice of a cell pair from a cell voltage and cell resistance. The current density was used within the middle layer along with a transport number and like-charge selectivity to compute the fluxes of all species across all membranes using Faraday's first law. This could then be converted to a concentration differential using a spatial material balance and integrated to generate an internal concentration profile. Acid-base reactions were also considered and assumed to be fast enough that active species were always at equilibrium. Their effect within the membranes of releasing additional current was also captured through the computation of an 'effective' current density. The outlet layer considers adaption to a real process that the stack is a part of, which in this work was a recirculating



batch experiment. A delayed temporal material balance was used to compute how the concentration of each species in each reservoir varies with time while accounting for the pipe dead-time encountered by each stream.

Experimental validation of the model was conducted in two orthogonal ways. The first method involved a standard recirculating batch experiment with a fixed voltage and comparing experimentally measured variables (current density, conductivity, and pH) with model predictions. A sub-model which computes the transport number in of each membrane proved vital for accurately computing how the selectivity of each membrane varies. Computed transport numbers fell from near unity to below 0.3, confirming that the use of a fixed transport number is not sufficient. In the second experimental validation, a series of steady-state currents were measured for a range of applied voltages, this time maintaining a constant inlet concentration. Transient currents present after each step-increase in the voltage were allowed to subside and the final steady-state current was compared to model predictions. Both validation methods showed excellent agreement despite the lack of parameter fitting, demonstrating that the model is valid over a wide range of concentrations and voltages.

The use of a delayed temporal material balance to account for pipe dead time is not typical in existing models but was shown here to have a large impact on the temporal evolution of important variables. Small differences were shown to aggregate over lengthy experimental periods and have significant outcomes, especially when streams have different time delays. Further, experimental fitting of a non-delayed model would result in erroneous predictions of important variables such as the electrical resistance or the transport number.

Analysis into the model predictions and calculated fluxes revealed that proton leakage over the AEM is a significant contributor to process inefficiency. Significant proton co-ion flux across the AEM was present throughout the experiment and by the end it was by far the dominating source of current across the membrane. This indicates a strong need to develop AEMs with a higher permselectivity to inhibit the transfer of protons relative to anionic counterions and increase process efficiency.

An exploration of the relative reaction rates for water recombination between the three streams revealed a model limitation where reactions are predicted to occur in multiple streams, rather than in a plane. This limitation arises from the assumptions of instantaneous transfer or ion hopping across membranes and plug flow within the channels. Despite this, it was determined this would have a low overall effect on the model's predictive power for the key variables. Further, the relative reaction rates in each stream could be used to discern an estimated location of the reaction plane within the unit cell.

The primary limitation of this model is that it has only been tested on a single case-study using NaCl as the electrolytic feedstock. This simple case was chosen to ensure that the fundamental phenomena driving BPMED were accurately captured. Future work should focus on expanding the application of the model to more commercially relevant scenarios.

Overall, the flexibility and lack of reliance on fitting to training data are core strengths of the model which can be built on to further improve its predictive capabilities. As BPMED systems become more commercially viable, models such as the one presented herein will prove to be powerful tools for both researchers and industry.



6.6 Tabulated model

| Equation | Unknown variables | Variables | Equations |
|--|-------------------------------------|-----------|-----------|
| $\frac{\partial C_{i,j}}{\partial x} = \frac{1}{u \ d} \sum_{m} \alpha_{i,j,m} \left(J_{i,m} + \beta_{i,j,m,r} \ J_{r,m} \right)$ | $C_{i,j}(t,x),J_{i,m},J_{r,m}$ | 26 | 12 |
| $J_{i,m} = \frac{i_{e,m} \overline{t}_m S_{i,m}}{ z_i F} \forall i \in ct$ | $i_{e,m}, \bar{t}_m, S_{i,m}$ | 8 | 4 |
| $J_{i,m} = \frac{i_{e,m}(1 - \overline{t}_m) S_{i,m}}{ z_i F} \forall i \in co$ | $S_{i,m}$ | 4 | 4 |
| $J_{H,BPM} = J_{OH,BPM} = \frac{i}{F}$ | i | 1 | 2 |
| $J_{Na,BPM} = J_{Cl,BPM} = 0$ | | | 2 |
| $\frac{1}{\bar{t}_m} = 1 + \frac{\sum_{i \in co} z_i C_{i,j}}{\sum_{i \in ct} z_i C_{i,d}} \left(\frac{1}{t_{m,0}} - 1\right)$ | - | | 2 |
| $S_{i \in ct} = \frac{z_i C_i D_i}{\sum_{i \in ct} z_i C_i D_i}$ | - | | 4 |
| $S_{i \in co} = \frac{z_i C_i D_i}{\sum_{i \in co} z_i C_i D_i}$ | | | 4 |
| $\xi_{H/OH,j} = C_{H,0,j} - C_{H,j} = C_{OH,0,j} - C_{OH,j}$ | $\xi_{H/OH,j} C_{H,0,j} C_{OH,0,j}$ | 9 | 6 |
| $\xi_{H/OH,j} = \frac{1}{2} \left[\left(C_{H,0,j} + C_{OH,0,j} \right) - \sqrt{\left(C_{H,0,j} - C_{OH,0,j} \right)^2 + 4 K_w} \right]$ | | | 3 |
| $J_{r,m}=\min\{J_{H,m};J_{OH,m}\}$ | | | 2 |
| $i_{e,CEM} = \min \left\{ \frac{i}{1 - S_{OH,CEM}(1 - \bar{t}_{CEM})} ; \frac{i}{1 - S_{H,CEM} \bar{t}_{CEM}} \right\}$ | | | 1 |
| $i_{e,AEM} = \min \left\{ \frac{i}{1 - S_{H,AEM}(1 - \bar{t}_{AEM})} ; \frac{i}{1 - S_{OH,CEM} \bar{t}_{AEM}} \right\}$ | | | 1 |
| $i = \frac{V_{cell}}{R_{cell}}$ | V_{cell}, R_{cell} | 2 | 1 |
| $V_{cell} = \frac{1}{n_c} (V_{stack} - V_{eq} - \eta - V_{ec}) - V_{bp}$ | η, V_{ec}, V_{bp} | 3 | 1 |
| $\eta = A_a \log \left(\frac{i}{i_{0,a}}\right) + A_c \log \left(\frac{i}{i_{0,c}}\right)$ | - | | 1 |
| $V_{ec} = 2 i \left(R_{eCEM} + \frac{d_{ec}}{\sum_{i} C_{ec,i} \kappa_{mc,i}} \right)$ | | | 1 |
| $V_{bp} = 2.3 \frac{R_g T}{F} \Delta p H$ | ΔрΗ | 1 | 1 |
| $C_{H,BPM} = 0.5 \left(C_{fix} + \sqrt{C_{fix}^2 + 4 \prod_{i} C_{i,a}} \right)$ | $C_{H,BPM}$ | 1 | 1 |



| $C_{OH,BPM} = 0.5 \left(C_{fix} + \sqrt{C_{fix}^2 + 4 \prod_{i} C_{i,b}} \right)$ | $C_{OH,BPM}$ | 1 | 1 |
|--|-----------------------------|-----|--------------|
| $\Delta pH = 14 + \log_{10}(C_{H,CEL} \times C_{OH,AEL})$ | $C_{OH,AEL}$ $C_{H,CEL}$ | 2 | 1 |
| $R_{cell} = \sum_{j} R_j + \sum_{m} R_m$ | R_j, R_m | 6 | 1 |
| $R_j = \frac{d}{\kappa_j}$ | κ_j | 3 | 3 |
| $\kappa_j = \frac{F^2}{R_g T} \sum_i z_i^2 C_{i,j} D_{i,s}$ | | | 3 |
| $R_{m} = \frac{d_{m} \ln \left(\frac{\kappa_{m,1}}{\kappa_{m,2}}\right)}{\kappa_{m,1} - \kappa_{m,2}} m = AEM, CEM$ | $\kappa_{m,1},\kappa_{m,2}$ | 4 | 2 |
| $\kappa_{m,j} = \frac{F^2}{R_g T} \sum_i z_i^2 C_{i,m,j} D_{i,m} m = AEM, CEM$ | $C_{i,m,j}, D_{i,m}$ | 24 | 4 |
| $R_{BPM} = \frac{R_g T}{F^2} \left(\frac{d_{AEL}}{D_{OH,AEL} C_{OH,AEL}} + \frac{d_{CEL}}{D_{H,CEL} C_{H,CEL}} \right)$ | $D_{OH,AEL} D_{H,CEL}$ | 2 | 1 |
| $D_{i,m} = D_{i,s} \left(\frac{f_w}{2 - f_w}\right)^2 exp(-\bar{A}_m z_i^2)$ | $ar{A}_m$ | 3 | 10 |
| $\bar{A}_m = \frac{\theta e^4 N_A^{2/3}}{16 \pi^4 \varepsilon_m^2 k_B^2 T^2} C_{fix}^{2/3}$ | | | 3 |
| $\prod_{i=1}^{2} C_{i,j}^{\nu_i} = \prod_{i=1}^{2} C_{i,m,j}^{\nu_i}$ | | | 12 |
| $C_{OH,AEL} = C_{fix,AEL}$ $C_{H,CEL} = C_{fix,CEL}$ | | | 2 |
| $\sum_{i} C_{i,j} z_i = z_m C_{fix} + \sum_{i} C_{i,m,j} z_i$ | | | 4 |
| $\frac{dC_{R,i,j}(t)}{dt} = -\frac{Q}{V_R} \Big(C_{R,i,j}(t) - C_{i,j}(L,t-\tau) \Big)$ | $C_{R,i,j}(t)$ | 12 | 12 |
| | Total | 103 | 103 |
| $C_{OH,AEL} = C_{fix,AEL} 	 C_{H,CEL} = C_{fix,CEL}$ $\sum_{i} C_{i,j} z_{i} = z_{m} C_{fix} + \sum_{i} C_{i,m,j} z_{i}$ | | | 2 4 12 |

| Initial Conditions | Number of Conditions |
|---------------------------------|----------------------|
| $C_{R,i,j}(t=0) = C_{R,i,j,0}$ | 12 |
| $C_{i,j}(t,x=0) = C_{R,i,j}(t)$ | 12 |



6.7 Nomenclature

| Latin Symbol | |
|---------------------|--|
| A | membrane physical parameter collection |
| A_a , A_c | Tafel slope parameters |
| AAD | average absolute difference |
| b | Wien effect dimensionless parameter |
| С | concentration |
| C_{fix} | fixed charge concentration |
| C_R | reservoir concentration |
| D | diffusivity |
| d | intermembrane distance |
| E | electric field strength |
| e | charge of an electron |
| F | Faraday's constant |
| f_w | water (void) fraction |
| G_0, E_{bp} | bipolar overpotential parameters |
| i | current density |
| i_{0a} , i_{0c} | Tafel exchange current density parameters |
| i_e | effective current density |
| J | ion flux |
| J_r | reaction flux |
| k_B | Boltzmann's constant |
| k_f, k_r | forward and reverse kinetic rate constants |
| K_w | water dissociation equilibrium constant |
| N_A | Avogadro's number |
| n_c | number of cell pairs |
| N_o | number of observations |
| R | resistance |
| R_g | gas constant |
| S | like-charge selectivity |
| T | temperature |
| t | temporal dimension |
| \bar{t} | transport number |
| t_p | membrane permeation time |
| u | velocity |
| V | voltage |
| V_R | reservoir volume |
| x | spatial dimension |



| Z | charge number |
|-------------|---|
| ΔpH | pH difference across the bipolar junction |

| Greek Symbol | |
|--------------------|--|
| α | flux directionality parameter |
| β | reaction handling parameter |
| 3 | permittivity |
| η | overpotential |
| θ | Coefficient of the summation of infinite vectors |
| κ | conductivity |
| μ | ion mobility |
| ν | ion stoichiometry |
| ξ | extent of reaction |
| τ | time delay |
| Φ | electric potential |
| $\chi, \bar{\chi}$ | experimental/model predicted variable value |

| Subscript | |
|---------------------|--------------------------------------|
| 0 | initial/intrinsic value |
| bp | bipolar junction |
| cell | referring to the repeating unit cell |
| со | set of membrane co-ions |
| ct | set of membrane counterions |
| ес | end chamber |
| eq | equilibrium |
| i (= Na, Cl, H, OH) | ionic species |
| j (= d, a, b) | stream |
| m (= AEM, CEM, BPM) | membrane |
| S | referring to solution domain |
| stack | referring to the entire stack |





Chapter 7

Conclusion and future work



7.1 Thesis conclusion

The work presented in this thesis falls under the broad description of the evaluation and improvement of the modelling of electrodialysis (ED) processes. An in-depth analysis of the existing literature focused on exploring models of ED and revealed that there are two broad categories of ED models: 'stipulated equation' and computational fluid dynamics (CFD), which differ based on their implementation. Models which use existing CFD software packages are able to be developed rapidly and are used to generate flow, concentration, and electric potential fields. Through this, a simple but holistic picture of ED is generated, and individual phenomena may be investigated in detail. A common area of study identified within CFD models was that of turbulence promotion, where researchers attempted to improve ED productivity directly through the fluid dynamics. In contrast, stipulated-equation models are developed from the ground up and typically seek to model entire ED systems. Their greater numerical expediency and adaptability proved invaluable for modelling entire units. However, it became clear that there is a huge variability in the existing literature pertaining to the underlying framework and the assumptions taken during the model development. Despite this, virtually all models that were experimentally validated were described as having 'good agreement' with empirical data. The explanation for this comes from a wide use of empirical fitting parameters which obfuscate the true underlying behaviour. This has arisen because modelling ED is very challenging due to the wide variety of interacting phenomena at the nano, micro, and macro scale. In order to capture these effects ranging from the electric double layer formed at the membrane-solution interface to the turbulence generated by the netted spacer, a multi-scale approach to modelling ED which avoids the use of fitting parameters was required. From these conclusions, the gaps in ED modelling literature became clear, which, formulated as questions are:

- i) In what circumstances are the common underlying assumptions used in ED valid?
- ii) What developments are required to produce a generally valid model of ED which avoids the use of training data?

Inroads to answering these questions were made in Part I and Part II of this thesis, respectively.

*

In Part I, an investigation into a ubiquitous assumption taken in all models of ED was performed. The assumption of channel uniformity takes advantage of the repetitive geometry within ED stacks and greatly simplifies modelling efforts. However, in this work, CFD simulations of a typical lab-scale stack geometry showed that a significant amount of flow maldistribution exists. It was seen that the flowrate in the fastest channel was almost twice that of the slowest. This was later validated experimentally using red-blue particle image velocimetry to measure the flow profile within a transparent flow cell with the same geometry as used in the CFD simulations. Experimental measurements using particle image velocimetry showed excellent agreement with CFD predictions, and a statistical analysis demonstrated no bias in the data collection method was present.

Following the establishment of the existence of maldistribution, work was performed to describe it analytically so as to avoid the need for computationally expensive CFD simulations. A maldistribution model originally derived for a plate-and-frame heat exchanger was adapted and compared to the CFD generated data. This simple model



was found to capture the distribution of flow between the channels well, quantifying the maldistribution in a single dimensionless number. This proved invaluable when conducting a case study to investigate how the stack geometry and fluid flow rate affects the degree of maldistribution. In general, it was found that design changes which increase the flow velocity in the manifold or reduce the channel pressure drop worsen the degree of maldistribution. The analytical model also indicated that maldistribution would be significantly worse for industrial scale stacks.

The presence of maldistribution in ED is interesting from an academic perspective, but this alone did not satisfy. Further work was performed to quantify the effect that maldistribution has on ED performance through two important metrics: the limiting current density (LCD) and the overall stack resistance, capturing local and global effects, respectively. It was found that while maldistribution only slightly increases the electric resistance, the LCD is significantly reduced. Consequently, it was indicated that the impact of maldistribution arises locally and in the slowest flowing channel. Further, it was concluded that the effect of maldistribution could be obfuscated by the use of highly empirical LCD models which explains why it has not been historically explored. Experimental validation of the effect maldistribution has on the LCD showed a similar qualitative behaviour and order of magnitude to model predictions. Greater numerical accuracy could arise from a more advanced model of the LCD.

Overall, this package of work demonstrated that one of the most fundamental assumptions in ED, that performance scales linearly as more cell pairs are added, is not valid. The next steps of this work would focus on remediation and is discussed in Section 7.2.2. This work also speaks to the danger of using untested assumptions in modelling. The assumption of channel uniformity is so ubiquitous that unbeknown maldistribution impacts hundreds, if not thousands of modelling and experimental ED publications. Models should be scrutinised at every step of development and no assumption should be taken for granted, not even those that form the *status quo* of the field. This philosophy was implemented in Part I where the highest level of scrutiny was applied to the maldistribution results. The modelling work was validated through experimentation, and the experiments were validated using a statistical model. Research should always be trying to disprove itself because it is where things don't work that discoveries are made.

*

Part II of this work consisted of using the lessons learned from the literature review and analysis of maldistribution to develop an advanced model of ED. There were several features that this model was required to have, including: flexibility, such that additional phenomena could be included ad hoc; applicability to adjacent electromembrane processes; strong predictive capabilities over a wide range of process conditions; and being not reliant on empirical training data and fitting parameters. The resulting model was based on an analogous circuit where different resistive elements represented the membranes and solutions. This provided a robust framework where fundamental equations such as Ohm's law and Faraday's first law could be leveraged, and additional phenomena could be introduced through modifications to the material balance and equivalent circuit. The separation of the model into different layers, each representing a different spatial domain, further facilitated modification and adaptation from a batch experiment to a continuous process.



Experimental validation was performed where the predictive capabilities of the model were tested through comparison to experimental data. This was performed in two orthogonal ways and provided scrutiny over a wide range of both concentration and stack voltage. Good agreement between model predictions and experimental data was seen, which is notable considering no experimental fitting was performed. There were two key novel model features which enabled this performance to be achieved. These were a transport number model which considers the changing membrane selectivity as a function of the trans-membrane concentration difference and a membrane resistance model. Consequently, this model will theoretically be able to perform accurate process design and optimisation across a range of processes and operating conditions. However, it is likely that complications will impede model accuracy when applied to a real process. A certain amount of experimentation will be required to understand the source of the complications, be it transient changes resulting from fouling or the preferential selectivity of membranes to a certain species. Nevertheless, the adaptability of the model framework along with the guiding principles of development will ensure that these complications can be handled.

The sixth chapter of this thesis explored the adaptation of the formulated model to bipolar membrane electrodialysis. This required the implementation of several new model aspects such as acid-base equilibrium reactions, the voltage drop at the bipolar junction, a like-charge membrane selectivity, and an 'effective current density' to account for current freed up by neutralisation reactions occurring within the membrane. Experimental validation showed that this model was also accurate across a wide range of concentrations and voltages but less so than the conventional ED model due to the added complexity. Nevertheless, the strength of the model framework was demonstrated.

*

Overall, this work has shown that superior methods of modelling ED exist and that empirical fitting parameters are not necessarily needed for accurately capturing the process. Electrodialysis is a very complex technology and requires careful consideration when modelling to avoid the phenomenon of over-fitting. There is a need to isolate complex phenomena such as the transport number and membrane resistance rather than lumping them together and retroactively compensating for them. The primary limitation of the two circuit-based models developed is that they have only been tested on a very simple system, sodium chloride. Further, they were only tested with one starting concentration. It was claimed that the model should have more general applicability than other ED models because the model agreed well with experimental data without needing to be fit. This assumption remains very much untested and could fall apart when the model is applied to another system. Despite this, the simplicity of sodium chloride is both a strength and a weakness. Accuracy of the model on this system shows that it can capture fundamental behaviour well. Further, it can do this at the industrially relevant concentration chosen for the experiments. Therefore, although this model may not be able to describe 'real' systems with their added complexity, it serves as a base framework that can be built upon. On the whole, it is hoped that this work will serve as an adequate guide for future research into ED modelling, some natural next steps of which are outlined in the next section.



7.2 Future work

It is believed that this work has laid a strong foundation in both the analysis of maldistribution within ED and development of advanced models of ED. However, there is still ample room to continue research in both areas. In this section, notable follow-on topics of study are explored. In most instances, work in these areas had already begun as part of this Ph.D. project but were cut short due to time constraints and existing research priorities.

7.2.1 Predictive maldistribution

The analytical maldistribution model developed in Chapter 3 was shown to be a powerful tool for representing the degree of maldistribution, notably through a single dimensionless number, m. However, extrapolation of this model is limited due to the need to find a 'mean channel pressure drop' before m can be computed. In Chapter 3, this pressure drop was computed either from a CFD simulation or retroactively extracted after fitting the analytical model to channel-velocity data. It would be incredibly valuable to calculate the maldistribution number and thus the flow distribution a priori. This would entirely circumvent the need to conduct computationally expensive 3D CFD simulations and fully generalise the work conducted. The greatest barrier to this goal is the prediction of the channel pressure drop. This was attempted through the use of the Darcy friction factor correlations for plate flow but did not achieve the desired accuracy (Figure 7.1). The greatest qualitative divergence between the predicted and fitted m was seen as the flow rate tended towards zero. The CFD simulations for the U-configuration geometry predicted that the maldistribution number would tend to a non-zero value (about 0.8). However, the formation of the Darcy friction factor equation and analytical maldistribution model meant a zero flow would always result in a zero pressure drop and thus an m of zero. Other pressure drop models were used including the Darcy-Weisbach equation but produced a similar result.

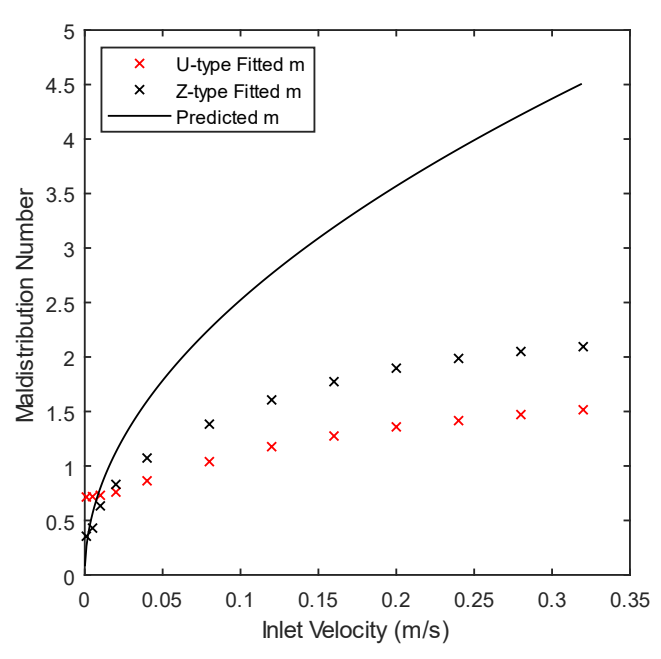


Figure 7.1: A comparison of the dimensionless maldistribution number computed from model fitting to CFD data generated in Ansys Fluent, and that predicted using the Darcy friction factor equation.



Possible sources of divergence result from the assumptions taken in these simple models. Channels are generally quite short and so entrance effects not considered by the correlations can be significant. Further, the pressure drop over both the manifolds and the distributors which connect the manifolds to the channels are also possibly non-trivial and neglected in the maldistribution model. Notably, the pressure drop over the manifold was identified as a significant source of divergence between the U and Z-type geometries which explains the behaviour at low flowrates seen in Figure 7.1. Consequently, this will prove to be a challenging but undoubtedly fruitful area of research.

7.2.2 Maldistribution on scaleup and remediation

According to the analytical maldistribution model used in Chapter 2, modifications to the geometry that increase the velocity in the manifold or reduce the pressure drop in the channel lead to an increase in the degree of maldistribution. The single greatest effect came from increasing the number of cell pairs since the inlet velocity and thus the manifold velocity will scale linearly as more cell pairs are added (assuming a constant average channel flow rate). The dimensionless maldistribution number is also directly proportional to the number of cell pairs. However, the fit of the maldistribution model to the Fluent data significantly worsened as the number of pairs investigated was increased. Most notably, the flow rate in the slowest channels in CFD simulations was shown to asymptote to a non-zero value when a large number of channels was used, whereas the analytical maldistribution model predicted velocities should tend to zero. The error could be in either of the models. In the CFD data, the predicted channel velocities do not decrease monotonically as would be expected, indicating numerical instabilities in the solution. The analytical maldistribution model has a fundamental assumption of a negligible pressure drop in the manifolds. This is likely to lose verisimilitude for large stacks.

Industrial-scale stacks typically have between 200 and 1000 cell pairs due to the high flow rates of the process streams encountered. Thus, according to the analytical model, maldistribution is predicted to be very severe. This has large implications for industrial operation of ED as it leads to a much lower LCD and the impact on overall electrical resistance could be significant. Consequently, the presence and impact of maldistribution on industrial scale stacks must be investigated experimentally. If the degree of maldistribution does lead to severe impacts on performance, then methods of maldistribution remediation can be investigated. The most obvious solution to this is to have a variable spacer geometry whereby the pressure drop is artificially increased in channels nearer to the entrance. This would encourage flow to channels further away that would otherwise be deprived. Through this, the adverse effects of maldistribution can be abated, and the productivity of ED units can be improved.

7.2.3 Compendium of the impacts of ED model assumptions

Through a comprehensive literature review, it was identified that there is wide variability in existing ED model formulations. This variability exists principally in the phenomena that models include or neglect. In the development of the models presented in Chapters 5 and 6, several choices were made to neglect phenomena that could not be robustly implemented without the use of fitting parameters or that were deemed to have a negligible



effect. Further, model aspects such as a variable transport number and membrane resistance were included here for the first time. For the conditions studied during experimental validation, the assumptions taken were adequate, as demonstrated by the good agreement between the model predictions and experimental results. However, at other conditions, the performance of the model is unknown. It is likely that model performance will vary significantly as key parameters such as the inlet concentration, applied voltage, species studied, membrane properties, spacer geometry, and flow rate are changed. As such, to create a truly general model, its performance must be adequate across all these variations.

To perform this research, the next step would be to include as many phenomena as possible which are likely to occur within ED, but still avoiding the use of fitting parameters. The phenomena neglected in this work that must be added include salt diffusion, water transport, concentration polarisation, Donnan potentials, and maldistribution. Concentration polarisation, in particular, will become very important to include when there is a high current density and a low concentration in the diluate. However, the degree of concentration polarisation is very difficult to predict without empirical relations. It is a strong function of the thickness of the boundary layer adjacent to the membrane which in turn is dictated by the degree of turbulence from the spacer. As such, modelling concentration polarisation accurately will prove to be a challenging but important area of research. Initially thoughts for a new class of ED model are explored in Section 7.2.4.

Once a comprehensive model has been built, the next stage of research can commence. One issue with simply adding as many phenomena as possible is that each one can introduce additional sources of error and uncertainty even if no parameter fitting is conducted. Thus, it would be incredibly valuable to know which phenomena are important in different circumstances. This can be investigated by comparing the model to a wide range of experimental data across a diverse set of concentrations, species, and voltages. Each model aspect can be turned on and off for all permutations of the model formulation. Through this, the impact of each model aspect and thus each phenomenon can be evaluated under a wide range of process conditions. Following this, dimensionless number parameters can be derived which compute the impact of different phenomena. For example, one of these could be the ratio of transmembrane ion flux from diffusion to electromigration, effectively representing the importance of diffusion. Then, suitable ranges of these dimensionless parameters can be defined where a modeller can be confident that assumptions will be valid. Once this has been carried out for a whole variety of dimensionless numbers, 'phase diagrams' could be created which comparatively show the importance of various phenomena under different circumstances. Alternatively, correlations could be derived which give an estimation of the uncertainty introduced for a particular assumption given the value of one of these dimensionless numbers.

7.2.4 Modelling the LCD and the next generation of model framework

The LCD is a very important performance parameter for ED units and being able to predict it is paramount for process designers. However, current modelling methods for the LCD depend on empirical correlations for good accuracy. The accuracy of the LCD model used to evaluate the effect of maldistribution was identified as a limitation when comparisons were drawn between model predictions and experimental results in Chapter 4.



Consequently, a robust model of ED which can both predict the LCD as well as performance in overlimiting conditions would be invaluable. To achieve this, a few model aspects are required that have historically proved difficult to represent.

The first of these is the degree of concentration polarisation in the boundary layers which dictates the concentration at the membrane-solution interface. Transport here is the most complex as it is affected by all three modes: convection, diffusion, and electromigration. In the other two domains, the bulk electrolyte and membrane, transport is typically dominated by convection (from turbulence generated by the netted spacer) and electromigration, respectively. One potential solution to this arises from the development of a new class of model using simplifications to the Nernst-Planck equation and dividing the repeating domain into the three distinct regions (bulk electrolyte, boundary layer, and membrane, Figure 7.2). The resultant 'stratified model' combines the benefits of Nernst-Planck models and circuit-based models by offering rapid calculation as well as the detail of a multidimensional concentration field. In this model, the bulk electrolyte would be solved in the same way as for the circuit-based models of Chapters 5 and 6 using a differential material balance and assuming plug flow. For the boundary layer and the membrane, a second order partial differential equation for the concentration field arises from a combination of the Nernst-Planck and conservation of mass equations. Analytical simplifications to this equation must be derived. Two appropriate boundary conditions are then required for each sub-domain. For the boundary layer, these conditions are a fixed concentration at the interface with the bulk electrolyte and a

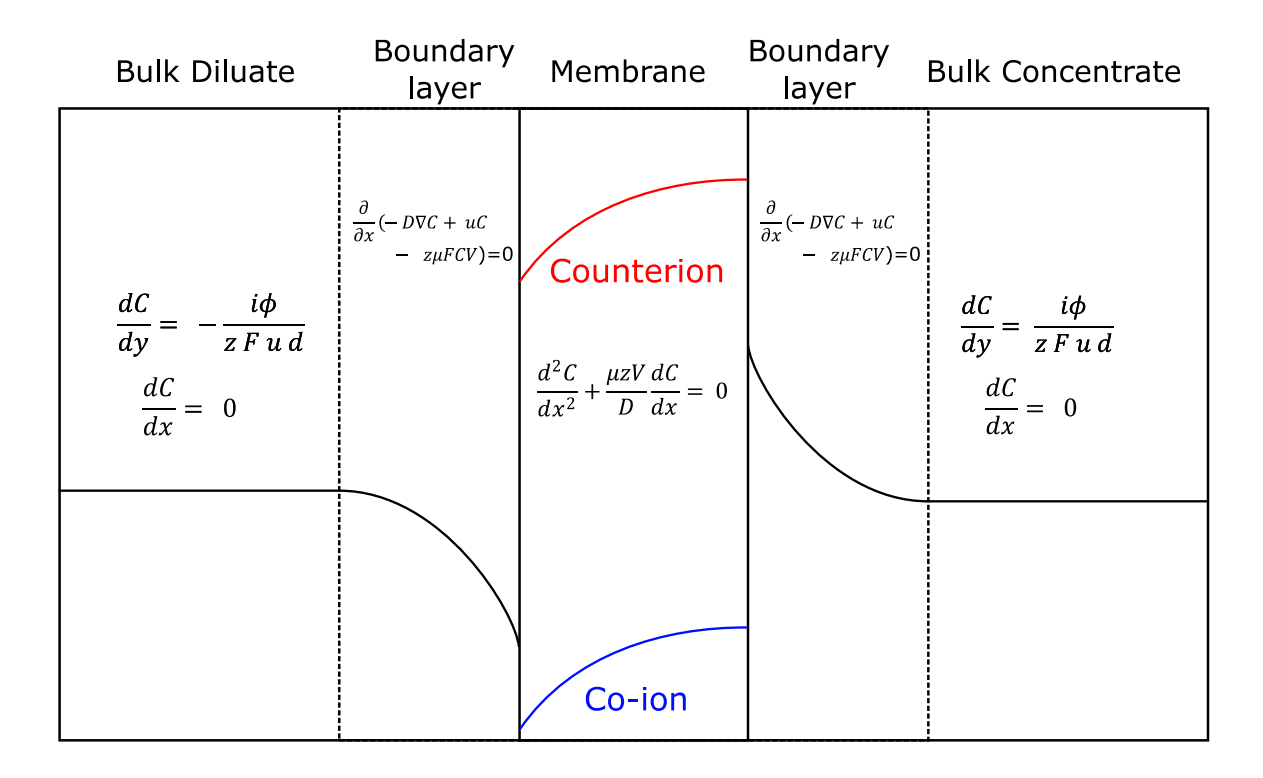


Figure 7.2: A schematic of the proposed 'stratified model' of ED where the repeating cell pair is divided into three sub-domains: the bulk electrolyte, the boundary layers, and the membranes. Each of these sub-domain types have their own governing equations which are solved to compute a two-dimensional concentration profile.



gradient of zero to maintain a smooth profile. For the membrane, two concentration boundary conditions can be used, one at either side, computed using the Donnan equilibrium equations. Simplifications will need to be made to the electric potential field which is typically very stiff and non-linearly coupled with the concentration field. One way of doing this is through Ohm's law and the Einstein-Smoluchowski equation. The electrical resistance profile can be calculated from the concentration using a resistors-in-series approach and then inverted to compute a voltage field. An iterative approach will probably be required due to the interaction with the current density. One of the major hurdles to producing a model like this lies in the boundary layer where all three modes of transport are present. Further, due to convection field being directed vertically (in reference to Figure 7.2) but varying horizontally, the PDE derived from the Nernst-Planck equation dictates transport in two dimensions. More work is required here before the model framework can be constructed.

Another key phenomenon required for accurately modelling conditions at and above the LCD is electroconvection. Classical ED models predict that at the LCD, total ion depletion at the membrane surface is achieved and corresponds to an infinite resistance leading to a hard limit on the ion flux. This is not what is observed experimentally, where an overlimiting current and ion migration is observed but with an increased electric resistance. To account for this, the theory of electroconvection was developed. Here, the strong electric field in regions of ion depletion adjacent to the membrane leads to a modification of the convection field. Flow, which is usually exclusively parallel to the membrane, begins to be driven perpendicular in vortices, causing mixing at the membrane surface. This mixing avoids a total concentration depletion and thus facilitates overlimiting ion transport. Electroconvection has been explored in CFD simulations through modifications to the Navier-Stokes equations through the addition of an electric field body force. However, these simulations are very computationally expensive and are mostly used for their qualitative predictions. Simplifying this effect to a stipulated-equation model will be necessary for rapid quantification of their effects. Combination with the proposed stratified model would be possible through the incorporation of a fourth domain for a space charge region which provides mixing through electroconvection. This would have a flat concentration profile and would require an additional energy penalty to account for electroconvection.

In summary, this new class of 'stratified model' will be able to combine the strengths of circuit-based models and Nernst-Planck models. As such, it would be able to compute two-dimensional concentration fields and notably, concentration polarisation, while maintaining a focus on the overall process performance. Further, this type of model would be able to directly account for the LCD and overlimiting operation which have historically proved challenging to describe mechanistically for simplified models. It is hoped that through this approach, models of ED may be greatly improved.



7.3 Final thoughts

Since stumbling into an internship in Amsterdam in the Summer of 2019, I have been captivated by electrodialysis. The elegance of the underpinning design along with the huge capacity for variation means that there is a large scope for clever solutions as a separation process. The additional attraction of ED being phenomenologically complex and thus challenging to represent mathematically meant that researching it over the course of a PhD project was irresistible. I have gained immense satisfaction from using the mathematical and scientific tools I've developed throughout my entire formal education to the best of my ability. Also, I've spent enough time searching the internet for ED that I'll be getting adverts for erectile dysfunction for the rest of my life...

My approach to research has always been to be an optimistic cynic. In the early stages this manifested as a distrust in the *status quo* and having the confidence to set out to better it. This was also reflected in the work I began to produce. The model presented in Part II of this thesis took the best part of four years and six distinct versions to refine. Each time the model was reconstructed I was not satisfied with the imperfections present and thus strived for better. A big lesson I learned was that 'perfectionism is paralysis' and that unyielding capitulation is counterproductive. Sometimes a sunken cost needs to be abandoned, even if you spent months staring at a COMSOL GUI trying to make it work. Even so, there was so much more I wish I had had time to do, perhaps evidenced by the bloated 'future work' section. Alas.

For a moment I was worried that some of the more personal flares I included in this thesis were too esoteric and self-gratuitous, but at the end of the day is that not fundamentally what a PhD is all about? Given that, I shall end with my favourite George Box quote which aptly summarises the guiding philosophy I have taken throughout my research [200]:

"Remember that all models are wrong; the practical question is how wrong do they have
to be to not be useful."

- George Box





Cited works

- [1] Ernest Hemmingway, The sun also rises, 1926.
- [2] UNESCO, Valuing water The United Nations World Water Development Report 2021, Water Politics (2021) 206. https://unesdoc.unesco.org/ark:/48223/pf0000375724 (accessed July 16, 2021).
- [3] S.L. Postel, G.C. Daily, P.R. Ehrlich, Human Appropriation of Renewable Fresh Water, Science (1979) 271 (1996) 785–788. https://doi.org/10.1126/SCIENCE.271.5250.785.
- [4] A. Boretti, L. Rosa, Reassessing the projections of the World Water Development Report, Nature Clean Water (2019). https://doi.org/10.1038/s41545-019-0039-9.
- [5] U.S. Global Change Research Program, Climate Science Special Report: Fourth National Climate Assessment, Volume I, Washington, DC, 2017. https://doi.org/10.7930/J0J964J6.
- [6] UN, The Paris Agreement | United Nations, (n.d.). https://www.un.org/en/climatechange/parisagreement (accessed August 16, 2021).
- [7] UN, The United Nations World Water Development Report 2023: partnerships and cooperation for water, (2023). https://unesdoc.unesco.org/ark:/48223/pf0000384655 (accessed June 27, 2023).
- [8] The State of Food and Agriculture 2020, The State of Food and Agriculture 2020 (2020). https://doi.org/10.4060/CB1447EN.
- [9] United Nations, The United Nations world water development report 2020: water and climate change UNESCO Digital Library, (2020). https://unesdoc.unesco.org/ark:/48223/pf0000372985.locale=en (accessed February 19, 2021).
- [10] G. Ferguson, J.C. McIntosh, D. Perrone, S. Jasechko, Competition for shrinking window of low salinity groundwater, Environmental Research Letters 13 (2018) 114013. https://doi.org/10.1088/1748-9326/AAE6D8.
- [11] Madagascar is headed toward a climate change-linked famine it did not create The Washington Post, (n.d.). https://www.washingtonpost.com/world/2021/07/01/madagascar-climate-famine/ (accessed March 21, 2024).
- [12] A.O. Jegede, P. Shikwambane, Water 'Apartheid' and the Significance of Human Rights Principles of Affirmative Action in South Africa, Water 2021, Vol. 13, Page 1104 13 (2021) 1104. https://doi.org/10.3390/W13081104.
- [13] A. Harding, Madagascar on the brink of climate change-induced famine BBC News, BBC (2021). https://www.bbc.co.uk/news/world-africa-58303792 (accessed August 25, 2021).
- [14] Circle of Blue, Experts Name the Top 19 Solutions to the Global Freshwater Crisis Circle of Blue, (n.d.). https://www.circleofblue.org/2010/world/experts-name-the-top-19-solutions-to-the-global-freshwater-crisis/ (accessed July 19, 2021).



Integrated Design and Simulation of Chemical Processes - Alexandre C. Dimian, Costin Sorin Bildea, Anton A. Kiss - Google Books, (n.d.). https://books.google.co.uk/books?hl=en&lr=&id=hoBzAwAAQBAJ&oi=fnd&pg=PP1&dq=the+b enefits+of+chemical+process+modelling&ots=nvHErRx9ln&sig=YSmTm09ynOI-HVIUcBQgVyLpU4#v=onepage&q=the%20benefits%20of%20chemical%20process%20modelling&f=false (accessed March 27, 2024).

- [16] V.A. Shaposhnik, K. Kesore, An early history of electrodialysis with permselective membranes, J Memb Sci 136 (1997) 35–39. https://doi.org/10.1016/S0376-7388(97)00149-X.
- [17] E. Jones, M. Qadir, M.T.H. van Vliet, V. Smakhtin, S. mu Kang, The state of desalination and brine production: A global outlook, Science of the Total Environment 657 (2019) 1343–1356. https://doi.org/10.1016/j.scitotenv.2018.12.076.
- [18] S. Al-Amshawee, M.Y.B.M. Yunus, A.A.M. Azoddein, D.G. Hassell, I.H. Dakhil, H.A. Hasan, Electrodialysis desalination for water and wastewater: A review, Chemical Engineering Journal 380 (2020) 122231. https://doi.org/10.1016/j.cej.2019.122231.
- [19] N.L. Le, S.P. Nunes, Materials and membrane technologies for water and energy sustainability, Sustainable Materials and Technologies 7 (2016) 1–28. https://doi.org/10.1016/j.susmat.2016.02.001.
- [20] A. Yusuf, A. Sodiq, A. Giwa, J. Eke, O. Pikuda, G. De Luca, J.L. Di Salvo, S. Chakraborty, A review of emerging trends in membrane science and technology for sustainable water treatment, J Clean Prod 266 (2020). https://doi.org/10.1016/j.jclepro.2020.121867.
- [21] M.T. Demeuse, Production and applications of hollow fibers, Handbook of Textile Fibre Structure 2 (2009) 485–499. https://doi.org/10.1533/9781845697310.3.485.
- [22] S. Roy, S. Ragunath, Emerging Membrane Technologies for Water and Energy Sustainability: Future Prospects, Constrains and Challenges, Energies (Basel) 11 (2018) 2997. https://doi.org/10.3390/en11112997.
- [23] A. Campione, L. Gurreri, M. Ciofalo, G. Micale, A. Tamburini, A. Cipollina, Electrodialysis for water desalination: A critical assessment of recent developments on process fundamentals, models and applications, Desalination 434 (2018) 121–160. https://doi.org/10.1016/j.desal.2017.12.044.
- [24] J. John, A. Gopikumar, G.P. Gayathry, A. Vincent, N.J. Kaleekkal, Enhanced recovery using membrane-based zero liquid discharge systems, Concept of Zero Liquid Discharge: Innovations and Advances for Sustainable Wastewater Management (2023) 129–161. https://doi.org/10.1016/B978-0-323-91745-2.00004-8.
- [25] H.B. Vibbert, A.W.S. Ooi, A.H.A. Park, Selective Recovery of Cerium as High-Purity Oxides via Reactive Separation Using CO2-Responsive Structured Ligands, ACS Sustain Chem Eng 12 (2024) 5186–5196. https://doi.org/10.1021/ACSSUSCHEMENG.3C08103/ASSET/IMAGES/LARGE/SC3C08103_00 07.JPEG.



[26] A. Abou-Shady, C. Peng, J. Almeria O, H. Xu, Effect of pH on separation of Pb (II) and NO 3- from aqueous solutions using electrodialysis, Desalination 285 (2012) 46–53. https://doi.org/10.1016/j.desal.2011.09.032.

- [27] H. Strathmann, Electrodialysis, a mature technology with a multitude of new applications, Desalination 264 (2010) 268–288. https://doi.org/10.1016/j.desal.2010.04.069.
- [28] Y. Kim, D.F. Lawler, Overlimiting current by interactive ionic transport between space charge region and electric double layer near ion-exchange membranes, Desalination 285 (2012) 245–252. https://doi.org/10.1016/J.DESAL.2011.10.009.
- [29] T.A. Davis, J.David. Genders, Derek. Pletcher, A first course in ion permeable membranes, (1997) 255.
 https://books.google.com/books/about/A_First_Course_in_Ion_Permeable_Membrane.html?id=kkdRAAAAMAAJ (accessed August 24, 2021).
- [30] L.M. Robeson, The upper bound revisited, J Memb Sci 320 (2008) 390–400. https://doi.org/10.1016/J.MEMSCI.2008.04.030.
- [31] S.K. Patel, B. Lee, P. Westerhoff, M. Elimelech, The potential of electrodialysis as a cost-effective alternative to reverse osmosis for brackish water desalination, Water Res 250 (2024) 121009. https://doi.org/10.1016/J.WATRES.2023.121009.
- [32] B. Chen, Z. Zhang, C. Jiang, R. Fu, J. Yan, H. Wang, R. Li, G. Cao, Y. Wang, T. Xu, Electromembrane reactor: A powerful tool for green chemical engineering, AIChE Journal 69 (2023) e18140. https://doi.org/10.1002/AIC.18140.
- [33] L.M. Camacho, J.A. Fox, J.O. Ajedegba, Optimization of electrodialysis metathesis (EDM) desalination using factorial design methodology, Desalination 403 (2017) 136–143. https://doi.org/10.1016/J.DESAL.2016.07.028.
- [34] J. Xu, G. Zhong, M. Li, D. Zhao, Y. Sun, X. Hu, J. Sun, X. Li, W. Zhu, M. Li, Z. Zhang, Y. Zhang, L. Zhao, C. Zheng, X. Sun, Review on electrochemical carbon dioxide capture and transformation with bipolar membranes, Chinese Chemical Letters 34 (2023) 108075. https://doi.org/10.1016/J.CCLET.2022.108075.
- [35] C.M. Liang, C.C. Wang, K.J. Huang, C.F. Yang, Production of biohydrogen and green platform compound 2, 5-furandicarboxylic acid using rice straw hydrolysate, Biochem Eng J 197 (2023) 108993. https://doi.org/10.1016/J.BEJ.2023.108993.
- [36] Y. Liu, M. Lv, X. Wu, J. Ding, L. Dai, H. Xue, X. Ye, R. Chen, R. Ding, J. Liu, B. Van der Bruggen, Recovery of copper from electroplating sludge using integrated bipolar membrane electrodialysis and electrodeposition, J Colloid Interface Sci 642 (2023) 29–40. https://doi.org/10.1016/J.JCIS.2023.03.154.
- [37] Y. Zhang, Z. Zhang, K. Guo, X. Liang, Controllable recovery and recycling of carboxylic acid-polyalcohol deep eutectic solvent for biomass pretreatment with electronically-controlled chemical methodology, Bioresour Technol 365 (2022) 128175. https://doi.org/10.1016/J.BIORTECH.2022.128175.



[38] Y. Liu, Y. Sun, Z. Peng, Evaluation of bipolar membrane electrodialysis for desalination of simulated salicylic acid wastewater, Desalination 537 (2022) 115866. https://doi.org/10.1016/J.DESAL.2022.115866.

- [39] Y. Zhao, X. Wang, J. Yuan, Z. Ji, J. Liu, S. Wang, X. Guo, F. Li, J. Wang, J. Bi, An efficient electrodialysis metathesis route to recover concentrated NaOH-NH4Cl products from simulated ammonia and saline wastewater in coal chemical industry, Sep Purif Technol 301 (2022). https://doi.org/10.1016/j.seppur.2022.122042.
- [40] H. Jaroszek, A. Lis, P. Dydo, Transport of impurities and water during potassium nitrate synthesis by electrodialysis metathesis, Sep Purif Technol 158 (2016) 87–93. https://doi.org/10.1016/J.SEPPUR.2015.12.009.
- [41] K. Haerens, P. De Vreese, E. Matthijs, L. Pinoy, K. Binnemans, B. Van Der Bruggen, Production of ionic liquids by electrodialysis, Sep Purif Technol 97 (2012) 90–95. https://doi.org/10.1016/J.SEPPUR.2012.02.017.
- [42] P.F. Li, Q.B. Chen, J. Wang, Y. Xu, L. Dong, J. Wang, Developing a reclamation strategy for softening nanofiltration brine: A scaling-free conversion approach via continuous two-stage electrodialysis metathesis, Science of The Total Environment 807 (2022) 150374. https://doi.org/10.1016/J.SCITOTENV.2021.150374.
- [43] A. Saravanan, P.R. Yaashikaa, P. Senthil Kumar, S. Karishma, P. Thamarai, V.C. Deivayanai, G. Rangasamy, R. Selvasembian, T.M. Aminabhavi, Environmental sustainability of toxic arsenic ions removal from wastewater using electrodeionization, Sep Purif Technol 317 (2023) 123897. https://doi.org/10.1016/J.SEPPUR.2023.123897.
- [44] C. Otero, A. Urbina, E.P. Rivero, F.A. Rodríguez, Desalination of brackish water by electrodeionization: Experimental study and mathematical modeling, Desalination 504 (2021) 114803. https://doi.org/10.1016/J.DESAL.2020.114803.
- [45] E.N. Sarıçiçek, M.M. Tuğaç, V.T. Özdemir, İ.Y. İpek, Ö. Arar, Removal of boron by boron selective resin-filled electrodeionization, Environ Technol Innov 23 (2021) 101742. https://doi.org/10.1016/J.ETI.2021.101742.
- [46] H. Julian, K. Khoiruddin, N. Julies, V. Edwina, I.G. Wenten, Pineapple juice acidity removal using electrodeionization (EDI), J Food Eng 304 (2021) 110595. https://doi.org/10.1016/J.JFOODENG.2021.110595.
- [47] D. Babilas, P. Dydo, Selective zinc recovery from electroplating wastewaters by electrodialysis enhanced with complex formation, Sep Purif Technol 192 (2018) 419–428. https://doi.org/10.1016/j.seppur.2017.10.013.
- [48] C. Jiang, H. Chen, Y. Zhang, H. Feng, M.A. Shehzad, Y. Wang, T. Xu, Complexation Electrodialysis as a general method to simultaneously treat wastewaters with metal and organic matter, Chemical Engineering Journal 348 (2018) 952–959. https://doi.org/10.1016/j.cej.2018.05.022.



[49] Z. Liu, D. Lu, H. Guo, J. Zhang, S. Tao, R. Chen, L.Y. Chen, M. Gong, Experimental study and prospect analysis of LiBr-H2O reverse electrodialysis heat engine, Appl Energy 350 (2023) 121791. https://doi.org/10.1016/J.APENERGY.2023.121791.

- [50] G. Campisi, A. Cosenza, F. Giacalone, S. Randazzo, A. Tamburini, G. Micale, Desalination of oilfield produced waters via reverse electrodialysis: A techno-economical assessment, Desalination 548 (2023) 116289. https://doi.org/10.1016/J.DESAL.2022.116289.
- [51] C. Simões, B. Vital, T. Sleutels, M. Saakes, W. Brilman, Scaled-up multistage reverse electrodialysis pilot study with natural waters, Chemical Engineering Journal 450 (2022) 138412. https://doi.org/10.1016/j.cej.2022.138412.
- [52] M.A. Maluleke, V.M. Linkov, Partial electrochemical oxidation of phenol on ceramic-based flat-sheet type electromembrane reactors, Sep Purif Technol 32 (2003) 377–385. https://doi.org/10.1016/S1383-5866(03)00065-0.
- [53] F. Karimi, S.N. Ashrafizadeh, F. Mohammadi, Process parameter impacts on adiponitrile current efficiency and cell voltage of an electromembrane reactor using emulsion-type catholyte, Chemical Engineering Journal 183 (2012) 402–407. https://doi.org/10.1016/J.CEJ.2011.12.031.
- [54] S. Ozkul, J.J. van Daal, N.J.M. Kuipers, R.J.M. Bisselink, H. Bruning, J.E. Dykstra, H.H.M. Rijnaarts, Transport mechanisms in electrodialysis: The effect on selective ion transport in multi-ionic solutions, J Memb Sci 665 (2023). https://doi.org/10.1016/j.memsci.2022.121114.
- [55] A. Kovalenko, V. Nikonenko, N. Chubyr, Mk. Urtenov, Mathematical modeling of electrodialysis of a dilute solution with accounting for water dissociation-recombination reactions, (2023). https://doi.org/10.1016/j.desal.2023.116398.
- [56] A. V. Kovalenko, M. Wessling, V. V. Nikonenko, S.A. Mareev, I.A. Moroz, E. Evdochenko, M.K. Urtenov, Space-Charge breakdown phenomenon and spatio-temporal ion concentration and fluid flow patterns in overlimiting current electrodialysis, J Memb Sci 636 (2021) 119583. https://doi.org/10.1016/j.memsci.2021.119583.
- [57] T. Brown, H.E. Jr, B. LeMay, J. Catherine, Chemistry: The Central Science: AP Edition, (2015). https://fumk.pw/819.pdf (accessed August 18, 2021).
- [58] J. Kaláb, Z. Palatý, Electrodialysis of Tartaric Acid: Batch Process Modelling, Separation Science and Technology (Philadelphia) 47 (2012) 2262–2272. https://doi.org/10.1080/01496395.2012.673042.
- [59] F. Dyson, A meeting with Enrico Fermi, Nature 427 (2004) 297. https://doi.org/10.1038/427297A.
- [60] B. De Jaegher, W. De Schepper, A. Verliefde, I. Nopens, Enhancing mechanistic models with neural differential equations to predict electrodialysis fouling, Sep Purif Technol 259 (2020) 118028. https://doi.org/10.1016/j.seppur.2020.118028.
- [61] L. Onsager, Reciprocal Relations in Irreversible Processes. I., Phys.Rev. 37 (1931) 405–426. https://doi.org/10.1103/PHYSREV.37.405.



[62] L. Onsager, Reciprocal Relations in Irreversible Processes. II., Phys.Rev. 38 (1931) 2265–2279. https://doi.org/10.1103/PHYSREV.38.2265.

- [63] S.B.B. Solberg, P. Zimmermann, Ø. Wilhelmsen, J.J. Lamb, R. Bock, O.S. Burheim, Heat to Hydrogen by Reverse Electrodialysis-Using a Non-Equilibrium Thermodynamics Model to Evaluate Hydrogen Production Concepts Utilising Waste Heat, (2022). https://doi.org/10.3390/en15166011.
- [64] M. Fidaleo, M. Moresi, Optimal strategy to model the electrodialytic recovery of a strong electrolyte, J Memb Sci 260 (2005) 90–111. https://doi.org/10.1016/j.memsci.2005.01.048.
- [65] S. Casas, N. Bonet, C. Aladjem, J.L. Cortina, E. Larrotcha, L.V. Cremades, Modelling Sodium Chloride Concentration from Seawater Reverse Osmosis Brine by Electrodialysis: Preliminary Results, Solvent Extraction and Ion Exchange 29 (2011) 488–508. https://doi.org/10.1080/07366299.2011.573451.
- [66] Y. xiang Jia, F. jiao Li, X. Chen, M. Wang, Model analysis on electrodialysis for inorganic acid recovery and its experimental validation, Sep Purif Technol 190 (2018) 261–267. https://doi.org/10.1016/j.seppur.2017.08.067.
- [67] H. Nafaa, M. Farhat, S. Lassaad, Mathematical model study of solar electrodialysis desalination, in: 2017 International Conference on Electrical and Computing Technologies and Applications, ICECTA 2017, Institute of Electrical and Electronics Engineers Inc., 2017: pp. 1–4. https://doi.org/10.1109/ICECTA.2017.8251946.
- [68] M. Tedesco, H.V.M. Hamelers, P.M. Biesheuvel, Nernst-Planck transport theory for (reverse) electrodialysis: I. Effect of co-ion transport through the membranes, J Memb Sci 510 (2016) 370–381. https://doi.org/10.1016/j.memsci.2016.03.012.
- [69] B.A. Qureshi, N.A.A. Qasem, S.M. Zubair, Normalized sensitivity analysis of electrodialysis desalination plants for mitigating hypersalinity, Sep Purif Technol 257 (2021). https://doi.org/10.1016/j.seppur.2020.117858.
- [70] A. Chandra, J.G.D. Tadimeti, E. Bhuvanesh, D. Pathiwada, S. Chattopadhyay, Switching selectivity of carboxylic acids and associated physico-chemical changes with pH during electrodialysis of ternary mixtures, Sep Purif Technol 193 (2018) 327–344. https://doi.org/10.1016/j.seppur.2017.10.048.
- [71] H.J. Lee, F. Sarfert, H. Strathmann, S.H. Moon, Designing of an electrodialysis desalination plant, Desalination 142 (2002) 267–286. https://doi.org/10.1016/S0011-9164(02)00208-4.
- [72] M. Della Monica, A. Ceglie, A. Agostiano, Extension of the Falkenhagen equation to the conductivity of concentrated electrolyte solutions, Journal of Physical Chemistry 88 (1984) 2124–2127. https://doi.org/10.1021/j150654a036.
- [73] M. Sadrzadeh, A. Kaviani, T. Mohammadi, Mathematical modeling of desalination by electrodialysis, Desalination 206 (2007) 538–546. https://doi.org/10.1016/j.desal.2006.04.062.
- [74] A. Ghorbani, A. Ghassemi, Brackish water desalination using electrodialysis: predictive mass transfer and concentration distribution model along the electrodialyzer, (2018). https://doi.org/10.2166/wst.2017.547.



[75] M.B.S. Ali, B. Hamrouni, Development of a predictive model of the limiting current density of an electrodialysis process using response surface methodology, Membrane Water Treatment 7 (2016) 127–141. https://doi.org/10.12989/mwt.2016.7.2.127.

- [76] H. Zhu, B. Yang, C. Gao, Y. Wu, Ion transfer modeling based on Nernst–Planck theory for saline water desalination during electrodialysis process, Asia-Pacific Journal of Chemical Engineering 15 (2020). https://doi.org/10.1002/apj.2410.
- [77] A. Campione, A. Cipollina, I.D.L. Bogle, L. Gurreri, A. Tamburini, M. Tedesco, G. Micale, A hierarchical model for novel schemes of electrodialysis desalination, Desalination 465 (2019) 79–93. https://doi.org/10.1016/j.desal.2019.04.020.
- [78] Y. Guo, A. Al-Jubainawi, Z. Ma, Mathematical modelling and simulation analysis of electrodialysis regeneration for LiCl liquid desiccant air conditioning systems, International Journal of Refrigeration 107 (2019) 234–245. https://doi.org/10.1016/j.ijrefrig.2019.08.006.
- [79] H. Luo, W.A.S. Agata, G.M. Geise, Connecting the Ion Separation Factor to the Sorption and Diffusion Selectivity of Ion Exchange Membranes, Ind Eng Chem Res 59 (2020) 14189–14206. https://doi.org/10.1021/acs.iecr.0c02457.
- [80] N.C. Wright, S.R. Shah, S.E. Amrose, A.G. Winter, A robust model of brackish water electrodialysis desalination with experimental comparison at different size scales, Desalination 443 (2018) 27–43. https://doi.org/10.1016/j.desal.2018.04.018.
- [81] B. Sun, M. Zhang, S. Huang, W. Su, J. Zhou, X. Zhang, Performance evaluation on regeneration of high-salt solutions used in air conditioning systems by electrodialysis, J Memb Sci 582 (2019) 224– 235. https://doi.org/10.1016/j.memsci.2019.04.004.
- [82] A. Luiz, D.D. McClure, K. Lim, H.G.L. Coster, G.W. Barton, J.M. Kavanagh, Towards a model for the electrodialysis of bio-refinery streams, J Memb Sci 573 (2019) 320–332. https://doi.org/10.1016/j.memsci.2018.11.047.
- [83] N.A.A. Qasem, B.A. Qureshi, S.M. Zubair, Improvement in design of electrodialysis desalination plants by considering the Donnan potential, Desalination 441 (2018) 62–76. https://doi.org/10.1016/j.desal.2018.04.023.
- [84] J.H.G. Van Der Stegen, A.J. Van Der Veen, H. Weerdenburg, J.A. Hogendoorn, G.F. Versteeg, Application of the Maxwell}Stefan theory to the transport in ion-selective membranes used in the chloralkali electrolysis process, 1999.
- [85] R. Kodým, P. Pánek, D. Šnita, D. Tvrzník, K. Bouzek, Macrohomogeneous approach to a two-dimensional mathematical model of an industrial-scale electrodialysis unit, J Appl Electrochem 42 (2012) 645–666. https://doi.org/10.1007/s10800-012-0457-6.
- [86] K. Tado, F. Sakai, Y. Sano, A. Nakayama, An analysis on ion transport process in electrodialysis desalination, Desalination 378 (2016) 60–66. https://doi.org/10.1016/j.desal.2015.10.001.



[87] A.H. Galama, G. Daubaras, O.S. Burheim, H.H.M. Rijnaarts, J.W. Post, Seawater electrodialysis with preferential removal of divalent ions, J Memb Sci 452 (2014) 219–228. https://doi.org/10.1016/j.memsci.2013.10.050.

- [88] L. Firdaous, T. Saheb, J.-P. Schlumpf, J.-P. Malériat, P. Bourseau, P. Jaouen, A mathematical model of multicomponent mass transfer in electrodialysis, n.d.
- [89] B. Sun, M. Zhang, S. Huang, J. Wang, X. Zhang, Limiting concentration during batch electrodialysis process for concentrating high salinity solutions: A theoretical and experimental study, Desalination 498 (2021) 114793. https://doi.org/10.1016/j.desal.2020.114793.
- [90] J.M. Ortiz, J.A. Sotoca, E. Expósito, F. Gallud, V. García-García, V. Montiel, A. Aldaz, Brackish water desalination by electrodialysis: Batch recirculation operation modeling, J Memb Sci 252 (2005) 65–75. https://doi.org/10.1016/j.memsci.2004.11.021.
- [91] P. Pánek, R. Kodým, D. Šnita, K. Bouzek, Spatially two-dimensional mathematical model of the flow hydrodynamics in a spacer-filled channel The effect of inertial forces, J Memb Sci 492 (2015) 588–599. https://doi.org/10.1016/j.memsci.2015.03.099.
- [92] M. La Cerva, L. Gurreri, M. Tedesco, A. Cipollina, M. Ciofalo, A. Tamburini, G. Micale, Determination of limiting current density and current efficiency in electrodialysis units, Desalination 445 (2018) 138–148. https://doi.org/10.1016/J.DESAL.2018.07.028.
- [93] S. Pawlowski, V. Geraldes, J.G. Crespo, S. Velizarov, Computational fluid dynamics (CFD) assisted analysis of profiled membranes performance in reverse electrodialysis, J Memb Sci 502 (2016) 179– 190. https://doi.org/10.1016/j.memsci.2015.11.031.
- [94] J. Veerman, J.W. Post, M. Saakes, S.J. Metz, G.J. Harmsen, Reducing power losses caused by ionic shortcut currents in reverse electrodialysis stacks by a validated model, J Memb Sci 310 (2008) 418– 430. https://doi.org/10.1016/j.memsci.2007.11.032.
- [95] J. Kamcev, R. Sujanani, E.S. Jang, N. Yan, N. Moe, D.R. Paul, B.D. Freeman, Salt concentration dependence of ionic conductivity in ion exchange membranes, J Memb Sci 547 (2018) 123–133. https://doi.org/10.1016/J.MEMSCI.2017.10.024.
- [96] M.M. Generous, N.A.A. Qasem, S.M. Zubair, The significance of modeling electrodialysis desalination using multi-component saline water, Desalination (2020). https://doi.org/10.1016/j.desal.2020.114347.
- [97] M. Bdiri, L. Dammak, C. Larchet, F. Hellal, M. Porozhnyy, E. Nevakshenova, N. Pismenskaya, V. Nikonenko, Characterization and cleaning of anion-exchange membranes used in electrodialysis of polyphenol-containing food industry solutions; comparison with cation-exchange membranes, Sep Purif Technol 210 (2019) 636–650. https://doi.org/10.1016/j.seppur.2018.08.044.
- [98] R. Audinos, Fouling of ion-selective membranes during electrodialysis of grape must, J Memb Sci 41 (1989) 115–126. https://doi.org/10.1016/S0376-7388(00)82395-9.
- [99] G. Grossman, A.A. Sonin, Membrane fouling in electrodialysis: a model and experiments, Desalination 12 (1973) 107–125. https://doi.org/10.1016/S0011-9164(00)80178-2.



[100] S. Pawlowski, C.F. Galinha, J.G. Crespo, S. Velizarov, Prediction of reverse electrodialysis performance by inclusion of 2D fluorescence spectroscopy data into multivariate statistical models, Sep Purif Technol 150 (2015) 159–169. https://doi.org/10.1016/j.seppur.2015.06.032.

- [101] M.L. La Cerva, M. Di Liberto, L. Gurreri, A. Tamburini, A. Cipollina, G. Micale, M. Ciofalo, Coupling CFD with a one-dimensional model to predict the performance of reverse electrodialysis stacks, J Memb Sci 541 (2017) 595–610. https://doi.org/10.1016/j.memsci.2017.07.030.
- [102] A. Al-Jubainawi, Z. Ma, Y. Guo, L.D. Nghiem, P. Cooper, W. Li, Factors governing mass transfer during membrane electrodialysis regeneration of LiCl solution for liquid desiccant dehumidification systems, Sustain Cities Soc 28 (2017) 30–41. https://doi.org/10.1016/j.scs.2016.08.021.
- [103] M. Zhao, J. Chen, H. Zhu, Mass transfer simulation of main species in swine biogas slurry in bipolar membrane electrodialysis, in: IOP Conf Ser Earth Environ Sci, Institute of Physics Publishing, 2020: p. 052049. https://doi.org/10.1088/1755-1315/546/5/052049.
- [104] R. Kodým, M. Drakselová, P. Pánek, M. Němeček, D. Šnita, K. Bouzek, Novel approach to mathematical modeling of the complex electrochemical systems with multiple phase interfaces, Electrochim Acta 179 (2015) 538–555. https://doi.org/10.1016/j.electacta.2015.01.039.
- [105] B. Kim, S. Choi, V.S. Pham, R. Kwak, J. Han, Energy efficiency enhancement of electromembrane desalination systems by local flow redistribution optimized for the asymmetry of cation/anion diffusivity, J Memb Sci 524 (2017) 280–287. https://doi.org/10.1016/j.memsci.2016.11.046.
- [106] Z. Jalili, J.G. Pharoah, O.S. Burheim, K.E. Einarsrud, Temperature and velocity effects on mass and momentum transport in spacer-filled channels for reverse electrodialysis: A numerical study, Energies (Basel) 11 (2018). https://doi.org/10.3390/en11082028.
- [107] M.C. Hatzell, B.E. Logan, Evaluation of flow fields on bubble removal and system performance in an ammonium bicarbonate reverse electrodialysis stack, J Memb Sci 446 (2013) 449–455. https://doi.org/10.1016/j.memsci.2013.06.019.
- [108] B. Estifanos, A. Gross, X. Xu, P. Xu, Simulation of flow through spacer of bench-scale electrodialysis desalination stack, in: AIAA Scitech 2020 Forum, American Institute of Aeronautics and Astronautics Inc, AIAA, 2020. https://doi.org/10.2514/6.2020-1802.
- [109] F. Dong, D. Jin, S. Xu, L. Xu, X. Wu, P. Wang, Q. Leng, R. Xi, Numerical simulation of flow and mass transfer in profiled membrane channels for reverse electrodialysis, Chemical Engineering Research and Design 157 (2020) 77–91. https://doi.org/10.1016/j.cherd.2020.02.025.
- [110] A. Chandra, D. Pathiwada, S. Chattopadhyay, COMSOL simulation and experimental validation of promoter geometries facilitating citric acid transport in electrodialysis, Chemical Engineering Research and Design 142 (2019) 386–411. https://doi.org/10.1016/j.cherd.2018.12.024.
- [111] K. Bawornruttanaboonya, S. Devahastin, T. Yoovidhya, N. Chindapan, Mathematical modeling of transport phenomena and quality changes of fish sauce undergoing electrodialysis desalination, J Food Eng 159 (2015) 76–85. https://doi.org/10.1016/j.jfoodeng.2015.03.014.



[112] G. Battaglia, L. Gurreri, A. Cipollina, A. Pirrotta, S. Velizarov, M. Ciofalo, G. Micale, Fluid-structure interaction and flow redistribution in membrane-bounded channels, Energies (Basel) 12 (2019). https://doi.org/10.3390/en12224259.

- [113] Z. Zourmand, F. Faridirad, N. Kasiri, T. Mohammadi, Mass transfer modeling of desalination through an electrodialysis cell, Desalination 359 (2015) 41–51. https://doi.org/10.1016/j.desal.2014.12.008.
- [114] Y. Zhao, H. Wang, C. Jiang, L. Wu, T. Xu, Electrodialysis with notched ion exchange membranes: Experimental investigations and computational fluid dynamics simulations, Sep Purif Technol 130 (2014) 102–111. https://doi.org/10.1016/j.seppur.2014.04.010.
- [115] Y. Sun, J. Li, M. Li, Z. Ma, X. Wang, Q. Wang, X. Wang, D. Xu, J. Gao, X. Gao, Towards improved hydrodynamics of the electrodialysis (ED) cell via computational fluid dynamics and cost estimation model: Effects of spacer parameters, Sep Purif Technol 254 (2021) 117599. https://doi.org/10.1016/j.seppur.2020.117599.
- [116] S. Pawlowski, T. Rijnaarts, M. Saakes, K. Nijmeijer, J.G. Crespo, S. Velizarov, Improved fluid mixing and power density in reverse electrodialysis stacks with chevron-profiled membranes, J Memb Sci 531 (2017) 111–121. https://doi.org/10.1016/j.memsci.2017.03.003.
- [117] R. Kodým, F. Vlasák, D. Šnita, A. Černín, K. Bouzek, Spatially two-dimensional mathematical model of the flow hydrodynamics in a channel filled with a net-like spacer, J Memb Sci 368 (2011) 171–183. https://doi.org/10.1016/j.memsci.2010.11.042.
- [118] Z. Jalili, O.S. Burheim, K.E. Einarsrud, Computational Fluid Dynamics Modeling of the Resistivity and Power Density in Reverse Electrodialysis: A Parametric Study, Membranes (Basel) 10 (2020) 209. https://doi.org/10.3390/membranes10090209.
- [119] R. Enciso, J.A. Delgadillo, O. Domínguez, I. Rodríguez-Torres, Analysis and validation of the hydrodynamics of an electrodialysis cell using computational fluid dynamics, Desalination 408 (2017) 127–132. https://doi.org/10.1016/j.desal.2017.01.015.
- [120] M. Ciofalo, M. Di Liberto, L. Gurreri, M. La Cerva, L. Scelsi, G. Micale, Mass transfer in ducts with transpiring walls, Int J Heat Mass Transf 132 (2019) 1074–1086. https://doi.org/10.1016/j.ijheatmasstransfer.2018.12.059.
- [121] Battaglia, Gurreri, Farulla, Cipollina, Pirrotta, Micale, Ciofalo, Membrane Deformation and Its Effects on Flow and Mass Transfer in the Electromembrane Processes, Int J Mol Sci 20 (2019) 1840. https://doi.org/10.3390/ijms20081840.
- [122] G. Battaglia, L. Gurreri, G.A. Farulla, A. Cipollina, A. Pirrotta, G. Micale, M. Ciofalo, Pressure-induced deformation of pillar-type profiled membranes and its effects on flow and mass transfer, Computation 7 (2019). https://doi.org/10.3390/computation7020032.
- [123] L. Gurreri, A. Tamburini, A. Cipollina, G. Micale, M. Ciofalo, CFD prediction of concentration polarization phenomena in spacer-filled channels for reverse electrodialysis, J Memb Sci 468 (2014) 133–148. https://doi.org/10.1016/j.memsci.2014.05.058.



[124] A. Fazlali, V.G. Khondabi, A. Tayyebi, M.K. Moraveji, CFD simulation of seawater desalination through a rectangular electrodialysis cell, Desalination Water Treat 139 (2019) 88–94. https://doi.org/10.5004/dwt.2019.23178.

- [125] J.G.D. Tadimeti, V. Kurian, A. Chandra, S. Chattopadhyay, Corrugated membrane surfaces for effective ion transport in electrodialysis, J Memb Sci 499 (2016) 418–428. https://doi.org/10.1016/j.memsci.2015.11.001.
- [126] L. Gurreri, A. Tamburini, A. Cipollina, G. Micale, M. Ciofalo, Flow and mass transfer in spacer-filled channels for reverse electrodialysis: a CFD parametrical study, J Memb Sci 497 (2016) 300–317. https://doi.org/10.1016/j.memsci.2015.09.006.
- [127] S. Pawlowski, J.G. Crespo, S. Velizarov, Profiled Ion Exchange Membranes: A Comprehensible Review, International Journal of Molecular Sciences 2019, Vol. 20, Page 165 20 (2019) 165. https://doi.org/10.3390/IJMS20010165.
- [128] M. Ciofalo, M. La Cerva, M. Di Liberto, A. Tamburini, Influence of the boundary conditions on heat and mass transfer in spacer-filled channels, in: J Phys Conf Ser, Institute of Physics Publishing, 2017. https://doi.org/10.1088/1742-6596/923/1/012053.
- [129] C.P. Koutsou, S.G. Yiantsios, A.J. Karabelas, Direct numerical simulation of flow in spacer-filled channels: Effect of spacer geometrical characteristics, J Memb Sci 291 (2007) 53–69. https://doi.org/10.1016/J.MEMSCI.2006.12.032.
- [130] R. Pärnamäe, S. Mareev, V. Nikonenko, S. Melnikov, N. Sheldeshov, V. Zabolotskii, H.V.M. Hamelers, M. Tedesco, Bipolar membranes: A review on principles, latest developments, and applications, J Memb Sci 617 (2021) 118538. https://doi.org/10.1016/J.MEMSCI.2020.118538.
- [131] D. V. Golubenko, A.B. Yaroslavtsev, Effect of current density, concentration of ternary electrolyte and type of cations on the monovalent ion selectivity of surface-sulfonated graft anion-exchange membranes: modelling and experiment, J Memb Sci 635 (2021) 119466. https://doi.org/10.1016/J.MEMSCI.2021.119466.
- [132] V.A. Shaposhnik, V.I. Vasil'eva, E. V. Reshetnikova, Concentration polarization of ion-exchange membranes in electrodialysis: An interferometric study, Russian Journal of Electrochemistry 36 (2000) 773–777. https://doi.org/10.1007/BF02757679.
- [133] L. Gurreri, A. Tamburini, A. Cipollina, G. Micale, CFD analysis of the fluid flow behavior in a reverse electrodialysis stack, Desalination Water Treat 48 (2012) 390–403. https://doi.org/10.1080/19443994.2012.705966.
- [134] M.R. Cruz-Díaz, A. Laureano, F.A. Rodríguez, L.F. Arenas, J. J. H. Pijpers, E.P. Rivero, Modelling of flow distribution within spacer-filled channels fed by dividing manifolds as found in stacks for membrane-based technologies, Chemical Engineering Journal 423 (2021) 130232. https://doi.org/10.1016/J.CEJ.2021.130232.
- [135] W. Li, P. Hrnjak, Single-phase flow distribution in plate heat exchangers: Experiments and models, International Journal of Refrigeration 126 (2021) 45–56. https://doi.org/10.1016/J.IJREFRIG.2021.01.026.



[136] A. Muhana, D.R. Novog, Validation of FLUENT for Prediction of Flow Distribution and Pressure Gradients in a Multi-Branch Header Under Low Flow Conditions, International Conference on Nuclear Engineering, Proceedings, ICONE 2 (2009) 221–226. https://doi.org/10.1115/ICONE16-48128.

- [137] S. Maharudrayya, S. Jayanti, A.P. Deshpande, Flow distribution and pressure drop in parallel-channel configurations of planar fuel cells, J Power Sources 144 (2005) 94–106. https://doi.org/10.1016/J.JPOWSOUR.2004.12.018.
- [138] R.J. Kee, P. Korada, K. Walters, M. Pavol, A generalized model of the flow distribution in channel networks of planar fuel cells, J Power Sources 109 (2002) 148–159. https://doi.org/10.1016/S0378-7753(02)00090-3.
- [139] J. Wang, Pressure drop and flow distribution in parallel-channel configurations of fuel cells: U-type arrangement, Int J Hydrogen Energy 33 (2008) 6339–6350. https://doi.org/10.1016/J.IJHYDENE.2008.08.020.
- [140] J. Wang, Pressure drop and flow distribution in parallel-channel configurations of fuel cells: Z-type arrangement, Int J Hydrogen Energy 35 (2010) 5498–5509. https://doi.org/10.1016/J.IJHYDENE.2010.02.131.
- [141] B. Kumar, S.N. Singh, Study of pressure drop in single pass U-type plate heat exchanger, Exp Therm Fluid Sci 87 (2017) 40–49. https://doi.org/10.1016/J.EXPTHERMFLUSCI.2017.04.028.
- [142] S. Al-Zahrani, M.S. Islam, S.C. Saha, Comparison of flow resistance and port maldistribution between novel and conventional plate heat exchangers, International Communications in Heat and Mass Transfer 123 (2021) 105200. https://doi.org/10.1016/J.ICHEATMASSTRANSFER.2021.105200.
- [143] M.K. Bassiouny, H. Martin, Flow distribution and pressure drop in plate heat exchangers—I U-type arrangement, Chem Eng Sci 39 (1984) 693–700. https://doi.org/10.1016/0009-2509(84)80176-1.
- [144] I. Rubinstein, E. Staude, O. Kedem, Role of the membrane surface in concentration polarization at ion-exchange membrane, Desalination 69 (1988) 101–114. https://doi.org/10.1016/0011-9164(88)80013-4.
- [145] Y. Tanaka, Limiting current density of an ion-exchange membrane and of an electrodialyzer, J Memb Sci 266 (2005) 6–17. https://doi.org/10.1016/J.MEMSCI.2005.05.005.
- [146] Y. Tanaka, A computer simulation of continuous ion exchange membrane electrodialysis for desalination of saline water, Desalination 249 (2009) 809–821. https://doi.org/10.1016/J.DESAL.2009.04.011.
- [147] Y. Tanaka, A computer simulation of feed and bleed ion exchange membrane electrodialysis for desalination of saline water, Desalination 254 (2010) 99–107. https://doi.org/10.1016/J.DESAL.2009.12.008.
- [148] A. Tamburini, M. Renda, A. Cipollina, G. Micale, M. Ciofalo, Investigation of heat transfer in spacer-filled channels by experiments and direct numerical simulations, Int J Heat Mass Transf 93 (2016) 1190–1205. https://doi.org/10.1016/J.IJHEATMASSTRANSFER.2015.11.034.



[149] T. Brown, H.E. Jr, B. LeMay, J. Catherine, Chemistry: The Central Science: AP Edition, (2015).

- [150] M.K. Bassiouny, H. Martin, Flow distribution and pressure drop in plate heat exchangers—II Z-type arrangement, Chem Eng Sci 39 (1984) 701–704. https://doi.org/10.1016/0009-2509(84)80177-3.
- [151] J. Ledingham, K.L. Sedransk Campbell, B. In 't Veen, L. Keyzer, A.N. Campbell, Barriers to electrodialysis implementation: Maldistribution and its impact on resistance and limiting current density, Desalination 531 (2022) 115691. https://doi.org/10.1016/J.DESAL.2022.115691.
- [152] J. Stefanini, G. Cognet, J.C. Vila, B. Merite, Y. Brenier, A colored method for PIV technique, (1992). https://doi.org/10.1007/978-94-011-2690-8 14.
- [153] The Engineering ToolBox, Water Dynamic (Absolute) and Kinematic Viscosity vs. Temperature and Pressure. [online] Available at: https://www.engineeringtoolbox.com/water-dynamic-kinematic-viscosity-d_596.html [Accessed 21st August 2024], (2004).
- [154] D. Di Carlo, Inertial microfluidics, (2009). https://doi.org/10.1039/b912547g.
- [155] M.S. Isaacson, A.A. Sonin, Sherwood Number and Friction Factor Correlations for Electrodialysis Systems, with Application to Process Optimization, Industrial and Engineering Chemistry Process Design and Development 15 (1976) 313–321. https://doi.org/10.1021/I260058A017/ASSET/I260058A017.FP.PNG_V03.
- [156] A. Culcasi, L. Gurreri, A. Zaffora, A. Cosenza, A. Tamburini, A. Cipollina, G. Micale, Ionic shortcut currents via manifolds in reverse electrodialysis stacks, Desalination 485 (2020). https://doi.org/10.1016/j.desal.2020.114450.
- [157] H. Fan, Y. Huang, N.Y. Yip, Advancing ion-exchange membranes to ion-selective membranes: principles, status, and opportunities, Frontiers of Environmental Science & Engineering 2023 17:2 17 (2022) 1–27. https://doi.org/10.1007/S11783-023-1625-0.
- [158] F. Scholz, Books on Fundamental Electrochemistry and Electroanalytical Techniques, Electroanalytical Methods (2010) 343–345. https://doi.org/10.1007/978-3-642-02915-8_19.
- [159] Poisson, Mémoire sur la théorie du magnétisme en mouvement, Mémoires de l'Académie Royale Des Sciences de l'Institut de France (1823) 441–570.
- [160] M.K. Urtenov, A.M. Uzdenova, A. V. Kovalenko, V. V. Nikonenko, N.D. Pismenskaya, V.I. Vasil'eva, P. Sistat, G. Pourcelly, Basic mathematical model of overlimiting transfer enhanced by electroconvection in flow-through electrodialysis membrane cells, J Memb Sci 447 (2013) 190–202. https://doi.org/10.1016/J.MEMSCI.2013.07.033.
- [161] W. Kujawski, A. Yaroshchuk, E. Zholkovskiy, I. Koter, S. Koter, Analysis of membrane transport equations for reverse electrodialysis (Red) using irreversible thermodynamics, Int J Mol Sci 21 (2020) 1–13. https://doi.org/10.3390/ijms21176325.
- [162] K.G. Nayar, P. Sundararaman, C.L. O'Connor, J.D. Schacherl, M.L. Heath, M.O. Gabriel, S.R. Shah, N.C. Wright, A.G. Winter, V, Feasibility study of an electrodialysis system for in-home water



desalination in urban India, Dev Eng 2 (2017) 38–46. https://doi.org/10.1016/J.DEVENG.2016.12.001.

- [163] H. Fan, Y. Huang, I.H. Billinge, S.M. Bannon, G.M. Geise, N.Y. Yip, Counterion Mobility in Ion-Exchange Membranes: Spatial Effect and Valency-Dependent Electrostatic Interaction, ACS ES and T Engineering 2 (2022) 1274–1286. https://doi.org/https://doi.org/10.1021/acsestengg.1c00457.
- [164] Julius Tafel, Über die Polarisation bei kathodischer Wasserstoffentwicklung, Zeitschrift Für Physikalische Chemie 50 (1905) 641–712.
- [165] A. Einstein, Über die von der molekularkinetischen Theorie der Wärme geforderte Bewegung von in ruhenden Flüssigkeiten suspendierten Teilchen, Ann Phys 322 (1905) 549–560.
- [166] M. von Smoluchowski, Zur kinetischen Theorie der Brownschen Molekularbewegung und der Suspensionen, Ann Phys 326 (1906) 756–780.
- [167] P. Fievet, Donnan Effect, in: Encyclopedia of Membranes, Springer Berlin Heidelberg, 2014: pp. 1–3. https://doi.org/10.1007/978-3-642-40872-4 1714-1.
- [168] J. Nielsen, A. Adamson, J. Cobble, The Self-diffusion Coefficients of the Ions in Aqueous Sodium Chloride and Sodium Sulfate at 25°, (1952).
- [169] A.A. Moya, Electrochemical Impedance of Ion-Exchange Membranes with Interfacial Charge Transfer Resistances, (2016). https://doi.org/10.1021/acs.jpcc.5b12087.
- [170] I. Renewable Energy Agency, Renewable Power Generation Costs in 2022, (2023). www.irena.org (accessed January 23, 2024).
- [171] IEA, World Energy Balances, (2019). https://www.iea.org/reports/world-energy-balances-overview/world (accessed January 23, 2024).
- [172] O. Edenhofer, Y. Sokona, J.C. Minx, E. Farahani, S. Kadner, K. Seyboth, A. Adler, I. Baum, S. Brunner, B. Kriemann, J. Savolainen Web Manager Steffen Schlömer, C. von Stechow, T. Zwickel Senior Scientist, Climate Change 2014 Mitigation of Climate Change Working Group III Contribution to the Fifth Assessment Report of the Intergovernmental Panel on Climate Change Edited by, (2014). www.cambridge.org (accessed January 23, 2024).
- [173] M. Wei, C.A. McMillan, S. de la Rue du Can, Electrification of Industry: Potential, Challenges and Outlook, Current Sustainable/Renewable Energy Reports 6 (2019) 140–148. https://doi.org/10.1007/S40518-019-00136-1/TABLES/1.
- [174] J. Deason, M. Wei, G. Leventis, S. Smith, L. Schwartz, Electrification of buildings and industry in the United States Drivers, barriers, prospects, and policy approaches, (2018).
- [175] L. Chen, Q. Xu, S.Z. Oener, K. Fabrizio, S.W. Boettcher, Design principles for water dissociation catalysts in high-performance bipolar membranes, Nature Communications 2022 13:1 13 (2022) 1–10. https://doi.org/10.1038/s41467-022-31429-7.



[176] T. Chen, J. Bi, Z. Ji, J. Yuan, Y. Zhao, Application of bipolar membrane electrodialysis for simultaneous recovery of high-value acid/alkali from saline wastewater: An in-depth review, Water Res 226 (2022) 119274. https://doi.org/10.1016/j.watres.2022.119274.

- [177] C. Huang, T. Xu, Electrodialysis with bipolar membranes for sustainable development, Environ Sci Technol 40 (2006) 5233–5243. https://doi.org/10.1021/ES060039P/ASSET/IMAGES/LARGE/ES060039PF00008.JPEG.
- [178] A. Culcasi, L. Gurreri, A. Cipollina, A. Tamburini, G. Micale, A comprehensive multi-scale model for bipolar membrane electrodialysis (BMED), Chemical Engineering Journal 437 (2022) 135317. https://doi.org/10.1016/J.CEJ.2022.135317.
- [179] J.L. Gineste, G. Pourcelly, Y. Lorrain, F. Persin, C. Gavach, Analysis of factors limiting the use of bipolar membranes: a simplified model to determine trends, J Memb Sci 112 (1996) 199–208. https://doi.org/10.1016/0376-7388(95)00284-7.
- [180] S. Koter, A. Warszawski, A new model for characterization of bipolar membrane electrodialysis of brine, Desalination 198 (2006) 111–123. https://doi.org/10.1016/J.DESAL.2006.09.016.
- [181] M.P. Mier, R. Ibañez, I. Ortiz, Influence of ion concentration on the kinetics of electrodialysis with bipolar membranes, Sep Purif Technol 59 (2008) 197–205. https://doi.org/10.1016/J.SEPPUR.2007.06.015.
- [182] E. Vera, J. Sandeaux, F. Persin, G. Pourcelly, M. Dornier, J. Ruales, Modeling of clarified tropical fruit juice deacidification by electrodialysis, J Memb Sci 326 (2009) 472–483. https://doi.org/10.1016/J.MEMSCI.2008.10.034.
- [183] L. Shi, Y. Hu, S. Xie, G. Wu, Z. Hu, X. Zhan, Recovery of nutrients and volatile fatty acids from pig manure hydrolysate using two-stage bipolar membrane electrodialysis, Chemical Engineering Journal 334 (2018) 134–142. https://doi.org/10.1016/J.CEJ.2017.10.010.
- [184] S.S. Melnikov, O.A. Mugtamov, V.I. Zabolotsky, Study of electrodialysis concentration process of inorganic acids and salts for the two-stage conversion of salts into acids utilizing bipolar electrodialysis, Sep Purif Technol 235 (2020) 116198. https://doi.org/10.1016/J.SEPPUR.2019.116198.
- [185] S. Mafé, P. Ramírez, A. Alcaraz, Electric field-assisted proton transfer and water dissociation at the junction of a fixed-charge bipolar membrane, Chem Phys Lett 294 (1998) 406–412. https://doi.org/10.1016/S0009-2614(98)00877-X.
- [186] J. Schiffbauer, N.Y. Ganchenko, G.S. Ganchenko, E.A. Demekhin, Overlimiting current due to electro-diffusive amplification of the second Wien effect at a cation-anion bipolar membrane junction, Biomicrofluidics 12 (2018). https://doi.org/10.1063/1.5066195/133883.
- [187] A. Ortega, L.F. Arenas, J.J.H. Pijpers, D.L. Vicencio, J.C. Martínez, F.A. Rodríguez, E.P. Rivero, Modelling water dissociation, acid-base neutralization and ion transport in bipolar membranes for acid-base flow batteries, J Memb Sci 641 (2022) 119899. https://doi.org/10.1016/J.MEMSCI.2021.119899.



[188] T. León, J. López, R. Torres, J. Grau, L. Jofre, J.L. Cortina, Describing ion transport and water splitting in an electrodialysis stack with bipolar membranes by a 2-D model: Experimental validation, J Memb Sci 660 (2022) 120835. https://doi.org/10.1016/J.MEMSCI.2022.120835.

- [189] Y. Wang, A. Wang, X. Zhang, T. Xu, Simulation of electrodialysis with bipolar membranes: Estimation of process performance and energy consumption, Ind Eng Chem Res 50 (2011) 13911–13921. https://doi.org/10.1021/IE200467S/ASSET/IMAGES/LARGE/IE-2011-00467S 0008.JPEG.
- [190] C. Jiang, S. Li, D. Zhang, Z. Yang, D. Yu, X. Chen, Y. Wang, T. Xu, Mathematical modelling and experimental investigation of CO2 absorber recovery using an electro-acidification method, Chemical Engineering Journal 360 (2019) 654–664. https://doi.org/10.1016/J.CEJ.2018.12.006.
- [191] S. Koter, Modeling of weak acid production by the EDB method, Sep Purif Technol 57 (2007) 406–412. https://doi.org/10.1016/J.SEPPUR.2006.03.005.
- [192] J. Ledingham, K.L. Sedransk Campbell, B. in 't Veen, L. Keyzer, N.Y. Yip, A.N. Campbell, The development and validation of a novel, parameter-free, modelling strategy for electromembrane processes: Electrodialysis, Desalination 576 (2024) 117386. https://doi.org/10.1016/J.DESAL.2024.117386.
- $[193] \qquad \text{G.S.} \qquad \text{Ohm,} \qquad \text{Die} \qquad \text{galvanische} \qquad \text{Kette,} \qquad \text{Bei} \qquad \text{T.H.} \qquad \text{Riemann,} \qquad 1827. \\ \qquad \qquad \text{https://doi.org/} 10.5479/\text{sil.}354716.39088005838644.}$
- [194] H. Strathmann, H.J. Rapp, B. Bauer, C.M. Bell, Theoretical and practical aspects of preparing bipolar membranes, Desalination 90 (1993) 303–323. https://doi.org/10.1016/0011-9164(93)80183-N.
- [195] L. Chen, Q. Xu, S.W. Boettcher, Kinetics and mechanism of heterogeneous voltage-driven water-dissociation catalysis, Joule 7 (2023) 1867–1886. https://doi.org/10.1016/J.JOULE.2023.06.011.
- [196] S. Honarparvar, D. Reible, Modeling multicomponent ion transport to investigate selective ion removal in electrodialysis, Environmental Science and Ecotechnology 1 (2020) 100007. https://doi.org/10.1016/J.ESE.2019.100007.
- [197] A.R. Khare, N.A. Peppas, Swelling/deswelling of anionic copolymer gels, Biomaterials 16 (1995) 559–567. https://doi.org/10.1016/0142-9612(95)91130-Q.
- [198] A.E. Kozmai, V. V. Nikonenko, S. Zyryanova, N.D. Pismenskaya, L. Dammak, A simple model for the response of an anion-exchange membrane to variation in concentration and pH of bathing solution, J Memb Sci 567 (2018) 127–138. https://doi.org/10.1016/J.MEMSCI.2018.07.007.
- [199] H. Roux-de Balmann, M. Bailly, F. Lutin, P. Aimar, Modelling of the conversion of weak organic acids by bipolar membrane electrodialysis, Desalination 149 (2002) 399–404. https://doi.org/10.1016/S0011-9164(02)00863-9.
- [200] G.E.P. Box, N.R. Draper, Empirical Model-Building and Response Surfaces, (1987) 1–669.



Jack Ledingham 2024

</thesis>

